Real-time exploratory dynamics, control and monitoring of dynamical systems on differentiable manifolds

THESIS

Submitted in partial fulfillment of the requirements

for the degree of

Doctorate of Philosophy

in the

Civil Engineering

with specialization in *Structural Engineering*

by

Satyam Panda

196104027

Under the Supervision of

Dr. Budhaditya Hazra

DEPARTMENT OF CIVIL ENGINEERING

INDIAN INSTITUTE OF TECHNOLOGY GUWAHATI

June, 2023

Certificate

This is to certify that the thesis titled, "***Real-time exploratory dynamics, control and monitoring of dynamical systems on differentiable manifolds***", submitted by Mr. Satyam Panda – 196104027, a research scholar in the *Department of Civil Engineering, Indian Institute of Technology, Guwahati*, for the award of the degree of Doctor of Philosophy, is a record of an original research work carried out by him under my supervision and guidance. The thesis has fulfilled all requirements as per the regulations of the institute and in my opinion has reached the standard needed for submission. The results embodied in this thesis have not been submitted to any other University or Institute for the award of any degree or diploma.

Signed: Budhaditya Hazra

Supervisor: Dr. Budhaditya Hazra,
Department of Civil Engineering,
Indian Institute of Technology Guwahati,
Guwahati–781039, Assam, India.

Place:
Date: IIT Guwahati, June-13, 2024.

Abstract

This thesis provides insights into three essential areas: real-time modal identification, dynamics of stochastic systems on configuration manifolds, and their subsequent damage detection. The work first introduces an innovative error-adaptive approach for real-time modal identification, premised on first-order eigen perturbation techniques, which exhibit quicker convergence compared to the existing algorithms. This approach proves to be adaptable, independent of sampling frequency, and effective in real-time modal control applications. This development serves as a foundational step towards the domain of health monitoring for systems that evolves on smooth differentiable manifolds. To facilitate effective health monitoring of such manifold-based systems, the establishment of a robust geometric preserving simulation strategy is essential. To this end, for the solution of stochastic systems on manifolds, the study proposes a novel method, leveraging an Ito-Taylor expansion and manifold-tangent space isomorphism, to accurately estimate higher-order terms and maintain geometric characteristics. Using benchmark case studies and concrete examples, this method is shown to be efficient in significant reduction in global error for coarser time steps thus reducing the computational costs particularly for systems evolving on the S^2 manifold under stochastic excitation. The research further introduces a framework for studying stochastic Hamiltonian systems on manifolds, involving stochastic Hamiltonian differential equations (SHDEs) and Ito-Taylor expansion-based numerical integration, resulting in accurate response trajectory computation while preserving geometric integrity and symplecticity. The formulation of SHDEs and geometric symplectic numerical integration scheme are extended towards general class of manifolds using metric tensor and intrinsic formulation. The system responses obtained using the proposed formulations, provide crucial data inputs for monitoring the health and performance of the system under consideration. Finally, a damage detection algorithm namely Recursive Principal Geodesic Analysis (RPGA), is proposed for systems evolving on configuration manifolds, successfully identifying anomalies, as demonstrated in the case of spherical pendulum, stochastic duffing oscillator on S^2 and inverted spherical pendulum-cart system. These findings collectively advance the understanding of structural dynamics, thus offering versatile tools and methodologies for real-time structural health monitoring and geometric symplectic analysis of stochastic systems on manifolds.

Acknowledgements

First, I would like to express my sincere thanks and gratitude to my supervisor, Dr. Budhaditya Hazra, for his inspirational guidance. My PhD has been an amazing experience and I thank Dr. Hazra wholeheartedly, not only for his tremendous academic support but also for his wonderful mentorship and bestowing me with so many amazing opportunities. The joy and enthusiasm he has for his research was motivational for me, even during tough times in the PhD pursuit, which instilled in me with a right attitude and impetus needed to complete the work on time. My sincere thanks to Dr. Arbind Kumar Singh, Dr. Amit Balasaheb Shelke, and Dr. Atanu Banerjee, for serving on my thesis committee.

Profound thanks to my collaborator, Dr. Vikram Pakrashi (University College Dublin, Ireland), for providing his insightful comments and valuable suggestions from time-to-time. The jovial conversations with him were instrumental in avoiding pitfalls that helped me immensely in approaching problems with a different perspective.

I extend my heartfelt gratitude to my research companions, Ankush Gogoi and Tapas Tripura. Tapas Da, your guidance and mentorship have been invaluable throughout this journey. Ankush has not only been a dedicated colleague but also a great friend who stood by me through all my ups and downs. Your insightful comments, critical feedback, and invaluable suggestions during thesis preparation were instrumental. Your unwavering support, whether in drafting or coding sessions, within our engaging environment, deserves deep acknowledgment. I also appreciate the contributions of Ayush Thakur, Mussa Kalimullah, Shivam Ojha, Naina Deb, and Dasari Shivakumar for making this journey memorable. My fond memories of our time together will forever hold a special place in my heart.

In the midst of challenging days filled with frustrations and disappointments, your unwavering presence, Sanjana, has been my constant source of strength. Thank you for always being there for me, for sharing my joys and sorrows, and for being an integral part of this journey.

With the unwavering love of my mother, the guidance of my father, and the unwavering support of my sister, Sneha Panda, I could not have completed this remarkable journey. Expressing my gratitude to my parents is an impossible task as their unconditional encouragement, boundless patience, limitless love, and steadfast support have been the bedrock of everything I have ever undertaken. Without their unwavering emotional support, this endeavor would have remained a distant dream.

Dedication

Dedicated to my loving parents,
whose unwavering support and endless love
have been my guiding light.

To my dear sister, Sneha Panda,
for her constant belief in me
and unwavering encouragement.

And, Sanjana Agrawal,
whose presence and support
have made this journey
even more meaningful.

Contents

List of Figures

List of Tables

List of Abbreviations

SDOF	Single degree–of–freedom
MDOF	Multi degree–of–freedom
DOF	Degree–of–freedom
AR	Auto Regressive
EVD	Eigen Value Decomposition
FOEP	First order Eigen Perturbation
LNM	Linear Normal Mode
MDOF	Multi Degree of Freedom
PC	Principle Component
POC	Principal Orthogonal Component
POM	Proper Orthogonal Mode
POV	Proper Orthogonal Values
RSSA	Recursive Singular Spectram Analysis
SSA	Singular Spectram Analysis
TVAR	Time Varying Auto Regressive
TMD	Tuned Mass Damper
MTMD	Multi Tuned Mass Damper
MSI	Multiple stochastic Integrals
ODE	Ordinary Differential Equation
SDE	Stochastic differential equation
GSDE	Geometric stochastic differential equation

General Notations

$\mathbf{R}_x$	Covariance matrix
$\mathbf{R}_Q$	Modal Covariance matrix
$\mathbf{R}_{\mathcal{P}}$	POC Covariance matrix
$\mathbf{V}$	Eigen vector matrix
$\mathbf{\Lambda}$	Eigen value matrix
α, $\mathcal{P}$	Proper Orthogonal Component
Δ_V, Δ_Λ	Perturbation matrices
$\mathbf{H}^Q(t-\tau)$	Impulse response matrix
$F^Q(\tau)$	Modal response vector
$\mathbf{W}$	Proper Orthogonal Mode matrix
$\mathbf{\Gamma}$	Principal Orthogonal Value matrix
$\mathcal{E}$	Perturbation error
a_1,a_2	Time varying AR coefficients
μ_k	recursive mean
$\mathbf{P}$, $\mathbf{\Upsilon}$	Eigenspace update
$\tilde{\mathbf{P}}$, $\tilde{\mathbf{\Upsilon}}$	Corrected Eigenspace update
$\mathbf{G}_k$	Error feedback matrix
$\mathbf{P}$	Total perturbation
$W_{\mathcal{P}}(k)$	Measurement noise
$W_f(k)$	Process noise
S^2	Unit two-sphere manifold embedded in $\mathbb{R}^3$
$\left(\mathrm{S}^2\right)^n$	N-fold unit two-sphere manifold, i.e. $\mathrm{S}^2 \times \ldots \times \mathrm{S}^2$
$\mathrm{SO}(3)$	Special orthogonal group, subset of Lie group $\mathcal{G}$

$\mathfrak{so}(3)$	Special orthogonal group, subset of Lie algebra $\mathfrak{g}$
$\mathrm{T}_q M$	Tangent space of the manifold M at $q \in$ M
$\mathrm{T}_q^* M$	Co-tangent space of the manifold M at $q \in$ M
$\mathrm{T}M$	Tangent bundle of the manifold M
T^*M	Co-tangent bundle of the manifold M
$\frac{\partial \mathbf{A}(q)}{\partial q} = \partial_q \mathbf{A}(q)$	Derivative of a matrix $\mathbf{A}(q)$ with respect to q
x	configuration vector on $\mathbb{R}^2$
$\dot{x}$	velocity vector on $\mathrm{T}_x\mathbb{R}^2$
p	Conjugate of velocity vector on $\mathrm{T}_x^*\mathbb{R}^2$
q	configuration vector on S^2
ω	Angular velocity vector on $\mathrm{T}_q\mathrm{S}^2$
π	Conjugate of angular velocity vector on $\mathrm{T}_q^*\mathrm{S}^2$
$\mathbf{R}$	Rotation matrix, configuration matrix on $\mathrm{SO}(3)$
Ω	Angular velocity vector on $\mathrm{T}_{\mathbf{R}}\mathrm{S}^2$
Π	Conjugate of angular velocity vector on $\mathrm{T}_{\mathbf{R}}^*\mathrm{S}^2$
ω^Λ	Isomorphism between $\mathrm{T}_q\mathrm{S}^2 \subset \mathbb{R}^3$ and $\mathfrak{so}(3)$
	$\omega^\Lambda q = \omega \times q \in \mathrm{T}_q\mathrm{S}^2 \subset \mathbb{R}^3$
$\mathrm{L} : \mathrm{T}M \to \mathbb{R}^1$	Lagrangian function
$\mathrm{T} : \mathrm{T}M \to \mathbb{R}^1$	Kinetic energy function
$\mathrm{V} : \mathrm{T}M \to \mathbb{R}^1$	Potential energy function
$\mathrm{H} : \mathrm{T}^*M \to \mathbb{R}^1$	Hamiltonian function
$\delta\mathbb{S}$	Infinitesimal variation δ of the action integral $\mathbb{S}$
$\exp : \mathfrak{g} \to \mathcal{G}$	Exponential map $exp_x(v)$
$\log : \mathcal{G} \to \mathfrak{g}$	Logarithmic map $log_v(x)$
$\mathrm{ad}_\eta : \mathfrak{g} \to \mathfrak{g}$	Adjoint operator
$\Im^o\mathfrak{g}$ and $\Im^r\mathfrak{g}$	Kolmogorov operators over g
$\dot{W}$	White Gaussian noise
$\partial_{\mathrm{S}_{ij}} \mathrm{e}^{\mathbf{S}} = \mathrm{dexp}_{\mathbf{S}}\left(\mathbf{E}_{ij}\right) \mathrm{e}^{\mathbf{S}}$	Derivative of an exponential
$\|\|V_x\|\|$	Local norm for $V \in T_xM$
$grad_x\psi$	Riemannian gradient of a function $\psi : \mathbb{R} \to M$ at point $x \in M$

$\nabla_v w$	Covariant derivative of a vector field $w \in TM$ in the direction of $v \in T_xM$
$P_r^{(x \to y)}$	Parallel transport operator from T_xM to T_yM
$d(x, y)$	Riemannian distance between points x and y in M

Chapter 1

Introduction

The study of dynamical phenomena has profound significance and pervasiveness in several domains, including civil engineering structures [1, 2] such as bridges, seismic events like earthquakes [3], the operation of complex machinery, large-scale infrastructures, and even within the domain of economics [4]. Further, dynamical systems find application in diverse fields like molecular dynamics [5], the control of spacecraft, celestial mechanics [6], epidemiology, and an array of other scientific and engineering disciplines. Notably, recent events such as the Chandrayaan-3 mission, an endeavor where dynamics plays a pivotal role in achieving precise lunar trajectory and landing, underscore the paramount importance of this dynamic perspective in contemporary scientific and technological developments. Most of these dynamic processes evolve within the mathematical framework of manifolds, which are complex mathematical spaces deviating from the flatness of Euclidean geometry [2, 7, 8, 9, 10]. However, attempting to analyze these intricate dynamical systems from the vantage point of Euclidean geometry often carries the risk of inadequate representation of the underlying physical phenomena. One intriguing physical phenomenon worth noting pertains to the motion of large pendulum-type Tuned Mass Dampers (PTMDs) [1, 11]. In these systems, the mass of the TMD typically comprises a substantial fraction, often in the order of 2-3$\%$ percent, of the total mass of the towering superstructure[1]. The presence of such a significant mass oscillating within a spherical manifold can introduce formidable challenges related to control and, moreover, engender complex interactions between the primary structure and the PTMDs. These intricate dynamics not only pique scientific curiosity but also hold practical implications for the effective design and operation of structures subjected to dynamic loads.

Existing literature underscores a notable challenge in the utilization of PTMDs for the control of circular towers [1, 12]. A description of the coordinates and the variables of PTMD is presented in Fig.

1.1[1]. It is to be noted that the formulation adopted by these literature are in the Euclidean space. When the frequencies of the first two orthogonal modes closely align, it becomes notably intricate to discern which specific mode the TMD is precisely tuned to and, subsequently, which mode it effectively controls. This ambiguity carries substantial implications for the optimal performance of the damping system [13]. These interactions frequently give rise to unfavorable outcomes when passive control mechanisms fall short, ultimately undermining the intended purpose of the control system. In such scenarios, a pressing need arises to delve deep into the nuanced dynamics of the spherical pendulum with a focus on geometric intricacies. A comprehensive understanding of this complex motion, coupled with precise geometric considerations, becomes imperative in order to devise effective control strategies and mitigate the unintended consequences of inadequate passive control measures. In Fig. 1.2, when comparing the trajectories of the spherical pendulum for different lateral frequency ratios, the motion exhibits elliptical paths and complex motions, particularly when the frequencies are well separated [1]. Accurate modeling of these trajectories, with the system's non-linearity and coupled nature, necessitates manifold based numerical integration, as Euclidean formulations tend to yield erroneous results in such scenarios. This precision is crucial for designing effective dampers for the structural system.

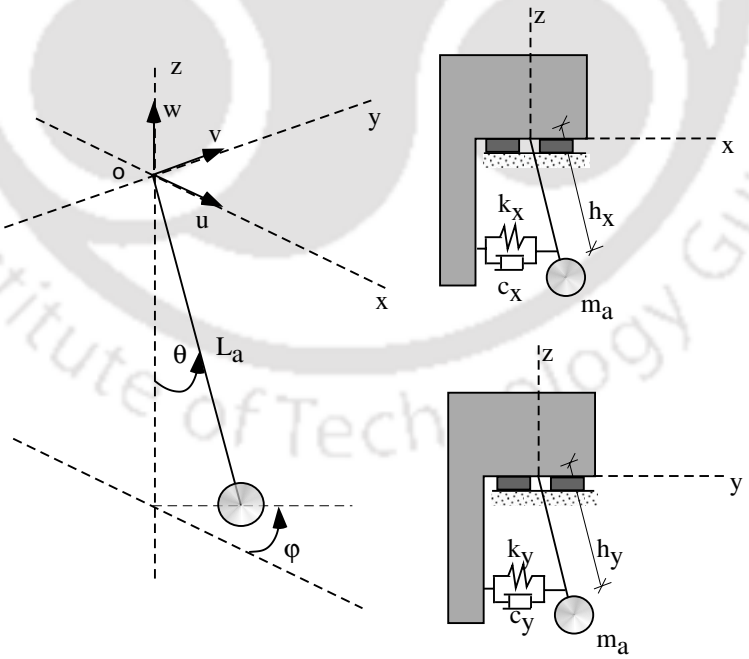

FIGURE 1.1: Geometry of the spherical PTMD coupled with the translational main structure [1]

Delving into the dynamics within the context of curved spaces offers a broader and more generalized

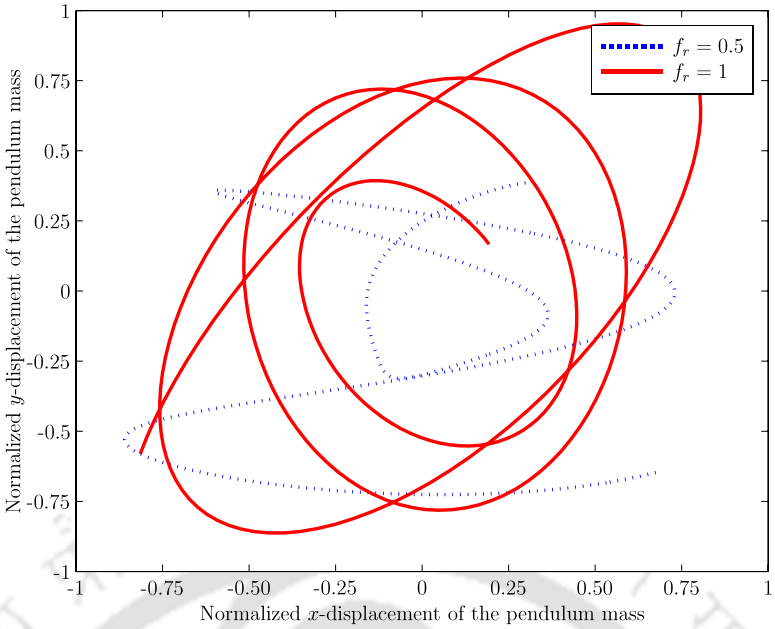

FIGURE 1.2: Complex motion of center of spherical pendulum in PTMD [1]

comprehension [9, 14], with Euclidean dynamics serving as a particular case within this broader framework[15]. Within the domain of control systems for structures, a clear dichotomy exists between active and passive control strategies [16, 17]. Notably, in recent years, a multitude of studies have been conducted to implement control strategies involving Tuned Mass Dampers (TMDs) [18], Tuned Liquid Column Dampers (TLCDs) [19], and Pendulum-type Tuned Mass Dampers (PTMDs)[12]. However, it is worth noting that these studies often overlook critical geometric considerations within their control strategies like flexible structure, systems with very large rotations, TMDs with arbitrarily large displacements, curved spaces where the system dynamics evolve, presenting a gap in the comprehensive understanding of the dynamics of these structures. These gaps are the lack of consideration regarding the dynamics of the structure with respect to geometric properties. The enduring aspect of dynamical systems pertains to the ongoing monitoring over extended periods. This need arises primarily due to the inherent presence of numerous uncertain factors in system design. Over time, these uncertainties may lead to unsatisfactory long-term performance. Addressing these challenges necessitates the exploratory dynamics in terms of linear normal modes for systems exhibiting linear behavior, non-normal modes for non-linear behaviour and a less explored yet significant aspect involves systems whose dynamics evolve on smooth geometrical surfaces.

A systematic and rational approach to addressing these complex dynamical problems involves the development of robust simulation strategies [20, 14, 21, 22, 10, 23, 24]. In cases where the dynamics of a

system can be readily expressed within the context of Euclidean planes, the existing simulation strategies within the literature often suffice. However, for systems evolving on more intricate manifolds, there exists a conspicuous gap in the available literature, thereby underscoring the pressing need for innovative and tailored simulation techniques to accurately model and analyze these complex dynamics. Towards interpretation of the realistic motion of physical systems, the incorporation of stochastic elements in dynamic simulations is imperative for a comprehensive understanding of dynamical systems. Stochasticity introduces the vital element of randomness [25, 15, 26], enabling a more realistic representation of real-world uncertainties and fluctuations that these systems often encounter. In recent years, SDEs have been utilized in the state estimation and system identification challenges that emerge in aerospace, surveying (GPS), computer vision, and robotics. These applications differ from typical ones in that the dynamics must adhere to certain geometrical limitations. This subclass is particularly interesting since the SDE evolves in a matrix Lie group [22] called geometric SDEs (GSDEs). Typical applications include predicting object motion from video sequences in computer vision, tracking [27] and modeling rigid things such as robots and satellites [2] and many others.

Fundamental challenges of numerical analysis arise when simulating geometric SDEs, system identification, or state estimation. As a result, the ability to simulate a geometric SDE in discrete-time while maintaining the geometry is required, i.e., the simulated SDE must adhere to the Lie group. As a result, practitioners must deal with the following two critical challenges. Firstly, there is a wide range of literature on solving ordinary differential equations (ODEs) on matrix Lie groups in the deterministic scenario. The existing research in the stochastic context only deals with SDEs on $\mathbb{R}^n$. The second concern is that these are difficult to adapt to approaches based on matrix Lie groups. The development of numerical techniques for geometric SDEs necessitates a thorough understanding of stochastic processes, such as Ito calculus and differential geometry. So far, the only literature on the subject has been directed at mathematicians and is unavailable to engineers. This has resulted in one of two consequences in applications: either the geometry is neglected, or the stochasticity involved with the problem is misused.

Therefore to address this literature gap, in the present study, physical systems which evolve on quadratic hypersurfaces formalized as S^2 (two-sphere) and $SO(3)$ (special orthogonal group in three dimensions) are considered. Such systems are modelled in the form of Hamiltonian SDEs in Stratonovich sense [7].

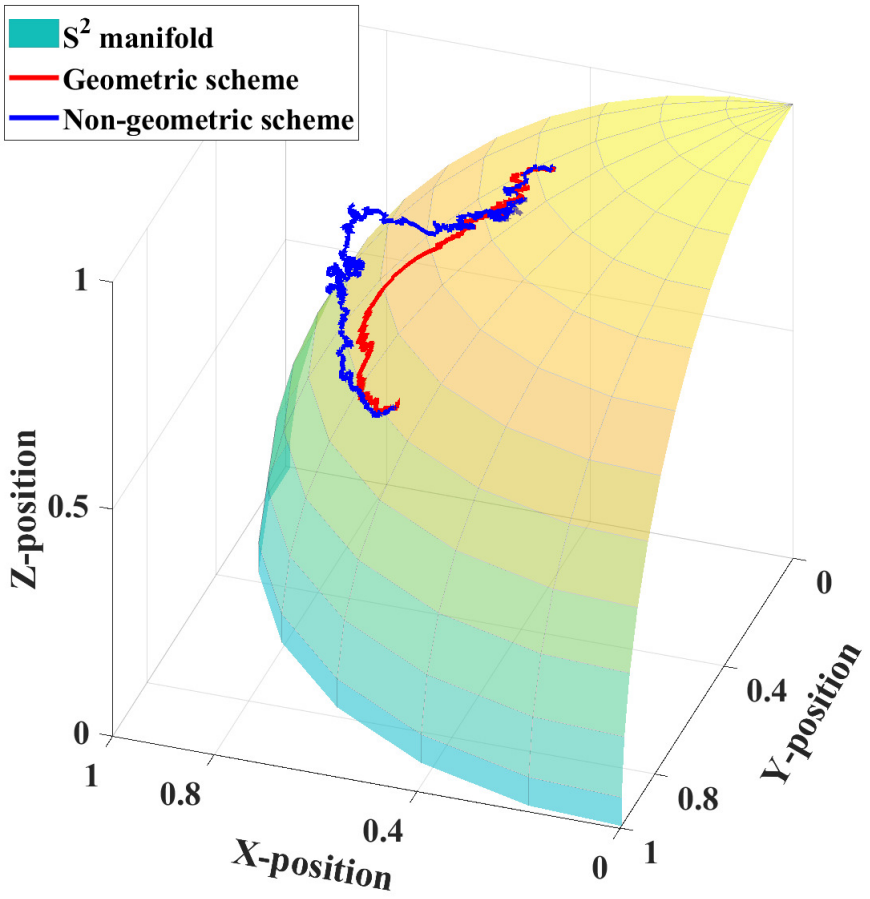

FIGURE 1.3: Measure of geometry preservation through geometric scheme

Using Wong-Zakai correction terms [28], the equivalent Ito diffusion equations on the manifold are formulated. Magnus expansion is employed for establishing the correspondence between the manifold and Lie algebra, providing a base for the formulation of strong higher order geometric Taylor-1.5 framework using Ito's formula [29]. This formulation leads to new expressions for the Kolmogorov operators considering the geometric aspects of the manifold and its corresponding Lie algebra. Results demonstrate that the solution using the proposed integration scheme satisfies the geometric constraints on both manifold and tangent space. A measure for geometry preservation is provided in Fig. 1.3, where the trajectory of stochastic duffing oscillator on S^2 manifold is shown using geometric and non-geometric schemes. Further, the global errors between the proposed scheme and the existing geometric EM and Milstein schemes are shown to be significantly less for coarser time steps. The proposed formulation is applicable to any Hamiltonian systems evolving on complex manifolds. A schematic of the proposed framework is expressed in Fig. 1.4 for the stochastically excited Hamiltonian systems.

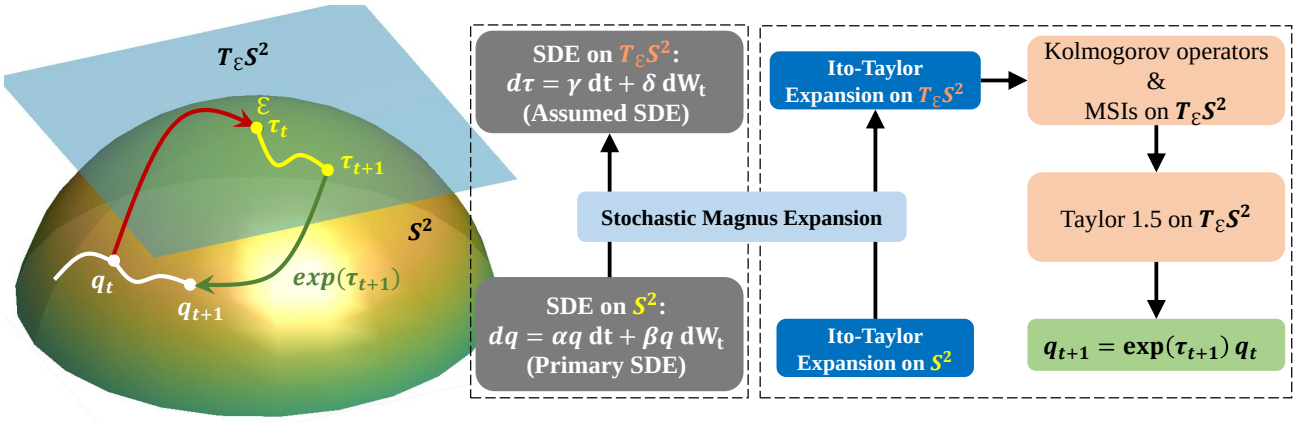

FIGURE 1.4: A schematic representation of proposed scheme for stochastically excited Hamiltonian systems

By first comprehensively solving the forward problem, a foundation needed to design effective solutions for the inverse problem can be obtained [30, 31]. Now, having obtained the geometrically accurate responses of the systems, through the developed robust simulation techniques, represent essential data inputs for the purpose of monitoring the health and performance of the system under investigation can be obtained. Before delving into the curved surface, it's necessary to address the issues related to health monitoring in Euclidean space $\mathbb{R}^n$, which is a special case of the Riemannian manifold. Towards this, the past decades have witnessed enormous advancements in the field of real time structural health monitoring (SHM) on the Euclidean spaces in terms of development of algorithms towards damage detection [32], modal identification [33] and control [34]. The traditional algorithms [30, 35, 36] possess practical challenges owing to their offline nature and cannot be implemented for time varying systems i.e. condition monitoring of wind turbines [37], interaction between bridge and vehicle and tuned mass dampers (TMDs), which are prone to detuning frequently due to change in loading condition, ambient changes and damages [38]. To cater these issues, there emerged first order eigen perturbation (FOEP) based real-time algorithms viz. recursive principal component analysis (RPCA) [39, 40], recursive canonical correlation analysis (RCCA) [41, 32, 33] and recursive singular spectrum analysis (RSSA) [34, 42], which are purely data driven, thus making them more reliable for dealing with complex multi-dimensional problems. In the perturbation framework, error arises due to the difference between linear normal modes (LNMs) and proper orthogonal modes (POMs), which if not adapted, results in requirement of large samples for the stabilization, convergence, accuracy in data processing to name a few. Convergence of an algorithm can be said to be achieved when there is a negligible error between LNMs and POMs. Existing literature [34, 32] ignore the first order error terms in the formulation of first order

perturbation technique. Due to their avoidance of the 1st order error terms, the RCCA algorithm [33] converges to the theoretical value of mode shapes in real-time at an approximate requirement of 18% of the total sample size. This becomes a problem if the monitoring is subjected to a short duration of time or when the sampling of the data is performed at lesser frequency. The proposed error-adapted FOEP algorithm exploits the standard EVP and generalized EVP for the estimation of error. The estimated error is used as a feedback for the estimation of error-adapted eigenspace. The error-adapted eigenspace can be taken up for post-processing for the purpose of real-time health monitoring of the stochastically excited dynamical systems.

After addressing the issues in $\mathbb{R}^n$, the study's focus shifts to health monitoring of systems in curved spaces. For the systems evolving on the geometrical surfaces, this monitoring process is achieved through the utilization of Recursive Principal geodesic Analysis (RPGA), a sophisticated analytical technique known for its effectiveness in extracting meaningful information from complex data streams. RPGA is a counterpart of a well-known technique used to analyze variability of a population of geometric objects in Euclidean space. This is currently a focus of my study and is opening new scopes in the area of real time monitoring through eigen space exploration. An efficient tool to perform such an analysis would be the principal component analysis (PCA) and its recursive version RPCA. However, these techniques are linear in essence, as it involves various results of linear algebra. Thus, to perform RPCA, the data must lie in an Euclidean space. Unfortunately, complex representations of shape do not fulfil such a requirement, forcing us to re-design the technique to nonlinear situations. More precisely, the data will lie in a differential manifold and the method of principal geodesics will be used to analyze its variability, in PCA fashion [43]. In the current work, RPGA is utilized to detect the damage in various examples like spherical pendulum, stochastic duffing oscillator on S^2 and inverted spherical pendulum cart system, traversing on a rough surface. The configuration manifold of the system is taken as $\left(\mathrm{S}^2 \times \mathbb{R}^3\right)$. Through the developments in this study, my work provides the advancements in the understanding of the geometric dynamics and real-time health monitoring altogether in an amalgamated framework. The key objectives of this thesis are highlighted below for the better understanding.

1.1 Objective of the study

The primary objective of my work is *health monitoring of the stochastically excited structures generally evolving on a manifold*, and, the key objectives of the study are as follows:

1. Developing error-adapted FOEP based real-time algorithms with quick convergence for the online condition monitoring of dynamical systems on Euclidean space.
2. To explore the possibilities of the error-adapted FOEP framework towards application specific problems like modal control of TMDs and Multi-TMDs, where the system is prone to detuning frequently.
3. Stochastic modelling of dynamical systems on smooth manifold through the use of Lagrangian and Hamiltonian dynamics to consider the geometric intricacies associated with physical systems.
4. Developing numerical integration techniques for the solution of stochastically excited systems on the manifold.
5. Developing FOEP based real time damage detection technique viz. Recursive principal geodesic analysis (RPGA) for the stochastically excited systems on the manifold, thereby amalgamating geometric concepts and online health monitoring.

Figure 1.5 articulates the aforementioned objectives in the form of a chart.

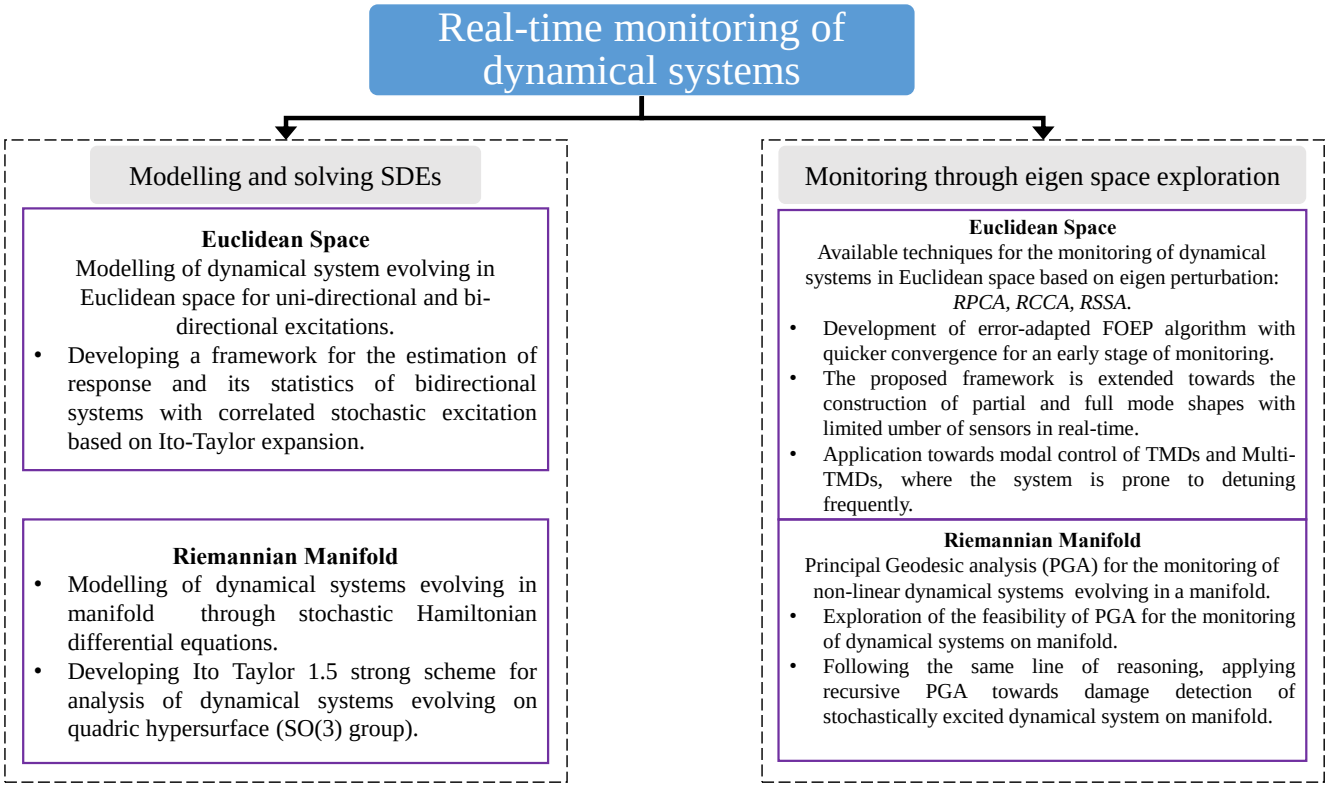

FIGURE 1.5: A flow chart showing the objectives of the present study

1.2 Overview of the study

The contents of the present study are sequentially arranged into the following chapters:

- Chapter 2: This chapter encompasses a brief background on the Ito Taylor expansion based numerical integration scheme in Euclidean domain and an introduction on the Manifold theory. Formulation of discrete deterministic and stochastic Hamiltonian dynamics on $\mathbb{R}^n$, and deterministic Hamiltonian dynamics on S^2 along with a brief overview on the Magnus expansion is provided.

- Chapter 3: This Chapter enhances real-time modal identification, particularly First Order Eigen Perturbation (FOEP) techniques, by introducing error-adapted FOEP, decentralized mode shape identification, online convergence indicators, and real-time passive control for vibrating structures. It also introduces "real-time decentralization" for efficient underdetermined modal identification.

- Chapter 4: This chapter deals with modelling of stochastic Hamiltonian dynamical equations on

differentiable manifold and developing a higher order time integration technique based on Ito-Taylor expansion to solve the dynamical systems evolving on S^2. The proposed methodology is compared with existing techniques to demonstrate its efficacy even at coarser time steps.

- Chapter 5: This chapter advances Stochastic Hamiltonian Differential Equations (SHDE) modeling by introducing a novel Itô-Taylor-based geometric numerical integration scheme (strong order 1.0) that prioritizes symplectic preservation on the manifold S^2. It addresses limitations in existing models, particularly in long-duration simulations, and showcases its effectiveness through versatile simulations of physical systems.
- Chapter 6: This chapter addresses real-world phenomena evolving on mathematical manifolds with non-Euclidean geometries, employing Stochastic Hamiltonian differential equations. It introduces a symplectic geometry-preserving Ito-Taylor numerical integration scheme, emphasizing its symplectic nature, to overcome limitations in traditional numerical techniques, ensuring accurate results for systems on a general class of manifolds. Additionally this chapter provides the development of symplectic geometric Itô-Taylor 1.5 strong scheme for the preservation of symplectic structure.
- Chapter 7: This chapter provides a framework for recursive principal geodesic analysis (RPGA) on manifold and discusses the possibilities of its application towards monitoring of the dynamical systems evolving on differentiable manifolds.
- Chapter 8: This chapter summarizes the key milestones achieved in the present work.

Chapter 2

Background

The dynamics of physical systems can be naturally described using the Lagrangian and Hamiltonian formulations that governs the system dynamics [2, 7, 8, 9, 10]. Considering the geometrical aspects of the system dynamics, literature [9] developed deterministic Lagrangian and Hamiltonian formulation of mechanical systems on several configuration manifolds based on Lie group theory. To simulate the deterministic dynamics, literature [24] proposed a lie group integrator for mechanical systems. A variational integrator for learning and control of robotic systems based on geometric mechanics was proposed in [44], and, for non-autonomous Lagrangian systems [45]. However, such integration schemes cannot be simply extended to cater to uncertainty in the system dynamics. Therefore, for systems with inherent randomness, geometry preserving stochastic Hamiltonian formulation and numerical integration scheme based on Lie approach is necessary. In the light of stochastic dynamics on Euclidean space, Ito-Taylor expansion based numerical integration schemes provide a handy tool for accurate simulation of stochastic mechanical systems [20]. Some of the recent works include the development of higher order integration schemes for simulation of stochastic nonlinear systems [15]. Although these algorithms result accurate simulation of dynamics of stochastic systems on Euclidean space, but the response trajectories of such systems lie on configuration manifolds $\left(\left(\mathrm{S}^2\right)^n, \mathrm{SO}\left(n\right), \mathrm{SE}\left(n\right)\right)$ [9, 46]. Thus, solving them with the existing Euclidean numerical schemes causes the solution to drift off from the surface of the manifold, thereby, failing to preserve the geometry [22].

Literature [23, 46, 47] proposed numerical integration schemes for stochastic differential equations whose solution evolves on a smooth manifold. A stochastic Magnus expansion based geometric Euler-Maruyama (g-EM) scheme for solving geometric SDEs without relying on extensive application of differential geometry was proposed in [22]. However, the solution techniques of SDEs on manifolds [7, 22] have been studied purely from a mathematical standpoint without adequately demonstrating

drift preservation. Moreover, the extension of this paradigm to physical systems is essential. Furthermore, from the stochastic integration schemes on the Euclidean space, it is evident that the lower order integration schemes require significantly smaller time steps for an accurate solution [15], thereby necessitating the use of higher order integration schemes. With this motivation in mind, the current study formulates stochastic Hamiltonian differential equations (SHDEs) for systems evolving on manifolds. A higher-order Ito-Taylor based geometric integration scheme is then developed to accurately preserve geometry in the presence of stochasticity, ensuring that the dynamics of these systems are accurately and reliably described.

Solving complex dynamic problems as aforementioned requires a systematic and logical approach, which involves creating reliable simulation methods. When it comes to systems that can be easily understood on Euclidean spaces, the existing simulation techniques in scientific literature [15, 29, 48, 49] usually work well. However, for systems whose trajectories evolves on the curved surfaces [2, 7, 8, 9, 10], there's a noticeable gap in the available literature. So, this chapter begins by providing an overview of the current state-of-the-art numerical simulation methods, specifically focusing on solving Stochastic Differential Equations (SDE). Thus, firstly, the mathematical concepts of Ito-Taylor expansion based stochastic integration scheme is discussed. Then a general formulation of the dynamics of a deterministic Hamiltonian system on the Euclidean space is demonstrated. However, when the dynamics of a Hamiltonian system lie on a differentiable manifold (non-Euclidean domain), then the solution of the Hamiltonian system, if obtained using the numerical integration methods for the Euclidean domain, may lead to the problem of drift pinning. Therefore, this chapter also contains the formalism of manifolds and the basic concepts of differential geometries. Thereafter towards the extension of Ito-Taylor expansion based stochastic integration scheme, the concept of a method known as Magnus expansion is utilized in developing the proposed algorithm, which can negate the problem of drift pinning and provide us with a geometric preserving solution.

2.1 Stochastic numerical integration in Euclidean Space $\mathbb{R}^2$

The dynamics of a structural system subjected to random excitation is governed by a stochastic differential equation (SDE) [29] which follows a diffusion process [29, 50]. For d different diffusion processes

driven by m-dimensional Wiener process ($B_j(t)$), the general equation is given as:

$$\mathrm{d}x_i(t) = a_i(t, x(t))\,\mathrm{d}t + \sum_{j=1}^{m} b_{ij}(t, x(t))\,\mathrm{d}B_j(t) \quad \text{where,} \quad i = 1, 2, \ldots d \tag{2.1}$$

Consider the SDE in Eq. (2.1) under the filtered probability space $(\Omega, (\mathscr{F}_t)_{t\geq 0}, P)$. Let the increasing sequence $\mathscr{F}_t$ be a filtration defined on the sub σ-field $\mathscr{F}$. Therefore, $x_i(t)$ is the $\mathscr{F}_t$-measurable stochastic process and $a_i(t, x(t))$ is the drift coefficient. $b_{ij}(t, x(t))$ is the diffusion coefficient and $B_j(t)$ is the $\mathscr{F}_t$-measurable Wiener process with $B(0) = 0$ and have stationary independent increments i.e. $[B(t) - B(s), t \geq s]$, $[B(t) - B(s)]$ is normally distributed and $E[B(t)] = 0$.

The stochastic process $x(t)$ with an initial condition, $x(0) = 0$ ($x(0)$ is independent of $B(s)$, $s \geq 0$) is an unique solution to the SDE in Eq. (2.1) if the drift and diffusion coefficients $a(t, x(t))$ and $b(t, x(t))$ satisfy the following conditions:

- The measurable functions $a(t, x(t))$ and $b(t, x(t))$ are continuous in $t \in [0, T]$ and satisfy the Lipschitz condition in x as: $|a(t,x) - a(t,y)| + |b(t,x) - b(t,y)| \leq C_1|x - y|$, $x, y \in \mathbb{R}$ and $0 \leq t \leq T$

  where, C_1 is a positive constant.

- $a(t, x(t))$ and $b(t, x(t))$ satisfy the linear growth condition for some positive constant C_2 as $|a(t,x)| + |b(t,x)| \leq C_2(1 + |x(t)|)$, $x \in \mathbb{R}$ and $0 \leq t \leq T$

- The solution $x(t)$ is bounded i.e. $E\left[\int_0^T |x(t)|^2 dt\right] < \infty$ if and only if the input excitation is bounded.

The solutions of the SDEs are often obtained numerically using numerical integration schemes of desired accuracy. Similar to the methodology of obtaining the solutions of ordinary differential equations using Taylor series expansion, the solutions to the SDEs of the form given in Eq. (2.1) are derived by developing numerical integration schemes through the incorporation of the integral form of Taylor series expansion in Eq. (2.1) [20, 29].

For the derivation of Ito-Taylor expansion based numerical integration schemes, consider a real valued function $f(x(t))$ defined in the interval $t \in [0, T]$ such that it is at least twice differentiable i.e.

$f\left(x\left(t\right)\right) \in C^2\left(\mathbb{R}\right)$. The Ito's lemma for multivariate diffusion equations is given as [20, 29, 51]:

$$\begin{aligned} \mathrm{d}f\left(x\left(t\right)\right) &= \sum_{i=1}^{d} \frac{\partial f(x(t))}{\partial x_i} \mathrm{d}x_i\left(t\right) + \frac{1}{2} \sum_{p=1}^{d} \sum_{q=1}^{d} \frac{\partial^2 f(x(t))}{\partial x_p \partial x_q} \mathrm{d}x_p\left(t\right) \mathrm{d}x_q\left(t\right) \\ \text{with} \quad \mathrm{d}x_p\left(t\right) \mathrm{d}x_q\left(t\right) &= \sum_{j=1}^{m} b_{pj}\left(x\left(t\right)\right) b_{qj}\left(x\left(t\right)\right) \mathrm{d}t \end{aligned} \tag{2.2}$$

Incorporating Eq. (2.2) in Eq. (2.1) and making suitable substitutions, different numerical integration schemes are derived by retaining the required terms from the expansion [15]. Considering all the single and double multiple stochastic integrals along with one of the MSIs of multiplicity 3, the k^{th} component of Taylor 1.5 mapping [15] for d-dimensional diffusion and m-dimensional Wiener process as scalar noise, i.e. $d = 1, 2, \ldots$ and $m = 1, 2, \ldots$, can be written as [20],

$$\begin{aligned} Y_{n+1}^{k} = \; & Y_n^k + a^k \Delta t + \sum_{j=1}^{m} b^{k,j} \Delta B^j + \tfrac{1}{2} \Im^0 a^k (\Delta t)^2 + \sum_{j=1}^{m} \left(\Im^0 b^{k,j} I_{(0,j)} + \Im^j a^k I_{(j,0)} \right) \\ & + \sum_{j_1, j_2 = 1}^{m} \Im^{j_1} b^{k,j_2} I_{(j_1,j_2)} + \sum_{j_1, j_2, j_3 = 1}^{m} \Im^{j_1} \Im^{j_2} b^{k,j_3} I_{(j_1,j_2,j_3)} \end{aligned} \tag{2.3}$$

The operators $\Im^0$ and $\Im^j$ are evaluated on the drift and diffusion coefficients to form the final Taylor 1.5 mapping. The definitions of the operators are given in Eq. (2.4) [20].

$$\begin{aligned} \Im^0\left(f\left(x\left(t\right)\right)\right) &= \frac{\partial (f(x(t)))}{\partial t} + \sum_{k=1}^{d} a_k \frac{\partial (f(x(t)))}{\partial x_k} + \frac{1}{2} \sum_{k,l=1}^{d} \sum_{j=1}^{m} b^{k,j} b^{l,j} \frac{\partial^2 (f(x(t)))}{\partial x_k \partial x_l} \\ \Im^j\left(f\left(x\left(t\right)\right)\right) &= \sum_{k=1}^{d} b^{k,j} \frac{\partial (f(x(t)))}{\partial x_k} \end{aligned} \tag{2.4}$$

For further evaluation of Eq. (2.3), the MSIs [15] $I_{(0,j)}, I_{(j,0)}, I_{(j_1,j_2)}$ and $I_{(j_1,j_2,j_3)}$, need to be evaluated first. The expressions for these MSIs are given as,

$$\begin{aligned} I_{(0,j)} &= \int_t^{t+h} \int_t^{s_1} \mathrm{d}s_2 \mathrm{d}B^j\left(s_1\right) & \qquad I_{(j_1,j_2)} &= \int_t^{t+h} \int_t^{s_1} \mathrm{d}B^{j_1}\left(s_2\right) \mathrm{d}B^{j_2}\left(s_1\right) \\ I_{(j,0)} &= \int_t^{t+h} \int_t^{s_1} \mathrm{d}B^j\left(s_2\right) \mathrm{d}s_1 & \qquad I_{(j_1,j_2,j_3)} &= \int_t^{t+h} \int_t^{s_1} \int_t^{s_2} \mathrm{d}B^{j_3}\left(s_3\right) \mathrm{d}B^{j_2}\left(s_2\right) \mathrm{d}B^{j_1}\left(s_1\right) \end{aligned} \tag{2.5}$$

where, $h = \Delta t$ is the uniform step size. The MSIs $I_{(j,0)}$ and $I_{(0,j)}$ in Eq. (2.5) can be expressed as [20, 29]:

$$\begin{aligned} I_{(j,0)} &= \Delta Z^j \\ I_{(0,j)} &= \Delta B^j \Delta t - I_{(j,0)} \end{aligned} \tag{2.6}$$

The Brownian increment at each step, ΔB^j and ΔZ^j are expressed numerically as [29]:

$$\begin{pmatrix} \Delta B^j \\ \Delta Z^j \end{pmatrix} = \begin{bmatrix} \Delta t^{\frac{1}{2}} & 0 \\ \frac{\Delta t^{\frac{3}{2}}}{2} & \frac{\Delta t^{\frac{3}{2}}}{2\sqrt{3}} \end{bmatrix} \begin{pmatrix} U_1 \\ U_2 \end{pmatrix} \tag{2.7}$$

where, U_1 and U_2 are Gaussian random variables. For any structural system under unidirectional stochastic excitation, the governing SDE in Eq. (2.1) considering one-dimensional Wiener can be rephrased as,

$$\mathrm{d}x_i\left(t\right) = a_i\left(t, x\left(t\right)\right)\mathrm{d}t + b_i\left(t, x\left(t\right)\right)\mathrm{d}B\left(t\right), \quad \text{where,} \quad i = 1, 2, \ldots m \tag{2.8}$$

Accordingly, the Taylor 1.5 mapping for unidirectional base excited systems can be expressed as follows:

$$\begin{aligned} Y_{n+1}^k = \; & Y_n^k + a^k\Delta t + b^k\Delta B + \tfrac{1}{2}\Im^0 a^k(\Delta t)^2 + \Im^0 b^k I_{(0,1)} + \Im^1 a^k I_{(1,0)} \\ & + \Im^1 b^k I_{(1,1)} + \Im^1\Im^1 b^k I_{(1,1,1)} \end{aligned} \tag{2.9}$$

The operators $\Im^0$ and $\Im^1$ in Eq. (2.4) and the MSIs in Eq. (2.6) are changed by replacing $j = 1$. Further, the MSIs $I_{(1,1)}$ and $I_{(1,1,1)}$ in Eq. (2.9) are also evaluated by substituting $j = 1$ in Eq. (2.5), the final expressions of which are given as [29, 20],

$$\begin{aligned} I_{(1,1)} &= \tfrac{1}{2}\left(\left(\Delta B\right)^2 - \Delta t\right) \\ I_{(1,1,1)} &= \tfrac{1}{6}\left(\left(\Delta B\right)^2 - 3\Delta t\right)\Delta B \end{aligned} \tag{2.10}$$

2.1.1 Order of approximation error

For the SDE in Eq. (2.1), consider the solution in the time interval $[0\ T]$. The partition in this time interval is given as: $t_0 = 0 < t_1 < t_2 < \ldots < t_n = T$ and $\Delta t = \max\left(t_{r+1} - t_r\right),\ 0 \leq r \leq n-1$. Consider $x_r^{(\Delta t)}$ to be an approximate solution to $x\left(t_r\right)$ corresponding to a discrete time instant $t = t_r$ in the partition. Following the mean square error criterion, the order of convergence (order of approximation error) is defined as:

$$\epsilon = \left(E\left[\left|x\left(t_r\right) - x_r^{(\Delta t)}\right|^2\right]\right)^{\frac{1}{2}} \leq Q\left(\Delta t\right)^{\beta} \tag{2.11}$$

where, $Q \in \mathbb{R}$ and is independent of Δt. ϵ represents a measure of pathwise deviation or closeness at a time instant, therefore Eq. (2.11) denotes a strong order of convergence [29]. For the stochastic integration scheme in Eq. (2.3), the value of β is $\frac{3}{2}$. Therefore, the order of convergence is given as: $\mathrm{O}\left(\left(\Delta t\right)^{\frac{3}{2}}\right)$.

2.1.2 Deterministic and Stochastic Hamiltonian dynamics on $\mathbb{R}^n$

For deterministic dynamics on $\mathbb{R}^n$, using Legendre transformation, the Hamiltonian, $\tilde{\mathrm{H}} : \mathrm{T}^*\mathbb{R}^n \to \mathbb{R}^1$ and its canonical equations can be expressed as (Eq. (3.10) of [9]),

$$\begin{aligned} \tilde{\mathrm{H}}(q,p) &= p \cdot \dot{q} - \mathrm{L}(q,\dot{q})|_{p=\frac{\partial \mathrm{L}}{\partial \dot{q}}} \\ \mathrm{d}q = -\frac{\partial \tilde{\mathrm{H}}}{\partial p}\mathrm{d}t \ , \ \mathrm{d}p &= \frac{\partial \tilde{\mathrm{H}}}{\partial q}\mathrm{d}t \end{aligned} \tag{2.12}$$

where, the Lagrangian, $\mathrm{L}(q,\dot{q}) = \mathrm{T}(q,\dot{q}) - \mathrm{V}(q)$, with $\mathrm{L}(q,\dot{q}) : \mathrm{T}\mathbb{R}^n \to \mathbb{R}^1$, and, $\mathrm{T}(q,\dot{q})$ and $\mathrm{V}(q)$ corresponding to the kinetic and potential energy terms respectively. $q \in \mathbb{R}^n$ is the critical point of action for the action integral and $\dot{q} \in \mathrm{T}_q\mathbb{R}^n$. $p = \frac{\partial \mathrm{L}}{\partial \dot{q}}$ is the generalized momentum and is the conjugate of $\dot{q}$. The equations of motion corresponding to stochastic Hamiltonian systems can be represented as, [7]

$$\begin{aligned} \mathrm{d}q &= -\frac{\partial \tilde{\mathrm{H}}}{\partial p}\mathrm{d}t - \frac{\partial \mathrm{h}_k}{\partial p} \circ \dot{W}_k(t) \\ \mathrm{d}p &= \frac{\partial \tilde{\mathrm{H}}}{\partial q}\mathrm{d}t + \frac{\partial \mathrm{h}_k}{\partial q} \circ \dot{W}_k(t) \end{aligned} \tag{2.13}$$

where, $W_k(t)$, $k = 1, \cdots, m$ corresponds to m-dimensional independent zero mean Wiener processes and $\circ$ denotes the SDE in Stratonovich sense. $H(q,p)$ is the deterministic Hamiltonian and $h(q,p)$ is another Hamiltonian governing the diffusion part of SDE [7]. For the SDEs defined in Eq. (2.13) under the filtered probability space, $\left(\mathcal{Z}, \mathscr{F}, (\mathscr{F}_t)_{t\geq 0}, \mathbb{P}\right)$, (q,p) are the $\mathscr{F}_t$ –measurable stochastic processes and $W_k(t)$ is the $\mathscr{F}_t$ –measurable Wiener process with $W(0) = 0$. Assuming that the Hamiltonian functions H and h_k are C^2– continuous and satisfy the Lipschitz continuity and linear growth conditions, unique solutions to Eq. (2.13) can be obtained in a given time interval $[t_a, t_b]$ with $t_b > t_a \geq 0$ by posing it in Ito sense. This is achieved by introducing the Wong Zakai correction terms such that the equivalent SDE in Ito sense can be written as [7],

$$\mathrm{d}z = A(z)\mathrm{d}t + B_k(z)\mathrm{d}W_k(t) \tag{2.14}$$

with $z = z(q,p)$ and the drift and diffusion coefficients can be revised as,

$$A(z) = \begin{pmatrix} -\frac{\partial \tilde{\mathrm{H}}}{\partial p} + \frac{1}{2}\frac{\partial^2 \mathrm{h}_k}{\partial p \partial q}\frac{\partial \mathrm{h}_k}{\partial p} - \frac{1}{2}\frac{\partial^2 \mathrm{h}_k}{\partial p^2}\frac{\partial \mathrm{h}_k}{\partial q} \\ \frac{\partial \tilde{\mathrm{H}}}{\partial q} - \frac{1}{2}\frac{\partial^2 \mathrm{h}_k}{\partial q^2}\frac{\partial \mathrm{h}_k}{\partial p} + \frac{1}{2}\frac{\partial^2 \mathrm{h}_k}{\partial q \partial p}\frac{\partial \mathrm{h}_k}{\partial q} \end{pmatrix}, \quad B(z) = \begin{pmatrix} -\frac{\partial \mathrm{h}_k}{\partial p} \\ \frac{\partial \mathrm{h}_k}{\partial q} \end{pmatrix} \tag{2.15}$$

where $\partial^2 \mathrm{h}_k/\partial q^2$, $\partial^2 \mathrm{h}_k/\partial p^2$, and $\partial^2 \mathrm{h}_k/\partial q \partial p$ corresponds to the Hessian matrices of h_k. Once the system dynamics are expressed in Ito diffusion form (Eq. (2.14)), suitable numerical or analytical integration schemes can be employed to obtain the solution of the system [15].

2.2 Manifolds

An abstract mathematical space known as a manifold $\mathcal{M}$ has a structure that may be more complex globally but is similar to the Euclidean geometry-described spaces $\mathbb{R}^n$ locally. For instance, the surface of the Earth is varied; although locally it appears flat, when seen globally from space, it is actually rounded. It is possible to 'glue' various Euclidean spaces together to create a manifold[52]. A circle S^1 is an example of a manifold. Although a small portion of a circle resembles a slightly bent portion of a straight-line segment, the circle and the segment are actually two different 1D manifolds. A segment of a straight line can be bent, and the ends can be joined with glue to create a circle. Examples of 2D manifolds include the surfaces of a sphere S^2 and a torus $\mathrm{S}^1 \times \mathrm{S}^1$. Manifolds are crucial components of mathematics, physics, and control theory because they enable the expression and comprehension of more complex structures in terms of the well-known characteristics of simpler Euclidean spaces.

There are numerous mathematical operations which arise in the analysis and operations of manifolds. So, it is a good practice to fix all the notations which will be then used to describe the mathematics in the further sections[53]. M stands for a Riemannian manifold. The tangent space to the manifold M at a point x ∈ M is designated as T_xM. The tangent bundle denoted by the symbol TM is defined as TM: = (x; v) x ∈ M; v ∈ T_xM. A manifold is endowed with a local metric, this local metric defines the local norm $||V_x|| = \sqrt{(V.V^T)}$ for V ∈ T_xM. The Riemannian gradient of a function $\psi : R \to M$ evaluated at any point x ∈ M is denoted as $grad_x\psi$. The covariant derivative of a vector field w ∈ TM in the direction of v ∈ T_xM is denoted by $\nabla_v w$. We assume M to be endowed with a metric connection. The parallel transport operator $P_r^{(x \to y)}$ transports a tangent vector from $TxM \to TyM$. A manifold exponential map exp:TM→M is applied as $exp_x(v)$. Its inverse 'log' is defined locally and is denoted by $log_y x$ where y is the reference point y ∈ M. Given two point in the manifold M the distance between them is denoted by d(x,y) which is termed as the Riemannian distance between x and y.

Take into consideration a set $\mathcal{M}$ that is a potential manifold. Any point x on $\mathcal{M}$ has an associated Euclidean chart, which is given by a one-one mapping and plotted onto the map $\theta_i : M \to R_n$, with an

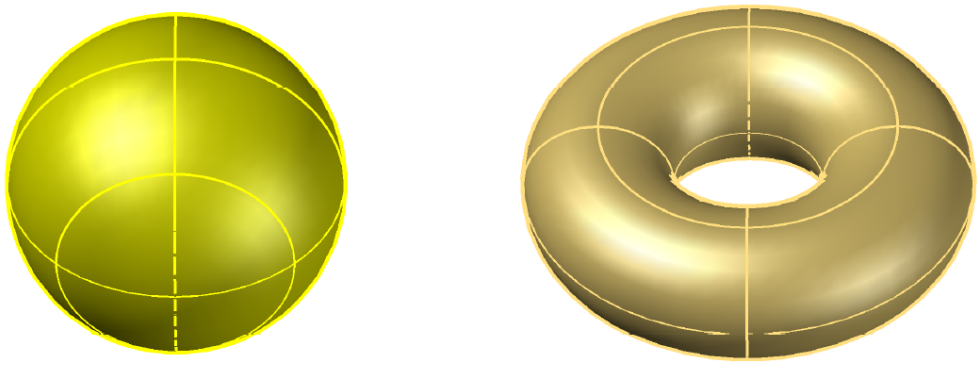

FIGURE 2.1: Manifolds (a) Hypersphere (b) Torus

associated Euclidean image $V_i = \theta_i(U_i)$. Where U_i belongs to M and $V_i \in R_n$.

2.3 Lie Groups and Lie Algebras

A Lie group $\mathcal{G}$ is a smooth manifold $\mathcal{M}$ that also carries a group structure whose product $\mathcal{G}_1 \times \mathcal{G}_2$ and inversion operations $\mathcal{G}^{-1}$ are smooth as maps of manifolds. These things naturally appear when describing physical symmetries. A Lie group $\mathcal{G}$ is a group whose elements can have continuous real number parametrization, like the rotation group $SO(3)$, which can have the Euler angles as its parametrization. An analytic real or complex manifold that is also a group, such that the group operations multiplication and inversion are analytic maps, is referred to as a Lie group in a more formal sense. *Group Axioms*:

1. Closure: If $a, b \in G$, then $\phi(a, b) \in G$.

2. Associative: If $a, b, c \in G$, then $\phi(a, \phi(b, c)) = \phi(\phi(a, b), c)$.

3. Identity: If $a \in G$, then there exists an $e \in G$ such that $\phi(a, e) = \phi(e, a) = a$.

4. Inverse: If $a \in G$, then there exists a unique element $a^{-1} \in G$ such that $\phi(a, a^{-1}) = \phi(a^{-1}, a) = e$.

We can assign a Lie algebra that fully encapsulates the group's local structure to every Lie Group.

2.3.1 Lie Group

A Lie group is a smooth manifold $\mathcal{M}$ with a group $\mathcal{G}$ structure that is concurrently consistent with its manifold M structure in the sense of group multiplication and group inversion. The group identity element is a point e at $\mathcal{G}$. The group structure mandates that each element's composition stay on the manifold, and that each element also has an inverse in the manifold. Calculus on groups is possible thanks to Lie groups, which connect the local characteristics of smooth manifolds.

2.3.2 Group Actions

It is important to highlight that Lie groups possess the ability to alter the elements of other sets, leading to transformations such as rotations, translations, scaling, and combinations thereof. These transformations find extensive application in both two-dimensional and three-dimensional dynamics. For instance, this study has utilized Lie groups to introduce rotations into a dynamical system. For a valid group ac-

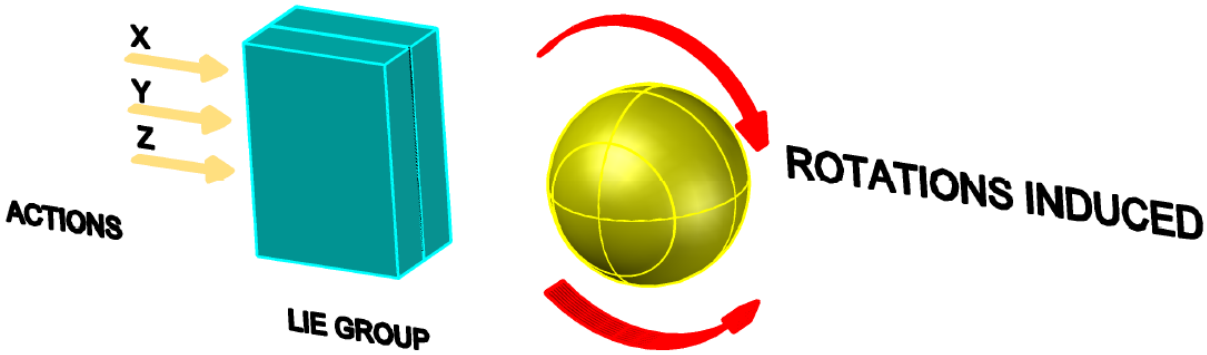

FIGURE 2.2: Action of Lie Groups

tion, it must satisfy the axioms of identity and compatibility.

2.3.3 Lie Algebra

If a point $X(t)$ moves on a manifold $\mathcal{M}$ associated with a Lie group, the velocity of this point belongs to the tangent space of the manifold, denoted as $\mathrm{T}_x\mathcal{M}$. The smoothness of the manifold ensures the presence of a unique tangent space at each point. The tangent space $\mathrm{T}\mathcal{M}$ at the identity element of the Lie group $\mathcal{G}$ is known as the Lie algebra $\mathfrak{g}$ of that particular group. It is important to note that every Lie group is accompanied by its own corresponding Lie algebra.

2.3.4 Exponential Map and Logarithmic Map

The exponential map is a mapping that establishes a diffeomorphism between the Lie algebra and the Lie group. It allows us to convert elements from the Lie algebra to corresponding elements in the Lie group. Conversely, the inverse of the exponential map is known as the logarithmic map, which enables us to go from the Lie group back to the Lie algebra. In this research, calculating the exponential mapping directly poses challenges as it necessitates a deep understanding of advanced concepts in

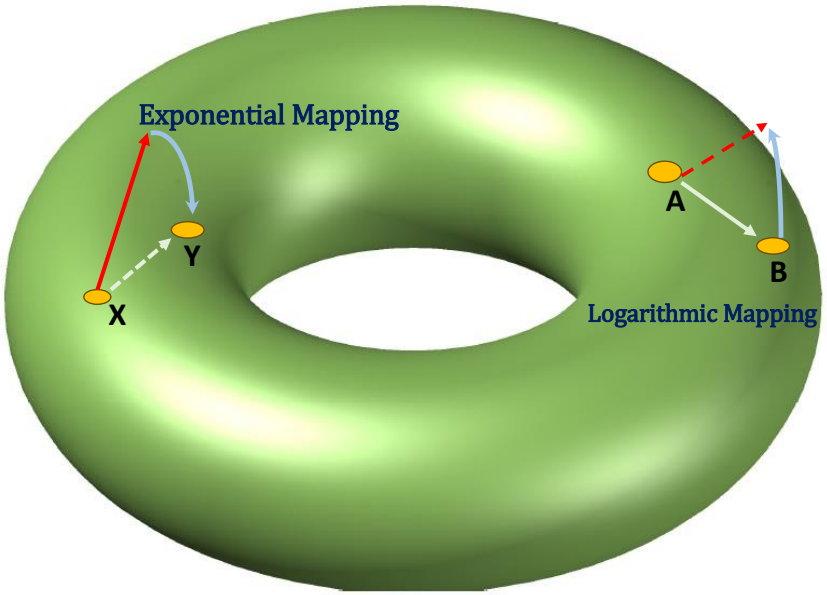

FIGURE 2.3: Exponential Mapping and Logarithmic Mapping on the surface of a torus

Differential Geometry. As a result, one can opt for a shortcut by leveraging the action exerted by Lie groups on the configuration manifold considered in this study. This approach provides us with a more accessible way to incorporate the effects of Lie groups in this analysis. These mappings are shown on the surface of a torus in Fig. 2.3. A summary of the above is shown below:

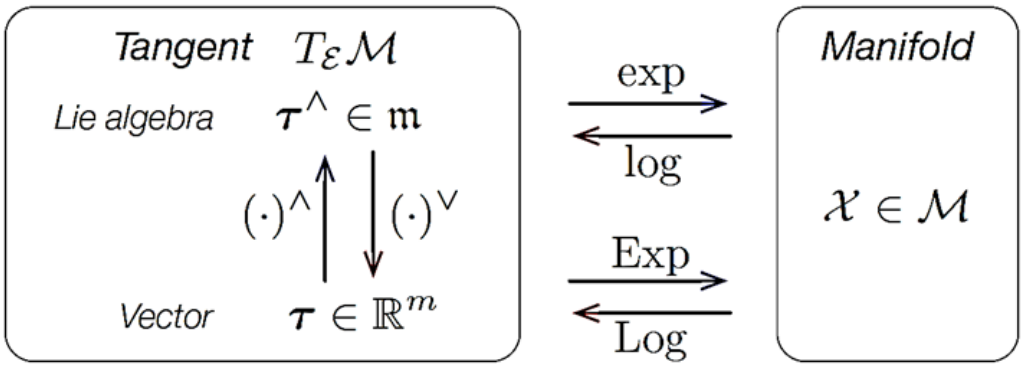

FIGURE 2.4: Working of Lie Groups and Lie Algebra[54]

2.3.5 Rotational Lie Groups

This group is the subset of the General Linear Group whose Group Action represents the rotations which are induced in any physical system. The Rotational Groups are nxn matrices where n is the

number of rotation axis. The Rotational group may be of n dimension but the rotations in 2 and 3 dimensions are important[54, 52].

1. *Uni-axial Rotation Groups or SO(2)*

   The following transformation of the joint coordinates results from the uni-axial joint rotation in a single Cartesian plane around a perpendicular axis, for example, the x-y plane about the z axis with rotation angle θ:

$$SO(2) = \begin{bmatrix} \cos\theta & -\sin\theta \\ \sin\theta & \cos\theta \end{bmatrix} \begin{bmatrix} x \\ y \end{bmatrix} \rightarrow \begin{bmatrix} x\cos\theta & -y\sin\theta \\ x\sin\theta & y\cos\theta \end{bmatrix} \tag{2.16}$$

   The Lie Algebra:

$$\mathfrak{so}(2) = \left\{ \begin{bmatrix} 0 & -t \\ t & 0 \end{bmatrix} \middle| \, t \in \mathbb{R} \right\}$$

   The Exponential Map:

$$\exp\left(\begin{bmatrix} 0 & -\theta \\ \theta & 0 \end{bmatrix} \right) = \gamma_\theta(1) = \begin{bmatrix} \cos t\theta & -\sin t\theta \\ \sin t\theta & \cos t\theta \end{bmatrix}$$

2. *Three-axial Rotation Groups or SO(3)*

   The group SO (3) is made up of rotation matrices or special orthogonal matrices in 3D space that are subject to matrix multiplication.

   As in all groups SO, inversion and composition are accomplished through transposition and product (n). The lie algebra of the group is defined by angular velocities $\omega_x, \omega_y, \omega_z$.

$$[\omega] = \begin{bmatrix} 0 & -\omega_z & \omega_y \\ \omega_z & 0 & -\omega_x \\ -\omega_y & \omega_x & 0 \end{bmatrix} \tag{2.17}$$

   The exponential map:

$$R = \exp([\omega]\theta) \in \mathrm{SO}(3), \text{ where } R \text{ is the rotation matrix.}$$

$$R = \sum_k \frac{\theta^k}{k!}([\omega])^k$$

$$R = I + [\omega]\left(\theta - \frac{1}{3!}\theta^3 + \frac{1}{5!}\theta^5 - \cdots\right) + [\omega]^2\left(\frac{1}{2}\theta^2 - \frac{1}{4!}\theta^4 + \frac{1}{6!}\theta^6 - \cdots\right)$$

Which can be reduced to:

$$R = I + [\omega]\sin(\theta) + [\omega]^2(1 - \cos(\theta)) \tag{2.18}$$

The Logarithm:

$$\theta[\omega] = \log(R) \triangleq \frac{\theta(R - R^\top)^V}{2\sin(\theta)} \tag{2.19}$$

Where,

$$\theta = \cos^{-1}\left(\frac{\text{trace}(R) - 1}{2}\right)$$

2.3.6 Lagrangian Dynamics on $\left(\mathbf{S}^2\right)^n$

The introduction commences with the presentation of a Lagrangian function. Subsequently, the Euler-Lagrange equations are derived via the application of Hamilton's principle, which necessitates that the variation of the action integral remains equal to zero. The Euler-Lagrange equations is derived by employing a modified Lagrangian that encompasses the configuration vector and the angular velocity vector. In both cases, the Euler-Lagrange equations are further simplified, particularly in scenarios where the kinetic energy function exhibits a quadratic dependence on the time derivative of the configuration vector.

Hamilton's Variational Principle in Terms of (q, ω)

An alternative formulation of the Euler-Lagrange equations can be derived by incorporating the angular velocity vector introduced in the preceding sections. The action integral is expressed within the framework of the modified Lagrangian function.

$$\tilde{L}(q, \omega) = L(q, \dot{q}), \tag{2.20}$$

In the context of the kinematic equations provided in the earlier sections, the notation $\dot{q} = (\dot{q}1, \ldots, \dot{q}n) \in \mathrm{T}q\left(\mathrm{S}^2\right)^n$ are used. As previously explained, $\omega = (\omega_1, \ldots, \omega_n) \in \mathrm{T}_q\left(\mathrm{S}^2\right)^n$. Consequently, the modified Lagrangian $\tilde{L}(q, \omega)$ is defined within the tangent bundle $\mathrm{T}\left(\mathrm{S}^2\right)^n$ while considering the kinematics.

With this setup, the infinitesimal variation of the modified action integral are expressed as:

$$\delta\tilde{\mathfrak{G}} = \int_{t_0}^{t_f} \sum_{i=1}^{n} \left\{ \frac{\partial \tilde{L}(q,\omega)}{\partial \omega_i} \cdot \delta\omega_i + \frac{\partial \tilde{L}(q,\omega)}{\partial q_i} \cdot \delta q_i \right\} dt \tag{2.21}$$

The infinitesimal variations in the motion are described as:

$$\begin{aligned} \delta q_i &= S(\gamma_i)\, q_i, && i = 1, \ldots, n, \\ \delta \dot{q}_i &= S(\dot{\gamma}_i)\, q_i + S(\gamma_i)\, \dot{q}_i, && i = 1, \ldots, n \end{aligned} \tag{2.22}$$

These variations correspond to curves $\gamma_i : [t_0, t_f] \to \mathbb{R}^3, i = 1, \ldots, n$, which satisfy the conditions $(\gamma_i \cdot q_i) = 0$ and $\gamma_i(t_0) = \gamma_i(t_f) = 0, i = 1, \ldots, n$.

Now, let's proceed to derive expressions for the infinitesimal variation of the angular velocity vector. Utilizing the relationship $\omega_i = S(q_i)\, \dot{q}_i$, the infinitesimal variation of the angular velocity vectors are expressed as:

$$\delta\omega_i = S(\delta q_i)\, \dot{q}_i + S(q_i)\, \delta\dot{q}_i, \quad i = 1, \ldots, n. \tag{2.23}$$

By substituting ∂q and $\partial \dot{q}$ and reorganizing, the following are obtained:

$$\delta\omega_i = (S(\gamma_i)\, q_i) \times \dot{q}_i + S(q_i)\, (S(\dot{\gamma}_i)\, q_i + S(\gamma_i)\, \dot{q}_i)\,. \tag{2.24}$$

Expanding each term using the vector identity for the triple cross product, namely $S(x)(S(y)z) = (x \cdot z)y - (x \cdot y)z$ for any $x, y, z \in \mathbb{R}^3$, one can acquire:

$$\begin{aligned} \delta\omega_i = &- (\dot{q}_i \cdot q_i)\, \gamma_i + (\dot{q}_i \cdot \gamma_i)\, q_i + (q_i \cdot q_i)\, \dot{\gamma}_i - (q_i \cdot \dot{\gamma}_i)\, q_i \\ &+ (q_i \cdot \dot{q}_i)\, \gamma_i - (q_i \cdot \gamma_i)\, \dot{q}_i, \quad i = 1, \ldots, n. \end{aligned} \tag{2.25}$$

Since $q_i \cdot q_i = 1$ and $q_i \cdot \dot{q}_i = q_i \cdot \gamma_i = 0$, this reduces to

$$\delta\omega_i = (\dot{q}_i \cdot \gamma_i)\, q_i + \dot{\gamma}_i - (q_i \cdot \dot{\gamma}_i)\, q_i, \quad i = 1, \ldots, n. \tag{2.26}$$

Employing the vector identity $x \cdot (S(y)z) = y \cdot (S(z)x) = z \cdot (S(x)y)$ for any $x, y, z \in \mathbb{R}^3$, the following are derive:

$$\begin{aligned}\delta\omega_i &= (\gamma_i \cdot (S(\omega_i) q_i)) q_i + \left(I_{3\times3} - q_i q_i^T\right) \dot{\gamma}_i \\ &= (q_i \cdot (S(\gamma_i) \omega_i)) q_i + \left(I_{3\times3} - q_i q_i^T\right) \dot{\gamma}_i \\ &= q_i q_i^T (S(\gamma_i) \omega_i) + \left(I_{3\times3} - q_i q_i^T\right) \dot{\gamma}_i, \quad i = 1, \ldots, n.\end{aligned} \tag{2.27}$$

The matrix $q_i q_i^T$ is associated with the orthogonal projection along q_i. This is pertinent because both γ_i and ω_i exhibit orthogonality with respect to q_i. Consequently, this information informs us about the infinitesimal variation of the angular velocity vector.

$$\delta\omega_i = -S(\omega_i)\gamma_i + \left(I_{3\times3} - q_i q_i^T\right)\dot{\gamma}_i, \quad i = 1, \ldots, n. \tag{2.28}$$

The infinitesimal change in ω_i comprises two components: The first term, $\gamma_i \times \omega_i$, aligns with q_i and signifies alterations related to the modification of q_i.The second term involves the orthogonal projection of $\dot{\gamma}_i$ onto the space orthogonal to q_i, reflecting variations due to the time-rate change in the alteration of q_i. These components collectively account for the infinitesimal variation in ω_i.

Euler-Lagrange Equations in Terms of (q, ω)

Substituting ∂q and $\partial\omega$ to obtain

$$\begin{aligned}\delta\tilde{\mathfrak{G}} &= \int_{t_0}^{t_f} \sum_{i=1}^{n} \Bigg\{ \left(S(\gamma_i)\omega_i + \left(I_{3\times3} - q_i q_i^T\right)\dot{\gamma}_i\right) \cdot \frac{\partial \tilde{L}(q,\omega)}{\partial \omega_i} \\ &\qquad + S(\gamma_i) q_i \cdot \frac{\partial \tilde{L}(q,\omega)}{\partial q_i} \Bigg\} dt \\ &= \int_{t_0}^{t_f} \Bigg\{ \sum_{i=1}^{n} \left\{ S(q_i) \frac{\partial \tilde{L}(q,\omega)}{\partial q_i} + S(\omega_i) \frac{\partial \tilde{L}(q,\omega)}{\partial \omega_i} \right\} \cdot \gamma_i \\ &\qquad + \left\{ \left(I_{3\times3} - q_i q_i^T\right) \frac{\partial \tilde{L}(q,\omega)}{\partial \omega_i} \right\} \cdot \dot{\gamma}_i \Bigg\} dt.\end{aligned} \tag{2.29}$$

Integrating the terms in the integral that multiply $\dot{\gamma}_i$ by parts, the infinitesimal variation of the modified action integral is given by

$$\begin{aligned}\delta\tilde{\mathfrak{G}} = &\sum_{i=1}^{n} \gamma_i \cdot \left(I_{3\times3} - q_i q_i^T\right) \frac{\partial \tilde{L}(q,\omega)}{\partial \omega_i}\Bigg|_{t_0}^{t_f} \\ &+ \sum_{i=1}^{n} \int_{t_0}^{t_f} \gamma_i \cdot \left\{ -\frac{d}{dt}\left(\left(I_{3\times3} - q_i q_i^T\right) \frac{\partial \tilde{L}(q,\omega)}{\partial \omega_i}\right)\right. \\ &\left. + S\left(q_i\right) \frac{\partial \tilde{L}(q,\omega)}{\partial q_i} + S\left(\omega_i\right) \frac{\partial \tilde{L}(q,\omega)}{\partial \omega_i} \right\} dt.\end{aligned} \tag{2.30}$$

In accordance with Hamilton's principle, $\delta\tilde{\mathfrak{G}} = 0$ holds for all differentiable functions $\gamma_i : [t_0, t_f] \rightarrow \mathbb{R}^3, i = 1, \ldots, n$, which satisfy $(\gamma_i \cdot q_i) = 0$ and vanish at both t_0 and $t_f, i = 1, \ldots, n$.

Applying the fundamental lemma of the calculus of variations, as detailed in Appendix A, implies that each term enclosed within the curly braces must be orthogonal to the tangent space Tqi S^2 or, equivalently, aligned with q_i. Consequently, we have:

$$S\left(q_i\right)\left\{\frac{d}{dt}\left(S^2\left(q_i\right)\frac{\partial \tilde{L}(q,\omega)}{\partial \omega_i}\right) + S\left(\omega_i\right)\frac{\partial \tilde{L}(q,\omega)}{\partial \omega_i} + S\left(q_i\right)\frac{\partial \tilde{L}(q,\omega)}{\partial q_i}\right\} = 0, \tag{2.31}$$

for $i = 1, \ldots, n$. Multiply both sides of these equations by $S\left(q_i\right)$,

$$\begin{aligned}&S\left(q_i\right)^4 \frac{d}{dt}\left(\frac{\partial \tilde{L}(q,\omega)}{\partial \omega_i}\right) + S\left(q_i\right)^2 S\left(\omega_i\right)\frac{\partial \tilde{L}(q,\omega)}{\partial \omega_i} \\ &+ S\left(q_i\right)^2 \left\{S\left(\dot{q}_i\right) S\left(q_i\right) + S\left(q_i\right) S\left(\dot{q}_i\right)\right\} \frac{\partial \tilde{L}(q,\omega)}{\partial \omega_i} + S\left(q_i\right)^3 \frac{\partial \tilde{L}(q,\omega)}{\partial q_i} = 0,\end{aligned} \tag{2.32}$$

for $i = 1, \ldots, n$. Using $S\left(q_i\right)^3 = -S\left(q_i\right)$, this can be written as

$$\begin{aligned}&- S\left(q_i\right)^2 \frac{d}{dt}\left(\frac{\partial \tilde{L}(q,\omega)}{\partial \omega_i}\right) + S\left(q_i\right)^2 S\left(\omega_i\right)\frac{\partial \tilde{L}(q,\omega)}{\partial \omega_i} \\ &+ S\left(q_i\right)^2 \left\{S\left(\dot{q}_i\right) S\left(q_i\right) + S\left(q_i\right) S\left(\dot{q}_i\right)\right\} \frac{\partial \tilde{L}(q,\omega)}{\partial \omega_i} - S\left(q_i\right)\frac{\partial \tilde{L}(q,\omega)}{\partial q_i} = 0,\end{aligned} \tag{2.33}$$

for $i = 1, \ldots, n$. To further simplify these expressions we use the matrix identities in Chapter 1 and the fact that $(\omega_i \cdot q_i) = 0$ to obtain

$$S\left(q_i\right) S\left(\omega_i\right) S\left(q_i\right) = S\left(q_i\right)\left\{-\omega_i^T q I_{3\times3} + q_i \omega_i^T\right\} = 0. \tag{2.34}$$

From this it follows that

$$\begin{aligned} S(q_i)\,S(\dot{q}_i) &= S(q_i)\,\{S(\omega_i)\,S(q_i) - S(q_i)\,S(\omega_i)\} \\ &= S(q_i)\,S(\omega_i)\,S(q_i) - S(q_i)^2\,S(\omega_i) \\ &= -S(q_i)^2\,S(\omega_i) \end{aligned} \tag{2.35}$$

and

$$\begin{aligned} S(\dot{q}_i)\,S(q_i) &= \{S(\omega_i)\,S(q_i) - S(q_i)\,S(\omega_i)\}\,S(q_i) \\ &= S(\omega_i)\,S(q_i)^2 - S(q_i)\,S(\omega_i)\,S(q_i) \\ &= S(\omega_i)\,S(q_i)^2\,. \end{aligned} \tag{2.36}$$

Consequently, these results can be used to obtain

$$S(q_i)^2\,\{S(\dot{q}_i)\,S(q_i) + S(q_i)\,S(\dot{q}_i)\} = -S(q_i)^4\,S(\omega_i) = S(q_i)^2\,S(\omega_i)\,. \tag{2.37}$$

Substituting this into the above expressions to simply the Euler-Lagrange equations we obtain

$$\begin{aligned} -S(q_i)^2\,\frac{d}{dt}\left(\frac{\partial \tilde{L}(q,\omega)}{\partial \omega_i}\right) + 2S(q_i)^2\,S(\omega_i)\,\frac{\partial \tilde{L}(q,\omega)}{\partial \omega_i} \\ - S(q_i)\,\frac{\partial \tilde{L}(q,\omega)}{\partial q_i} = 0, \quad i = 1,\ldots,n. \end{aligned} \tag{2.38}$$

Hence, the Euler-Lagrange equations take the following form. The Euler-Lagrange equations for a modified Lagrangian function $\tilde{L} : \mathrm{T}\left(\mathrm{S}^2\right)^n \to \mathbb{R}^1$ are given by

$$\begin{aligned} \left(I_{3\times 3} - q_i q_i^T\right)\left\{\frac{d}{dt}\left(\frac{\partial \tilde{L}(q,\omega)}{\partial \omega_i}\right) - 2S(\omega_i)\,\frac{\partial \tilde{L}(q,\omega)}{\partial \omega_i}\right\} \\ - S(q_i)\,\frac{\partial \tilde{L}(q,\omega)}{\partial q_i} = 0, \quad i = 1,\ldots,n. \end{aligned} \tag{2.39}$$

2.3.7 Magnus Expansion

Before venturing into the formulation of the proposed algorithm, the concept of Magnus expansion is considered a prerequisite for the development. Consider a vector valued function $\Gamma(t) \in \mathbb{R}^n$, whose

non-autonomous linear ordinary differential equation is defined as,

$$\frac{\mathrm{d}\Gamma(t)}{\mathrm{d}t} = \mathbf{P}(t)\Gamma(t) \tag{2.40}$$

where, the elements of $\mathbf{P}(t) \in \mathbb{R}^{n\times n}$ are continuous in t. Following Magnus expansion [46], the solution of Eq. (2.40) is approximated as the exponential of a $n \times n$ matrix given as: $\Gamma(t) = \mathrm{e}^{\mathbf{S}(t)}\Gamma_0$. The matrix $\mathbf{S}(t)$ is constructed as a series expansion, where, the composition law for the elements of the individual terms of Magnus series is given by the Lie bracket [46]. Suppose $\Gamma\left(t\right)$ is evolving on a lie group of a differentiable manifold and is a function of the variables of its lie algebra $\mathbf{S}(t)$, then by using chain rule, the following expression is obtained,

$$\frac{\mathrm{d}\Gamma\left(t\right)}{\mathrm{d}t} = \frac{\mathrm{d}\Gamma}{\mathrm{d}\mathrm{S}_{ij}}\frac{\mathrm{d}\mathrm{S}_{ij}}{\mathrm{d}t} = \left(\partial_{\mathrm{S}_{ij}}\Gamma\right)\dot{\mathrm{S}}_{ij} \tag{2.41}$$

where, $\partial_{\mathrm{S}_{ij}}(\cdot) = \frac{\mathrm{d}(\cdot)}{\mathrm{d}\mathrm{S}_{ij}}$. Noting that $\Gamma(t) = \mathrm{e}^{\mathbf{S}(t)}\Gamma_0$, $\partial_{\mathrm{S}_{ij}}\Gamma$ is computed by applying the Power-Gradient Theorem and Exponential-Gradient Theorem [22], for a square matrix $\mathbf{S}$. The expression for $\partial_{\mathrm{S}_{ij}}\mathrm{e}^{\mathbf{S}}$ is obtained as,

$$\begin{aligned}\partial_{\mathrm{S}_{ij}}\mathrm{e}^{\mathbf{S}} &= \mathrm{dexp}_{\mathbf{S}}\left(\mathbf{E}_{ij}\right)\mathrm{e}^{\mathbf{S}}\\ &= \mathrm{e}^{\mathbf{S}}\mathrm{dexp}_{-\mathbf{S}}\left(\mathbf{E}_{ij}\right)\end{aligned} \tag{2.42}$$

where, $\mathrm{dexp}_{\mathbf{A}}(\mathbf{B}) = \sum_{k=0}^{\infty}\frac{\mathrm{ad}_{\mathbf{A}}^{k}(\mathbf{B})}{(k+1)!}$. Accordingly, Eq. (2.41) is revised as,

$$\begin{aligned}\dot{\Gamma} &= \mathrm{dexp}_{\mathbf{S}}\left(\dot{\mathrm{S}}_{ij}\mathbf{E}_{ij}\right)\mathrm{e}^{\mathbf{S}}\Gamma_0\\ &= \mathrm{dexp}_{\mathbf{S}}\left(\dot{\mathbf{S}}\right)\Gamma\end{aligned} \tag{2.43}$$

Comparing Eq. (2.43) with Eq. (2.40), $\mathbf{P} = \mathrm{dexp}_{\mathbf{S}}\left(\dot{\mathbf{S}}\right)$. Using Baker's Inverse theorem [22], the following ODE in $\dot{\mathbf{S}}$ is obtained,

$$\frac{\mathrm{d}\mathbf{S}}{\mathrm{d}t} = \mathrm{dexp}_{\mathbf{S}}^{-1}\left(\mathbf{P}\right) \tag{2.44}$$

Eq. (2.44) establishes the relation between $\mathbf{P}\left(t\right)$ defined on a differentiable manifold, with the matrix $\mathbf{S}$ defined on its Lie Algebra for the deterministic case. For the generation of SDEs in lie groups, a stochastic process is first defined on the Lie algebra from which it is mapped into the group using the exponential mapping [22]. If a n-dimensional Lie algebra is represented as an Euclidean space, the exponential map can be used to transfer this sample path on to the appropriate Lie group. However, with the evolution of the states, nonlinearities begin to appear as the exponentiated path veers away

from the lie group's identity element [47]. Therefore, it is necessary to reset everything to identity before injecting from algebra to group such that the system states are properly evaluated in the Lie algebra first.

To conclude this chapter, a set of working principles have been established, providing the necessary background for the subsequent discussions within this thesis. The analysis of simulation strategies, from the Ito-Taylor expansion-based stochastic integration scheme to the dynamics of deterministic Hamiltonian systems on both Euclidean and non-Euclidean domains, bridges the gap between conventional approaches and the demand for innovative techniques. The exploration of manifolds and differential geometries equips us with the essential tools to venture into the domain of geometric-preserving solutions, employing the Magnus expansion method. This approach holds the promise of overcoming the challenges posed by drift pinning when dealing with systems on non-Euclidean domains.

As we progress through the following chapters, the knowledge and insights established here will serve as the conceptual bedrock upon which further explorations into the domain of dynamic systems will be constructed. With this comprehensive background, the thesis is well-prepared to delve into the heart of the matter, where these principles will be applied to tackle complex real-world problems and illuminate new paths in the area of numerical simulations.

The foundation laid in this chapter serves as the critical underpinning for the advancements and innovations presented in the following chapter. Building upon the principles of simulation strategy on $\mathbb{R}^n$, the subsequent chapter dives into the domain of real-time modal identification and control techniques. In the context of dynamic systems, the need for efficient and accurate methods is paramount, and this study takes a significant step in addressing this challenge.

Chapter 3

Real-time health monitoring on $\mathbb{R}^n$

In recent years, there has been significant research on real-time modal identification using techniques like First Order Eigen Perturbation (FOEP) [34]. These algorithms operate in a recursive framework and have found applications in modal identification, damage detection, and filtering. However, existing FOEP-based algorithms often neglect higher-order error terms, requiring a large number of samples for convergence [55], which can lead to delayed convergence issues. This study addresses these challenges by introducing a mathematically consistent framework for error-adapted FOEP, enabling real-time error feedback for accurate eigenspace estimation. Additionally, the algorithm is applied to partial mode shape identification in a decentralized manner, and an online convergence indicator based on diagonal dominance is proposed. The utility of the algorithm is extended to real-time passive control using multi-tuned mass dampers [56] and condition monitoring of such systems. Moreover, the study explores a novel concept of "real-time decentralization" where a single-channel data approach is employed for underdetermined modal identification, reducing the number of required sensors. This approach breaks down complex problems into manageable sub-problems, providing an efficient alternative to conventional methods [57]. In summary, this research contributes a comprehensive framework for enhancing FOEP-based real-time modal identification, with applications spanning decentralized modal identification, convergence indicators, and real-time passive control and condition monitoring of vibrating structures.

3.1 Motivation of the present study

The key motivations for conducting this study are:

- Current techniques for modal identification face limitations when applied to dynamic and time-varying systems, such as wind turbines, bridge-vehicle interactions, and tuned mass dampers.

- These limitations hinder the practical implementation of traditional modal identification algorithms in real-time monitoring and control applications.
- Modern real-time algorithms like Recursive Principal Component Analysis (RPCA), Recursive Canonical Analysis (RCCA), and Recursive Singular Spectrum Analysis (RSSA) hold promise but often suffer from extended convergence times due to neglecting higher-order perturbation terms.
- Prolonged convergence times pose a significant challenge, delaying the achievement of accurate mode identification and impacting the timely decision-making and control in dynamic systems.

Towards this, the study aims to address these challenges by introducing an error-adapted First Order Eigen Perturbation (FOEP) algorithm, which incorporates error feedback to enhance the accuracy and efficiency of real-time mode identification. Additionally, the research explores the potential application of the FOEP algorithm to decentralized mode shape identification, offering a novel approach to handling large-dimensional problems with fewer sensors. Ultimately, the primary goal of this study is to bridge the gap between theoretical modal identification methods and practical real-world applications, providing a robust framework that accelerates and improves mode identification in dynamic systems. The findings of this research have the potential to advance various fields, including structural health monitoring and adaptive control of vibrating structures, by enabling faster and more accurate mode identification in real-time scenarios.

3.2 Background

Eigenvalue decomposition (EVD) of time windowed co-variance matrices is analytically possible yet computationally exhaustive for large systems [30]. This issue can be accounted for using a host of computational techniques of which eigen perturbation theory for adaptive EVD [34, 58, 59] provide an attractive alternative. A brief discussion on eigen perturbation technique is presented in this section. In order to understand the eigen-perturbation framework in the purview of generalized eigenvalue problem, consider two multi-block data matrices $\mathbf{X}_1$ and $\mathbf{X}_2$. For the given data matrix the following eigenvalue problem (GEVP) $\mathbf{AV} = \mathbf{BV}\bar{\mathbf{\Lambda}}$ can be solved to find eigenvectors and eigenvalues [60]. The matrix of interest is defined in the terms of *between-set* co-variance matrix $\mathbf{A}$ (contains cross-covariance matrices of $\mathbf{X}_1$ and $\mathbf{X}_2$) and *within-set* co-variance matrix $\mathbf{B}$ (contains auto-covariance matrices of $\mathbf{X}_1$

and $\mathbf{X}_2$) as:

$$\mathbf{A} = \begin{pmatrix} \mathbf{0} & \mathbf{R}_{12} \\ \mathbf{R}_{21} & \mathbf{0} \end{pmatrix}; \qquad \mathbf{B} = \begin{pmatrix} \mathbf{R}_{11} & \mathbf{0} \\ \mathbf{0} & \mathbf{R}_{22} \end{pmatrix} \tag{3.1}$$

where, the co-variance matrix for the data matrices $\mathbf{X}_i$ and $\mathbf{X}_j$ of length N can be obtained as $R_{ij} = 1/(N-1)\mathbf{X}_i\mathbf{X}_j$. By adding $\mathbf{BV}$ on both side of GEVP an equivalent EV problem similar to GEVP can be obtained as:

$$\mathbf{RV} = \mathbf{BV}\mathbf{\Lambda} \tag{3.2}$$

where $\mathbf{R} = \mathbf{A} + \mathbf{B}$ is the multi-block covariance matrix of the data $\mathbf{X} = [\mathbf{X}_1, \mathbf{X}_2]$ and $\mathbf{\Lambda} = \mathbf{I} + \bar{\mathbf{\Lambda}}$ is the associated eigenvalue of Eq.(3.2). For real-time implementation as the data streams in, the real-time update of the total and auto covariance matrices are given using the following update rule [33]:

$$\begin{aligned} \mathbf{R}_k &= (1-\lambda)\mathbf{R}_{k-1} + \lambda X_k X_k^T \\ \mathbf{B}_k &= (1-\lambda)\mathbf{B}_{k-1} + \lambda \mathbf{U}_k \mathbf{U}_k^T \end{aligned} \tag{3.3}$$

where, $\mathbf{U}_k = \begin{pmatrix} \mathbf{X}_{1k} & \mathbf{0} \\ \mathbf{0} & \mathbf{X}_{2k} \end{pmatrix}$, and λ is the memory depth parameter which varies with time within $0 \leq \lambda \leq 1$. It is straightforward to assume that the eigen value decomposition (EVD) of the total covariance matrix at k^{th} time step has a form $\mathbf{R}_k = \mathbf{V}_k \mathbf{\Lambda}_k {\mathbf{V}_k}^T$. Through a suitable transformation, the transformed coordinates of the physical responses $\mathbf{X}$ can be written in terms of the following perturbation framework:

$$\beta_k = \alpha_k + \sum_{i=1}^{m} \Upsilon_i \tag{3.4}$$

where, $\alpha_k = \mathbf{V}_k^T \mathbf{X}_k$ is the actual coordinate and $\Upsilon_i = \mathcal{E}_i^T \mathbf{X}_k$ is the i^{th} error vector corresponding to the i^{th} order perturbation. Thus, Eq.(3.3) can be rephrased as [34]:

$$\begin{aligned} \mathbf{V}_k \mathbf{\Lambda}_k \mathbf{V}_k^T &= \mathbf{V}_{k-1} \left((1-\lambda)\mathbf{\Lambda}_{k-1} + \lambda \alpha_k \alpha_k^T \right) \mathbf{V}_{k-1}^T \\ &+ \mathbf{V}_{k-1} \left(\alpha_k \sum_{i=1}^{m} {\Upsilon_i}^T + \sum_{i=1}^{m} \Upsilon_i \alpha_k^T + \mathcal{O}(\epsilon^2) \right) \mathbf{V}_{k-1}^T \\ &= \mathbf{V}_{k-1} \left[\mathbf{\Lambda}_{k-1} + \lambda \left(\beta_k \beta_k^T - \mathbf{\Lambda}_{k-1} \right) \right] \mathbf{V}_{k-1}^T \end{aligned} \tag{3.5}$$

The problem of eigenspace update reduces to finding the EVD of the matrix $\left(\mathbf{\Lambda}_{k-1} + \lambda \left(\beta_k \beta_k^T - \mathbf{\Lambda}_{k-1}\right)\right)$, where update of $\mathbf{\Lambda}_k$ can be found out by applying a small correction to the eigenspace at $\mathbf{\Lambda}_{k-1}$. In order to use the perturbation theory, it is important to note that the term $\left(\mathbf{\Lambda}_{k-1} + \lambda \left(\beta_k \beta_k^T - \mathbf{\Lambda}_{k-1}\right)\right)$

should be diagonally dominant which allows the application of Gersgorin's theorem. Gersgorin's theorem provides an ease for evaluating the eigenspace without performing the actual eigen-decomposition, by virtue of which the EVD is expressed as $\mathbf{V}_{k-1}\mathbf{\Lambda}_{k-1}\mathbf{V}_{k-1}^T$ [34]. However, estimation of EVD for $\left(\mathbf{\Lambda}_{k-1} + \lambda\left(\beta_k\beta_k^T - \mathbf{\Lambda}_{k-1}\right)\right)$ analytically is difficult for a large data dimension. This problem can be solved in an computationally less exhaustive way using matrix perturbation theory. Assuming $\mathbf{\Delta}_V$ and $\mathbf{\Delta}_\Lambda$ be the perturbation matrices, the perturbation series can be represented as:

$$\begin{aligned}\mathbf{V}_k &= \mathbf{V}_{k-1}\left(I + \mathbf{\Delta}_V + \mathbf{\Delta}_V^2 + \ldots + \mathbf{\Delta}_V^m\right), \\ \mathbf{\Lambda}_k &= \mathbf{\Lambda}_{k-1} + \mathbf{\Delta}_\Lambda + \mathbf{\Delta}_\Lambda^2 + \ldots + \mathbf{\Delta}_\Lambda^m\end{aligned} \tag{3.6}$$

With the above m^{th} order perturbations, the eigenspace update of $\left(\mathbf{\Lambda}_{k-1} + \lambda\left(\beta_k\beta_k^T - \mathbf{\Lambda}_{k-1}\right)\right)$ can be evaluated by expanding $\mathbf{V}_k\mathbf{\Lambda}_k\mathbf{V}_k^T$ in terms of the generalized perturbation framework as:

$$\begin{aligned}\mathbf{V}_k\mathbf{\Lambda}_k\mathbf{V}_k^T &= \mathbf{V}_{k-1}\left(I + \mathbf{\Delta}_V + \mathbf{\Delta}_V^2 + \ldots\right) \\ &\quad \left(\mathbf{\Lambda} + \mathbf{\Delta}_\Lambda + \mathbf{\Delta}_\Lambda^2 + \ldots\right)\left(I + \mathbf{\Delta}_V + \mathbf{\Delta}_V^2 + \ldots\right)^T\mathbf{V}_{k-1}^T\end{aligned} \tag{3.7}$$

The perturbation series is truncated in such a way that it yields an acceptable result with the reduction in computational complexity [34]. For a perturbation of order m, terms with order greater than m are truncated. After truncating higher order terms, Eq.(3.7) yields an equation for the m^{th} order perturbation. Since the main aim of the present work is to provide an efficient framework for the FOEP, the perturbation series and error estimate is limited upto first order, therefore a combination of Eq.(3.5) and Eq.(3.7) reduces to the following form [34]:

$$\begin{aligned}&\left[(1-\lambda)\mathbf{\Lambda}_{k-1} + \lambda\left(\alpha_k\alpha_k^T + \alpha_k{\Upsilon_1}^T + \Upsilon_1\alpha_k^T\right)\right] \\ &= \left(I + \mathbf{\Delta}_V\right)\left(\mathbf{\Lambda}_{k-1} + \mathbf{\Delta}_\Lambda\right)\left(I + \mathbf{\Delta}_V\right)^T\end{aligned} \tag{3.8}$$

3.2.1 FOEP in MDOF structural dynamics

Above section explains the use of FOEP in a generalized fashion, it is narrowed down to the domain of structural dynamics in this section. As the dynamics of a large class of vibrating systems involve modal analysis in the form of eigen analysis and spectral decomposition, it becomes necessary to highlight the application of FOEP in this area [34]. Recursive update of eigenspace through FOEP has proved to be efficient for vibrating systems in literature [34]. For a better understanding of the FOEP technique in this area, consider a typical MDOF vibrating system with mass **M**, stiffness **K** and damping **C** matrices,

excited with a broadband stationary stochastic excitation $\mathbf{F}(t)$, expressed as:

$$\mathbf{M}\ddot{\mathbf{X}}(t) + \mathbf{C}\dot{\mathbf{X}}(t) + \mathbf{K}\mathbf{X}(t) = \mathbf{F}(t) \tag{3.9}$$

where, $\mathbf{X}(t)$ is the dynamical response of the system. The relation between physical and modal form of output response and input force can be represented with the use of normalized modal matrix $\mathbf{V}$ as: $X_j(t) = \sum_{i=1}^{N} V_{ji} z_i(t)$ and $f_j(t) = \sum_{i=1}^{N} V_{ij} F_i(t), \forall j = 1, 2, \ldots, N$. The modal forces $f_i(t)$ are assumed to be as ergodic random excitations and the solution for the modal responses $z_i(t)$ can be obtained through the use of convolution integral: $z_i(t) = \int_0^t f_i(t-\tau) h_i(\tau) d\tau$. The impulse response function is given as, $h_i(t-\tau) = e^{-\zeta_i \Lambda_{n,i}(t-\tau)} \sin \Lambda_{d,i}(t-\tau)/m_i \Lambda_{d,i}$, where $\Lambda_{d,i}^2$ is the damped modal frequency. In order to perform the EVD of data covariance matrix, it is instructive to understand the relation between linear normal coordinates ($\mathcal{P}$) and proper orthogonal components (Q). Considering $\mathbf{V}$ to be the POMs and $\hat{\mathbf{V}}$ to be the LNMs, $\mathcal{P}$ can be expressed as a sum of $Q = \mathbf{V}^T\mathbf{X}$ and error terms $\Upsilon_i = \mathcal{E}_i^T \mathbf{X}, \forall i = 1, 2 \ldots m$ as:

$$\begin{aligned} \mathcal{P} &= \hat{\mathbf{V}}^T \mathbf{X} \\ &= \mathbf{V}^T \mathbf{X} + \sum_{i=1}^{m} \mathcal{E}_i^T \mathbf{X} \forall i = 1, 2 \ldots m \\ &= Q + \sum_{i=1}^{m} \Upsilon_i \forall i = 1, 2 \ldots m \end{aligned} \tag{3.10}$$

The traditional FOEP algorithms provide POMs, which are approximation of true LNMs. However, with the inclusion of error terms, approximate LNMs can be improved and achieved faster. For the cases of engineering structures, where modal frequencies are well separated and damping is low, the responses due to two different modes are statistically independent, which leads to negligible error terms $\mathcal{E}$ [34]. However, the errors need to be accounted in the estimation of covariance matrix for non-stationary and time-varying dynamical systems in order to have a computationally efficient and effective formulation. With the use of Eq.(3.10), the elements of zero lag modal covariance matrix are obtained as:

$$\begin{aligned} \mathbf{R}_{\mathcal{P}_k \mathcal{P}_j} &= \sum_{l=1}^{N} V_{kl} V_{jl} \int_{-\infty}^{\infty} \int_{-\infty}^{\infty} h_l(\tau_1) h_l(\tau_2) \mathbf{R}_{f_m f_m}(\tau_1 - \tau_2) d\tau_1 d\tau_2 \\ &+ \sum_{l=1}^{N} V_{kl} \sum_{i=1}^{m} \mathcal{E}_{i,jl} \int_{-\infty}^{\infty} \int_{-\infty}^{\infty} h_l(\tau_1) h_l(\tau_2) \mathbf{R}_{f_l f_l}(\tau_1 - \tau_2) d\tau_1 d\tau_2 \\ &+ \sum_{l=1}^{N} \sum_{i=1}^{m} \mathcal{E}_{i,kl} V_{jl} \int_{-\infty}^{\infty} \int_{-\infty}^{\infty} h_l(\tau_1) h_l(\tau_2) \mathbf{R}_{f_l f_l}(\tau_1 - \tau_2) d\tau_1 d\tau_2 + \epsilon(\mathcal{O}^2) \end{aligned} \tag{3.11}$$

Following the Equation (3.5), the EVD of $\mathbf{R}_{\mathcal{PP}}$ can be expressed in the following form:

$$\begin{aligned}\mathbf{V}_k\mathbf{\Lambda}_k\mathbf{V}_k^T &= (1-\lambda)\mathbf{V}_{k-1}\mathbf{\Lambda}_{k-1}\mathbf{V}_{k-1}^T + \lambda\mathbf{V}_{k-1}Q_{k-1}Q_{k-1}^T\mathbf{V}_{k-1}^T + \\ &\quad \lambda\mathbf{V}_{k-1}Q_{k-1}\sum_{i=1}^{m}{\Upsilon_{i,k-1}}^T\mathbf{V}_{k-1}^T + \\ &\quad \lambda\mathbf{V}_{k-1}\sum_{i=1}^{m}\Upsilon_{1,k-1}Q_{k-1}^T\mathbf{V}_{k-1}^T + \mathcal{O}\left(\varepsilon^2\right)\end{aligned} \tag{3.12}$$

It can be noted that, the contribution of higher order error terms $\mathcal{O}(\varepsilon^2)$ towards diagonally dominant behavior of $\left(\mathbf{\Lambda}_{k-1} + \lambda\left(\beta_k\beta_k^T - \mathbf{\Lambda}_{k-1}\right)\right)$ is insignificant compared to the computational exhaustiveness, and mathematical complexity associated with in the analysis of them and thus can be safely neglected. Further the adaptation of more error terms i.e. considering higher order perturbations might lead to quicker convergence, yet may not be amenable to formulate inverse vibration problems with ease [58, 61]. An alternative way of approaching the above problem would entail consideration of the first order error terms and seek a mathematically consistent way of feeding them back to achieve faster convergence.

3.3 Proposed error-adapted FOEP framework

The basic principle of the proposed error-adapted algorithm primarily premises on three primary segments operating *simultaneously* in a recursive framework: *Firstly*, the update of initial covariance matrix using generalized eigenvalue decomposition (GEVD), *Secondly*, estimation of error terms and *Finally*, feedback of the estimated error terms for the evaluation of error-adapted eigenspace. For estimation of the error terms in real-time two approaches (GEVD and standard EVD) are considered. This error term is used as a feedback for the eigenspace using GEVD to estimate the error-adapted eigenspace.

The present framework uses the GEVD for the evaluation of perturbation matrices $\mathbf{\Delta_V}$ and $\mathbf{\Delta_\Lambda}$. Substituting Eq.(3.3) in Eq.(3.2), and considering that the updated eigenspace satisfies the GEVP at k^{th} as well as $(k-1)^{th}$ time instant, the update of eigenspace of co-variance matrix can be obtained after performing suitable arrangement as:

$$\begin{aligned}&\left[(1-\lambda)\mathbf{R}_{k-1} + \lambda X_kX_k^T\right]\hat{\mathbf{V}}_k = \mathbf{B}_k\hat{\mathbf{V}}_k\mathbf{\Lambda}_k \\ &\Rightarrow \hat{\mathbf{V}}_k\mathbf{\Lambda}_k\hat{\mathbf{V}}_k^T = \mathbf{B}_k^{-1}\left[(1-\lambda)\mathbf{B}_{k-1}\hat{\mathbf{V}}_{k-1}\mathbf{\Lambda}_{k-1}\hat{\mathbf{V}}_{k-1}^T + \lambda X_kX_k^T\right] \\ &\qquad = \hat{\mathbf{V}}_{k-1}\Big[\mathbf{\Lambda}_{k-1} + \lambda\Big(\hat{\mathbf{V}}_{k-1}^T\mathbf{B}_k^{-1}X_kX_k^T\hat{\mathbf{V}}_{k-1} \\ &\qquad - \hat{\mathbf{V}}_{k-1}^T\mathbf{B}_k^{-1}\mathbf{U}_k\mathbf{U}_k^T\hat{\mathbf{V}}_{k-1}\mathbf{\Lambda}_{k-1}\Big)\Big]\hat{\mathbf{V}}_{k-1}^T\end{aligned} \tag{3.13}$$

As mentioned earlier, the update of eigenspace in Eq.(3.13) can not be obtained analytically for large size of data matrix due to dimensional complexities. With the assumption of $\hat{\mathbf{V}}_k = \hat{\mathbf{V}}_{k-1}(\mathbf{I} + \boldsymbol{\Delta}_V)$ and $\boldsymbol{\Lambda}_k = \boldsymbol{\Lambda}_{k-1} + \boldsymbol{\Delta}_\Lambda$, where,$\boldsymbol{\Delta}_V$ and $\boldsymbol{\Delta}_\Lambda$ are the small perturbation matrices, Eq.(3.13) can be reduced as:

$$\mathbf{P}_k = \boldsymbol{\Delta}_\Lambda + \boldsymbol{\Lambda}\boldsymbol{\Delta}_V{}^T + \boldsymbol{\Delta}_V\boldsymbol{\Lambda} + \boldsymbol{\Delta}_\Lambda\boldsymbol{\Delta}_V{}^T + \boldsymbol{\Delta}_V\boldsymbol{\Delta}_\Lambda + \boldsymbol{\Delta}_V\boldsymbol{\Lambda}\boldsymbol{\Delta}_V{}^T \tag{3.14}$$

Here, $\mathbf{P}_k = \lambda\left(\hat{\mathbf{V}}_{k-1}^T\mathbf{B}_k^{-1}X_kX_k^T\hat{\mathbf{V}}_{k-1} - \hat{\mathbf{V}}_{k-1}^T\mathbf{B}_k^{-1}\mathbf{U}_k\mathbf{U}_k^T\hat{\mathbf{V}}_{k-1}\boldsymbol{\Lambda}_{k-1}\right)$ is the total perturbation applied on the eigenspace. By the virtue of Eq.(3.10), Eq.(3.14) can be expressed in terms of POMs and first order error terms ignoring $(\mathcal{E}_2, \mathcal{E}_2, \ldots)$ as:

$$\begin{aligned}\mathbf{P}_k &= \lambda\left(\mathbf{V}_{k-1}^T\mathbf{B}_k^{-1}X_kX_k^T\mathbf{V}_{k-1} - \mathbf{V}_{k-1}^T\mathbf{B}_k^{-1}\mathbf{U}_k\mathbf{U}_k^T\mathbf{V}_{k-1}\boldsymbol{\Lambda}_{k-1}\right)\\ &+\lambda\left(\mathcal{E}_{1,k-1}^T\mathbf{B}_k^{-1}X_kX_k^T\mathbf{V}_{k-1} - \mathcal{E}_{1,k-1}^T\mathbf{B}_k^{-1}\mathbf{U}_k\mathbf{U}_k^T\mathbf{V}_{k-1}\boldsymbol{\Lambda}_{k-1}\right)\\ &+\lambda\left(\mathbf{V}_{k-1}^T\mathbf{B}_k^{-1}X_kX_k^T\mathcal{E}_{1,k-1} - \mathbf{V}_{k-1}^T\mathbf{B}_k^{-1}\mathbf{U}_k\mathbf{U}_k^T\mathcal{E}_{1,k-1}\boldsymbol{\Lambda}_{k-1}\right)\end{aligned} \tag{3.15}$$

However, as it is not efficient to calculate inverse of the co-variance matrix $\mathbf{B}_k$ from Eq.(3.3) in real time, ${\mathbf{B}_k}^{-1}$ is obtained by using matrix inversion lemma [33] as:

$$\begin{aligned}{\mathbf{B}_k}^{-1} &= \Big[\tfrac{1}{(1-\lambda)}\mathbf{B}_{k-1}^{-1} - \tfrac{1}{(1-\lambda)^2}\mathbf{B}_{k-1}^{-1}\mathbf{U}_k\left(\tfrac{1}{\lambda}\mathbf{I}\right.\\ &\left.+\tfrac{1}{(1-\lambda)}\mathbf{U}_k^T\mathbf{B}_{k-1}^{-1}\mathbf{U}_k\right)^{-1}\mathbf{U}_k^T\mathbf{B}_{k-1}^{-1}\Big]\end{aligned} \tag{3.16}$$

After substituting ${\mathbf{B}_k}^{-1}$ in Eq.(3.13) and obtaining $\mathbf{P}_k$, the primary aim is to estimate the perturbation matrices $\boldsymbol{\Delta}_V$ and $\boldsymbol{\Delta}_\Lambda$. Since there are two unknowns $\boldsymbol{\Delta}_V$ and $\boldsymbol{\Delta}_\Lambda$, Eq.(3.14) alone is not sufficient to elicit the perturbation matrices, therefore an additional equation is required. This is obtained from the orthogonality of eigenvectors i.e. $\mathbf{V}_k^T\mathbf{B}_k\mathbf{V}_k = \mathbf{I}$. On proper substitution of $\mathbf{B}_k$ and $\mathbf{V}_k$ in $\mathbf{V}_k^T\mathbf{B}_k\mathbf{V}_k = \mathbf{I}$, an additional equation in the form of $\boldsymbol{\Delta}_V$ can be obtained as:

$$\left[(1-\lambda)\left(\boldsymbol{\Delta}_V + \boldsymbol{\Delta}_V^T\right) + \lambda\left(\mathcal{S}_k\mathcal{S}_k^T\boldsymbol{\Delta}_V + \boldsymbol{\Delta}_V^T\mathcal{S}_k\mathcal{S}_k^T\right) = \lambda\left(\mathbf{I} - \mathcal{S}_k\mathcal{S}_k^T\right)\right] \tag{3.17}$$

where, $\mathcal{S} = \mathbf{V}_{k-1}^T\mathbf{U}_k$ is the transformed response for the within-set data matrix. By taking first two terms of the total perturbation of Eq.(3.14), $\boldsymbol{\Delta}_V$ can be expressed as $\boldsymbol{\Delta}_V = (\mathbf{P} - \boldsymbol{\Delta}_\Lambda)\boldsymbol{\Lambda}_{k-1}^{-1}$. On substitution of $\boldsymbol{\Delta}_V$ in Eq.(3.17), the following can be obtained:

$$(2(1-\lambda)\mathbf{I} + \mathbf{J}_k)\mathbf{D}_k + \mathbf{D}_k\mathbf{J}_k = \boldsymbol{\Theta}_k \tag{3.18}$$

where,

$$\begin{aligned}\mathbf{D}_k &= \mathbf{\Lambda}_{k-1}^{-1}\mathbf{\Delta}_\Lambda, \quad \mathbf{J}_k = \mathbf{V}_{k-1}^T\mathbf{U}_k{\mathbf{U}_k}^T\mathbf{V}_{k-1}\\ \mathbf{\Theta}_k &= (1-\lambda)\left(\mathbf{\Lambda}_{k-1}^{-1}\mathbf{P} + \mathbf{P}^T\mathbf{\Lambda}_{k-1}^{-1}\right)\\ &\quad +\lambda\left(\mathbf{J}_k\mathbf{\Lambda}_{k-1}^{-1}\mathbf{P} + \mathbf{P}^T\mathbf{\Lambda}_{k-1}^{-1}\mathbf{J}_k\right) - \lambda\left(\mathbf{I}-\mathbf{J}_k\right)\end{aligned}$$

The term $\mathbf{\Delta}_\Lambda$ can be obtained after $\mathbf{D}$ is calculated from Eq.(3.18). Since, the total perturbation, $\mathbf{P}$ and diagonal perturbation matrix $\mathbf{\Delta}_\Lambda$ are known, $\mathbf{\Delta}_V$ can be obtained using the form: $(\mathbf{\Lambda}+\mathbf{\Delta}_\Lambda){\mathbf{\Delta}_V}^T + \mathbf{\Delta}_V(\mathbf{\Lambda}+\mathbf{\Delta}_\Lambda) = (\mathbf{P}-\mathbf{\Delta}_\Lambda)$. After the evaluation of the estimates of $\mathbf{\Delta}_V$ and $\mathbf{\Delta}_\Lambda$, the updated eigenspace of covariance matrix R_k can be obtained at each instant k by utilizing the following equations:

$$\mathbf{V}_k = \mathbf{V}_{k-1}\left(\mathbf{I}+\mathbf{\Delta}_V\right) \quad \& \quad \mathbf{\Lambda}_k = \mathbf{\Lambda}_{k-1}+\mathbf{\Delta}_\Lambda \tag{3.19}$$

Here, $\mathbf{V}_k$ and $\mathbf{\Lambda}_k$ are the eigenspace update which satisfies the generalized eigenvalue problem (GEVP) in Eq.(3.2).

3.3.1 Recursive error estimation and feedback

The proposed algorithm uses GEVD for the recursive update of initial covariance matrix. However, as mentioned in the above section, a separate eigenspace can also be obtained by solving the standard eigenvalue problem (traditional FOEP algorithm), where, the within-set co-variance matrix is replaced by an identity matrix ($\mathbf{B}=\mathbf{I}$) resulting $\mathbf{RV}=\mathbf{V\Lambda}$, the detailed derivation of the perturbation for this algorithm can be found from the literature [34]. As an essential part for the calculation of error feedback ($\mathcal{E}_1$), this eigenspace is utilized in the present algorithm for the evaluation of α_k, as the traditional FOEP algorithms ignores the use of error adaptation [34]. Total perturbation for the traditional FOEP algorithm can be expressed as:

$$\lambda\alpha_k\alpha_k^T \;=\; \mathbf{\Delta_\Lambda} + \mathbf{\Lambda}_{k-1}{\mathbf{\Delta_V}}^T + \mathbf{\Delta_V\Lambda} + \mathbf{\Delta_\Lambda}{\mathbf{\Delta_V}}^T + \mathbf{\Delta_V\Delta_\Lambda} \tag{3.20}$$

where, λ is the memory depth parameter as defined in Eq.(3.3). The proposed framework adapts the error obtained from the use of both eigenvalue problem and is used as a feedback to obtain the error-corrected eigenspace. The error can be obtained after obtaining the error perturbation vector Δ_V^C as:

$$\mathcal{E}_{1,k} = \mathbf{V}_{k-1}(\mathbf{I}+\mathbf{\Delta}_V^c) \tag{3.21}$$

The complete process for evaluation of corrected error-adapted eigenvector matrix can be summarized as follows:

Total perturbation for GEVP:

$$\begin{aligned}\mathbf{P}_k = \;& \lambda\left(\mathbf{V}_{k-1}^T\mathbf{B}_k^{-1}X_kX_k^T\mathbf{V}_{k-1} - \mathbf{V}_{k-1}^T\mathbf{B}_k^{-1}\mathbf{U}_k\mathbf{U}_k^T\mathbf{V}_{k-1}\mathbf{\Lambda}_{k-1}\right)\\ &+\lambda\left(\mathcal{E}_{1,k-1}^T\mathbf{B}_k^{-1}X_kX_k^T\mathbf{V}_{k-1} - \mathcal{E}_{1,k-1}^T\mathbf{B}_k^{-1}\mathbf{U}_k\mathbf{U}_k^T\mathbf{V}_{k-1}\mathbf{\Lambda}_{k-1}\right)\\ &+\lambda\left(\mathbf{V}_{k-1}^T\mathbf{B}_k^{-1}X_kX_k^T\mathcal{E}_{1,k-1} - \mathbf{V}_{k-1}^T\mathbf{B}_k^{-1}\mathbf{U}_k\mathbf{U}_k^T\mathcal{E}_{1,k-1}\mathbf{\Lambda}_{k-1}\right)\end{aligned} \tag{3.22}$$

Additional equation for the estimation of $\mathbf{\Delta}_V$ and $\mathbf{\Delta}_\Lambda$:

$$\begin{aligned}\lambda\left(\mathbf{I} - \mathcal{S}_k\mathcal{S}_k^T\right) = \;& (1-\lambda)\left(\mathbf{\Delta}_V + \mathbf{\Delta}_V^T\right)\\ &+\lambda\left(\mathcal{S}_k\mathcal{S}_k^T\mathbf{\Delta}_V + \mathbf{\Delta}_V^T\mathcal{S}_k\mathcal{S}_k^T\right)\end{aligned} \tag{3.23}$$

Recursive estimation of eigenspace:

$$\mathbf{V}_k = \;\mathbf{V}_{k-1}\left(\mathbf{I} + \mathbf{\Delta}_V\right)\;\&\;\mathbf{\Lambda}_k = \mathbf{\Lambda}_{k-1} + \mathbf{\Delta}_\Lambda \tag{3.24}$$

Estimation of Error in real-time:

$$\mathbf{\Delta}_V^c\mathbf{\Lambda}\mathbf{\Delta}_V^{c\,T} = \mathbf{P}_k - \lambda\alpha_k\alpha_k^T \tag{3.25}$$

where, α_k = $\mathbf{V}_{k-1}^TX_k$, and $\mathcal{E}_{1,k} = \mathbf{V}_{k-1}(\mathbf{I} + \mathbf{\Delta}_V^c)$

In order to provide a feedback for the error eigenvector matrix $\mathcal{E}_1$ associated with rank one perturbation of eigenspace, the error perturbation matrix $\mathbf{\Delta}_V^c$ can be obtained by performing the operation as mentioned above. Once $\mathcal{E}_1$ is evaluated, it used as a feedback to $\mathbf{P}$ for the evaluation of error-corrected eigenvector in real-time. The recursive feedback of the error terms results in a quick converging eigenspace which will demonstrated later. A brief representation of the proposed error-adapted FOEP framework is presented by a flowchart in Fig.(3.1). Here, the multivariate data is collected from sensors and taking first few samples, initial eigenspace corresponding to batch covariance matrix $\mathbf{\Lambda}_0$ and $\mathbf{V}_0$ is constructed. The batch covariance matrix is then updated in two different ways for the estimation of error-corrected eigenspace: one for the estimation of α_k and another for the estimation of error-adapted eigenspace $\mathbf{\Lambda}_k$ and $\mathbf{V}_k$. The covariance update using GEVD provides total perturbation $\mathbf{P}_k$ and perturbation matrices $\mathbf{\Delta}_V$ and $\mathbf{\Delta}_\Lambda$. The alternative approach of covariance update using standard EVD provides the transformed response α_k. These two approaches are utilised together for the estimation of error matrix $\mathcal{E}_1$ and the estimated error is used as an error feedback to the eigenspace obtained using GEVP for the

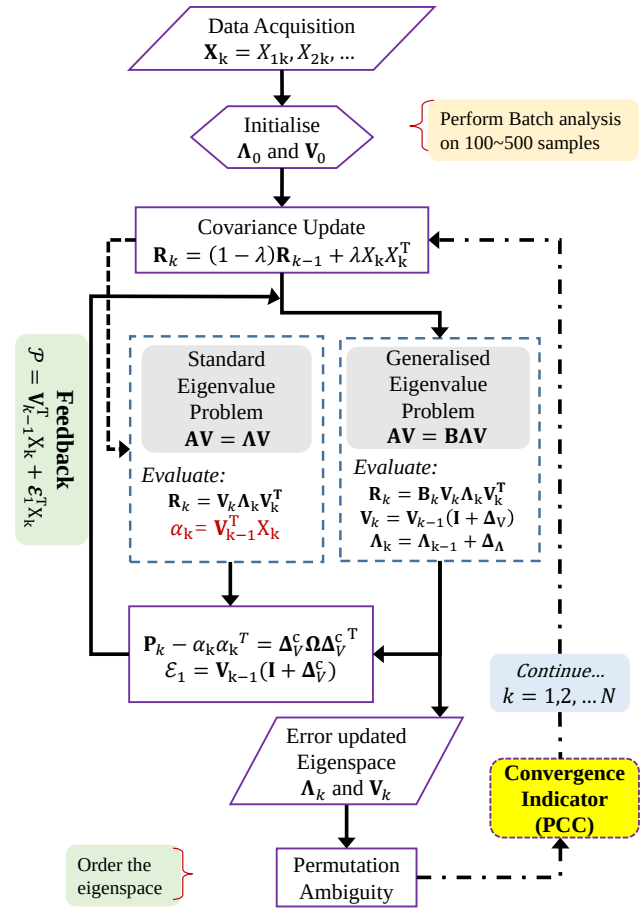

FIGURE 3.1: Flow chart of the error-adapted FOEP framework

estimation of error-adapted eigenspace $\mathbf{\Lambda}_k$ and $\mathbf{V}_k$ in real-time. The entire process is repeated at each time instant and to assess the convergence of algorithm, a *convergence* indicator is proposed.

3.3.2 Error-adapted framework for single channel data

Identification of modal properties from limited number of sensor information has been of keen interest among the research community [57]. Of the available techniques the proposed framework utilizes a decentralized approach in order to obtain the modes of a dynamic system. The algorithm uses data from a single channel and decomposes it into d number of components with a length of $D = N - d + i;\ i = 1, 2, \ldots d$ and estimates the initial Hankel matrix [34], where d is the embedding dimension. The initial Hankel covariance matrix is updated in real time through the proposed error adapted framework to obtain the transformed responses corresponding to each embedding dimension by projecting them to an uncorrelated subspace. Considering a set of random data taken from a sensor

to be $\tilde{X}^j = [x_1^j, x_2^j, \ldots, x_N^j]$, the Hankel matrix [34] and its covariance update can be obtained as:

Hankel matrix:

$$\mathbf{H}_X^j = \begin{bmatrix} x_1^j & x_2^j & x_3^j & \ldots & x_{N-d+1}^j \\ x_2^j & x_3^j & x_4^j & \ldots & x_{N-d+2}^j \\ \vdots & \vdots & \vdots & \ddots & \vdots \\ x_d^j & x_{d+1}^j & x_{d+2}^j & \ldots & x_N^j \end{bmatrix} \tag{3.26}$$

Covariance update of Hankel matrix:

$$\begin{aligned} \mathbf{R}_{HH}(k) &= \mathbf{R}_{HH}(k-1) + \lambda \left(\tilde{X}_k \tilde{X}_k^T - \lambda \mathbf{R}_{HH}(k-1) \right) \\ \mathbf{B}_{HH}(k) &= \mathbf{B}_{HH}(k-1) + \lambda \left(\tilde{U}_k \tilde{U}_k^T - \lambda \mathbf{B}_{HH}(k-1) \right) \end{aligned}$$

where, $\mathbf{R}_{HH}$ and $\mathbf{B}_{HH}$ are the total and within-set Hankel co-variance matrices as in Eq.(3.3). Then the EVD of Hankel covariance matrix follows $\mathbf{R}_{HH}(k) = \mathbf{B}_{HH}(k)\mathbf{W}_k\mathbf{\Sigma}_k\mathbf{W}_k^T$. The recursive update of the eigenspace then can be evaluated by following similar approach as in Eq.(3.19) and the estimate of error $\mathcal{E}_k$ can be obtained with the help of $\mathbf{P}$, which is the total perturbation using GEVP and the transformed responses (ψ_k) as mentioned in Eq.(3.27). With the recursive feedback of estimated error in the proposed framework, the error-corrected eigenvector matrix, thereby the transformed responses ($\mathcal{P}_k$) corresponding to each embedding dimension can be obtained [34]. The PCs with higher modal participation are retained and then projected back to the original subspace, which provides modal responses corresponding to modes with higher participation. This further facilitates the removal of sensor noise and unwanted signal components. Now taking the assumption that, out of d-PCs, m trajectories are retained and the response $\mathcal{R}^{ji}(k); i \in 1, 2, \ldots m$ corresponding to i^{th} embedding dimension can be constructed by projecting the retained PCs back into its original subspace. The proposed framework for the single channel data of i^{th} component can be represented through following set of equations:

$$\left.\begin{aligned}
&\mathbf{\Delta}_W^{\mathbf{c}}\mathbf{\Sigma}_k{\mathbf{\Delta}_W^{\mathbf{c}}}^T = \mathbf{P}_k - \psi_k[\psi_k^i]^T \\
&\mathcal{E}_k^{ji} = \mathbf{W}_{k-1}^{ji}(\mathbf{I} + \mathbf{\Delta}_W^{\mathbf{c}}) \\
&\mathcal{P}_k[\mathcal{P}_k]^T = \psi_k[\psi_k]^T + \psi_k[\Upsilon_k]^T + \Upsilon_k[\psi_k]^T + \Upsilon_k[\Upsilon_k]^T \\
&\mathcal{R}_k^j = \mathbf{W}_k^{ji}\mathcal{P}_k \quad \forall\, i \in 1, 2, \ldots, m
\end{aligned}\right\} \tag{3.27}$$

where,

$$\begin{aligned}
\psi_k^j \quad &= \mathbf{W}_k^{ji}\tilde{X}^{ji}; \quad \forall\, i \in 1, 2, \ldots, d \\
\mathbf{P} \quad &= \lambda\left(\mathbf{W}_{k-1}^T\mathbf{B}_k^{-1}\tilde{X}_k X_k^T\mathbf{W}_{k-1} - \mathbf{W}_{k-1}^T\mathbf{B}_k^{-1}\tilde{\mathbf{U}}_k\tilde{\mathbf{U}}_k^T\mathbf{W}_{k-1}\mathbf{\Sigma}_{k-1}\right) \\
&\quad \lambda\left(\mathcal{E}_{k-1}^T\mathbf{B}_k^{-1}\tilde{X}_k X_k^T\mathbf{W}_{k-1} - \mathcal{E}_{k-1}^T\mathbf{B}_k^{-1}\tilde{\mathbf{U}}_k\tilde{\mathbf{U}}_k^T\mathbf{W}_{k-1}\mathbf{\Sigma}_{k-1}\right) \\
&\quad \lambda\left(\mathbf{W}_{k-1}^T\mathbf{B}_k^{-1}\tilde{X}_k X_k^T\mathcal{E}_{k-1} - \mathbf{W}_{k-1}^T\mathbf{B}_k^{-1}\tilde{\mathbf{U}}_k\tilde{\mathbf{U}}_k^T\mathcal{E}_{k-1}\mathbf{\Sigma}_{k-1}\right)
\end{aligned}$$

Algorithm 1 Algorithm for Finding Lag Parameter and Embedding Dimension

Input: Time series data x, maximum embedding dimension m_{max}
  Compute autocorrelation function of x
  Initialize lag parameter τ to 1
  while Autocorrelation function not stabilized **do**
    Increment τ by 1
    Compute autocorrelation function with lag τ
  Choose τ when autocorrelation function stabilizes
  Initialize arrays E and Ey for storing ratios
  for $m = 1$ to m_{max} **do** ▷ Iteration for embedding dimension
    Reconstruct phase space using m and τ
    for each embedded vector **do**
      Compute distances to nearest neighbors
      Find nearest neighbor
  Compute ratios $E1$ and $E2$
Output: Embedding dimension ratios $E1$ and $E2$

Although, this framework provides the modal responses in real time, nevertheless, the embedding dimension and lag parameters are to be chosen carefully and fixed, as this part of the algorithm is parameter driven. In our implementation, we adopt a method proposed by Cao (1997) [62] to determine the embedding dimension. This method involves iteratively testing different embedding dimensions and analyzing certain ratios derived from the data. The specific steps are outlined in the function, where we calculate these ratios (E1 and E2) and plot them against different embedding dimensions. This process helps identify a suitable embedding dimension. Additionally, for fixing the lag parameter (τ), we utilize the autocorrelation function of the time series. The lag parameter τ is selected when the autocorrelation function stabilizes, indicating a point where the time series exhibits significant temporal dependencies.

An algorithm showing the steps for the calculation of lag parameter τ and minimum embedding dimension d is provided in Algrithm 1. This framework provides corrected eigenspace which yields the modal responses in real time. As these responses are mono-component in nature, this will facilitate the accurate identification of the vibrating modes of the dynamical system. For this the system response $\mathbf{X}$ of j^{th} DOF can be written in the form of modal coordinate matrix $\mathbf{q}$ as:

$$X_k^j = \sum_{i=1}^{m} \bar{\phi}_k^{ji} \mathbf{q}_k^i \quad \forall\, i \in 1, 2, \ldots, m \tag{3.28}$$

Here, For the proposed framework, system response can be expressed as:

$$X_k^j = \sum_{i=1}^{m} \mathcal{R}_k^{ji} \quad \forall\, i \in 1, 2, \ldots, m \tag{3.29}$$

where, m is the number of modes considered. From Eq.(3.28) and Eq.(3.28) modal response for i^{th} mode and j^{th} DOF can be obtained as:

$$\mathcal{R}_k^{ji} = \bar{\phi}_k^{ji} \mathcal{P}_k^i \tag{3.30}$$

From Eq.(3.30), the normalized vibrating mode of j^{th} DOF with respect to first DOF can be obtained as:

$$\frac{\bar{\phi}_k^{ji}}{\bar{\phi}_k^{1i}} = \mathbf{\Phi}_{ji}(k) \tag{3.31}$$

However, in practice, as the proposed algorithm is implemented in real time and modal responses obtained from it are mono-component, the sparsity in time domain allows to express the normalized vibrating modes as ratio of energy of each DOFs with respect to first DOF at each sample instant as followed:

$$\mathbf{\Phi}_{ji}(k) = A_{ji} \frac{(\sigma_{\mathcal{R}})_{ji}^2}{(\sigma_{\mathcal{R}})_{1i}^2} \tag{3.32}$$

where, The energy of the component can be estimated by taking variance on the principal axis and estimate of the variance ($\sigma_{\mathcal{R}}^2$) in real-time is performed using the relation:

$$\sigma_k^2 = (1 - \lambda)\sigma_{k-1}^2 + \lambda(X_k - \mu_k)^2 \tag{3.33}$$

And, A_{ji} is the sign of correlation coefficient $sign(\rho_{1i,ji})$ of each DOFs with respect to first DOF, and, i and j are indexed for mode and DOF respectively. The variable A_{ji} is particularly necessary for the higher modes to identify zero crossing. It can be accomplished through a correlation analysis on first few batch samples and identifying the position of the axes of correlation coefficient for each DOFs with

respect to first DOF, based on the sign of the correlation coefficient.

3.3.3 Perturbation convergence criterion (PCC)

The above section provides the recursive update of covariance matrix in an error adapted perturbation framework. In practical implementation of the proposed approach for continuous monitoring of a system it is required to define a convergence criterion in order to identify the stability of the algorithm. The use of modal assurance criterion (MAC) for understanding the correlation between the theoretical and proper orthogonal modes has been of keen interest in the area modal parameter estimation [33]. However, in practical and experimental applications the modes are not known in advance, but the identification of the modal parameters is actually the objective of test. Since the estimation of MAC values requires prior knowledge of actual modes and finding that may not be possible in real-life scenario, towards which this section provides an efficient and robust criterion to identify the convergence of the algorithm.

Here, a perturbation convergence criterion (PCC) at each time instant is presented in Eq.(3.34), which premises on the diagonally dominance of $(\Lambda + P)$ matrix. As mentioned in above section, rank one update of Λ is assumed to be diagonally dominant for the successful application of Gershgorin theorem and subsequent identification of modes. The proposed algorithm utilizes error feedback ($\mathcal{E}_1$) to achieve a nearly diagonal $(\Lambda + P)$ matrix in few samples, which is corroborated by the results presented in the following section.

$$PCC(k) = \left(\frac{\sum_{i=1}^{n} \sum_{j=1}^{n} (\Lambda + P)^2_{i,j \neq i}}{\sum_{i=1}^{n} (\Lambda + P)^2_{i,i}} \right)^{1/2} \tag{3.34}$$

where, n is the number of DOF. In Eq.(3.34), the numerator provides norm of off-diagonal terms of $(\Lambda + P)$ matrix and the double summation arises due to addition of the elements in both dimension of matrix. whereas, the denominator estimates the trace of $(\Lambda+P)$ matrix. Physically, as samples increases the value of PCC will asymptotically converge to a near-zero value, which provides a convergence criterion of the proposed algorithm.

3.3.4 Computational complexity

This section provides the computational complexity of the proposed real-time error-adapted FOEP framework with respect to other batch algorithm viz. principal component analysis (PCA), canonical correlation analysis (CCA) and second order blind identification (SOBI). For this consider a system having 'd' degree of freedom with response data of length 'N'. For PCA and CCA algorithm, cost of covariance estimate of (d x N) matrix is $\mathcal{O}(dN\ min(d,N))$ operations and that of EVD of (d x d) matrix is $\mathcal{O}(min(d,N)^3)$, resulting in total computational complexity of $\mathcal{O}(d^2N + d^3)$. And as for the dynamical system $N > d$, the computational complexity for the PCA and CCA will be $\mathcal{O}(d^2N)$. In SOBI, for the estimation of unitary matrix, (d x N) data vector is broken down to L numbers (L is the lag parameter) of (d x d) matrices for more accurate estimation of eigenspace. Here, estimation of time delayed covariance matrix and approximate joint diagonalization method have dominating computational cost of $\mathcal{O}(dNL\ min(d,N))$ and $\mathcal{O}(d^3\ max(d,L))$, respectively, resulting in total computational complexity of $\mathcal{O}(dNL\ min(d,N) + d^3\ max(d,L))$. For $N > d$ and $N > L$, the computational complexity will be $\mathcal{O}(d^2NL)$. A recent FOEP based algorithm RPCA requires $\mathcal{O}(d^2)$ operations per iteration for the estimation of perturbation matrices and as the update of eigenspace requires multiplication of two (d x d) matrices, it requires $\mathcal{O}(d^3)$ operations per iteration. The resulting computational complexity of RPCA is found out to be $\mathcal{O}(d^3N)$. RCCA is another recent FOEP based algorithm which requires $\mathcal{O}(d^3N)$ operations. Proposed error-adapted real-time FOEP framework requires $\mathcal{O}(d^3)$ operations per iteration for formation of total perturbation matrix in Eq.(3.15), matrix inversion lemma in Eq.(3.16), solution of Sylvester equation by Bartel-Stewarts algorithm in Eq.(3.18) and error calculation by Riccati equation in Eq.(3.25). Therefore total computational cost for the proposed algorithm is $\mathcal{O}(d^3N)$. The computational complexity for each of the aforementioned algorithm is shown in Table 3 for $N > d$. If an attempt is made to implement SOBI in recursive framework consistent with FOEP, the dominant computational cost of $\mathcal{O}(d^3L)$ per iteration is consumed by joint diagonalization, as the covariance matrix is updated at each instant of time. Therefore total computational complexity of recursive SOBI is found to be $\mathcal{O}(d^3LN)$.

TABLE 3.1: computational complexity

Algorithm	Computational complexity
Batch PCA	O(d^2N)
Batch CCA	O(d^2N)
SOBI	O(d^2LN)
RPCA	O(d^3N)
RCCA	O(d^3N)
Proposed	O(d^3N)

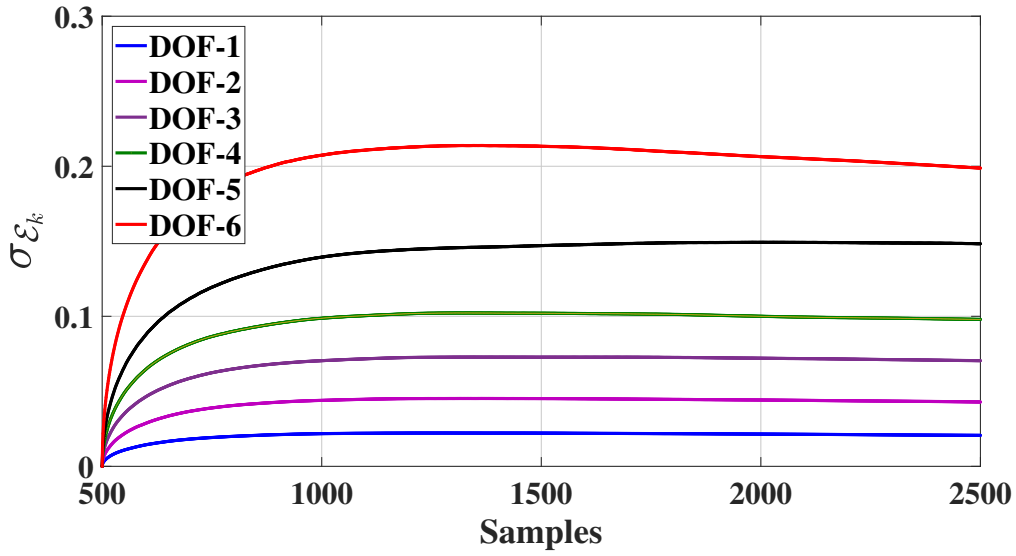

FIGURE 3.2: Standard deviation of the error feedback ($\mathcal{E}_1$) for linear 6-DOF system

3.4 Numerical demonstrations

This section considers a numerically simulated 6-DOF linear system for the demonstration of efficacy of the proposed algorithm for real-time modal identification with quick convergence. Here, two cases are undertaken which are as follows: (i) Full mode shape identification of the structure with sensors at every storey and (ii) partial mode shape identification of the structure with sensors at first, third and fifth storey.

3.4.1 Description of 6-DOF linear system

A 6-DOF system is modelled as mass, daspot and linear spring idealized as a linear vibrating structure. The equation of motion of the 6-DOF linear system is expressed using Eq.(3.9). The state-space representation for the system subjected to a zero mean white gaussian noise force vector $F(t)$ can be written

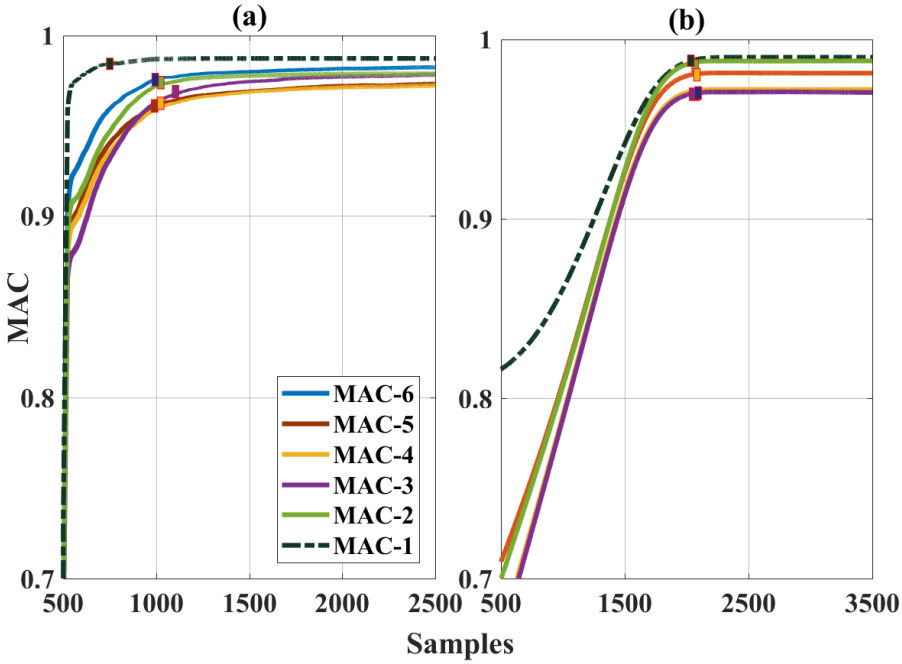

FIGURE 3.3: MAC for linear 6-DOF system (a) with adapting error, (b) without adapting error

as,

$$\begin{aligned} \dot{X}(t) &= \mathbf{E}_1 X(t) + \mathbf{E}_2 F(t) \\ Y(t) &= \mathbf{E}_3 X(t) \end{aligned} \tag{3.35}$$

where, $X(t)$ is the vector of states, and $Y(t)$ represents system response vector. The system matrices $\mathbf{E}_1$, excitation matrix $\mathbf{E}_2$ and observation matrix $\mathbf{E}_3$ under consideration are given by,

$$\begin{aligned} \mathbf{E}_1 &= \begin{bmatrix} [\mathbf{0}]_{6\times6} & [\mathbf{I}]_{6\times6} \\ -\mathbf{M}^{-1}\mathbf{K} & -\mathbf{M}^{-1}\mathbf{C} \end{bmatrix}; \quad \mathbf{E}_2 = \begin{bmatrix} [\mathbf{0}]_{6\times6} & \mathbf{M}^{-1} \end{bmatrix}^T; \\ \mathbf{E}_3 &= \begin{bmatrix} [\mathbf{I}]_{6\times6} & [\mathbf{0}]_{6\times6} \\ -\mathbf{M}^{-1}\mathbf{K} & -\mathbf{M}^{-1}\mathbf{C} \end{bmatrix} \end{aligned} \tag{3.36}$$

The mass of the system is considered as $10kg$ at each floor level and the stiffness of the individual floors are assumed to be $15kN/m$ and natural frequencies obtained are 1.48 Hz, 4.37 Hz, 7 Hz, 9.23 Hz, 10.91 Hz and 11.97 Hz. The damping ratio for the system is kept at $\zeta = 2.0\%$ critical for each mode. The excitation is simulated for a total duration of $50s$ at a sampling frequency of $100Hz$.

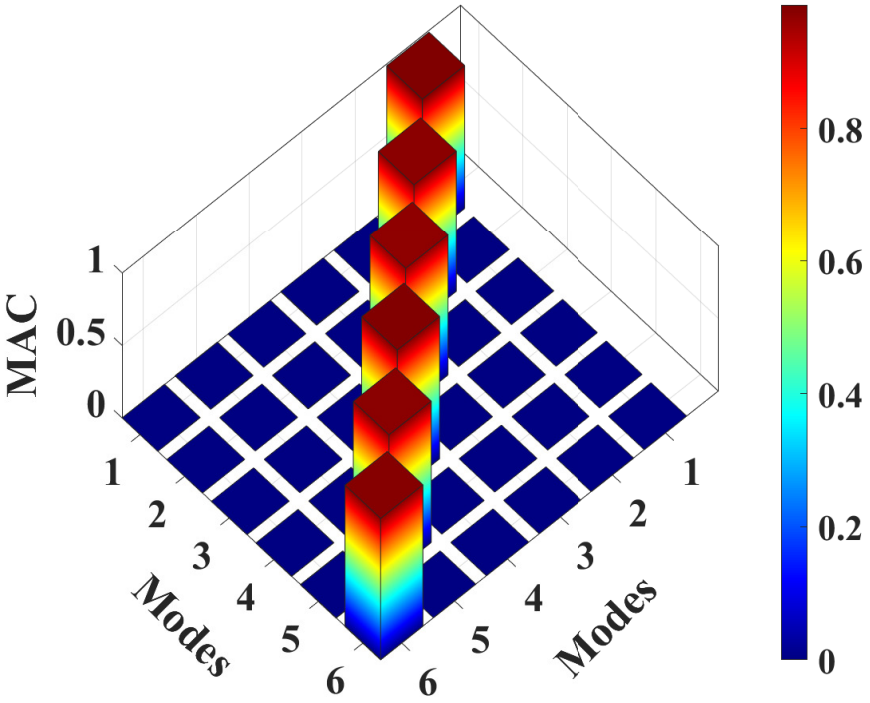

FIGURE 3.4: 3D representation of MAC for linear 6-DOF system

3.4.2 Results for full mode shape identification

For identification of full mode shape matrix of the undertaken structure with sensors at all the storey, the proposed algorithm takes data from all the channels and forms an initial covariance matrix with a few initial samples which contributes to the formation of initial eigenspace. This eigenspace is updated recursively with the proposed error-adapted algorithm, providing full mode shape matrix at each instant of time, at each data point in real-time. The statistics of the error feedback ($\mathcal{E}_1$) for different DOFs of the MDOF system are shown in Fig.3.2, where, $\sigma_{\mathcal{E}_k}$ is the variance of error feedback and can be estimated as $\sigma_{\mathcal{E}_k} = \sqrt{(1-\lambda)\sigma^2_{\mathcal{E}_k} + \lambda(\mathcal{E}_k - \mu_{\mathcal{E}_k})^2}$.

The error statistics of different DOFs provides an indication about the stabilization of the error adapted framework as the standard deviation of the error feedback ($\mathcal{E}_1$) reaches at a stationary value at approximately 1000 samples. Modal Assurance criterion (MAC) for all DOFs with and without adaption of error are represented in Fig.3.3(a) and Fig.3.3(b), respectively. In Fig.3.3(a) it can be observed that the MAC value for all DOFs achieves a value greater than 0.97 after around 1000 samples, however in Fig.3.3(b) the algorithm without error adaptation converges at around 1800 samples, which clearly

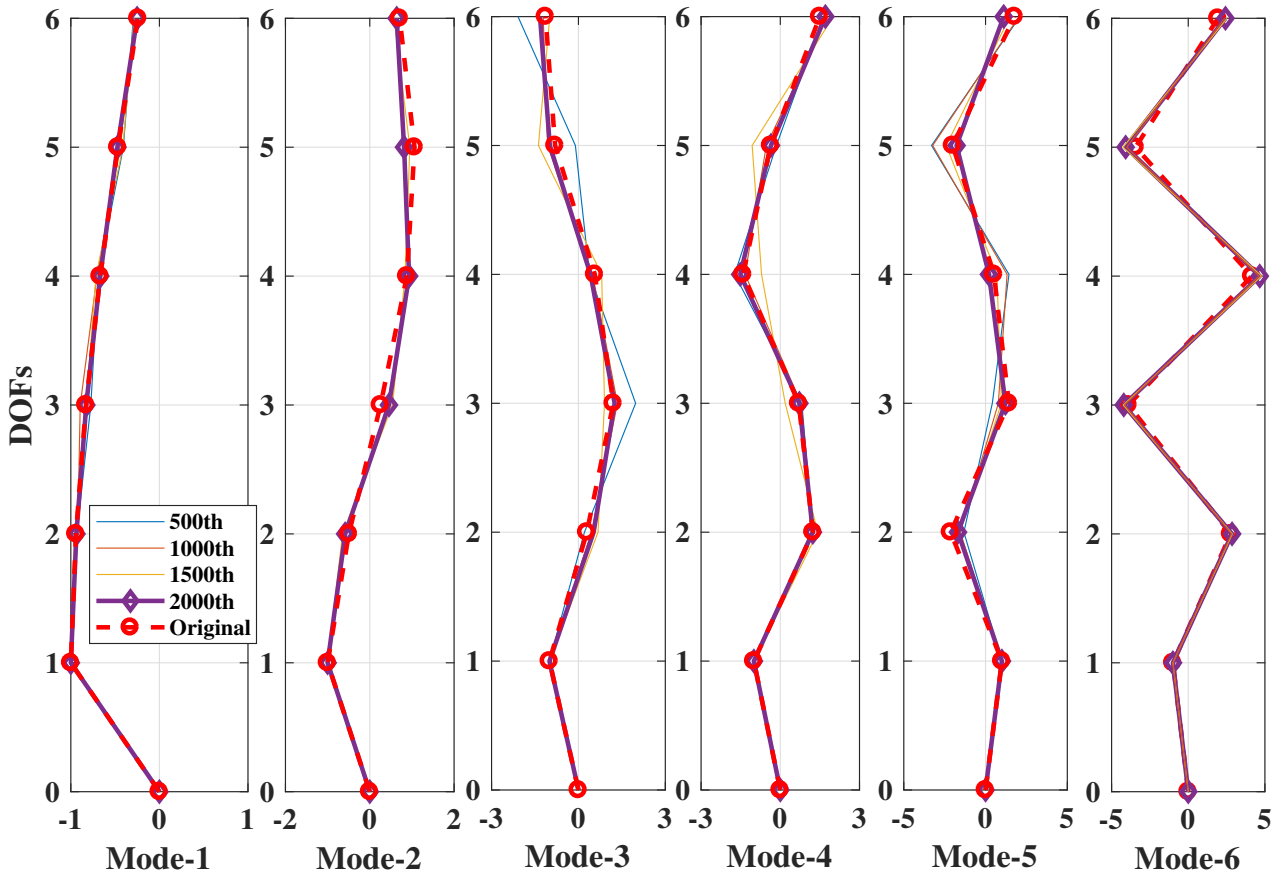

FIGURE 3.5: Full mode shapes identification for 6-DOF system

shows quick convergence of the error-adapted proposed algorithm.The approximate convergence location of the MAC value is pointed out by the pointers. A 3D plot with MAC values on z-axis is provided for the converged value in Fig. 3.4 Snapshots of full mode shape for the undertaken system is presented in the Fig.3.5, which shows the convergence of the real time mode shapes to the true mode-shapes within 1000 samples (or 10s based on sampling frequency).

However MAC may not be a suitable candidate for assessing the convergence of algorithm as this criteria requires prior knowledge the actual mode shapes of the system. This can be attributed to the fact that in real case scenario, actual mode shapes may not be available. A convergence criteria based on diagonalization of rank one update of $\mathbf{\Lambda}$ is proposed which can be applied in real-time without any prior knowledge of the system. Fig.3.6 shows asymptotic convergence of the algorithm as samples increases. It can be observed that the sample requirement of the proposed algorithm is approximately 1000, a fact corroborated by the convergence of both the MAC as well as PCC.

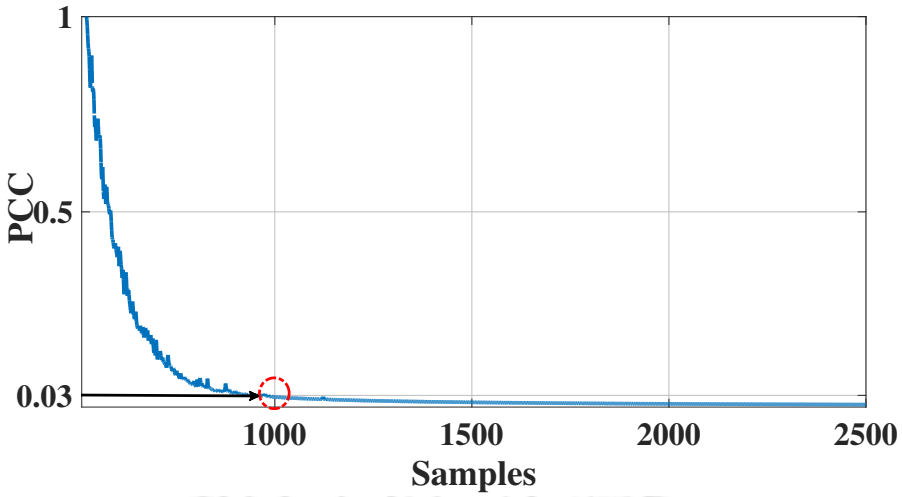

FIGURE 3.6: Evolution of PCC for the 6-DOF linear MDOF system

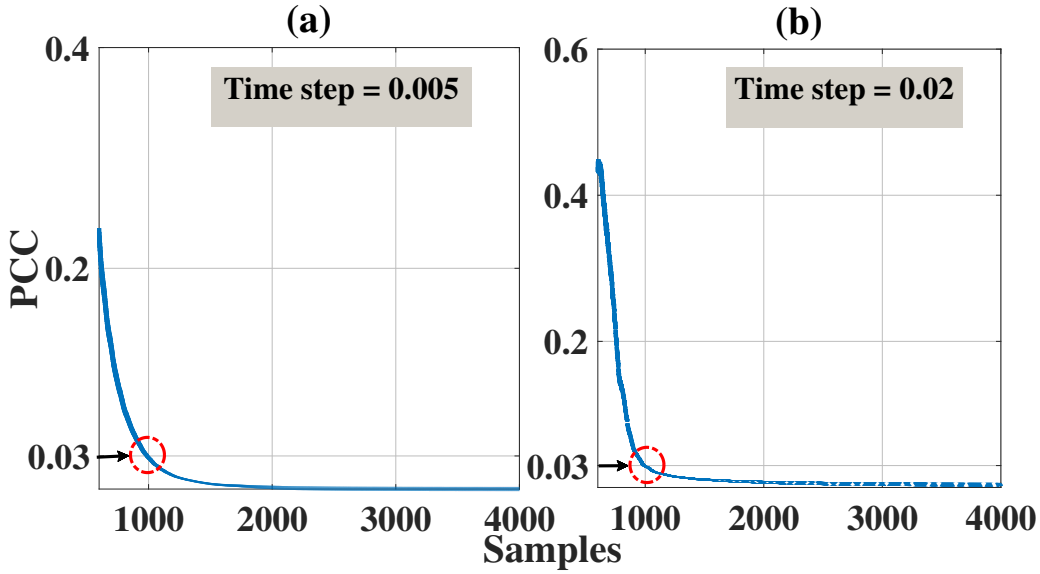

FIGURE 3.7: Evolution of PCC for the 6-DOF linear MDOF system with time step (a) 0.005sec (b) 0.02sec

To ascertain that the convergence is achieved, first a threshold needs to be defined. In order to determine the threshold value several numerical simulations for a wide range of sampling frequencies is carried out and a particular value of PCC is set at 0.03. Fig.3.7 presents the results for another two different sampling frequencies i.e. $50Hz$ and $200Hz$ or time step $0.02sec$ and $0.005sec$ respectively. It can be observed from the Fig.3.7 that for both the sampling frequencies the proposed algorithm converges at 1000 samples.

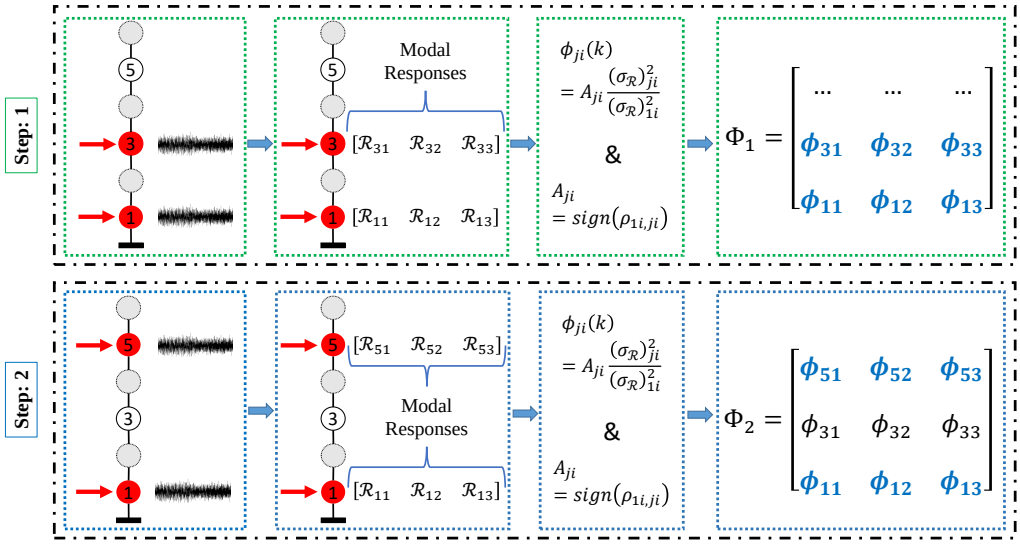

FIGURE 3.8: Methodology of decentralization for partial mode shapes identification of 6-DOF system

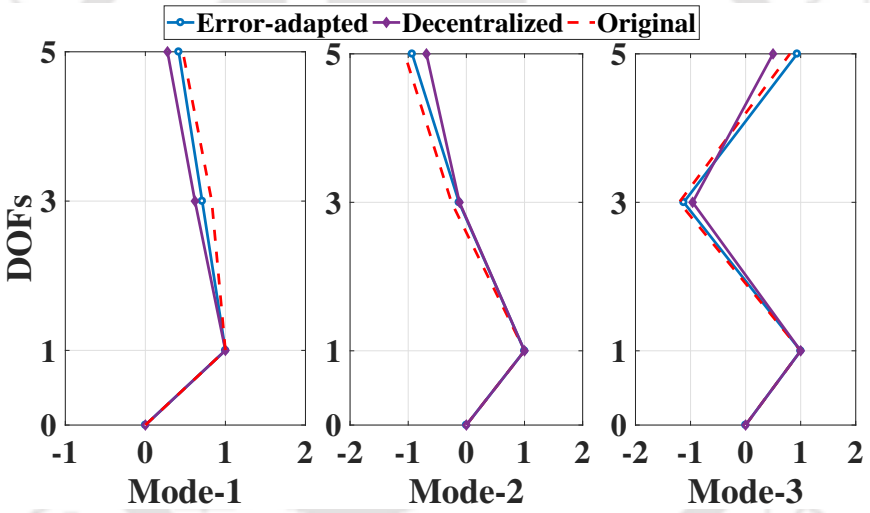

FIGURE 3.9: Partial mode shapes identification for 6-DOF system

3.4.3 Results for partial mode shape identification

For the partial mode shape recovery it is assumed that in the undertaken system only first, third and fifth responses are available. In this context two different approaches are considered. *First approach*: the response from sensors at DOF-1, DOF-3 and DOF-5 are recorded at each instant of time and mode-shape coordinates of those DOFs normalized with respect to DOF-1 are identified in real time through the update of data covariance matrix. *Second*, is the decentralized technique, where responses of three storey i.e DOF-1, DOF-3 and DOF-5 are obtained by taking two sensors at a time, with one sensor fixed at DOF-1 and another kept mobile or switched on/off between DOF-3 and DOF-5. The decentralised technique in this work is applied as follows:

1. At first data is recorded from DOF-1 and DOF-3 as shown in step-1 of Fig.3.8, and, these data are processed through the special case of proposed error-adapted algorithm by updating the hankel covariance matrix, as mentioned in Section 3.3.2. This provides the recursive modal response $\mathcal{R}_k$ for each of the undertaken DOFs.

2. As the model responses are mono-component in nature, modes corresponding to the undertaken DOFs can be obtained as per Eq.3.32, where ratio of energy $(\sigma_{\mathcal{R}})^2_{ji} \,/\, (\sigma_{\mathcal{R}})^2_{1i}$ provides the magnitude and correlation of modal responses $sign(\rho_{1i,ji})$ of batch samples (100-500 samples) between the corresponding DOF and the first DOF of the same mode. This provides the sign of the normalized mode-shapes ϕ_{ji}.

3. Thereafter the sensor on DOF-3 is switched off and moved to DOF-5 and data from DOF-1 and DOF-5 are recorded as presented in step-2 of Fig.3.8. These data are then processed through the aforementioned procedure to find normalized partial mode shape for DOF-5.

Figure 3.9 represents first three normalised modes of the undertaken 6-DOF structure. It is clearly observed from the figure that the partial mode shape identification using the first approach gives sufficiently accurate results with respect to the original mode shapes. As for the modal identification using the decentralized technique, it also provides a fare match of the modes to the original one. It is to be noted that, for the decentralization technique, the formation of the hankel matrix with suitable lag and embedding dimension is an important as well as a parameter dependent part. Proper formation of hankel matrix produces accurate modal response, in turn providing accurate mode shapes.

3.5 Case study for the IASC-ASCE benchmark structure

The efficacy of proposed algorithm for the problem of computationally efficient real-time modal identification is addressed in this section by undertaking the phase I (IASC-ASCE) SHM benchmark problem [34]. The structure is a four-story 2-bay by 2-bay steel frame modal with a height of $3.6m$ and bearing a base dimension of $2.5m \times 2.5m$ as presented in Fig. 3.10. The present case study considers the 12-DOF finite element model of the benchmark structure. Here, for modal identification undamaged and damaged (pattern (i) and (ii)) cases are considered. The parameter used for the benchmark structure to generate response are damping ratio-0.01 (default), sampling time step size-0.002s, total time duration-50s, noise level-10 (default) and force coefficient-150 (default).

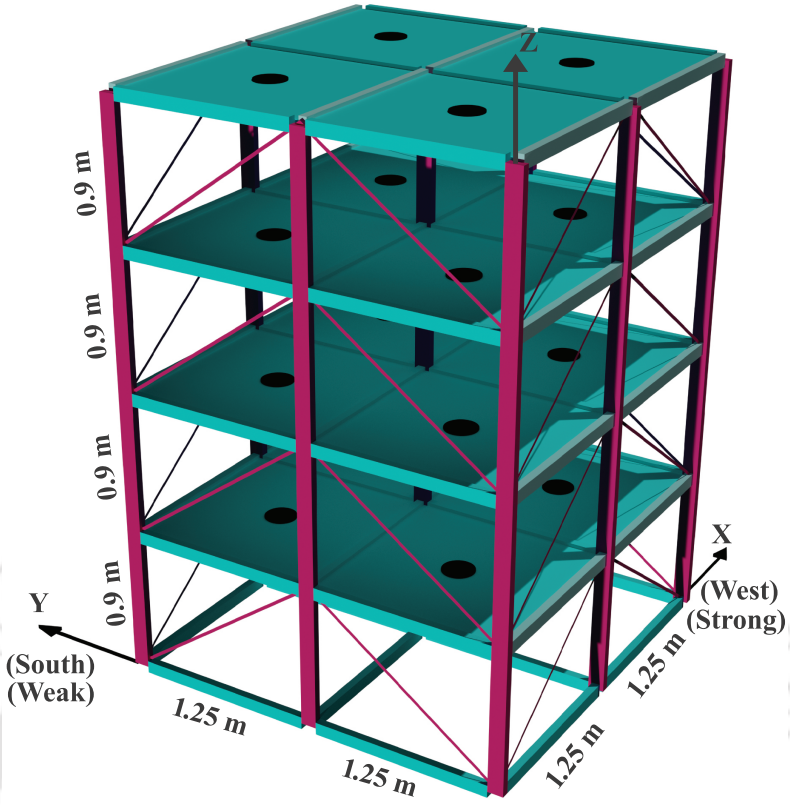

FIGURE 3.10: IASC-ASCE SHM benchmark model

3.5.1 Results for the benchmark problem

Here, effectiveness of the proposed algorithm is assessed with the use of MAC and PCC plots that are presented in Fig.3.11 and Fig.3.12, respectively. Fig.3.11(a) and Fig.3.11(b) presents the MAC values with and without the adaptation of error. Evident from Fig.3.11(a) for all DOFs MAC value at approximately 1000 samples is greater than or equal to 0.97 after the convergence is achieved. However, for the algorithm without adaptation of error term, in Fig.3.11(b) the convergence is achieved after around 10,000 samples. From the figures it can be well observed that sample requirement reduces drastically with error adaptation. Further it can be observed from Fig.3.12 that the algorithm requires around 1000 samples or 2 sec (500Hz sampling frequency) for it to converge to a nearly constant value. The quick convergence is one of the key features of the proposed algorithm which is of utmost importance from the point of practical consideration.

In order to further assess the robustness of the proposed algorithm, the numerical case study is extended for identifying damage pattern (i) and (ii), of the benchmark problem. Here, for the undamaged

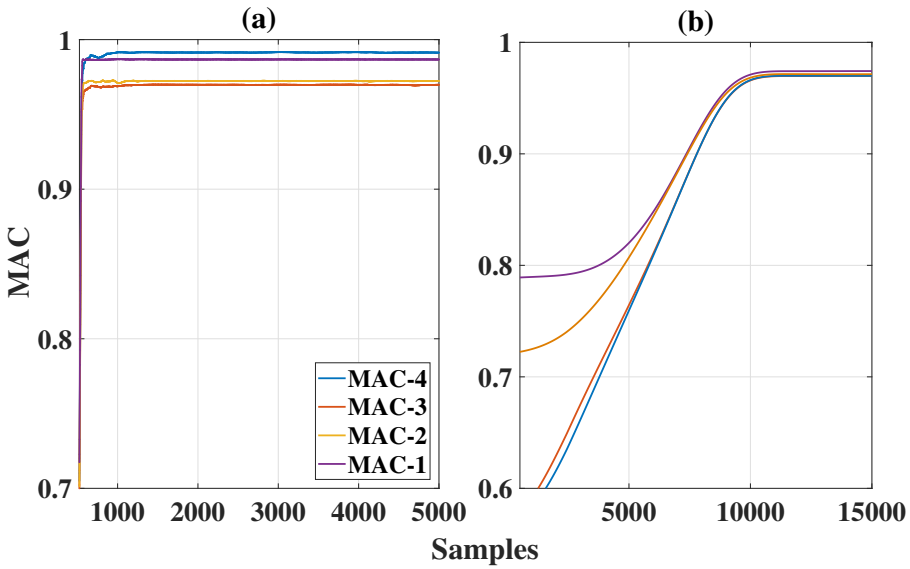

FIGURE 3.11: MAC for IASC-ASCE SHM benchmark structure (a) with adapting error, (b) without adapting error

structure, MAC is utilized to assess the degree of consistency between original and identified modes of the undamaged structure. And for the damaged structure, modal comparison criterion (**MCC**), which is an indicator for degree of consistency between the original modes of the pristine structure and the identified modes of damaged structure. For undamaged structure, both MCC and MAC are same. The undamaged, damage pattern (i) and (ii) cases are concatenated and shown in Fig.3.13 for the presentation purpose only. In the figure, it is evident that for both the damaged cases, the MCC values are significantly different. If the location of damage is unknown, the proposed algorithm can also be utilised for the identification of approximate location of the damaged storeys much along the same lines as discussed in [34]. It shows that the proposed algorithm can also be employed for benchmark structures to identify damages.

3.6 Application: Real-time passive control using MTMD

The previous sections demonstrates the efficacy of the proposed error adapted algorithm for real-time identification of modes with a quicker convergence. In this section the ability of the proposed algorithm is extended for real-time passive control through real-time tuning of Multi-tuned Mass Damper (MTMD)[38, 34]. For an MTMD to work efficiently in real-time, effective tuning for the desired modes is required which can be achieved through accurate real-time modal identification. Extensive studies involving tuned mass dampers (TMD) are presented in several literature for passive vibration control.

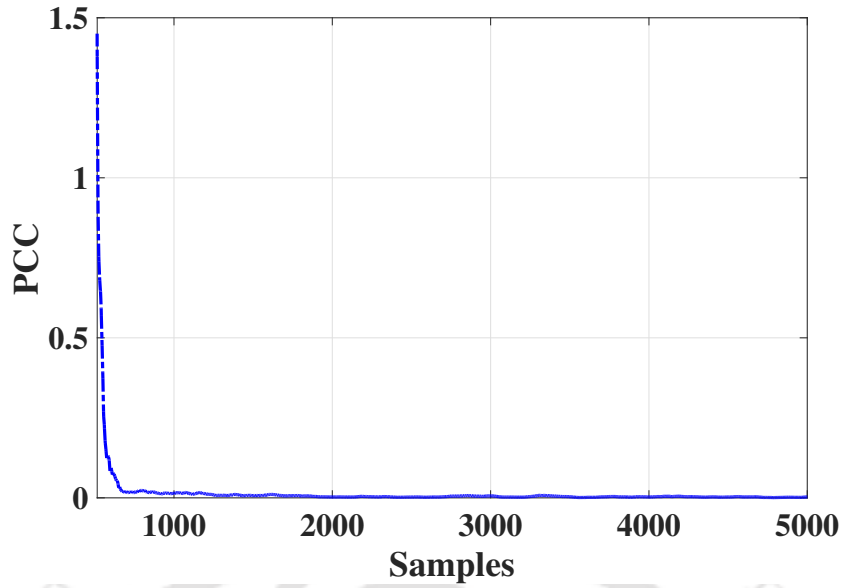

FIGURE 3.12: Evolution of PCC for IASC-ASCE SHM benchmark structure

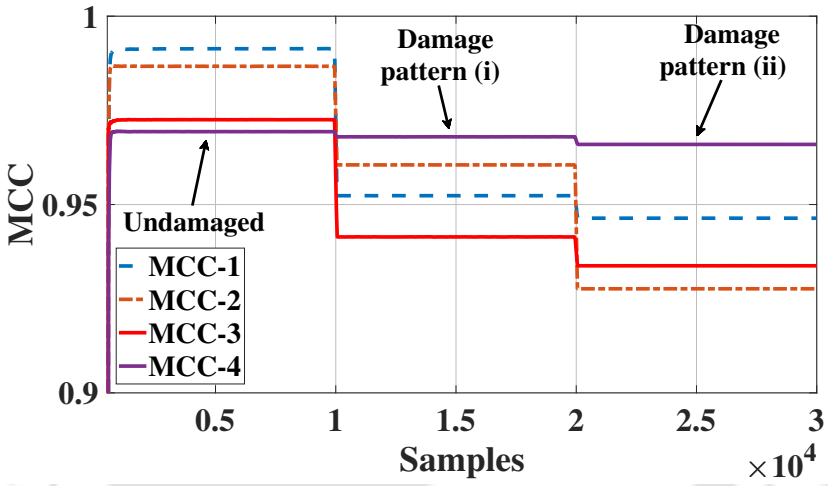

FIGURE 3.13: Concatenated MCC plot for undamaged and damaged IASC-ASCE structure

However, most of the approaches for tuning of TMD are offline in nature and the structure may require repetitive tuning due to the problem of de-tuning in structure. This limitation of non-adaptive approaches can be overcome by real-time identification of the vibrating modes for a dynamically vibrating system through adaptive tuning [56].

3.6.1 Description of the model

The undertaken system is a 3-DOF structural model idealized as spring mass and dashpot system that is adopted from the literature [38]. Figure 3.14 shows the arrangement of MTMD for the undertaken 3-DOF system. First and second floors are equipped with TMD in each floor in order to provide control

over the first two modes.

The governing equations of the vibrating system are analogous to the Eq.(3.9) where the system properties can be referred from [38, 34]. To suppress the response of a structural system, TMD is attached to the primary structure according to its presumably dominant mode(s). In the undertaken system, mass participation factor for first and second modes are 84.15% and 10.72% respectively and are considered for the real-time control. The mass of TMD corresponding to the first and second floor are considered as 2% and 0.25% of the entire primary structure mass. The estimation of modal parameters in real-time requires evaluation of eigenspace from the primary structure, which can be facilitated through the real-time identification of modes using the proposed algorithm. Although this work presents real-time modal control with the use of MTMD, nevertheless, does not explore control through modal updating in real-time. Rather, this work presents an application of modal identification in real-time control for known system properties of the primary structure. The estimation of modal parameter of MTMD requires online mode shapes of the primary structure normalised to the first mode and are represented at k_{th} instant as $\phi_1(k), \phi_2(k)$ and $\phi_3(k)$. The damping ratio of TMD corresponding to first and second modal masses at k_{th} instant can be estimated as follows.

$$\eta_1(k) = \frac{0.02\sum_{i=1}^{3} M_i}{\phi_1(k)^T \mathbf{M} \phi_1(k)} \quad \& \quad \eta_2(k) = \frac{0.0025\sum_{i=1}^{3} M_i}{\phi_2(k)^T \mathbf{M} \phi_2(k)} \tag{3.37}$$

The optimum damper parameters $f_{opt}(k)$ and $\xi_{d,opt}(k)$ for the TMD at first and second modes at each instant k can be obtained from the following equations [38],

$$f_{opt}(k) = \frac{1}{1+\eta(k)} \quad \& \quad \xi_{d,opt}(k) = \sqrt{\frac{3\eta(k)}{8(1+\eta(k))}} \tag{3.38}$$

Once the parameters $f_{opt}(k)$ and $\xi_{d,opt}(k)$ are obtained, the optimum stiffness and damping parameters $k_{opt}(k)$ and $c_{opt}(k)$ of the MTMD in real-time can be evaluated using the following relationship:

$$\begin{aligned} k_{opt}(k) &= f_{opt}^2(k)\Lambda_1^2 m_{tmd} \\ c_{opt}(k) &= 2\xi_{d,opt}(k) f_{opt}(k)\Lambda_1 m_{tmd} \end{aligned} \tag{3.39}$$

The TMDs at first and second mode are augmented in the primary structure as DOF-1 and DOF-3. For the 5-DOF secondary structure the first, second and third modes are located as DOF-2, DOF-4 and DOF-5 for the same. The new system matrix for the 5-DOF secondary system is represented in

Eq.(3.40), where, **M,K** and **C** are the properties of primary structure.

$$\mathbf{M}_{s,i} = \begin{bmatrix} \mathbf{m}_{tmd1} & 0 & 0 & 0 & 0 \\ 0 & 0 & 0 & 0 & 0 \\ 0 & 0 & \mathbf{m}_{tmd2} & 0 & 0 \\ 0 & 0 & 0 & 0 & 0 \\ 0 & 0 & 0 & 0 & 0 \end{bmatrix} + \mathbf{M},$$

$$\mathbf{K}_{s,i} = \begin{bmatrix} \mathbf{k}_{opt1,i} & -\mathbf{k}_{opt1,i} & 0 & 0 & 0 \\ -\mathbf{k}_{opt1,i} & \mathbf{k}_{opt1,i} & 0 & 0 & 0 \\ 0 & 0 & \mathbf{k}_{opt2,i} & -\mathbf{k}_{opt2,i} & 0 \\ 0 & 0 & -\mathbf{k}_{opt2,i} & \mathbf{k}_{opt2,i} & 0 \\ 0 & 0 & 0 & 0 & 0 \end{bmatrix} + \mathbf{K} \tag{3.40}$$

$$\mathbf{C}_{s,i} = \begin{bmatrix} \mathbf{c}_{opt1,i} & -\mathbf{c}_{opt1,i} & 0 & 0 & 0 \\ -\mathbf{c}_{opt1,i} & \mathbf{c}_{opt1,i} & 0 & 0 & 0 \\ 0 & 0 & \mathbf{c}_{opt2,i} & -\mathbf{c}_{opt2,i} & 0 \\ 0 & 0 & -\mathbf{c}_{opt2,i} & \mathbf{c}_{opt2,i} & 0 \\ 0 & 0 & 0 & 0 & 0 \end{bmatrix} + \mathbf{C},$$

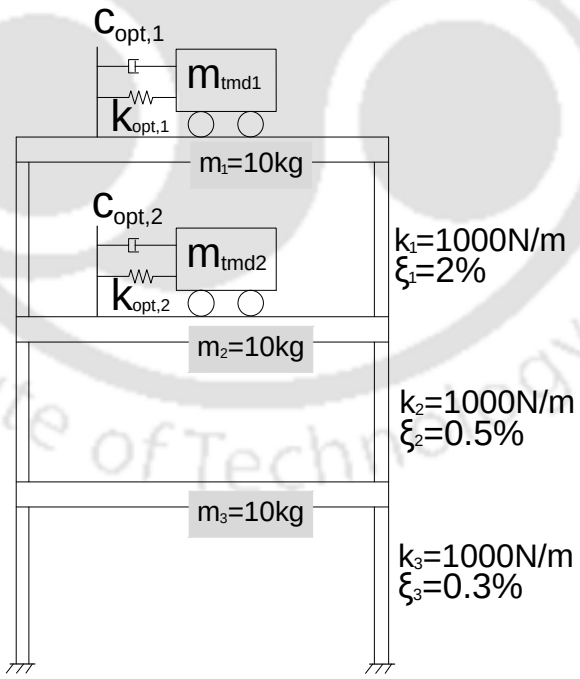

FIGURE 3.14: MTMD arrangement for 3-DOF structure

3.6.2 Real time modal control results and discussion

As discussed in the previous sections the proposed algorithm evaluates the eigen-decomposition of the recursive covariance matrix in real-time in order to facilitate the recursive eigenspace. In this regard,

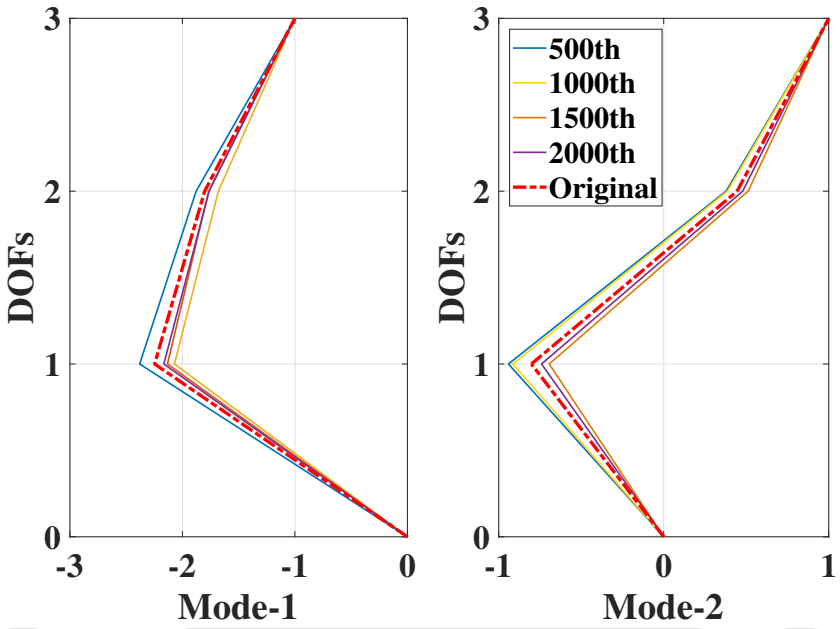

FIGURE 3.15: First and second modes of the primary 3-DOF structure

the error-adapted approach of the proposed FOEP framework provides an appropriate handle for accurate identification of the time varying behavior of the vibrating system. This in turn provides flexibility for easy modal control through the adaptive tuning of multiple modes in a MDOF system with the use of standard tuning devices. The 1^{st} and 2^{nd} vibrating modes of the undertaken structural system is presented in Fig.3.15, which depicts the ability of the proposed algorithm in accurate identification of the vibrating modes. The modes obtained in real-time are then utilized to find the optimum damping and stiffness parameters of MTMD which is essential for adaptive design of the MTMD system and facilitates subsequent real-time control of the undertaken system. For easy understanding of the reduction in modal responses, the FFTs of the tuned system corresponding to the recursive eigen modes are plotted in Fig.3.16. From the FFTs of the tuned structure at uncontrolled and controlled stages it is evident that the reduction of 1^{st} and 2^{nd} modal response is significantly large as the system is tuned with respect to 1^{st} and 2^{nd} modes.

In their service life, TMDs often suffer from de-tuning issues due to changes in the original system, for example damages incurred due to stiffness reduction. In such cases, re-tuning of the TMD module

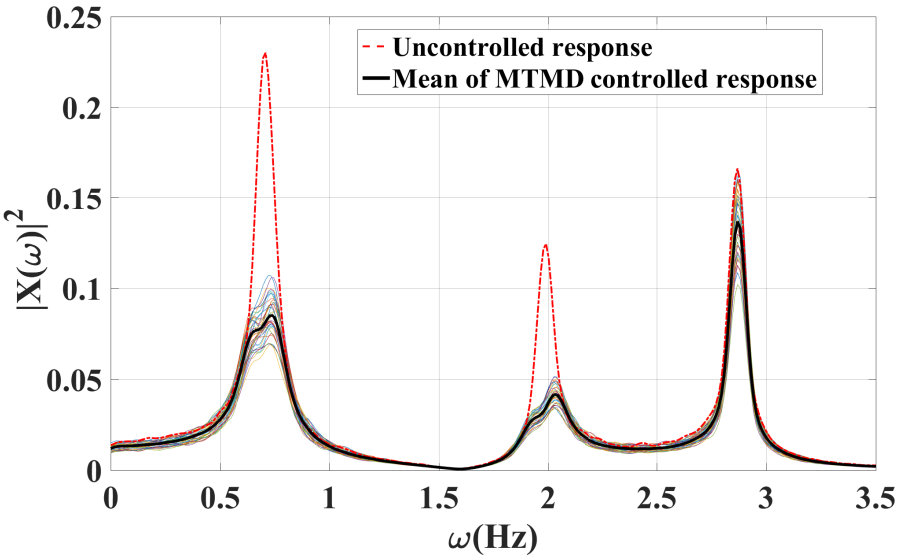

FIGURE 3.16: FFT of the uncontrolled and controlled response of 3-DOF structure

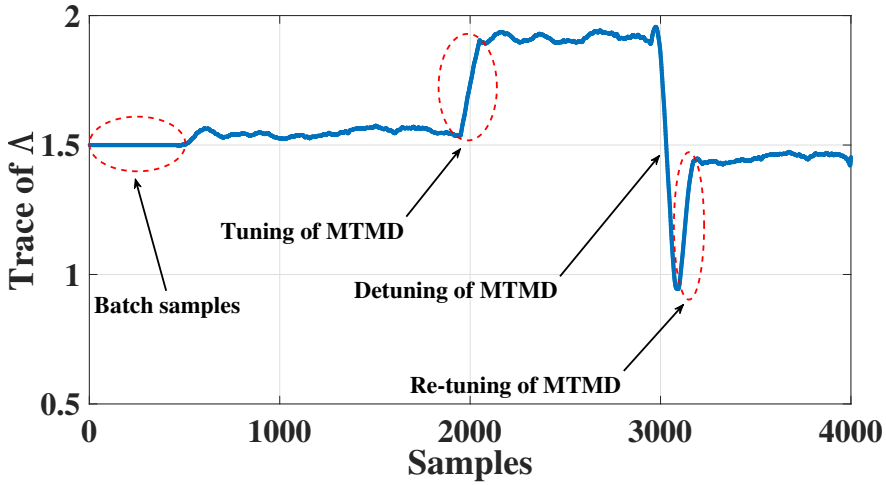

FIGURE 3.17: Trace of Eigenvalue showing Tuning and re-tuning of the MTMD

is essential to avoid amplification in the system vibration. The fidelity of the proposed algorithm in real-time passive control is examplified by considering a sudden damage of 25% exactly at 30 sec in the primary structure and then re-tuning the MTMD in real-time. It may be noted that the error-adapted formulation of eigenspace update at every sample instant is the key approach here, since if damage occurs in the system the eigenspace can identify the change in system property by comparing the information from previous instant and accordingly adjusting the instantaneous eigenspace retuning the MTMD. The aforementioned steps are demonstrated through the Fig.3.17, which shows the trace of the updated eigenvalue matrix of data covariance matrix ($\mathbf{R}_k$) in real-time. For the formation of initial eigenspace, first 500 samples are utilised, then a primary structure phase is considered from 500 to 2000 samples. Fig.3.17 shows a sharp elevation in the trace at 2000 samples, which indicates

the addition of MTMD to the primary structure and the tuning phase is achieved from 2000 to 3000 samples. The proposed algorithm is capable of tuning the MTMD from the instant the normal modes of primary structure converge. However in order to discern the transitions, here, the MTMD is introduced into the system at 2000 samples. Thereafter, a sudden damage in the form of loss of stiffness is applied on the first storey of the primary structure, which results in de-tuning of the MTMD. Then the MTMD is re-tuned automatically based on the real-time estimation of primary modes resulting in a re-tuning phase from 3000 samples onward. The estimated primary modes first update the η_1 and η_2 values, which in turn provides the updated optimal parameters (i.e. real-time re-tuning of the MTMD). Thus it suffices to state that the proposed algorithm is not only applicable for real-time passive control but also for real-time implementation of retuning in case the controller gets detuned.

3.7 Case study for non-linear system

In order to assess the expected performance of the proposed algorithm on non-linear systems, a 6-DOF non-linear system where the non-linearity is represented by a base isolated Bouc-Wen oscillator is undertaken in the present section. The equations governing the dynamics of the non-linear oscillator is adopted from literature [34], wherein the non-linearity is introduced by varying the parameter κ. The system behaviour can be assumed to be approximately linear for $\kappa = 0.995$. The variation of PCC values at 1000 samples with the change in non-linearity is presented in Table 3.2. It can be observed that the required number of samples for convergence (increase in PCC value) increases with increase in non-linearity of the system. It is to be noted that, for a linear system, PCC and MAC corroborate well with each other, however, for non-linear systems the converged PCC value doesn't imply that the identified modes converge to the true modes. Therefore, with the increase in non-linearity, inferring MAC from PCC and vice-versa, may lead to erroneous conclusions. The performance analysis of the proposed algorithm for non-linear system is not within the ambit of the present work, as the modal analysis of non-linear systems involve non-normal modes and this is kept as a scope for future study.

TABLE 3.2: PCC and average MAC in non-linear system for different level of non-linearity

Non-linearity	κ	PCC	Average MAC at sample			
		(1000 sample)	1000	2000	3000	4000
0.5 %	0.995	0.032	0.9673	0.9720	0.9722	0.9723
5 %	0.95	0.09	0.9544	0.9633	0.9648	0.9654
10 %	0.9	0.28	0.9062	0.9133	0.9204	0.9243

3.8 Research Findings

The outcomes of this chapter can be summarized as follows:

- Error Adaptive Formulation: This work introduces an error adaptive formulation for real-time modal identification using first-order eigen perturbation techniques (FOEP). This formulation significantly enhances convergence compared to other FOEP algorithms.
- Error Feedback Emphasis: The proposed framework focuses on estimating error feedback for first-order error terms rather than employing complex higher-order perturbation formulations.
- Improved Convergence: Numerical experiments and a standard benchmark problem demonstrate faster convergence of the algorithm, achieving convergence at approximately 1000 samples, regardless of the sampling frequency, showcasing its adaptability.
- Anomaly Detection: The algorithm is capable of detecting anomalies within structures, enhancing its utility beyond modal identification.
- Under-determined System Identification: The research showcases the applicability of the proposed feedback-based framework for identifying modal properties in under-determined systems, incorporating the Hankel covariance matrix-based formulation.
- Perturbation Convergence Criterion: The study presents a practical criterion for identifying correlations between recursive and theoretical eigen structures, contributing to the understanding of system dynamics.
- Vibration Control Application: A case study demonstrates the potential of the proposed approach for real-time tuning of modal frequencies in a 3-DOF structure, hinting at its promise in modal control applications.
- Future Work: While this research offers insights into real-time under-determined modal identification using a decentralized approach, it acknowledges the need for further comprehensive exploration in this area as future work.

This chapter initiates an exploration into real-time monitoring, primarily within the context of dynamical systems evolving in Euclidean space ($\mathbb{R}^n$) through the utilization of the FOEP-based framework. This investigation serves as a foundational step toward the more complex domain of health monitoring

for systems that operate on smooth differentiable manifolds. To facilitate effective health monitoring of such manifold-based systems, the establishment of a robust simulation strategy is essential. By rigorously addressing the forward problem within this framework, a foundation can be laid that offers insights and methodologies, enabling the subsequent development of efficient solutions techniques for the inverse problem. Therefore, the subsequent chapter provides the modeling and solution of Hamiltonian systems evolving on S^2.

Chapter 4

Geometric–stochastic numerical integration scheme on S^2

In the domain of stochastic differential equations (SDEs), where randomness governs physical systems, traditional solution methods are well-established for Euclidean spaces [20, 15]. However, when dealing with stochastic dynamical systems evolving on manifolds, preserving geometry becomes challenging [22], particularly for complex systems where the objects are subject to geometric constraints [2, 8, 2, 8, 9, 10]. Existing deterministic integration schemes for manifolds are inadequate for handling both stochasticity and geometry simultaneously. To address this, this chapter introduces a novel Ito-Taylor 1.5 strong integration scheme designed for mechanical systems on manifolds, ensuring geometric preservation at each time step while accounting for inherent uncertainties in the system, thus providing accurate and reliable results. The Lagrangian and Hamiltonian formulations offer a natural description of system dynamics, with recent developments extending these formulations to mechanical systems on various configuration manifolds based on Lie group theory [24, 44, 45].

Deterministic integration schemes for such systems have been proposed, they cannot straightforwardly accommodate the inherent randomness in system dynamics. Therefore, for systems with inherent randomness, there is a need for geometry-preserving stochastic Hamiltonian formulation and numerical integration schemes based on the Lie approach. Existing stochastic integration schemes, although suitable for Euclidean spaces, fail to maintain geometry when applied to configuration manifolds. To bridge this gap, the study formulates stochastic Hamiltonian differential equations (SHDEs) for manifold-evolving systems and introduces a higher-order Ito-Taylor-based geometric integration scheme that accurately preserves geometry while accounting for stochasticity, ensuring the faithful description of these dynamic systems.

In this work, physical systems which evolve on quadratic hypersurfaces formalized as S^2 (two-sphere) and $SO(3)$ (special orthogonal group in three dimensions) are considered. Such systems are modelled in the form of Hamiltonian SDEs in Stratonovich sense [7]. Using Wong-Zakai correction terms [28], the equivalent Ito diffusion equations on the manifold are formulated. Magnus expansion is employed for establishing the correspondence between the manifold and Lie algebra, providing a base for the formulation of geometric Taylor-1.5 framework using Ito's formula [29]. This formulation leads to new expressions for the Kolmogorov operators considering the geometric aspects of the manifold and its corresponding Lie algebra. Results demonstrate that the solution using the proposed integration scheme satisfies the geometric constraints on both manifold and tangent space. Further, the global errors between the proposed scheme and the existing geometric EM and Milstein schemes is significantly less for coarser time steps. The proposed formulation is applicable to any Hamiltonian systems evolving on complex manifolds.

The key contributions of the present work are as follows: *Firstly*, a stochastic Hamiltonian dynamics for the systems evolving on the manifold $(S^2)^n$ is developed. Although the development of deterministic Hamiltonian dynamics on different manifolds is well established, stochastic Hamiltonian formulation on the manifold $(S^2)^n$ has not been explored. *Secondly*, a mathematically elaborate framework for geometry preserving higher order Ito-Taylor expansion for non-linear systems evolving on configuration manifolds $SO(3)$ and $(S^2)^n$ is proposed. The formulation of a geometric Taylor 1.5 strong integration scheme for the solution of geometric SDEs on manifolds is not available in literature. *Thirdly*, the application of the proposed numerical integration scheme towards the solution of practical physical systems such as spherical pendulum on a cart and two quadrotors transporting a mass point on the configuration manifolds $S^2 \times \mathbb{R}^2$ and $\left(S^2\right)^2 \times (SO(3))^2 \times \mathbb{R}^3$, respectively is demonstrated.

4.1 Need for the dynamic analysis of stochastically excited systems evolving on Manifolds

1. **Complexity of Stochastically Excited Systems on manifolds:** Stochastic differential equations (SDEs) are essential for modeling physical systems with inherent randomness. These systems often exhibit complex behaviors that cannot be simplified into Euclidean-based models, especially when they evolve on manifolds. Examples include 3D pendulums with both spherical and

planar motions [1, 2], ball vibration absorber [8], quadrotors transporting a payload [9], a rotating spacecraft and control moment gyroscope [9], geometric analysis and design of mechanical control systems [10]. Systems evolving on manifolds require the preservation of their inherent geometry during dynamic analysis. Traditional deterministic integration schemes work well in Euclidean spaces but struggle to maintain both stochasticity and geometry on manifolds simultaneously. This challenge necessitates the development of specialized integration methods.

2. **Stochasticity and Geometry Preservation:** Previous research has successfully formulated deterministic Lagrangian and Hamiltonian formulations for mechanical systems on configuration manifolds using Lie group theory. While these approaches work for deterministic dynamics, they cannot be readily adapted to handle the uncertainty inherent in stochastic systems. To address the limitations of existing methods, there is a need for integration schemes that can handle both stochasticity and geometry preservation for systems evolving on manifolds. These schemes should accurately simulate the dynamics of such systems, ensuring reliable results.

3. **Proposed Ito-Taylor Integration Scheme:** Lower-order integration schemes for stochastic systems on Euclidean spaces require small time steps for accuracy. This necessitates the development of higher-order integration schemes to efficiently handle the complexity of stochastically excited systems. The work proposes a novel Ito-Taylor 1.5 strong integration scheme for mechanical systems on manifolds. This method preserves geometry at each time step while accounting for inherent uncertainties in the system, ensuring both accuracy and reliability in the dynamic analysis of stochastically excited systems.

4. **Development of Health Monitoring Techniques:** The study's focus on manifold theory and stochastic excitations leads to the development of health monitoring techniques tailored for systems operating within unique configuration spaces. This promises more accurate and efficient methods for monitoring system health. The work introduces a damage detection algorithm called recursive principal geodesic analysis (RPGA), designed for systems evolving on manifolds. This algorithm offers a novel approach to analyze the variability of geometric objects in manifold-based systems, akin to RPCA in Euclidean space.

The study focuses on physical systems that evolve on specific manifolds, including the two-sphere

(S^2) and the special orthogonal group in three dimensions ($SO(3)$). These manifolds represent complex configuration spaces that require specialized treatment. Wong-Zakai correction terms are used to formulate Ito diffusion equations on the manifold, bridging the gap between the manifold and its corresponding Lie algebra. This provides the foundation for the proposed geometric Taylor-1.5 framework. Results from the proposed integration scheme demonstrate that it successfully satisfies the geometric constraints on both the manifold and its tangent space. This validates its ability to preserve geometry during dynamic analysis. The research highlights the limitations of traditional Euclidean methods for monitoring systems' behaviors within specific configuration spaces. The example of a pendulum tuned mass damper (PTMD) design [1] showcases the shortcomings of Euclidean approaches and underscores the need for more accurate manifold-based methods. The research applies the RPGA algorithm to identify damage in a stochastically excited inverted spherical pendulum-cart system traversing on a rough surface, demonstrating its practical utility in real-world scenarios.

4.2 Proposed framework

This section presents the mathematical formulation of stochastic Hamiltonian dynamics defined on the configuration manifold S^2, which is two-sphere embedded in $\mathbb{R}^3$, as well as a geometric approach for developing an geometric Ito-Taylor 1.5 strong scheme for the solution of the stochastic Hamiltonian system of equations. The Hamiltonian dynamical systems may be stochastic due to unpredictable location and momentum at each step of their trajectory, which is considered when constructing the Hamiltonian dynamics. This development differs significantly from the most widely published literature's traditional technique [1], which uses trigonometric functions for S^2. The formulation steps for geometric integration scheme follows the same approach as literature [22]. However, to develop higher order integration schemes, one must resort to Taylor series expansion as found in [29]. New formulations of higher order schemes using integral form of Taylor series in the context of geometric SDEs is formulated below. While the procedural framework for the geometric integration scheme aligns with existing literature [22], the progression towards higher-order integration schemes necessitates the utilization of Taylor series expansion, as detailed in [29]. Novel formulations of higher-order schemes, employing the integral representation of Taylor series within the domain of geometric stochastic differential equations, are delineated subsequently

4.2.1 Stochastic Hamiltonian dynamics on $\left(\mathrm{S}^2\right)^n$

A stochastic Hamiltonian formulation [7, 63] in S^2 is developed by considering a non-conservative physical system with action integral $\mathbb{S}$ as a function of modified Lagrangian $\hat{\mathrm{L}}\left(q,\omega\right)$. Here, $q \in \mathrm{S}^2$ is the position, $\omega \in \mathrm{T}_q\mathrm{S}^2$ is the angular velocity of the system. For a dynamical system excited by a stochastic process $\dot{W}(t)$, with $W(t)$ being a Wiener process [29], the work done by $\dot{W}(t)$ is given as $\mathrm{h}_1 \circ \dot{W}(t)$, where, h_1 is a function of the system states and can be treated as the intensity of randomness associated with the system. The action integral for a stochastic Lagrangian system can be defined as [7, 63],

$$\mathbb{S} = \int_{t_0}^{t_f} \hat{\mathrm{L}}(q,\omega)dt - \int_{t_0}^{t_f} \mathrm{h}_1 \circ dW(t) \tag{4.1}$$

Eq. (4.1) can be revised as,

$$\mathbb{S} = \int_{t_0}^{t_f} \left(\pi \cdot \omega - \mathrm{H}(q,\pi)\right) dt - \int_{t_0}^{t_f} \mathrm{h}_1 \circ dW(t) \tag{4.2}$$

For any variable $q \in \mathrm{S}^2$ in the domain $[t_0, t_f]$, the variation can be defined as $q^\eta \in \mathrm{S}^2 \; \forall \; \eta \in (-c, c)$ for $c > 0$ such that at the initial and final points in time, the variation of q is zero. The variations of q and $\dot{q}$ are expressed as [9],

$$\delta q = \xi^\Lambda q, \quad \delta\dot{q}_i(t) = \dot{\xi}^\Lambda q + \xi^\Lambda \dot{q} \tag{4.3}$$

where, ξ is a differentiable curve $\xi : [t_0, t_f] \to \mathbb{R}^3$ with its initial and final value as zero, and, $(\cdot)^\Lambda$ is the wedge operator. Angular velocity ω can be expressed in terms of q and $\dot{q}$ as, $\omega = q^\Lambda \dot{q}$ and its variation is estimated as,

$$\delta\omega = \delta q^\Lambda \dot{q} + q^\Lambda \delta\dot{q} \tag{4.4}$$

Substituting Eq. (4.3) in Eq. (4.4) and utilizing the constraints on S^2 and $\mathrm{T}_q\mathrm{S}^2$ [5, 9], the final form of $\delta\omega$ is obtained as,

$$\delta\omega = \left(\xi^\Lambda \omega\right) + \left(\mathbb{I}_{3\times3} - qq^T\right)\dot{\xi} \tag{4.5}$$

where, $\left(\mathbb{I}_{3\times3} - qq^T\right)\dot{\xi}$ is the orthogonal projection of $\dot{\xi}$ along the vector q. The variation of the action integral (Eq. (4.2)) is given as,

$$\begin{aligned}\delta\mathbb{S} = &\int_{t_0}^{t_f}\left(\pi\cdot\delta\omega - \frac{\partial \mathrm{H}(q,\pi)}{\partial q}\cdot\delta q + \left(\omega - \frac{\partial \mathrm{H}(q,\pi)}{\partial \pi}\right)\cdot\delta\pi\right)dt \\ &- \int_{t_0}^{t_f}\left(\frac{\partial \mathrm{h}_1(q,\pi)}{\partial \pi}\delta\pi + \frac{\partial \mathrm{h}_1(q,\pi)}{\partial q}\delta q\right)\circ dW(t)\end{aligned} \tag{4.6}$$

Substituting Eqs. (4.3) and (4.5) into the infinitesimal variation of $\mathbb{S}$ and with some rearrangements the following are obtained,

$$\begin{aligned}\delta\mathbb{S} = &\int_{t_0}^{t_f}\left(\left(\omega - \frac{\partial \mathrm{H}(q,\pi)}{\partial \pi}\right)dt - \frac{\partial \mathrm{h}_1(q,\pi)}{\partial \pi}\circ dW(t)\right)\cdot\delta\pi \\ &+\left(\left(-\dot{\pi} + \omega^{\Lambda}\pi - q^{\Lambda}\frac{\partial \mathrm{H}(q,\pi)}{\partial q}\right)dt - q^{\Lambda}\frac{\partial \mathrm{h}_1(q,\pi)}{\partial q}\circ dW(t)\right)\cdot\xi\end{aligned} \tag{4.7}$$

Hamilton variational principle [7, 9, 64] states that: $\delta\mathbb{S} = 0$ for all possible functions $\xi : [t_0, t_f] \to \mathbb{R}^3$ and $\delta\pi : [t_0, t_f] \to \mathbb{R}^3$ that belongs in $\mathrm{T}^*_q\,\mathrm{S}^2$. So, each of the two parts of Eq. (4.7) are equated to zero.

$$\begin{aligned}\omega =& \frac{\partial \mathrm{H}(q,\pi)}{\partial \pi} + \frac{\partial \mathrm{h}_1(q,\pi)}{\partial \pi}\circ\dot{W}(t) \\ \dot{\pi} =& \left(\omega^{\Lambda}\pi - q^{\Lambda}\frac{\partial \mathrm{H}(q,\pi)}{\partial q}\right) - q^{\Lambda}\frac{\partial \mathrm{h}_1(q,\pi)}{\partial q}\circ\dot{W}(t)\end{aligned} \tag{4.8}$$

Finally, the stochastic Hamiltonian equation on the configuration manifold S^2 can be written as,

$$\begin{aligned}\dot{q} =& q\times\omega \\ =& q\times\frac{\partial \mathrm{H}(q,\pi)}{\partial \pi} + q\times\frac{\partial \mathrm{h}_1(q,\pi)}{\partial \pi}\circ\dot{W}(t) \\ \dot{\pi} =& \left(\omega\times\pi - q\times\frac{\partial \mathrm{H}(q,\pi)}{\partial q}\right) - q\times\frac{\partial \mathrm{h}_1(q,\pi)}{\partial q}\circ\dot{W}(t) \\ =& \left(-q\times\frac{\partial \mathrm{H}(q,\pi)}{\partial q} + \frac{\partial \mathrm{H}(q,\pi)}{\partial \pi}\times\pi\right) - \left(q\times\frac{\partial \mathrm{h}_1(q,\pi)}{\partial q} + \frac{\partial \mathrm{h}_1(q,\pi)}{\partial \pi}\times\pi\right)\circ\dot{W}(t)\end{aligned} \tag{4.9}$$

The SDE in Eq. (4.9) can be represented in the matrix form as,

$$\begin{bmatrix}\dot{q}\\ \dot{\pi}\end{bmatrix} = \begin{bmatrix}\left(\frac{\partial \mathrm{H}}{\partial \pi}\right)^{\Lambda} & 0_{3\times3}\\ \left(\frac{\partial \mathrm{H}}{\partial q}\right)^{\Lambda} & \left(\frac{\partial \mathrm{H}}{\partial \pi}\right)^{\Lambda}\end{bmatrix}\begin{bmatrix}q\\ \pi\end{bmatrix} + \begin{bmatrix}\left(\frac{\partial \mathrm{h}_k}{\partial \pi}\right)^{\Lambda} & 0_{3\times3}\\ \left(\frac{\partial \mathrm{h}_k}{\partial q}\right)^{\Lambda} & \left(\frac{\partial \mathrm{h}_k}{\partial \pi}\right)^{\Lambda}\end{bmatrix}\begin{bmatrix}q\\ \pi\end{bmatrix}\circ\dot{W}_k(t) \tag{4.10}$$

Eq. (4.10) represents Stratonovich SDE and is transformed into Ito counterpart aided by Wong-Zakai correction terms [65, 28] as follows,

$$\begin{bmatrix}\dot{q}\\ \dot{\pi}\end{bmatrix} = \left\{\begin{bmatrix}\left(\frac{\partial \mathrm{H}}{\partial \pi}\right)^{\Lambda} & 0_{3\times3}\\ \left(\frac{\partial \mathrm{H}}{\partial q}\right)^{\Lambda} & \left(\frac{\partial \mathrm{H}}{\partial \pi}\right)^{\Lambda}\end{bmatrix} + \frac{1}{2}\sum_{k=1}^{m}\Psi_k\right\}\begin{bmatrix}q\\ \pi\end{bmatrix} + \begin{bmatrix}\left(\frac{\partial \mathrm{h}_k}{\partial \pi}\right)^{\Lambda} & 0_{3\times3}\\ \left(\frac{\partial \mathrm{h}_k}{\partial q}\right)^{\Lambda} & \left(\frac{\partial \mathrm{h}_k}{\partial \pi}\right)^{\Lambda}\end{bmatrix}\begin{bmatrix}q\\ \pi\end{bmatrix}\dot{W}_k(t) \tag{4.11}$$

where, the term $\frac{1}{2}\sum_{k=1}^{m}\Psi_k$ corresponds to the Wong-Zakai correction term, evaluated as,

$$\Psi_k = \frac{1}{2}\partial_{[q,\pi]}\begin{bmatrix} q\times\frac{\partial \mathrm{h}_k}{\partial\pi} \\ q\times\frac{\partial \mathrm{h}_k}{\partial q} - \frac{\partial \mathrm{h}_k}{\partial\pi}\times\pi \end{bmatrix}\begin{bmatrix} q\times\frac{\partial \mathrm{h}_k}{\partial\pi} \\ q\times\frac{\partial \mathrm{h}_k}{\partial q} - \frac{\partial \mathrm{h}_k}{\partial\pi}\times\pi \end{bmatrix} \tag{4.12}$$

where, $\partial_{[q,\pi]}\begin{bmatrix} q\times\frac{\partial \mathrm{h}_k}{\partial\pi} \\ q\times\frac{\partial \mathrm{h}_k}{\partial q} - \frac{\partial \mathrm{h}_k}{\partial\pi}\times\pi \end{bmatrix}$ is a Hessian matrix [7]. The Wong-Zakai correction terms are reduced to only first order terms and the SDEs for $q \in \mathrm{S}^2$ and $\pi \in \mathrm{T}_q\mathrm{S}^2$ are obtained as,

$$\begin{aligned} \mathrm{d}q &= \left(-q\times\frac{\partial \mathrm{H}}{\partial\pi} - \frac{1}{2}\frac{\partial \mathrm{h}_k}{\partial\pi}\times\left(q\times\frac{\partial \mathrm{h}_k}{\partial\pi}\right)\right)dt - q\times\frac{\partial \mathrm{h}_k}{\partial\pi}\mathrm{d}W_k(t) \\ \mathrm{d}\pi &= \left(-q\times\frac{\partial \mathrm{H}}{\partial q} + \frac{\partial \mathrm{H}}{\partial\pi}\times\pi + \frac{1}{2}\left(q\times\frac{\partial \mathrm{h}_k}{\partial\pi}\right)\times\frac{\partial \mathrm{h}_k}{\partial q}\right)dt - \left(q\times\frac{\partial \mathrm{h}_k}{\partial q} - \frac{\partial \mathrm{h}_k}{\partial\pi}\times\pi\right)\mathrm{d}W_k(t) \end{aligned} \tag{4.13}$$

Here, h_k is another Hamiltonian governing the diffusion part of the SDE and in the present study, h_k can be expressed as: $h_k = \sigma_{i,k}\,\xi_i$, with ξ_i and $\sigma_{i,k}$ being the states of the undertaken system and constant vectors, respectively. For the solution of Eq. (4.13), a geometric numerical integration framework is necessary, which preserves the geometry of the solution path on the manifold. A new geometry preserving higher order Ito-Taylor based numerical integration scheme is developed in the subsequent part of this chapter.

4.2.2 Proposed geometric Ito-Taylor–1.5 strong scheme

Consider a general SDE of Γ on the differentiable manifold $\left(\mathrm{S}^2\right)^n$ of the following form,

$$\mathrm{d}\Gamma(t) = \mathbf{a}(\Gamma,t)\Gamma(t)\mathrm{d}t + \sum_{r=1}^{d}\boldsymbol{\sigma}_r(\Gamma,t)\Gamma(t)\mathrm{d}W_r(t) \tag{4.14}$$

where, $\Gamma(0) = \Gamma_0$ with $\mathbf{a}\left(\Gamma,t\right)$ and $\boldsymbol{\sigma}\left(\Gamma,t\right)$ being $n\times n$ and $n\times n\times d$ valued stochastic processes respectively. Based on Magnus expansion [22, 66], a solution of the form, $\Gamma = \exp\left(\boldsymbol{\mathcal{T}}\right)\Gamma_0$ is assumed, where, $\boldsymbol{\mathcal{T}}$ is a matrix on the Lie algebra and $\boldsymbol{\mathcal{T}}\left(0\right) = \mathbf{0}_{n\times n}$. Define a general C^2–continuous matrix valued function $\mathbf{g}\left(\boldsymbol{\Gamma}\right)$ such that the differential of $\mathbf{g}$ can be obtained by truncating the Taylor expansion [49] up to second order as follows,

$$\mathrm{d}\mathbf{g} = \left(\partial_\Gamma\mathbf{g}\right)\left(\partial_{\mathcal{T}_{ij}}\Gamma\right)\mathrm{d}\mathcal{T}_{ij} + \frac{1}{2}\partial_{\mathcal{T}_{kl}}\left(\left(\partial_\Gamma\mathbf{g}\right)\partial_{\mathcal{T}_{ij}}\Gamma\right)\mathrm{d}\mathcal{T}_{ij}\mathrm{d}\mathcal{T}_{kl} \tag{4.15}$$

where, $\partial_{\mathcal{T}_{ij}} = \frac{\partial(.)}{\partial \mathcal{T}_{ij}}$ and $\partial_\Gamma = \frac{\partial(.)}{\partial \Gamma}$. It is assumed that the components of $\boldsymbol{\mathcal{T}}$ evolve on a Lie algebra as a stochastic process, the SDE of which is described by,

$$\mathrm{d}\mathcal{T}_{ij} = \alpha_{ij}\mathrm{d}t + \beta_{r,ij}\,\mathrm{d}W_r \tag{4.16}$$

Invoking quadratic variation for independent Wiener processes [29], the following relation is derived,

$$\mathrm{d}\mathcal{T}_{ij}\mathrm{d}\mathcal{T}_{kl} = \left(\alpha_{ij}\mathrm{d}t + \beta_{r,ij}\,\mathrm{d}W_r\right)\left(\alpha_{kl}\mathrm{d}t + \beta_{s,kl}\,\mathrm{d}W_s\right) = \left(\beta_{r,ij}\;\beta_{r,kl}\right)\mathrm{d}t \tag{4.17}$$

Following Eqs. (4.16) and (4.17), Eq. (4.15) can be rewritten as,

$$\begin{aligned}\mathrm{d}\mathbf{g} \;&= \left(\left(\partial_\Gamma \mathbf{g}\right)\alpha_{ij}\left(\partial_{\mathcal{T}_{ij}}\Gamma\right) + \tfrac{1}{2}\partial_{\mathcal{T}_{kl}}\left(\left(\partial_\Gamma \mathbf{g}\right)\partial_{\mathcal{T}_{ij}}\Gamma\right)\beta_{r,ij}\;\beta_{r,kl}\right)\mathrm{d}t \\ &\quad + \left(\partial_\Gamma \mathbf{g}\right)\beta_{r,ij}\left(\partial_{\mathcal{T}_{ij}}\Gamma\right)\mathrm{d}W_r\end{aligned} \tag{4.18}$$

Eq. (4.18) can be modified as,

$$\mathbf{g}\left(t\right) = \mathbf{g}\left(t_0\right) + \int_{t_0}^{t} \Im^0\mathbf{g}\left(s\right)\mathrm{d}s + \int_{t_0}^{t} \Im^r\mathbf{g}\left(s\right)\mathrm{d}W_r(s) \tag{4.19}$$

where, $\Im^o\mathbf{g}$ and $\Im^r\mathbf{g}$ are the Kolmogorov operators over function $\mathbf{g}$, defined as,

$$\begin{aligned}\Im^o\mathbf{g} &= \left(\left(\partial_\Gamma \mathbf{g}\right)\alpha_{ij}\left(\partial_{\mathcal{T}_{ij}}\Gamma\right) + \frac{1}{2}\partial_{\mathcal{T}_{kl}}\left(\left(\partial_\Gamma \mathbf{g}\right)\partial_{\mathcal{T}_{ij}}\Gamma\right)\beta_{r,ij}\;\beta_{r,kl}\right) \\ \Im^r\mathbf{g} &= \left(\partial_\Gamma \mathbf{g}\right)\beta_{r,ij}\left(\partial_{\mathcal{T}_{ij}}\Gamma\right)\end{aligned} \tag{4.20}$$

Substituting the function $\mathbf{g}$ by $\Im^o\mathbf{g}$ and $\Im^r\mathbf{g}$, and making suitable rearrangements with repetitive substitutions, the following expression for $\mathbf{g}$ is obtained,

$$\begin{aligned}\mathbf{g}\left(t\right) &= \mathbf{g}\left(t_0\right) + \int_{t_0}^{t} \Im^0\mathbf{g}\left(t\right)\,\mathrm{d}s_1 + \int_{t_0}^{t} \Im^r\mathbf{g}\left(t\right)\,\mathrm{d}W_r(s_1) \\ &= \mathbf{g}\left(t_0\right) + \Im^0\mathbf{g}\left(t_0\right)\int_{t_0}^{t}\mathrm{d}s_1 + \Im^r\mathbf{g}\left(t_0\right)\int_{t_0}^{t}\mathrm{d}W_r(s_1) + \Im^0\Im^0\mathbf{g}\left(t_0\right)\int_{t_0}^{t}\int_{t_0}^{s_1}\mathrm{d}s_2\mathrm{d}s_1 \\ &\quad + \Im^r\Im^0\mathbf{g}\left(t_0\right)\int_{t_0}^{t}\int_{t_0}^{s_1}\mathrm{d}W_r(s_2)\mathrm{d}s_1 + \Im^0\Im^r\mathbf{g}\left(t_0\right)\int_{t_0}^{t}\int_{t_0}^{s_1}\mathrm{d}s_2\mathrm{d}W_r(s_1) \\ &\quad + \Im^{r_1}\Im^{r_2}\mathbf{g}\left(t_0\right)\int_{t_0}^{t}\int_{t_0}^{s_1}\mathrm{d}W_{r_1}(s_2)\mathrm{d}W_{r_2}(s_1) + \mathcal{R}\left(\mathcal{O}^3\right)\end{aligned} \tag{4.21}$$

where, $\mathcal{R}$ is the remainder term. It can be observed that the terms in Eq. (4.21) along with the remainder terms contain two types of multiple stochastic integrals (MSIs) [15, 29]. The MSIs of the type $I^a_{j_1,j_2,\ldots,j_k}\left(t\right)$ occur in the truncated series, while those of the type $I^b_{j_1,j_2,\ldots,j_k}\left(z,t\right)$ occur in the remainder

term, $\mathcal{R}$. The integrals can be defined as (Eqs. 5.72a and 5.72b of [29]),

$$\begin{aligned} I^a_{j_1,j_2,\ldots,j_k}(t) &= \int_{t_0}^{t}\int_{t_0}^{s_1}\ldots\int_{t_0}^{s_{k-1}} \mathrm{d}W_{j_1}(s_k)\,\mathrm{d}W_{j_2}(s_{k-1})\ldots\mathrm{d}W_{j_k}(s_1) \\ I^b_{j_1,j_2,\ldots,j_k}(z,t) &= \int_{t_0}^{t}\int_{t_0}^{s_1}\ldots\int_{t_0}^{s_{k-1}} \Im^{j_k}\Im^{j_{k-1}}\ldots\Im^{j_1}z(s_{k-1})\,\mathrm{d}W_{j_1}(s_k)\,\mathrm{d}W_{j_2}(s_{k-1})\ldots\mathrm{d}W_{j_k}(s_1) \end{aligned} \tag{4.22}$$

where, $j_k = 0$ corresponds to the integral with respect to s. Following this compact notation for the MSIs, Eq. (4.21) can be restated as,

$$\begin{aligned} \mathbf{g}(t) &= \mathbf{g}(t_0) + \Im^0\mathbf{g}(t_0)\,I_0 + \Im^r\mathbf{g}(t_0)\,I_1 + \Im^0\Im^0\mathbf{g}(t_0)\,I_{00} + \Im^r\Im^0\mathbf{g}(t_0)\,I_{10} \\ &\quad + \Im^0\Im^r\mathbf{g}(t_0)\,I_{01} + \Im^{r_1}\Im^{r_2}\mathbf{g}(t_0)\,I_{11} + \mathcal{R}(\mathcal{O}^3) \end{aligned} \tag{4.23}$$

where, the expanded form of the MSIs with the compact notation is defined as follows [15],

$$\begin{aligned} &I_0 = \int_{t_0}^{t}(t)\;\mathrm{d}s_1, && I_1 = \int_{t_0}^{t}(t)\;\mathrm{d}W_r(s_1), && I_{00} = \int_{t_0}^{t}\int_{t_0}^{s_1}\mathrm{d}s_2\mathrm{d}s_1 \\ &I_{10} = \int_{t_0}^{t}\int_{t_0}^{s_1}\mathrm{d}W_r(s_2)\mathrm{d}s_1, && I_{01} = \int_{t_0}^{t}\int_{t_0}^{s_1}\mathrm{d}s_2\mathrm{d}W_r(s_1), && I_{11} = \int_{t_0}^{t}\int_{t_0}^{s_1}\mathrm{d}W_{r_1}(s_2)\mathrm{d}W_{r_2}(s_1) \end{aligned} \tag{4.24}$$

Based on the aforementioned compact notation for the MSIs, the remainder term of Eq. (4.23) is described in Eq. (A.1) of A. Further extracting the Brownian integral of multiplicity 3 (the term with the integral, I_{111}) and substituting $g_{ij} = \mathcal{T}_{ij}$ in Eq. (4.21), the expansion is obtained as,

$$\begin{aligned} \mathcal{T}_{ij}(t) =& \mathcal{T}_{ij}(t_0) + \alpha_{ij}(t_0)\,I_0 + \beta_{r,ij}(t_0)\,I_1 + \Im^r\beta_{r,ij}(t_0)\,I_{11} + \Im^0\alpha_{ij}(t_0)\,I_{00} \\ &+ \Im^r\alpha_{ij}(t_0)\,I_{10} + \Im^0\beta_{r,ij}(t_0)\,I_{01} + \Im^r\Im^r\beta_{r,ij}(t_0)\,I_{111} + \tilde{\mathcal{R}}\left(\mathcal{O}^3\right) \end{aligned} \tag{4.25}$$

where, the revised remainder term, $\tilde{\mathcal{R}}$ is given in Eq. (A.2) of A. Eq. (4.25) exclusive of the remainder term is the proposed form of the geometric Taylor 1.5 strong scheme on the Lie algebra $\mathrm{T}_\Gamma\mathcal{M}$. Since this mapping holds in the neighbourhood of the locally Euclidean space $\mathcal{T}_{ij}$, the MSIs in Eq. (4.25) upon discretization will result in an identical expression [15]. Accordingly Eq. (4.25) can be re-written as,

$$\begin{aligned} \mathcal{T}_{ij}(n+1) = \;& \mathcal{T}_{ij}(n) + \alpha_{ij}\Delta t + \beta_{r,ij}\Delta W_r + \Im^0\alpha_{ij}\tfrac{(\Delta t)^2}{2} \\ &+ \Im^0\beta_{r,ij}\;(\Delta W_r\Delta t - \Delta Z_r) + \Im^r\beta_{r,ij}\tfrac{(\Delta W_r)^2-\Delta t}{2} \\ &+ \Im^r\alpha_{ij}\Delta Z_r + \Im^r\Im^r\beta_{r,ij}\left(\tfrac{(\Delta W_r)^3}{6} - \tfrac{\Delta W_r\Delta t}{2}\right) \end{aligned} \tag{4.26}$$

Eq. (4.26) updates $\mathcal{T}_{ij}$ on the tangent space at identity, to yield the evolution at $(n+1)^{\text{th}}$ instant. Once this is achieved, a standard exponential mapping can be utilized to evaluate the evolution of Γ at $(n+1)^{\text{th}}$ step as illustrated in Fig. 4.1. This is given by,

$$\Gamma(n+1) = \exp^{(\mathcal{T}(n+1))}\Gamma(n) \tag{4.27}$$

the expressions for $\alpha_{ij}\left(\partial_{\mathcal{T}_{ij}}\Gamma_j\right)$ can be re-written using Theorem 2 (Exponential-Gradient Theorem)

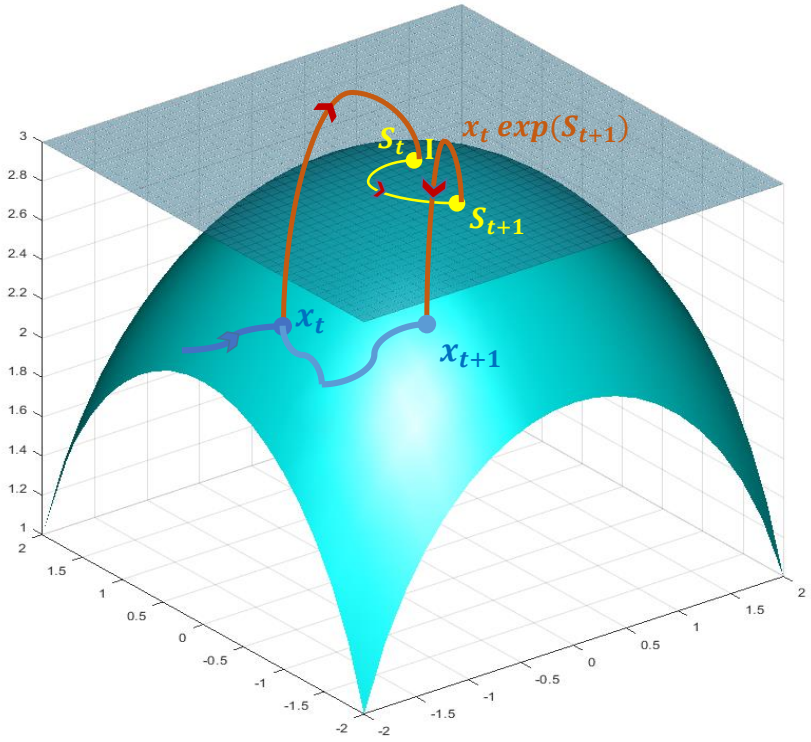

FIGURE 4.1: Illustration of geometric integration scheme. The stochastic process x_t lies on the configuration manifold. The current state (x_t) is mapped to the identity element, $\mathbb{I}$ of the manifold using Magnus expansion to arrive at S_t. SDE in S_t is solved using proposed scheme to obtain S_{t+1}. The solution x_{t+1} is evaluated by exponential mapping from lie algebra to manifold.

of [22] as,

$$\begin{aligned}\alpha_{ij}\partial_{\mathcal{T}_{ij}}\Gamma &= \alpha_{ij}\partial_{\mathcal{T}_{ij}}\mathrm{e}^{\mathcal{T}}\Gamma_0 \\ &= \alpha_{ij}\mathrm{dexp}_{\mathcal{T}}\left(\mathbf{E}_{ij}\right)\mathrm{e}^{\mathcal{T}}\Gamma_0 \\ &= \alpha_{ij}\mathrm{dexp}_{\mathcal{T}}\left(\mathbf{E}_{ij}\right)\Gamma \\ &= \mathrm{dexp}_{\mathcal{T}}\left(\alpha_{ij}\mathbf{E}_{ij}\right)\Gamma \\ &= \mathrm{dexp}_{\mathcal{T}}(\boldsymbol{\alpha})\Gamma\end{aligned} \tag{4.28}$$

using the same procedure as in Eq. (4.28) for the expression $\beta_{r,ij}\ \partial_{\mathcal{T}_{ij}}\Gamma$ we can write,

$$\beta_{r,ij}\ \partial_{\mathcal{T}_{ij}}\Gamma = \mathrm{dexp}_{\mathcal{T}}\left(\boldsymbol{\beta}_r\right)\Gamma \tag{4.29}$$

Further $\partial_{\mathcal{T}_{kl}}\left(\left(\partial_{\Gamma}\mathbf{g}\right)\partial_{\mathcal{T}_{ij}}\Gamma\right)\beta_{r,ij}\ \beta_{r,kl}$ is also re-written using Theorem 2 (Exponential-Gradient Theorem) of [22] as,

$$\begin{aligned}
\partial_{\mathcal{T}_{kl}}\left(\left(\partial_{\Gamma}\mathbf{g}\right)\partial_{\mathcal{T}_{ij}}\Gamma\right)\beta_{r,ij}\ \beta_{r,kl} =&\partial_{\mathcal{T}_{kl}}\left(\partial_{\Gamma}\mathbf{g}\right)\beta_{r,ij}\partial_{\mathcal{T}_{ij}}\Gamma\ \beta_{r,kl}+\left(\partial_{\Gamma}\mathbf{g}\right)\partial_{\mathcal{T}_{kl}}\left(\partial_{\mathcal{T}_{ij}}\Gamma\right)\beta_{r,ij}\ \beta_{r,kl}\\
=&\partial_{\Gamma}\left(\partial_{\mathcal{T}_{kl}}\mathbf{g}\right)\beta_{r,ij}\partial_{\mathcal{T}_{ij}}\Gamma\ \beta_{r,kl}+\left(\partial_{\Gamma}\mathbf{g}\right)\beta_{r,ij}\beta_{r,kl}\partial_{\mathcal{T}_{kl}}\left(\partial_{\mathcal{T}_{ij}}\Gamma\right)\\
=&\partial_{\Gamma}\left(\left(\partial_{\Gamma}\mathbf{g}\right)\partial_{\mathcal{T}_{kl}}\Gamma\right)\beta_{r,ij}\partial_{\mathcal{T}_{ij}}\Gamma\ \beta_{r,kl}+\left(\partial_{\Gamma}\mathbf{g}\right)\beta_{r,ij}\beta_{r,kl}\partial_{\mathcal{T}_{kl}}\left(\partial_{\mathcal{T}_{ij}}\Gamma\right)\\
=&\left(\partial_{\Gamma}\left(\partial_{\Gamma}\mathbf{g}\right)\partial_{\mathcal{T}_{kl}}\Gamma+\partial_{\Gamma}\left(\partial_{\mathcal{T}_{kl}}\Gamma\right)\partial_{\Gamma}\mathbf{g}\right)\beta_{r,ij}\partial_{\mathcal{T}_{ij}}\Gamma\ \beta_{r,kl}\\
&+\left(\partial_{\Gamma}\mathbf{g}\right)\beta_{r,ij}\beta_{r,kl}\partial_{\mathcal{T}_{kl}}\left(\partial_{\mathcal{T}_{ij}}\Gamma\right)\\
=&\left(\partial_{\Gamma}\partial_{\Gamma}\mathbf{g}\right)\mathrm{dexp}_{\boldsymbol{\mathcal{T}}}\left(\boldsymbol{\beta}_r\right)\Gamma\mathrm{dexp}_{\boldsymbol{\mathcal{T}}}\left(\boldsymbol{\beta}_r\right)\Gamma\\
&+\left(\partial_{\Gamma}\mathbf{g}\right)\left(\left(\mathrm{dexp}_{\boldsymbol{\mathcal{T}}}\left(\boldsymbol{\beta}_r\right)\right)\Gamma+\mathcal{M}_r\Gamma\right)
\end{aligned}\tag{4.30}$$

where, $\mathcal{M}_r=\beta_{r,kl}\ \beta_{r,ij}\mathcal{M}_{ij}^{kl}$ [22] with

$$\mathcal{M}_r=\sum_{p=0}^{\infty}\sum_{q=0}^{\infty}\frac{1}{(p+q+2)}\frac{(-1)^p}{p!(q+1)!}\mathrm{ad}_{\boldsymbol{\mathcal{T}}}^{p}\left(\mathrm{ad}_{\boldsymbol{\beta}_r}\left(\mathrm{ad}_{\boldsymbol{\mathcal{T}}}^{q}\left(\boldsymbol{\beta}_r\right)\right)\right)\tag{4.31}$$

Here, Eqs. (4.28), (4.29) and (4.30) are substituted in in Eq. (4.20) for obtaining the Kolmogorov operators, and it can be written as,

$$\begin{aligned}
\Im^{o}\mathbf{g}=&\frac{\partial\mathbf{g}}{\partial\Gamma}\left(\mathrm{dexp}_{\boldsymbol{\mathcal{T}}}(\boldsymbol{\alpha})\Gamma+\frac{1}{2}\mathrm{dexp}_{\boldsymbol{\mathcal{T}}}\left(\boldsymbol{\beta}_r\right)^2\Gamma+\frac{1}{2}\mathcal{M}_r\Gamma\right)\\
&+\frac{1}{2}\frac{\partial^2\mathbf{g}}{\partial\Gamma^2}\mathrm{dexp}_{\boldsymbol{\mathcal{T}}}\left(\boldsymbol{\beta}_r\right)\Gamma\mathrm{dexp}_{\boldsymbol{\mathcal{T}}}\left(\boldsymbol{\beta}_r\right)\Gamma\\
\Im^{r}\mathbf{g}=&\frac{\partial\mathbf{g}}{\partial\Gamma}\mathrm{dexp}_{\boldsymbol{\mathcal{T}}}(\boldsymbol{\beta}_r)\Gamma
\end{aligned}\tag{4.32}$$

By employing a reasoning approach akin to that used in Equation (4.15), one can represent the Taylor series expansion of a vector-valued function Γ as follows:

$$\mathrm{d}\Gamma=\left(\partial_{\mathcal{T}_{ij}}\Gamma\right)\mathrm{d}\mathcal{T}_{ij}+\frac{1}{2}\left(\partial_{\mathcal{T}_{ij}}\partial_{\mathcal{T}_{kl}}\Gamma\right)\mathrm{d}\mathcal{T}_{ij}\mathrm{d}\mathcal{T}_{kl}\tag{4.33}$$

By substituting the expressions of $\mathrm{d}\mathcal{T}_{ij}$ and $\mathrm{d}\mathcal{T}_{ij}\mathrm{d}\mathcal{T}_{kl}$ in Eq. (4.33), the following expression is obtained,

$$\mathrm{d}\Gamma=\left(\boldsymbol{\alpha}_{ij}\left(\partial_{\mathcal{T}_{ij}}\right)+\frac{1}{2}\boldsymbol{\beta}_{r,ij}\ \boldsymbol{\beta}_{r,kl}\left(\partial_{\mathcal{T}_{ij}}\partial_{\mathcal{T}_{kl}}\right)\right)\Gamma\mathrm{d}t+\boldsymbol{\beta}_{r,ij}\ \left(\partial_{\mathcal{T}_{ij}}\right)\Gamma\mathrm{d}W_r\tag{4.34}$$

By equating Eq. (4.14) with Eq. (4.34) and utilizing Eqs. (4.28), (4.29) and (4.30), the relationship between the coefficients $\mathbf{a}\Gamma$ and $\boldsymbol{\sigma}r\Gamma$ with $\boldsymbol{\alpha}$ and $\boldsymbol{\beta}r$ can be derived.

$$\begin{aligned}\mathbf{a} &= \left(\text{dexp}_{\boldsymbol{\mathcal{T}}}(\boldsymbol{\alpha}) + \frac{1}{2}\left(\text{dexp}_{\boldsymbol{\mathcal{T}}}(\boldsymbol{\beta}_r)\right)^2 + \mathcal{M}_r\right) \\ \boldsymbol{\sigma}_r &= \text{dexp}_{\boldsymbol{\mathcal{T}}}(\boldsymbol{\beta}_r), \quad \forall\, r = 1, \ldots, d\end{aligned} \tag{4.35}$$

By solving Eq. (4.35) for $\boldsymbol{\alpha}$ and $\boldsymbol{\beta}_r$ and utilizing Baker's inverse identity [22], the coefficients are obtained as follows:

$$\begin{aligned}\boldsymbol{\alpha} &= \text{dexp}^{-1}_{\boldsymbol{\mathcal{T}}}\left(\mathbf{a}\right) - \frac{1}{2}\text{dexp}^{-1}_{\boldsymbol{\mathcal{T}}}\left(\boldsymbol{\sigma}_r^2\right) - \frac{1}{2}\text{dexp}^{-1}_{\boldsymbol{\mathcal{T}}}\left(\mathcal{M}_r\right) \\ \boldsymbol{\beta}_r &= \text{dexp}^{-1}_{\boldsymbol{\mathcal{T}}}\left(\boldsymbol{\sigma}_r\right)\end{aligned} \tag{4.36}$$

The equation represented by Eq. (4.36) provides the means to estimate the unknown drift and diffusion coefficients, $\boldsymbol{\alpha}$ and $\boldsymbol{\beta}r$, of Eq. (4.16), using the provided drift and diffusion coefficients, $\mathbf{a}$ and $\boldsymbol{\sigma}r$, of Eq. (4.14), thereby facilitating the solution of stochastic differential equations. The concepts introduced in the current chapter serve as the foundation for the ideas presented in the following chapters. While the variables may be denoted by distinct symbols, the formulations remain consistent until the establishment of the integration schemes. This consistency is reiterated in Chapters 5 and 6 to ensure comprehensiveness.

4.2.3 Convergence of the proposed geometric Ito-Taylor 1.5 strong scheme

Consider the one-step approximation [29] for the explicit integration scheme in Eq. (4.25). It is assumed that the drift and diffusion coefficients satisfy the Lipschitz and linear growth conditions, and the SDE in Eq. (4.14) (for a one-step approximation) has a unique $t-$continuous solution. The strong order of convergence corresponds to a measure of path-wise deviation at a time instant. The global order of strong convergence is determined based on the error in the mean and mean-square sense of the approximation. For a stochastic process, $Y\left(t\right)$, the error is given as,

$$\epsilon_s = Y\left(t + \Delta t\right) - \tilde{Y}\left(t + \Delta t\right) \tag{4.37}$$

where, $Y\left(t + \Delta t\right)$ is the true solution and $\tilde{Y}\left(t + \Delta t\right)$ is the approximate solution. Assuming uniform time-step size, the errors in the mean and mean square for the one-step approximation are given as (Eqs.

(5.5a) and (5.5b) of [29]),

$$\begin{aligned} E\left[\left|Y_{t_j,y}\left(t_j+\Delta t\right)-\tilde{Y}_{t_j,y}\left(t_j+\Delta t\right)\right|\right] &\leq C\left(1+|y|^2\right)^{\frac{1}{2}}(\Delta t)^{c_1} \\ \left(E\left[\left|Y_{t_j,y}\left(t_j+\Delta t\right)-\tilde{Y}_{t_j,y}\left(t_j+\Delta t\right)\right|^2\right]\right)^{\frac{1}{2}} &\leq C\left(1+|y|^2\right)^{\frac{1}{2}}(\Delta t)^{c_2} \end{aligned} \tag{4.38}$$

where, $y = Y\left(t_j\right)$ is the initial condition. If $c_2 \geq \frac{1}{2}$ and $c_1 \geq c_2 + \frac{1}{2}$, with $k = 0, 1, \ldots, N$ for the partition Ξ_N of the interval $[0, T]$, the global order of convergence over the interval $[t_0, t_k]$ is given as (Eq. (5.6b) of [29]),

$$\left(E\left[\left|Y_{t_0,y_0}\left(t_k\right)-\tilde{Y}_{t_0,y_0}\left(t_k\right)\right|^2\right]\right)^{\frac{1}{2}} \leq C\left(1+E\left[|y_0|^2\right]\right)^{\frac{1}{2}}(\Delta t)^c \tag{4.39}$$

For a one-step approximation, the order of accuracy is given as, $C = c_2 - \frac{1}{2}$, with C being independent of $k, \Delta t$ and x_0. For the proposed geometric Ito-Taylor 1.5 strong scheme in Eq. (4.25) to solve the geometric SDE in Eq. (4.14), the error in Eq. (4.37) is revised as,

$$\epsilon_s \quad = \Gamma_i\left(t+\Delta t\right) - \tilde{\Gamma}_i\left(t+\Delta t\right) \tag{4.40}$$

Substituting the solution using Magnus expansion and for the case of one-step approximation, Eq. (4.40) is restated as,

$$\begin{aligned} \epsilon_s &= \exp\left(\mathcal{T}_{t+\Delta t}\right)\Gamma_0 - \exp\left(\tilde{\mathcal{T}}_{t+\Delta t}\right)\Gamma_0 \\ &= \left(\left(\mathcal{T}_{t+\Delta t} - \tilde{\mathcal{T}}_{t+\Delta t}\right) + \tfrac{1}{2!}\left(\mathcal{T}^2_{t+\Delta t} - \tilde{\mathcal{T}}^2{}_{t+\Delta t}\right) + \ldots\right)\Gamma_0 \end{aligned} \tag{4.41}$$

As outlined in Eq. (4.22), two types of integrals appear in the one-step approximation. The mean of the integrals can be evaluated easily to find the order of smallness and is given as (Sec 5.6.1 of [29]),

$$\begin{aligned} E\left[I^a_{j_1,j_2,\ldots,j_k}\left(t\right)\right] &= \begin{cases} 0, & \text{if at least one } \; j_i \neq 0 \\ O\left((\Delta t)^k\right), & \text{if all } \; j_i = 0 \end{cases} \\ E\left[I^b_{j_1,j_2,\ldots,j_k}\left(z,t\right)\right] &= 0, \quad \text{if at least one } \; j_i \neq 0 \end{aligned} \tag{4.42}$$

Further, the order of the MSIs in mean square sense are evaluated using the following results (Eqs. (5.73) and (5.74) of [29]),

$$\left(E\left[I^a_{j_1 j_2 \cdots j_k}(t)\right]^2\right)^{1/2} = O\left(\Delta t^{\left(1-\sum_{i=1}^{k}\frac{\bar{j}_i}{2}\right)}\right) \tag{4.43}$$

where, $\bar{j}_i = \begin{cases} 0 \text{ if } j_i = 0 \\ 1 \text{ if } j_i \neq 0 \end{cases}$

$$\left(E\left[I^b_{j_1 j_2 \dots j_k}(z,t)\right]^2\right)^{1/2} \leq K\left(1 + E\left[|\mathcal{T}_{mn}(t)|^2\right]\right)^{1/2} \Delta t^{\left(1-\sum_{i=1}^{k}\frac{\bar{j}_i}{2}\right)} \tag{4.44}$$

provided that, $|L^{j_k} L^{j_{k-1}} \dots L^{j_1} z(t, \mathcal{T}_{mn}(t_0))| \leq K\left((1 + |\mathcal{T}_{mn}(t_0)|^2)^{1/2}\right)$. It should be noted that the values of c_1 and c_2 are governed by the minimum order of smallness of the integrals. To determine the order of convergence based on Eq. (4.38), c_1 is evaluated by taking the expectation of Eq. (4.41). It can be observed that minimum order of smallness in the mean sense is given by $\int_{t_0}^{t}\int_{t_0}^{s_1}\int_{t_0}^{s_2} \Im^0\Im^0\alpha_{ij}(s_3)\, \mathrm{d}s_3\mathrm{d}s_2\mathrm{d}s_1$. Accordingly, following Eq. (4.42), $c_1 = 3$. Assuming that the integrands in $\mathcal{R}$ satisfy the condition in Eq. (4.44), $E[\epsilon_s^2] = O\left((\Delta t)^4\right)$, providing $c_2 = 2$. Since $c_2 \geq \frac{1}{2}$ and $c_1 \geq c_2 + \frac{1}{2}$, the order of convergence of the geometric Taylor 1.5 scheme is $c = c_2 - \frac{1}{2} = 1.5$.

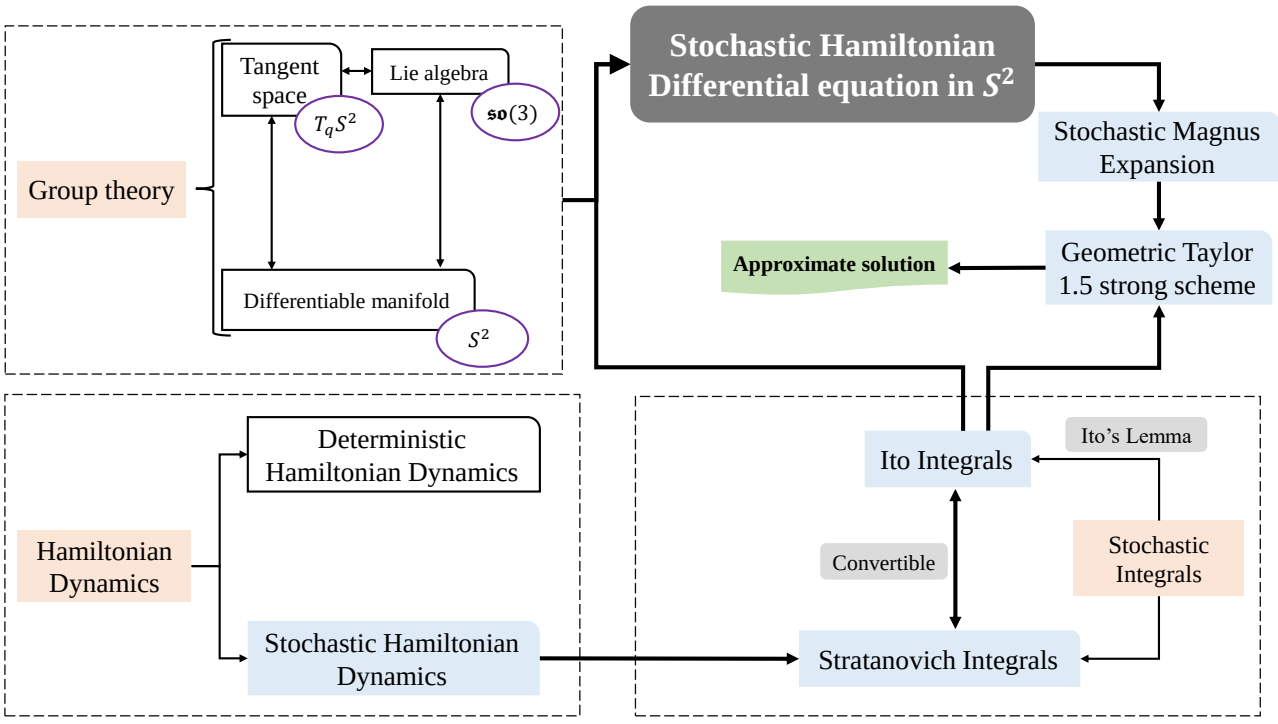

FIGURE 4.2: Proposed geometry preserving Ito-Taylor based numerical integration scheme for Stochastic Hamiltonian dynamics.

4.3 Implementation of the proposed algorithm

This section briefly describes the two objectives of the present work: (i) formation of stochastic Hamiltonian equation of motion for the systems on $\left(\mathrm{S}^2\right)^n$ and (ii) mathematically consistent formulation of

geometric Taylor–1.5 scheme. For any physical system evolving on the Euclidean space, the Hamiltonian equations of motion can be obtained using the classical formulation. However, for the systems evolving on the smooth manifold $\left(\mathrm{S}^2\right)^n$, the theory of matrix Lie group is employed such that the variables on the manifold are mapped on the lie algebra using matrix exponential. Based on this observation, this work has derived expressions for stochastic Hamiltonian dynamics on $\left(\mathrm{S}^2\right)^n$ using variational principle on Lie algebra. The equations of motion for stochastic Hamiltonian dynamics are written in the form of stochastic integrals, which can be either Stratonovich or Ito SDEs. In the present work, Ito SDEs are utilized using the Wong-Zakai correction terms [28]. Thereafter, as the proposed method utilizes matrix exponential for the differential equations, a suitable tool for this approach is the Magnus expansion. Finally, the system states are updated on the manifold by exploiting its relationship with lie algebra. A flow chart explaining this is portrayed in Fig. 4.2, and an algorithm summarizing the steps to execute the proposed framework is given in Algorithm 5.

Algorithm 2 Geometric Taylor–1.5 algorithm for stochastic Hamiltonian system

Input: $\mathrm{H}\left(q_i, \pi_i\right) \forall i = 1, \ldots, n$ ▷ Hamiltonian of the system
Estimate $\frac{\partial \mathrm{H}(q_i,\pi_i)}{q_i}$ and $\frac{\partial \mathrm{H}(q_i,\pi_i)}{\pi_i}$
Obtain equation of motion for the states q_i and π_i in the form of Eq. (4.14). ▷ Refer Eqs. (4.13) and (4.14)
Initialization for the simulation:
for $k = 1 : N_{iteration}$ **do** ▷ Iteration for sample length
Estimate the drift $\boldsymbol{\alpha}$ and diffusion $\boldsymbol{\beta}$ coefficients for SDE in lie algebra. ▷ Refer Eq. (4.36)
Estimate the kolmogorov operators for drift $\boldsymbol{\alpha}$ and diffusion $\boldsymbol{\beta}$ matrices for Γ_n. ▷ Refer Eq. (4.32)
Estimate the MSIs similar to the Euclidean case.
Update states $\mathcal{T}_{ij}(n+1)$ on lie algebra using geometric Taylor–1.5 scheme. ▷ Refer Eq. (4.26)
Update states $\Gamma(n+1)$ on manifold using the exponential mapping from lie algebra. ▷ Refer Eq. (4.27)
Output: Geometry preserving response of the stochastic Hamiltonian system

4.3.1 Computational complexity of the proposed algorithm

This section provides the computational complexity of the proposed geometric Taylor 1.5 framework. The execution time of the algorithm is influenced by two variables: the degree of freedoms (dof) and the number of samples $(\frac{T}{\mathrm{d}t})$, where T represents the final time point and $\mathrm{d}t$ is the required time step for the sampling of the system response. The time complexities of each essential subroutine are outlined in detail in Algorithm 3.

Algorithm 3 Computational complexity of geometric Taylor–1.5 algorithm

Input: State space representation of the system	▷ $\mathcal{O}\left(dof^2\right)$
Wedge operation on state vector	▷ $\mathcal{O}\left(dof^2\right)$
Obtaining Kolmogorov operator $\Im^0\mathbf{g}$.	▷ $\mathcal{O}\left(dof^6\right)$
Obtaining Kolmogorov operator $\Im^r\mathbf{g}$ and $\Im^0\Im^r\mathbf{g}$.	▷ $\mathcal{O}\left(dof^4\right)$
Initialization for the simulation.	▷ $\mathcal{O}\left(dof^2\right)$
for $k = 1 : N$ **do**	▷ Iteration for sample length
Estimate the MSIs similar to the Euclidean case.	▷ $\mathcal{O}\left(dof^2\right)$
Update states $\mathcal{T}_{ij}(n+1)$ on lie algebra using geometric Taylor–1.5 scheme.	▷ $\mathcal{O}\left(dof^2\right)$
Using the exponential mapping on $\mathcal{T}_{ij}(n+1)$.	▷ $\mathcal{O}\left(dof^3\right)$
Update states $\Gamma(n+1)$ on manifold using the exponential mapping from lie algebra.	▷ $\mathcal{O}\left(dof^2\right)$
Output: Computational complexity of the algorithm	▷ $\mathcal{O}\left(dof^3 N\right)$

4.4 Numerical case studies

To showcase the suitability of the proposed framework for the solution of stochastic dynamical systems on differentiable manifolds, the first step involves the examination of a benchmark system. Subsequently, numerical studies are conducted on one oscillator and two physical systems. These case studies serve to further illustrate the practicality of the algorithm in such scenarios. In this context, (i) Stochastic free rigid body, (ii) Kuramoto oscillator, (iii) Pendulum cart system, and, (iv) Dynamics of two quad rotors transporting a mass point are undertaken. Mathematical illustration of the aforementioned systems are provided in this section and their trajectories, and, geometry preserving results are discussed in the next section.

4.4.1 Stochastic free rigid body- a benchmark problem

A stochastic free rigid body with center of mass at the origin is considered as the benchmark in this section [46]. Denoting the angular momentum by the vector z and referring I_1, I_2 and I_3 as the principal moments of inertia, the motion for the rigid body can be described as,

$$dz = \mathbf{a}\left(z\right) z\,\mathrm{d}t + \boldsymbol{\sigma}\left(z\right) z\,\mathrm{d}W\left(t\right) \tag{4.45}$$

where, $\boldsymbol{\sigma}\left(z\right)$ is given as,

$$\boldsymbol{\sigma}\left(z\right) = \begin{bmatrix} \frac{z_1}{I_1} & \frac{z_2}{I_2} & \frac{z_3}{I_3} \end{bmatrix}^{\Lambda} \tag{4.46}$$

$\mathbf{a}\left(z\right)$ is computed from the relation, $\mathbf{a}\left(z\right)+\mathbf{a}^T\left(z\right) = \boldsymbol{\sigma}^2\left(z\right)$. This is achieved by setting the matrix $\mathbf{a}\left(z\right)$ as the lower triangular matrix of $\boldsymbol{\sigma}^2\left(z\right)$, where, the diagonal entries of $\mathbf{a}\left(z\right)$ are 0.5 times the diagonal entries of $\boldsymbol{\sigma}^2\left(z\right)$. The simulation is carried out for 100s and 1000 Monte Carlo simulations with the

initial conditions as: $z_0 = [\sin(1.1), 0, \cos(1.1)]^T$ and the moments of inertia as, $I_1 = 2$, $I_2 = 1$ and $I_3 = \frac{2}{3}$.

A comparative analysis for the error in the solution using different geometric stochastic integration schemes, namely geometric Euler-Maruyama (g-EM [22]), geometric Milstein (g-Milstein) and the proposed geometric Taylor 1.5 (g-Taylor 1.5) scheme for varying time steps is portrayed in Fig. 4.3. The global error is computed as, $\epsilon = \log_2(\max(E[z_{ref}]) - \max(E[z]))$, where the reference solution corresponds to g-EM with $\Delta t = 2^{-12}$s. It is clearly observed from Fig. 4.3, that the error for any arbitrary step size using proposed geometric integration scheme is lesser than g-EM and g-Milstein. This demonstrates the efficiency of the proposed integration scheme for coarser time steps.

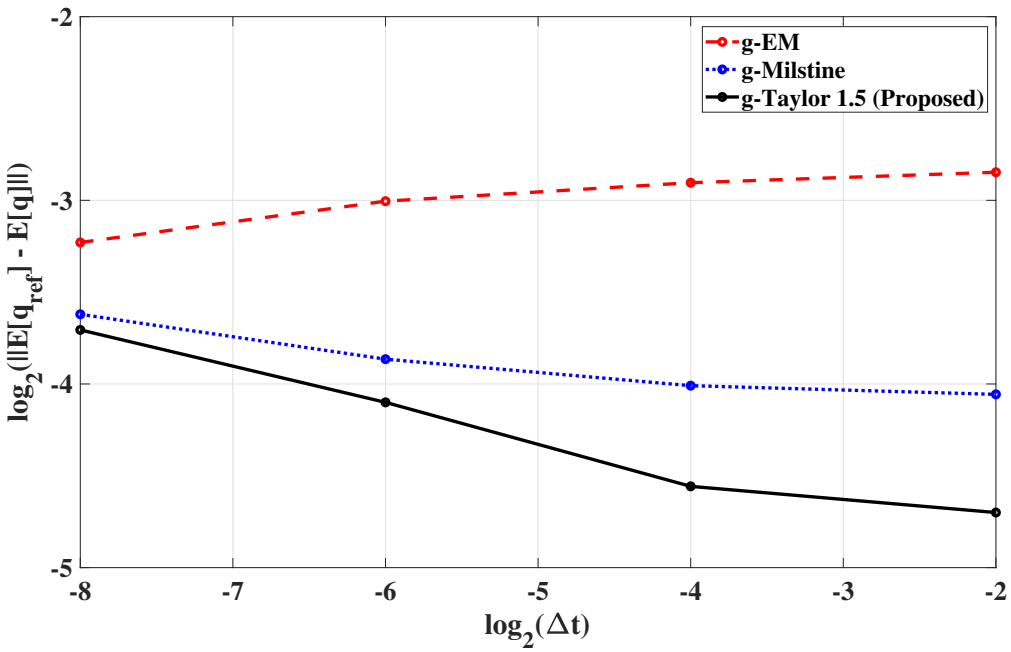

FIGURE 4.3: Comparison of the global error $\log_2(\max(E[q_{ref}]) - \max(E[q]))$ for the proposed scheme in comparison with existing geometric EM [22] and geometric Milstein for different time steps $\Delta t = 2^{-8}, 2^{-6}, 2^{-4}$ and 2^{-2} for the benchmark problem. Geometric EM with $\Delta t = 2^{-12}$ is the benchmark solution.

It should be noted that Fig. 4.3 presents the global error of the system response simulated over a duration of 100 seconds. Therefore, there isn't a discernible general trend for the slope of the error, making it challenging to compare the numerical error to the analytical one described in Eq. (4.38). The objective of this study was to provide a comprehensive comparison between the proposed method and existing methods on a global scale. However, as highlighted in the literature [29], simulations of the stochastic rigid model for 1 second revealed interesting insights. Specifically, the error at the endpoint,

$\log_2\left(\max\left(E\left[q_T^{ref}\right]\right) - \max\left(E\left[q_T\right]\right)\right)$, for various time steps $\Delta t = 2^{-8}, 2^{-6}$, and 2^{-4} demonstrated an increasing trend with increasing Δt, as depicted in Fig. 4.4. Upon analysis, it was observed that the average slope of the numerical error was approximately 1 for the geometric Euler-Maruyama (EM) scheme and around 1.5 for the proposed geometric Taylor 1.5 scheme demonstrating the convergence of proposed method compared to the analytical rate (Eq. (4.38)).

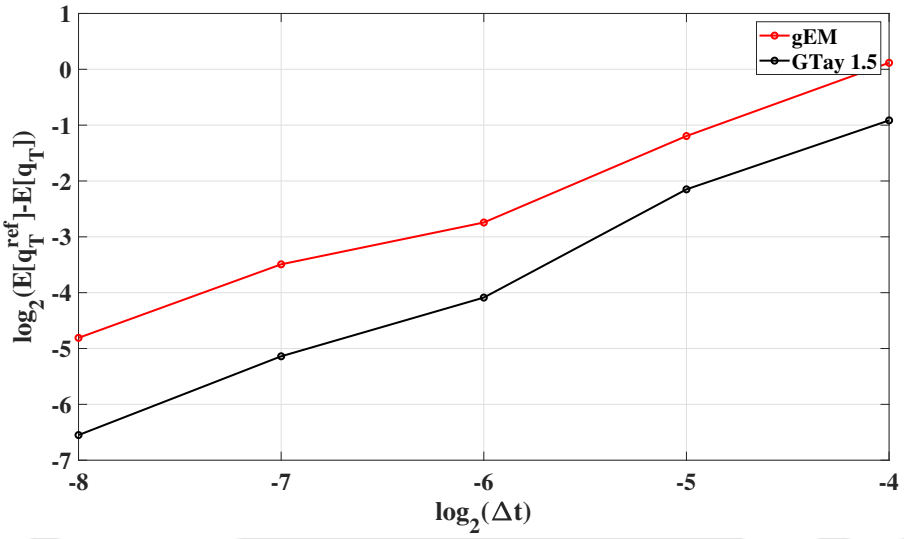

FIGURE 4.4: Comparison of the error at end point $\log_2\left(\max\left(E\left[q_T^{ref}\right]\right) - \max\left(E\left[q_T\right]\right)\right)$ for the proposed scheme in comparison with existing geometric EM [22] for different time steps $\Delta t = 2^{-8}, 2^{-6}$ and 2^{-4} for the benchmark problem. Geometric EM with $\Delta t = 2^{-12}$ is the benchmark solution. Here, for the demonstration the convergence of the proposed method compared to the analytical rate, the simulation is done for 1s

4.4.2 Canonical oscillator: stochastic Duffing oscillator on S^2

Non-linear oscillators are widely studied for their ability to model complex physical phenomena and modern structures on the Euclidean space. On manifold, these oscillators are currently being investigated for modeling of satellite and drone trajectory [24, 67], control of artificial limbs and modeling of robots [68]. To this end, this section provides the geometrically accurate solution of a Duffing oscillator on a sphere to prove the efficacy of the proposed algorithm. Literature [53] has provided the basis of extension of the known potential function to the Riemannian manifold by extending the Euclidean distance to the Riemannian distance function. This idea elegantly extends the concept of defining canonical oscillator (well defined on Euclidean space) on the Riemannian manifold. For this, the Riemannian distance function defined by $\mathfrak{m}(a,b) = \|\log_a(b)\|_a$ is the distance between two points

a and b on Riemannian manifold, where log is the manifold logarithm. For the undertaken Duffing oscillator under the excitation of a white Gaussian process $\dot{\mathrm{W}}$ and evolving on a Riemannian manifold S^2 the kinetic and potential energies are given as,

$$K = \frac{1}{2}\langle \omega, \omega \rangle, \quad V = \frac{1}{2}\mathfrak{m}^2\left(p, r\right) + \frac{1}{4}\mathfrak{m}^4\left(p, r\right) \tag{4.47}$$

After defining Lagrangian function through energies of the oscillator and using the theory of stochastic variational principle, equation of motion for the undertaken system can be defined as,

$$\dot{\omega} = \gamma\left(p \times \left[1 + \alpha\mathfrak{m}\left(p, r\right)\right] \log_p\left(r\right)\right) - \eta\langle \omega, \omega \rangle^{(\nu-1)}\left(\omega \times p\right) + F cos\left(\zeta t\right) + \beta\dot{\mathrm{W}} \tag{4.48}$$

where, $(p, \omega) \in \mathrm{S}^2 \times \mathrm{T}_p\mathrm{S}^2$ are the manifold valued state variables, and the kinematic equations is given by $\dot{p} = \omega \times p$. $\eta = 0.5 \in \mathbb{R}$ is the damping coefficient, $\nu = 1.3 \in \mathbb{R}$ is the damping degree, $\alpha = 0.5 \in \mathbb{R}$ is the coefficient of non-linearity and $r = [1, 0, 0] \in \mathrm{S}^2$ denotes the reference point. The harmonic excitation $F cos\left(\zeta t\right)$ has the amplitude $F = 0.2$ and the forcing frequency $\zeta = 1$. For the numerical simulation on a unit hypersphere S^2 equipped with the canonical metric $\langle x, y \rangle = x^T y$, the following results [53] are used: $\mathfrak{m}^2\left(p, r\right) = \cos^{-1}\left(p^T r\right)$, $\log_p\left(r\right) = \left(\mathrm{I}_{3\times 3} - pp^T\right) r \left(\frac{\mathfrak{m}(p,r)}{\sin(\mathfrak{m}(p,r))}\right)$. For the simulation, initial position and angular velocity are taken as $[1\ 0\ 0]^T$ and $[0\ 0.5\ 0]^T$, respectively. The results for the undertaken system is provided in Fig. 4.7. From Fig. 4.5(a) the necessity of the geometric numerical integration scheme is assessed, where, it can be observed that the solution from non-geometric scheme drifts off from the manifold. The geometric constraints $\langle p, p \rangle - 1 \in \mathrm{S}^2$ of the order 10^{-15} and $\langle p, \omega \rangle \in \mathrm{T}_p\mathrm{S}^2$ of order 10^{-15} can be observed for the proposed scheme in Fig. 4.5(b), which shows the geometric preserving ability of the proposed framework.

In the field of dynamical systems, the response basin probability is a measure of the likelihood that a system will respond to a specific input or initial condition by reaching a particular attractor or equilibrium state. This concept is particularly important in the study of complex systems such as chaotic systems and networks, where the response of the system to different inputs or initial conditions can be highly sensitive and nonlinear. Overall, the response basin probability is considered an important metric for understanding the behavior of complex systems, and the literature [69, 70] has highlighted its significance in various applications. As depicted in Fig. 4.6, the probability density function (PDF) of the response basin is presented, and it is apparent that the PDF for a white noise intensity of 0.01 (Fig. 4.6(a)) displays a mixture of bivariate Gaussian distributions. With an increase in the white noise

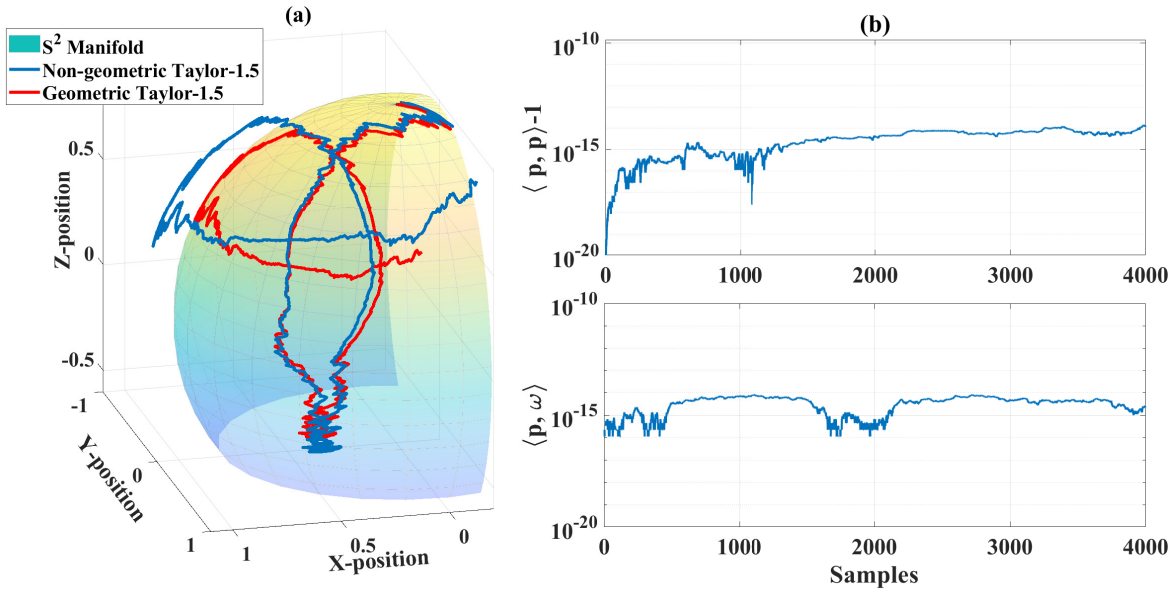

FIGURE 4.5: (a) Assessment of geometric preservation through non-geometric and proposed scheme, and (b) geometric constraints on S^2 and T_pS^2 for Duffing oscillator on S^2

intensity (Fig. 4.6(b)), the distribution tends to exhibit a single bivariate Gaussian distribution.

4.4.3 Kuramoto oscillator

Kuramoto oscillator has been a very successful model in simulating and explaining various synchronization phenomenon in neuroscience, flame dynamics, robotics and chemical systems. Literature [71] provides the original Kuramoto model as,

$$\dot{\theta}_i = \omega_i + \mathrm{k} \sum_{l=1}^{n} \sin\left(\theta_l - \theta_i\right), \quad \forall\, i = 1, 2, \ldots, m \tag{4.49}$$

where, for phase θ_i for agent i, the associated natural frequency is ω_i and k is the normalized coupling gain for m number of oscillators. As the pioneering results of the Kuramoto model on a unit circle are interesting, several researchers have tried to generalize the dynamic behaviour of the oscillator to quadratic hypersurface [72]. Particularly, a system of particle moving on S^2 has been used to model the 3 dimensional orientation of swarm of drones. The generalized form of the Kuramoto model constrained on a unit sphere in the literature [72] is given as,

$$\dot{x}_i = \Omega_i x_i + a_i x_i - \left(a_i x_i \cdot x_i\right) x_i \tag{4.50}$$

where, $x_i \in \mathrm{S}^d \subset \mathbb{R}^{d+1}$ is the state vector associated with the d-sphere and a_i are real constants. Ω_i is an antisymmetric matrix and is analogues to the intrinsic frequency ω_i of the original Kuramoto model. Ω_i

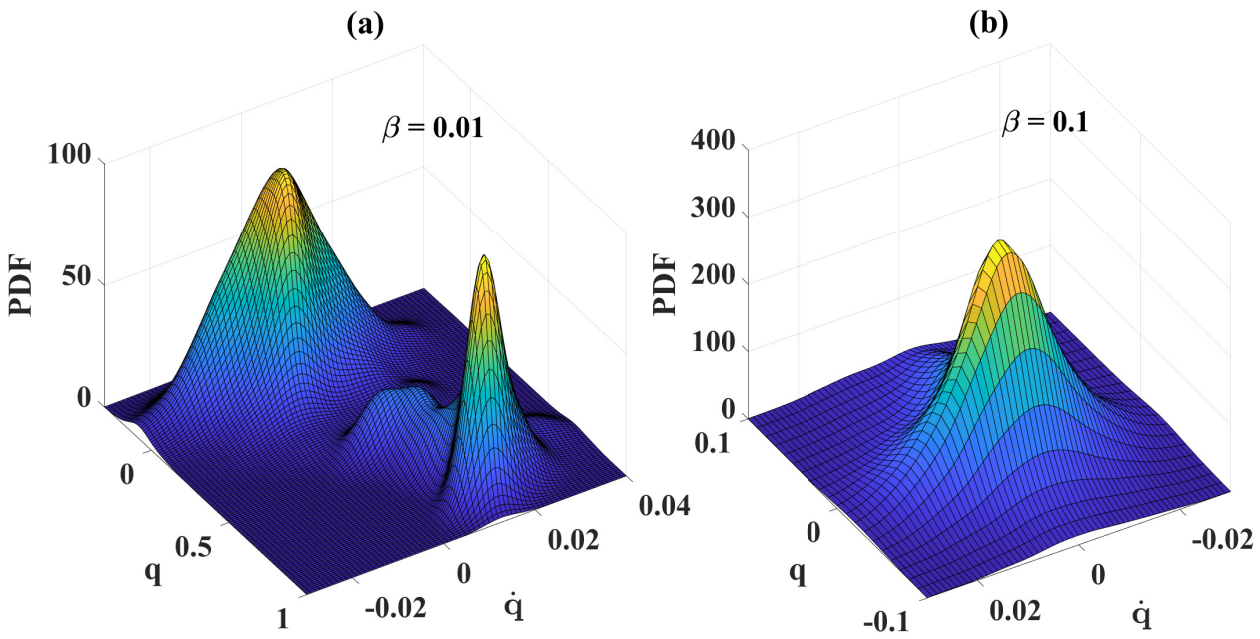

FIGURE 4.6: response basin probability density function for Duffing oscillator on S^2 with white noise intensity (a) $\beta = 0.01$, and (b) $\beta = 0.1$

is higher-dimensional in nature and for $n = 2$ is represented as $\Omega_i = \omega_i[1\ 1\ 1]^\Lambda$. Eq. (4.50) represents the generalized Kuramoto model on N-fold d-sphere manifold $\left(S^d\right)^N$. For the present study $d = 2$ and $N = 1$ is considered and the modified Kuromoto model with its state evolving on S^2 can be written as,

$$\dot{x} = \left(\Omega + a\left(1 - x^T x\right)\right) x \tag{4.51}$$

The stochastic counterpart of the modified Kuramoto model in Eq. (4.51) can be expressed in the form of an SDE as,

$$\dot{x} = \left(\Omega + a\left(1 - x^T x\right)\right) x + \sigma_r\left(x\right) x\, \dot{W}_r \tag{4.52}$$

where, $x_i \in S^2 \subset \mathbb{R}^3$ is the state vector associated with the 2-sphere and a_i are real constants. $\mathbf{\Omega}_i$ is a skew-symmetric matrix given by, $\mathbf{\Omega}_i = [0.5\ 0.8\ 0.3]^\Lambda$ and $\sigma_1(x) = [2.5\ 0.5\ 2.9]^\Lambda x$. The SDE in Eq. (4.52) on S^2 is analogues to the SDE in Eq. (4.14) and can be solved using the proposed geometric Ito-Taylor–1.5 strong algorithm. As this SDE can not be solved directly on the manifold, another SDE of the form Eq. (4.16) on the lie algebra of the undertaken configuration manifold is assumed, where, its drift and diffusion coefficients α and β_r, respectively, can be expressed as,

$$\begin{aligned} \boldsymbol{\alpha} &= \mathrm{dexp}^{-1}_{\boldsymbol{\mathcal{T}}}\left(\Omega + a\left(1 - x^T x\right)\right) - \frac{1}{2}\mathrm{dexp}^{-1}_{\boldsymbol{\mathcal{T}}}\left(\boldsymbol{\sigma}_r^2\right) - \frac{1}{2}\mathrm{dexp}^{-1}_{\boldsymbol{\mathcal{T}}}\left(\mathcal{M}_r\right) \\ \boldsymbol{\beta}_r &= \mathrm{dexp}^{-1}_{\boldsymbol{\mathcal{T}}}\left(\boldsymbol{\sigma}_r\right) \end{aligned} \tag{4.53}$$

where, $\mathcal{M}_r$ can be obtained from Eq. (4.31). Having obtained the drift and diffusion coefficients of the SDE on lie algebra, it can be solved using the proposed algorithm as in Eq. (4.26) and Eq. (4.27).

4.4.4 Pendulum Cart system

The dynamics of a spherical pendulum under constant gravitational force, attached to the center of mass of a cart that translates on a frictionless horizontal plane is considered. The spherical pendulum is assumed to be composed of a thin massless rigid rod, whose outboard end has a concentrated mass and the other end is attached to the cart through a spherical joint or pivot. The cart is modeled as a spring-mass-dashpot system. The system configuration is provided in Fig. 4.7 (a). The mass of the cart and the pendulum is considered to be M and m respectively with the length of the pendulum defined as l. The stiffness for the cart is denoted by k and c is the damping coefficient of the dashpot. Accordingly, the configuration of the underlying system is described by $(q, x) \in \mathrm{S}^2 \times \mathbb{R}^2$, such that the dynamics lies on the manifold given by $\mathrm{S}^2 \times \mathbb{R}^2$. Since the position of the center of mass of the cart is given

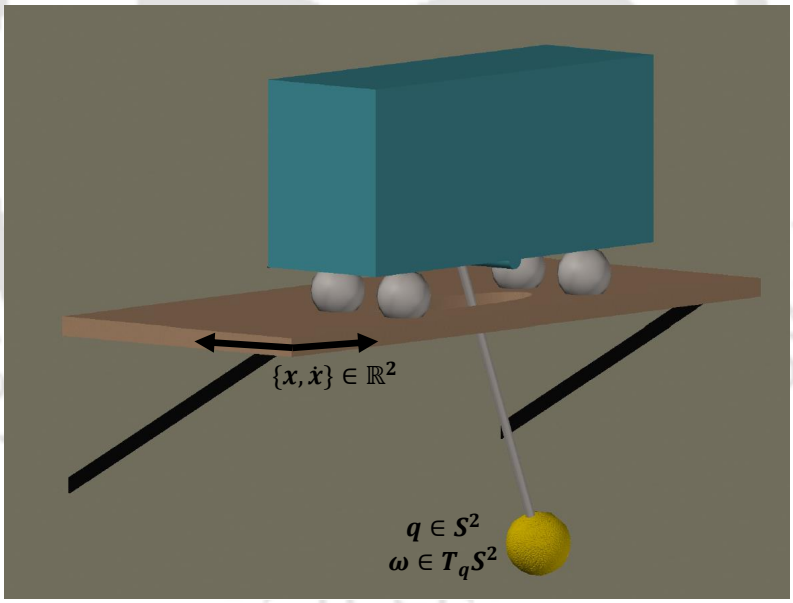

FIGURE 4.7: Schematic representation of Pendulum cart system with the position and angular velocity of pendulum w.r.t inertial frame on $q \in \mathrm{S}^2$ and $\omega \in \mathrm{T}_q\mathrm{S}^2$, states of cart on $x, \dot{x} \in \mathbb{R}^2$.

by, $x \in \mathbb{R}^2$, its location in the inertial frame is obtained by a 3×2 matrix $\mathbf{C}$, such that $\mathbf{C}x \in \mathbb{R}^3$. The matrix $\mathbf{C}$ is given as,

$$\mathbf{C} = \begin{bmatrix} 1 & 0 \\ 0 & 1 \\ 0 & 0 \end{bmatrix} \tag{4.54}$$

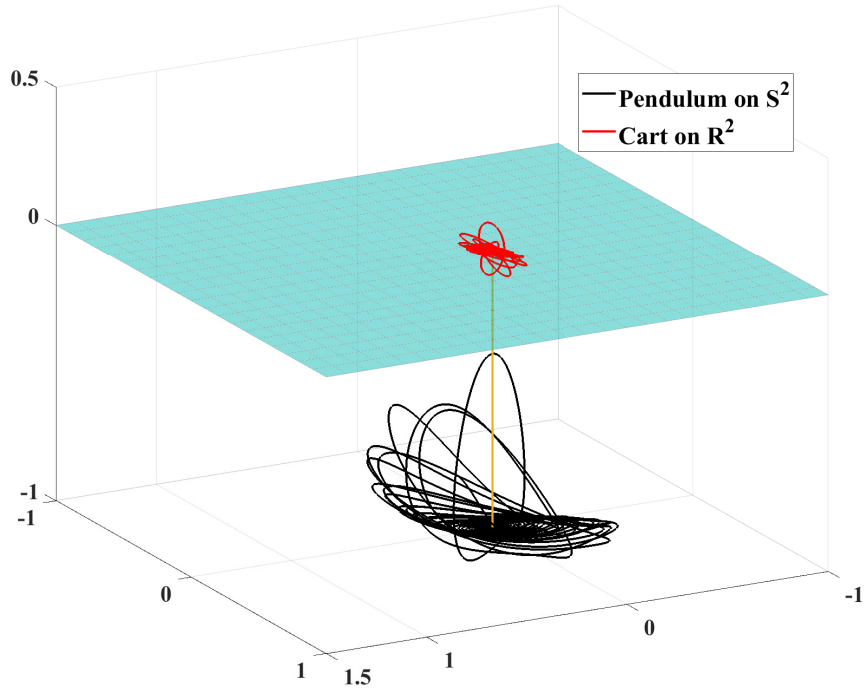

FIGURE 4.8: Trajectory of the cart in $\mathbb{R}^2$ and pendulum in S^2 with the initial conditions $x(0) = [0, 0], \dot{x} = [0, 0], q = [0, 0, -1], \omega = [0.2, 0.3, 0.5]$.

Following a similar approach, the center of mass of the the spherical pendulum mass can be projected onto the inertial frame using the following expression:

$$x_l = \mathbf{C}x + lq \tag{4.55}$$

where, $x_l \in \mathbb{R}^3$. The total kinetic energy of the undertaken system on the inertial frame can be defined as,

$$T(q, x, \dot{q}, \dot{x}) = \frac{1}{2} M_c \|\dot{x}\|^2 + \frac{1}{2} m \|\dot{x}_l\|^2 \tag{4.56}$$

where, the first term on the right hand side of Eq. (4.56) is the kinetic energy of the cart and the second term denotes the kinetic energy of the mass element defining the spherical pendulum. Incorporating Eq. (4.55) in the above equation leads to,

$$T(q, x, \dot{q}, \dot{x}) = \frac{1}{2}(M_c + m)\|\dot{x}\|^2 + \frac{1}{2} m l \dot{x}^T \mathbf{C}^T \dot{q} + \frac{1}{2} m l \dot{q}^T \mathbf{C} \dot{x} + \frac{1}{2} m l^2 \|\dot{q}\|^2 \tag{4.57}$$

The potential energy of the system is comprised of the potential energy of the undertaken spherical pendulum due to gravity, as well as the potential energy of the spring element of the cart. This is expressed as:

$$U(q, x) = mgle_3^T q + \frac{1}{2} k \|x\|^2 \tag{4.58}$$

Here, e_3 is the standard basis vector in $\mathbb{R}^3$. Finally, the Lagrangian function defined on $\mathrm{L} : \mathrm{T}_q\mathrm{S}^2 \times \mathbb{R}^2 \rightarrow \mathbb{R}^1$ is written as,

$$\mathrm{L}(q, x, \dot{q}, \dot{x}) = \frac{1}{2}(M_c + m)\langle \dot{x}, \dot{x} \rangle + ml\dot{x}^T \mathbf{C}^T \dot{q} + \frac{1}{2} ml^2 \langle \dot{q}, \dot{q} \rangle - mgle_3^T q - \frac{1}{2} k \langle x, x \rangle \tag{4.59}$$

As $\dot{q} = \omega \times q$, the modified Lagrangian function can be expressed using the wedge operator as,

$$\hat{\mathrm{L}}(q, x, \omega, \dot{x}) = \frac{1}{2}(M_c + m)\langle \dot{x}, \dot{x} \rangle - ml\dot{x}^T \mathbf{C}^T q^{\Lambda} \omega + \frac{1}{2} ml^2 \langle \omega, \omega \rangle - mgle_3^T q - \frac{1}{2} k \langle x, x \rangle \tag{4.60}$$

where, the system properties for simulation are provided in Table 4.1. $\mathbf{C}$ given by Eq. (4.54), is a transition matrix required to maintain the associativity between the variables q and x in the inertial frame. Considering two additional variables p and π representing conjugate of $\dot{x}$ and ω, respectively, the Hamiltonian for (x, q, p, π) is written as,

$$\mathrm{H} = \langle p, \dot{x}\,(p) \rangle + \langle \pi, \omega\,(\pi) \rangle - \hat{\mathrm{L}}(x, \dot{x}\,(p), p, \omega\,(\pi)) \tag{4.61}$$

where, $\dot{x}\,(p)$ and $\omega\,(\pi)$ can be obtained through Legendre transformation. Using Eq. (5.58), the equations of motion in $\mathbb{R}^2$ and $\mathrm{S}^2$are formulated based on Eqs. (2.13) and (4.13), respectively. The equation of motion can be represented in matrix form as,

$$\mathrm{d}\underbrace{\begin{bmatrix} \hat{\mathbf{p}} \\ \hat{\boldsymbol{\omega}} \\ x_c \\ \dot{x}_c \end{bmatrix}}_{\tau} = \underbrace{\begin{bmatrix} \omega^{\Lambda} \\ -\left(A_{11}\left(mglp \times r\right) + A_{12}\left(ml\left(\omega^{\Lambda}\right)^2 p + C\dot{x}_c + Kx_c\right)\right)^{\Lambda} \\ \dot{x}_c \\ -A_{21}\left(mglp \times r\right) - A_{22}\left(ml\left(\omega^{\Lambda}\right)^2 p + C\dot{x}_c + Kx_c\right) \end{bmatrix}}_{\gamma} \mathrm{d}t + \underbrace{\begin{bmatrix} 0 \\ \left(A_{11}p \times \beta_1\right)\mathrm{d}B_1 + \left(A_{12}\beta_2\right)\mathrm{d}B_2 \\ 0 \\ \left(A_{21}p \times \beta_1\right)\mathrm{d}B_1 + \left(A_{22}\beta_2\right)\mathrm{d}B_2 + \sigma \mathrm{d}B_3 \end{bmatrix}}_{\boldsymbol{\delta}_r \ \mathrm{dB}_r} \tag{4.62}$$

where, $\begin{bmatrix} (A_{11})_{3\times3} & (A_{12})_{3\times2} \\ (A_{21})_{2\times3} & (A_{22})_{2\times2} \end{bmatrix} = \begin{bmatrix} ml^2 I_3 & mlp^{\Lambda} \\ -mlp^{\Lambda} & (M+m) \end{bmatrix}^{-1}$.

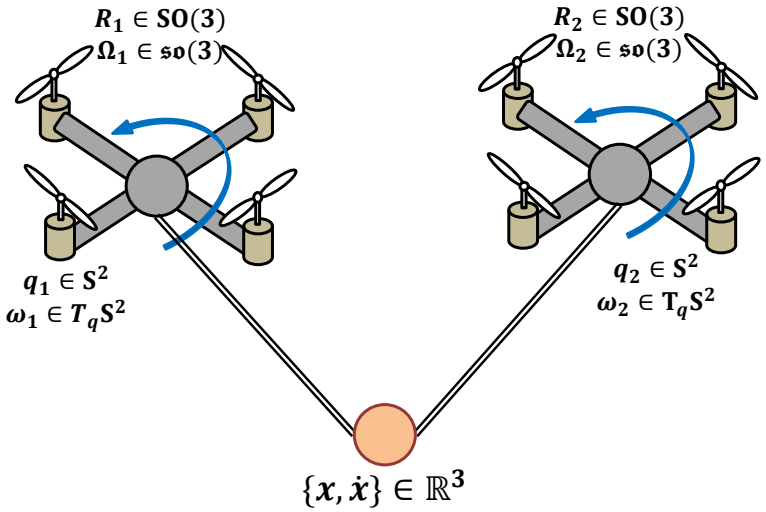

FIGURE 4.9: Schematic representation of quadrotors transporting a mass point with the position and angular velocity of the quadrotors w.r.t inertial frame on $q \in S^2$ and $\omega \in T_qS^2$, respectively, rotation and angular velocity w.r.t. body frame on $\mathbf{R} \in SO(3)$ and $\Omega \in \mathfrak{so}(3)$, states of mass point on $x, \dot{x} \in \mathbb{R}^3$.

TABLE 4.1: System parameters for the Pendulum-Cart system and Quadrotors transporting a mass point

Pendulum-Cart system		Quadrotors transporting mass point	
Pendulum on S^2		Mass of Q-1 (m_1)	0.755 kg
Mass (m)	$0.09M_c$ kg	Mass of Q-2 (m_2)	
Length (m)	1 m	Inertia matrix $\mathbf{J}_1 = \mathbf{J}_2$	diag $[j_1\ j_2\ j_3]$
Cart on $\mathbb{R}^2$			$j_1 = 0.0820, j_2 = 0.0845, j_3 = 0.1377$ kg-m^2
Mass (M_c)	15 kg	Length of Q-1 (l_1)	0.6 m
Stiffness (k)	50 N/m	Length of Q-2 (l_2)	0.8 m
Damping (c)	5 Ns/m	mass of point (m_p)	0.4 kg

4.4.5 Dynamics of two quadrotors transporting a mass point

A multibody system comprising of two quad rotors transporting a mass point suspended on a cable as shown in the Fig. 4.9 is discussed here [9, 24]. The two cables attached with the mass are considered to be massless rigid links. The orientation of the inertial frame along with the schematic representation of the multibody system is shown in Fig. 4.9. The masses of the transported mass point and the quad rotors are considered to be m_p, m_1 and m_2 respectively with $\mathbf{J}_1, \mathbf{J}_2 \in \mathbb{R}^{3\times3}$ being the inertia matrices of the quad rotors. The position of the mass point is denoted by $x_p \in \mathbb{R}^3$ and the center of mass of the quad rotors with respect to the inertial frame are designated as, $x_1, x_2 \in \mathbb{R}^3$. The lengths of the rigid links are considered to be L_1, L_2. Since the motion of the cables is in S^2, therefore, the direction of the links connecting the center of mass of the quad rotors to the mass point is $q_1, q_2 \in \left(S^2\right)^2$. Further, the attitude matrices of the quad rotors are described by $\mathbf{R}_1, \mathbf{R}_2 \in (SO(3))^2$. Accordingly, the

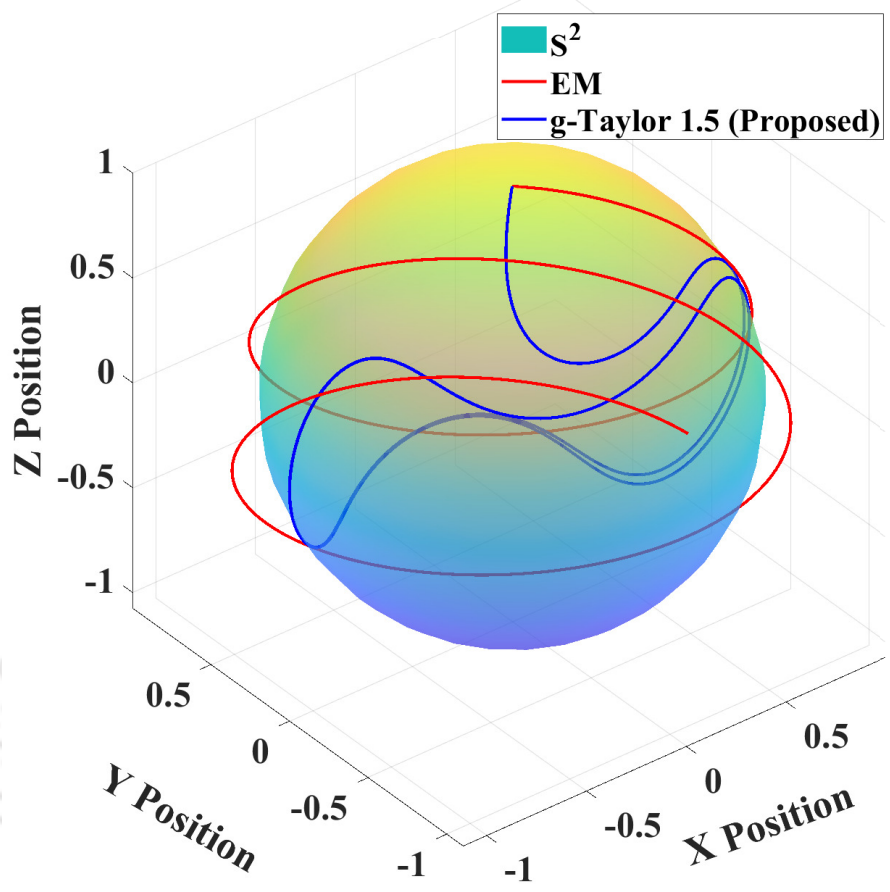

FIGURE 4.10: Measure of geometry preservation through the response trajectory of Kuramoto oscillator in time interval $T = [0, 5]$ with initial condition $x(0) = [0, 1]$ for non-geometric EM and g-Taylor 1.5 scheme.

dynamics of the quad rotors transporting a mass point can be defined on the configuration manifold, $\mathbb{R}^3 \times \left(\mathrm{S}^2 \times (\mathrm{SO}(3))^2\right)^2$. For the underlying system, the kinematic equations are given as,

$$\begin{aligned} \dot{q}_i &= \hat{\omega}_i q_i \qquad \text{and} \quad \dot{\mathbf{R}}_i = \mathbf{R}_i \hat{\Omega}_i, \qquad i = 1, 2 \\ &= S(\omega_i)\, q_i \qquad\qquad = \mathbf{R}_i S(\Omega_i) \end{aligned} \tag{4.63}$$

where, $\omega_i \in \mathrm{T}_{q_i}\mathrm{S}^2, i = 1, 2$ is angular velocity of i^{th} connecting cable such that $q_i \cdot \omega_i = 0$ and $\Omega_i \in \mathrm{T}_{\mathbf{R}_i}\mathrm{SO}(3), i = 1, 2$ is angular velocity of i^{th} quadrotor in connection with its body-fixed frame. The center of mass position of the quad rotors in the inertial frame can be expressed as $x_i = x_p - L_i q_i$ for $i = 1, 2$. Therefore, the translational velocity vector is obtained as,

$$\begin{aligned} \dot{x}_i &= \dot{x}_p - L_i \dot{q}_i \\ &= \dot{x}_p - L_i S(\omega_i)\, q_i \end{aligned} \tag{4.64}$$

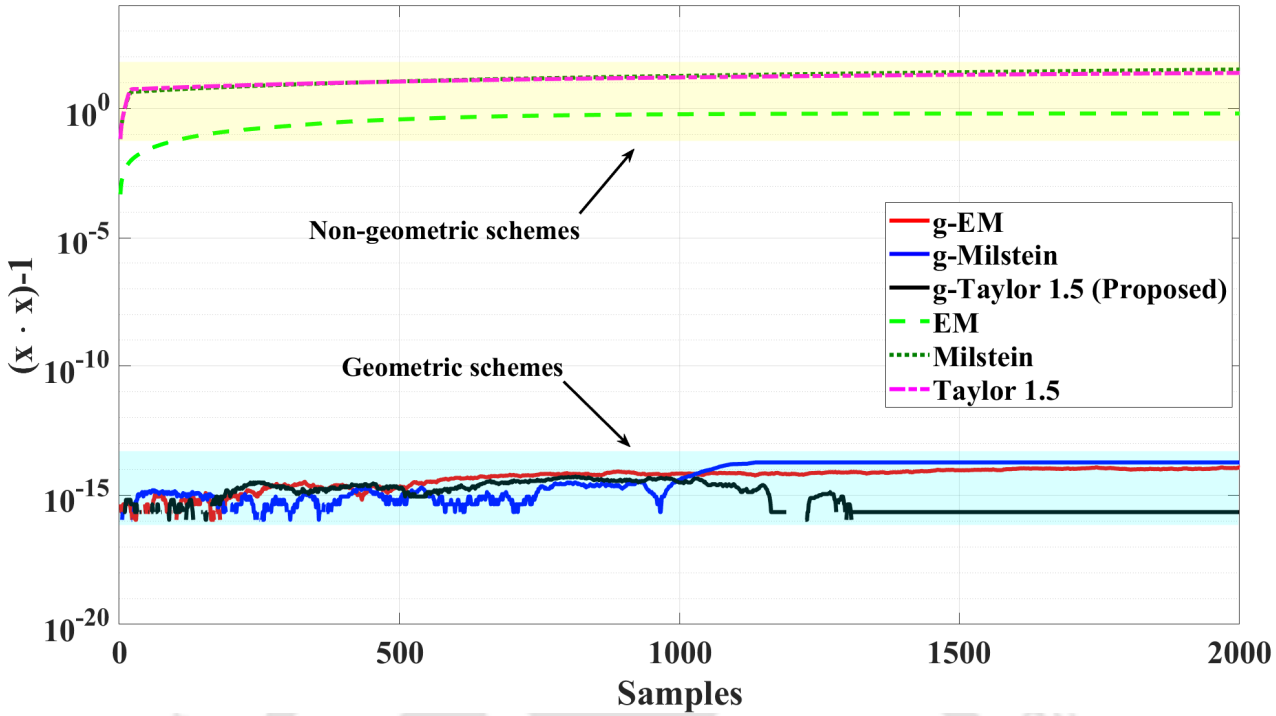

FIGURE 4.11: Geometric constraints of Kuramoto oscillator for different geometric and non-geometric algorithms for initial condition $x(0) = [0, 1]$.

Kinetic energy of the undertaken system is composed of the translational kinetic energy of the mass point and quadrotors, as well as the rotational kinetic energy of the quadrotors. The expression for the kinetic energy on the tangent bundle of the configuration manifold of the multibody system is given by:

$$\begin{aligned} \mathrm{T} &= \tfrac{1}{2}m_p\|\dot{x}_p\|^2 + \tfrac{1}{2}m_1\|\dot{x}_1\|^2 + \tfrac{1}{2}m_2\|\dot{x}_2\|^2 + \tfrac{1}{2}\Omega_1^T\mathbf{J}_1\Omega_1 + \tfrac{1}{2}\Omega_2^T\mathbf{J}_2\Omega_2 \\ &= \tfrac{1}{2}m_p\|\dot{x}_p\|^2 + \tfrac{1}{2}m_1\|\dot{x}_p - L_1S\left(\omega_1\right)q_1\|^2 + \tfrac{1}{2}m_2\|\dot{x}_p - L_2S\left(\omega_2\right)q_2\|^2 + \tfrac{1}{2}\Omega_1^T\mathbf{J}_1\Omega_1 + \tfrac{1}{2}\Omega_2^T\mathbf{J}_2\Omega_2 \end{aligned} \tag{4.65}$$

The quadrotors and the mass point are under the action of constant gravity. The potential energy is given as,

$$\begin{aligned} \mathrm{U} &= m_pge_3^Tx_p + m_1ge_3^Tx_1 + m_2ge_3^Tx_2 \\ &= m_pge_3^Tx_p + m_1ge_3^T\left(x_p - L_1q_1\right) + m_2ge_3^T\left(x_p - L_2q_2\right) \end{aligned} \tag{4.66}$$

Having obtained the kinetic energy and potential energy of the system, the modified Lagrangian defined on the tangent bundle, $\mathrm{T}\left(\mathbb{R}^3 \times \left(\mathrm{S}^2 \times \left(\mathrm{SO}\left(3\right)\right)^2\right)^2\right) \to \mathbb{R}^1$ as a function of the angular velocity can be

expressed as,

$$\begin{aligned}\hat{\mathrm{L}}\left(x_p, \dot{x}_p, \Omega_1, \Omega_2, q_1, \omega_1, q_2, \omega_2\right) &= \mathrm{T} - \mathrm{U} \\ &= \tfrac{1}{2} m_p \|\dot{x}_p\|^2 + \tfrac{1}{2} m_1 \|\dot{x}_p - L_1 S\left(\omega_1\right) q_1\|^2 + \tfrac{1}{2} m_2 \|\dot{x}_p - L_2 S\left(\omega_2\right) q_2\|^2 \\ &+ \tfrac{1}{2} \Omega_1^T \mathbf{J}_1 \Omega_1 + \tfrac{1}{2} \Omega_2^T \mathbf{J}_2 \Omega_2 - m_p g e_3^T x_p - m_1 g e_3^T \left(x_p - L_1 q_1\right) \\ &- m_2 g e_3^T \left(x_p - L_2 q_2\right)\end{aligned} \tag{4.67}$$

The system properties considered for simulation are given in Table 4.1. Since the motion of the

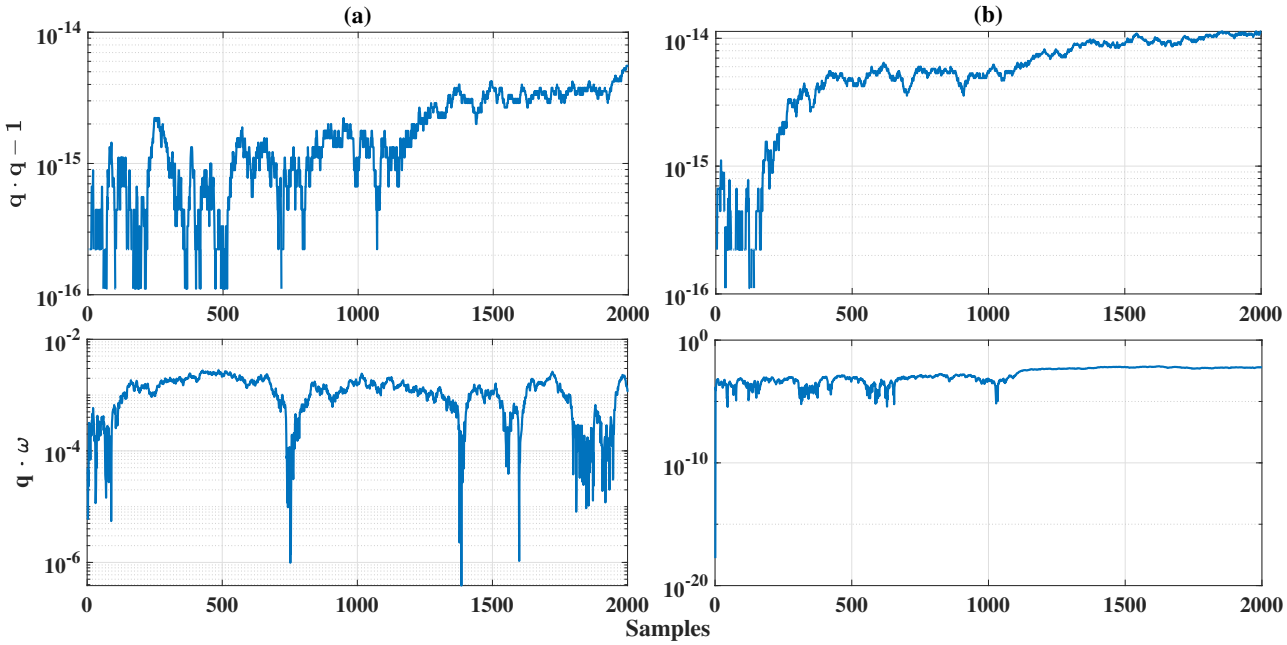

FIGURE 4.12: Geometric constraints for (a) pendulum (b) quadrotor in S^2 and $\mathrm{T}_q\mathrm{S}^2$ i.e. $(q \cdot q - 1)$ and $(q \cdot \omega)$, respectively. The initial conditions adopted are: Case (a) $x(0) = [0, 0], \dot{x} = [0, 0], q = [0, 0, -1], \omega = [0.2, 0.3, 0.5]$, and, Case (b) $x_p\left(0\right) = [1, 0, 0]^T$, $\mathbf{R}_1, \mathbf{R}_2 = \mathbf{I}$, $q_1\left(0\right) = [\sin 30°, 0, \cos 30°]^T$, $q_2\left(0\right) = [0, \sin 30°, \cos 30°]$.

cables is in S^2, therefore, the direction of the links connecting the center of mass of the quad rotors to the mass point is $q_1, q_2 \in \left(\mathrm{S}^2\right)^2$. Further, the attitude matrices of the quad rotors are described by $\mathbf{R}_1, \mathbf{R}_2 \in \left(\mathrm{SO}\left(3\right)\right)^2$. Accordingly, the dynamics of the quad rotors transporting a mass point can be defined on the configuration manifold, $\mathbb{R}^3 \times \left(\mathrm{S}^2 \times \left(\mathrm{SO}\left(3\right)\right)^2\right)^2$. The Lagrangian on the tangent bundle,

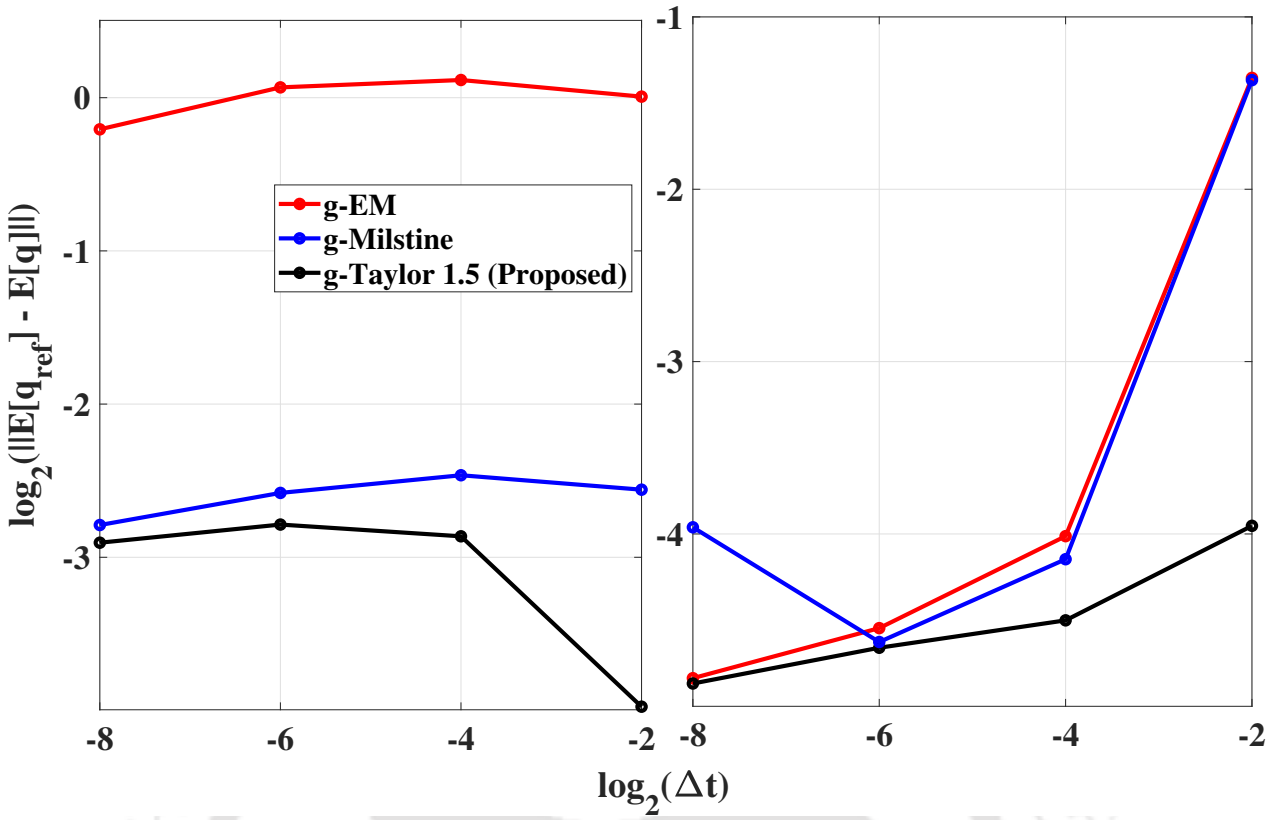

FIGURE 4.13: Comparison of the global error $\log_2\left(\max\left(E\left[q_{ref}\right]\right) - \max\left(E\left[q\right]\right)\right)$ for the proposed scheme in comparison with existing geometric EM [22] and geometric Milstein scheme for different time steps $\Delta t = 2^{-8}, 2^{-6}, 2^{-4}$ and 2^{-2} for (a) Kuramoto model and (b) pendulum cart system with initial conditions described in Figs. 4.10 and 4.12 respectively. Geometric EM with $\Delta t = 2^{-12}$ is the benchmark solution.

$\mathrm{T}\left(\mathbb{R}^3 \times \left(\mathrm{S}^2 \times \left(\mathrm{SO}\left(3\right)\right)^2\right)^2\right) \rightarrow \mathbb{R}^1$ for the states $\left(x_p, \dot{x}_p, \Omega_1, \Omega_2, q_1, \omega_1, q_2, \omega_2\right)$ is defined as,

$$\begin{aligned}\hat{\mathrm{L}} \;&= \tfrac{1}{2}m_p\|\dot{x}_p\|^2 + \tfrac{1}{2}m_1\|\dot{x}_p - L_1 S\left(\omega_1\right) q_1\|^2 \\ &+\tfrac{1}{2}m_2\|\dot{x}_p - L_2 S\left(\omega_2\right) q_2\|^2 + \tfrac{1}{2}\Omega_1^T \mathbf{J}_1 \Omega_1^T \\ &+\tfrac{1}{2}\Omega_2^T \mathbf{J}_2 \Omega_2^T - m_p g e_3^T x_p \\ &-m_1 \mathrm{g} e_3^T\left(x_p - L_1 q_1\right) - m_2 \mathrm{g} e_3^T\left(x_p - L_2 q_2\right)\end{aligned} \tag{4.68}$$

where, $\omega_i \in \mathrm{T}_{q_i}\mathrm{S}^2, i = 1, 2$ and $\Omega_i \in \mathrm{T}_{R_i}\mathrm{SO}\left(3\right), i = 1, 2$ are the angular velocities of the i^{th} cable $(q_i \cdot \omega_i = 0)$ and i^{th} quad rotor, respectively, with reference to its body-fixed frame. The Hamiltonian equation for the conjugate variables $\pi_1, \pi_2, \Pi_1, \Pi_2$ and p of, $\dot{x}_p$, Ω_1, Ω_2, ω_1 and ω_2, respectively can be written as,

$$\begin{aligned}\mathrm{H} =&\left\langle p, \dot{x}\left(p\right)\right\rangle + \left\langle \pi_1, \omega_1\left(\pi_1\right)\right\rangle + \left\langle \pi_2, \omega_2\left(\pi_2\right)\right\rangle \\ &+ \left\langle \Pi_1, \Omega_1\left(\Pi_1\right)\right\rangle + \left\langle \Pi_2, \Omega_2\left(\Pi\right)\right\rangle - \hat{\mathrm{L}}\end{aligned} \tag{4.69}$$

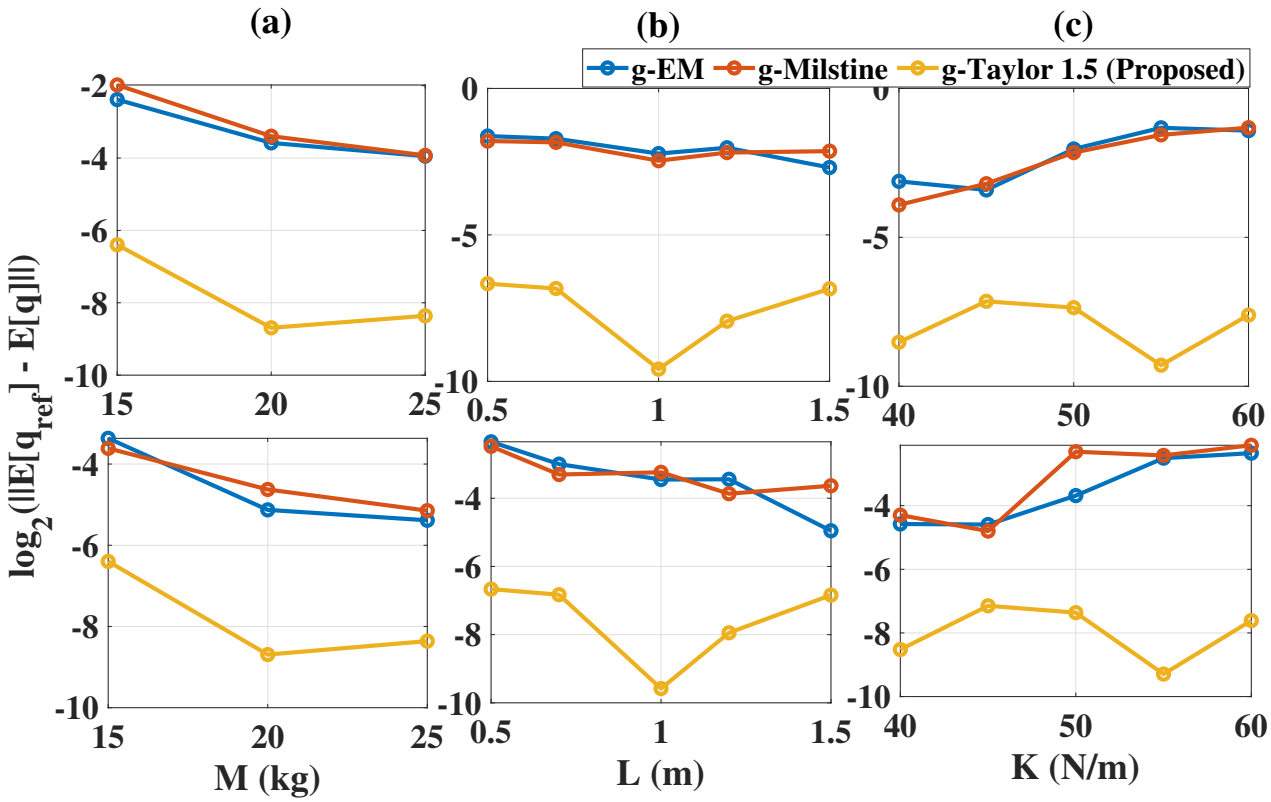

FIGURE 4.14: Comparison of the global error $\log_2(\max(E[q_{ref}]) - \max(E[q]))$ for the proposed scheme in comparison with existing geometric EM [22] and geometric Milstein for time steps $\Delta t = 2^{-2}$ for pendulum cart system with different parameter values.

The response trajectories are obtained by solving the geometric SDEs using the proposed geometric Taylor–1.5 framework. The results corresponding to the undertaken systems is described in the upcoming section.

4.5 Discussion of Results

The validation results for the geometry preservation are presented in Figs. 4.10, 4.11 and 4.12. Fig. 4.10 portrays the solution trajectory of the Kuramoto oscillator on the quadratic hyper-surface S^2 for geometry and non-geometry preserving schemes. The use of non-geometric integration schemes (EM) for geometric SDEs result in drifting off the solution from the manifold whereas the proposed scheme (g-Taylor 1.5) preserves the geometry of the solution on the manifold. Similar observations can be seen with other non-geometric schemes like Milstein and Taylor 1.5, the results of which are skipped here for brevity. Fig. 4.11 shows the error in the geometric constraints for different geometric (g-EM, g-Milstein and g-Taylor 1.5) and non-geometric stochastic integration schemes (EM, Milstein and Taylor 1.5). The error is significantly less for the geometric integration schemes as compared to

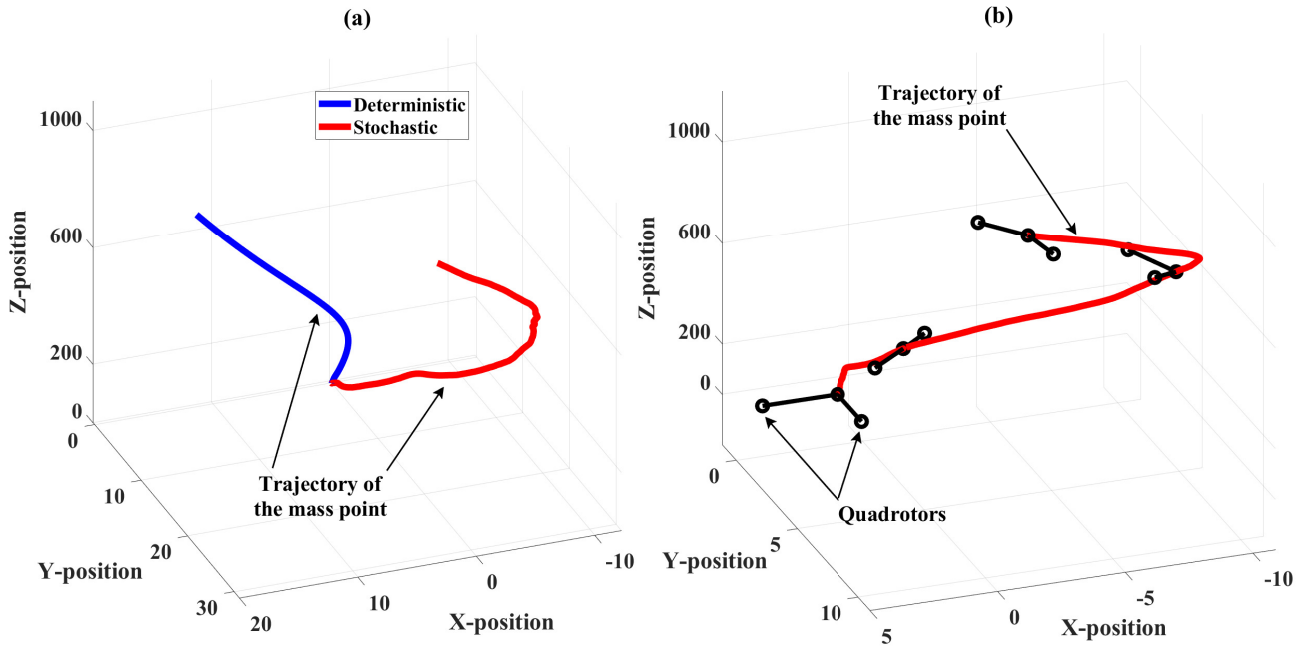

FIGURE 4.15: (a) Trajectory of the mass point under deterministic and stochastic cases. (b) Snapshot of the quadrotors transporting the point mass at every 500 samples. The initial conditions are: $x_p(0) = [1, 0, 0]^T$, $\mathbf{R}_1, \mathbf{R}_2 = \mathbb{I}$, $q_1(0) = [\sin 30°, 0, \cos 30°]^T$, $q_2(0) = [0, \sin 30°, \cos 30°]$.

the non-geometric schemes which results in drifting off the solution from the manifold. This clearly highlights the need for geometric stochastic integration schemes for geometric oscillators. For the sake of concision, the results obtained for the pendulum cart system and the quadrotors carrying a point mass are omitted, which exhibit similar characteristics as previously discussed.

The extent of geometry preservation can not be measured just by merely observing the solution trajectory, it requires tracking the geometric constrains as the system evolves with time. For both the pendulum cart system and quadrotors transporting a point mass with stochasticity, the error in geometric constraints for S^2 and T_qS^2 are of the order 10^{-14} and 10^{-4}, respectively as shown in Fig. 4.12. As opposed to the deterministic case [24], the consideration of stochastic nature of the system dynamics on the tangent space renders the error in the geometric constraint of T_qS^2 in the order of 10^{-4} which is rather significant as compared to the error in the geometric constraint of S^2 (which is in the order of 10^{-14}). The improvement on the order of error on T_qS^2 can be assessed by undertaking a detailed parametric study which is beyond the scope of this work. It is clearly observed that the proposed integration scheme provides accurate solution for coarser time step ($\Delta t = 2^{-4}$s), whereas, the g-EM scheme requires finer time step for accurate solution, thus resulting in increased computational cost.

After assessing the geometry preservation of the system solution on the manifold, the accuracy of the proposed algorithm for the Kuramoto oscillator and the pendulum cart system is compared with the existing geometric EM scheme [22] and g-Milstein scheme, where, the criteria for comparison is taken as the global error, $\epsilon = \log_2 (\max (E [q_{ref}]) - \max (E [q]))$ for different time steps $\Delta t = 2^{-8}, 2^{-6}, 2^{-4}$ and 2^{-2}s. The global error for existing g-EM [22] and g-Milstein in Fig 4.13 increases as Δt becomes coarser, resulting in decreased computational efficiency, whereas, the proposed geometric Taylor–1.5 scheme provides solution with relatively less error for both finer as well as coarser time steps. This is due to the incorporation of the Kolmogorov operators in the proposed scheme that relates the SDE on manifold to that on the Lie algebra, which are not accounted for in the g-EM and g-Milstein mapping.

To further demonstrate the efficiency of the proposed scheme, a comparative study for a range of system parameters for the pendulum cart system is undertaken in Fig. 4.14. The mass of the cart, length of the pendulum string and the stiffness of the cart are varied in the range of $[15 - 25]$kg, $[0.5 - 1.5]$m and $[40 - 60]$N/m respectively. It is observed that irrespective of the range of system parameters considered, error corresponding to the proposed scheme is significantly lesser than g-EM and g-Milstein. Figs. 4.8 and 4.15 demonstrate the motion trajectories of the the pendulum cart system and quadrotors transporting a point mass with stochasticity in their both position and momentum. Fig. 4.15(a) portrays the difference in the trajectory of the mass point transported by two quadrotors with stochasticity in its states, with reference to the deterministic case. The trajectory of the point mass for the stochastic case with the snapshot of the quadrotors at every 2000 samples is shown in Fig. 4.15(b). From the presented results, it is evident that the proposed algorithm preserves geometry of the system trajectories and provides accurate solution for coarser time step with reference to the geometric Ito-Taylor based Euler Maruyama and Milstein scheme, thus resulting in increased computational efficiency. The Matlab codes for the simulation of the numerical illustrations can be found in the link: Source Codes:(https://github.com/SDaGLab/Geometric-Taylor-1.5).

4.6 Research Findings

The outcomes of this chapter can be summarized as follows:

- Novel Approach for Stochastic Hamiltonian Systems: The research introduces an innovative

approach to analyze stochastic Hamiltonian systems on smooth manifolds, employing geometry-preserving higher-order stochastic integration techniques.

- Stochastic Hamiltonian Canonical Equations: The study develops stochastic Hamiltonian canonical equations for physical systems operating on the manifold $\left(\mathrm{S}^2\right)^n$, followed by the solution of geometric Stochastic Differential Equations (SDEs) on the Lie algebra using an Ito-Taylor expansion-based numerical integration scheme.
- Formulation of Kolmogorov Operators: A novel formulation of Kolmogorov operators for the geometric SDEs is presented, extending the understanding beyond its Euclidean counterpart. This formulation sheds light on the geometric relationship between the configuration manifold and its Lie algebra.
- Benchmark and Concrete Examples: The research extends benchmark case studies and three specific examples, originally known for their deterministic Hamiltonian dynamics on differentiable manifolds, to the stochastic domain.
- Accuracy Assessment: The accuracy of the proposed integration scheme is assessed by comparing global errors for various time step values ranging from $\Delta t = [2^{-8}, 2^{-2}]$.
- Reduction in Global Error: Notably, a significant reduction in global error is observed for a coarser time step of $\Delta t = 2^{-2}$s when using the proposed method, compared to the existing g-EM method, demonstrating a 90% reduction for the stochastic Kuramoto model and an 80% reduction for the pendulum cart system. This reduction translates into reduced computational costs.

The current chapter's development of stochastic Hamiltonian dynamics and geometry-preserving numerical integration schemes on manifold S^2 paves the way for a seamless transition into the next chapter's exploration of Stochastic Hamiltonian Differential Equations (SHDE) and the essential focus on achieving symplectic preservation of the proposed geometric Ito-Taylor scheme. While the present work fills gaps in stochastic Hamiltonian formulation and their solution, the upcoming chapter addresses the symplectic nature of these solutions, providing innovative numerical techniques to overcome their inherent limitations of long term simulation. This connection ensures a continuous progression from theoretical developments to real-world applicability, enhancing the understanding and capabilities in the field of manifold-based systems.

Chapter 5

Symplectic numerical integration scheme on $(S^2)^n$

Stochastic Hamiltonian Differential Equations (SHDE) have emerged as a powerful framework for modeling complex natural phenomena, offering insights into stochasticity and Hamiltonian mechanics [2, 8, 9, 10, 7]. They enhance our understanding of intricate dynamics in various fields and improve prediction accuracy [73, 74, 6]. However, existing models require advanced numerical techniques to address non-linearity [14, 21], stochasticity[22, 20] and geometry [10, 23, 24], and they often face limitations in long-duration simulations due to their non-symplectic nature [6]. Symplectic integration schemes are crucial for preserving phase space integrity in various scientific and engineering applications. There are many symplectic integration schemes which preserves the geometry of the Hamiltonian for a stochastic system [75, 76, 77, 78, 79, 80, 81], however, there is a dearth of literature in the domain of symplectic integration schemes for the stochastic Hamiltonian systems whose response evolves on geometrical spaces or manifolds. The main novelty in this chapter lies in the multistepping approach, which facilitates the preservation of symplecticity within the geometric Ito-Taylor 1.0 strong scheme and proposing a practical "weak symplectic condition" for complex systems. The scheme's effectiveness is demonstrated through simulations of physical systems, showcasing its versatility and broad applicability.

5.1 Motivations

- Stochastic Hamiltonian Differential Equations (SHDE) offer a powerful framework for modeling complex natural phenomena, combining stochasticity and Hamiltonian mechanics. This approach enhances our understanding of intricate dynamics in fields like statistical physics, fluid dynamics, and celestial mechanics while improving prediction accuracy and insightful analysis.

- Existing models addressing these properties require advanced numerical techniques due to the complex, long-duration dynamics, non-linearity, stochasticity, and geometry involved. Recent numerical techniques consider geometric aspects and stochasticity but have limitations for long-duration simulations due to their non-symplectic nature.
- Symplectic integration schemes are crucial in various scientific and engineering applications, ensuring the preservation of important phase space properties. However, existing methods may lead to discrepancies and inaccuracies over extended simulation periods.

5.2 Mathematical background for rotational group $SO(3)$ and 2-sphere (S^2)

The current study initiates by laying down the essential mathematical groundwork encompassing the rotational group $SO(3)$ and the 2-sphere (S^2) [9]. This foundational exploration forms the basis for the subsequent discussions in this section. The group $\mathrm{SO}(3)$, also known as the rotation group in three dimensions, possesses a well-defined group structure. This structure involves matrix multiplication as the group operation and is characterized by a dimension of three. The elements of $\mathrm{SO}(3)$, denoted by R, satisfy the following conditions:

$$R^T R = R R^T = I_{3\times 3} \quad \text{and} \quad \det(R) = +1. \tag{5.1}$$

Here, $I_{3\times 3}$ is the identity matrix of size 3×3. Each element R belonging to $\mathrm{SO}(3)$ adheres to these conditions. The tangent space of $\mathrm{SO}(3)$ at a particular point R, denoted by $\mathrm{T}R\mathrm{SO}(3)$, is the set comprising all tangent matrices associated with $\mathrm{SO}(3)$ at the point R. Mathematically, this is expressed as:

$$\mathrm{T}_R\mathrm{SO}(3) = \left\{ R\,\mathfrak{p} \in \mathbb{R}^{3\times 3} : \mathfrak{p} \in \mathfrak{so}(3) \right\} \tag{5.2}$$

where $\mathfrak{p}$ is an element of the Lie algebra $\mathfrak{so}(3)$, the space of skew-symmetric 3×3 matrices. The tangent bundle of $\mathrm{SO}(3)$, denoted as $\mathrm{TSO}(3)$, is described as:

$$\mathrm{TSO}(3) = \left\{ (R, R\,\mathfrak{p}) \in \mathrm{SO}(3) \times \mathbb{R}^{3\times 3} : \mathfrak{p} \in \mathfrak{so}(3) \right\} \tag{5.3}$$

This tangent bundle contains pairs of the form $(R, R\mathfrak{p})$, where R is an element of $\mathrm{SO}(3)$ and $\mathfrak{p}$ is a corresponding tangent matrix from the Lie algebra $\mathfrak{so}(3)$. Transitioning to the concept of the two-sphere, it's essential to note that it is a manifold within $\mathbb{R}^3$, which is defined as follows:

$$\mathrm{S}^2 = \left\{ q \in \mathbb{R}^3 : |q| = 1 \right\}. \tag{5.4}$$

The Cartesian product of n spheres in $\mathbb{R}^3$, denoted as $(\mathrm{S}^2)^n = \mathrm{S}^2 \times \cdots \times \mathrm{S}^2$, encompasses all ordered n-tuples of vectors $q = (q_1, \ldots, q_n)$, where $q_i \in \mathrm{S}^2$ for $i = 1, \ldots, n$. Alternatively, this manifold can also be represented as:

$$\left(\mathrm{S}^2\right)^n = \left\{ q \in \mathbb{R}^{3n} : q_i \in \mathrm{S}^2, i = 1, \ldots, n \right\}. \tag{5.5}$$

The tangent space of $\left(\mathrm{S}^2\right)^n$ at the point $q \in \left(\mathrm{S}^2\right)^n$ is given by:

$$\mathrm{T}q \left(\mathrm{S}^2\right)^n = \left\{ (\eta_1, \ldots, \eta_n) \in \mathbb{R}^{3n} : (q_i \cdot \eta_i) = 0, i = 1, \ldots, n \right\}. \tag{5.6}$$

Here, each $\eta \in \mathrm{T}_q \left(\mathrm{S}^2\right)^n$ is recognized as a tangent vector to $\left(\mathrm{S}^2\right)^n$ at the point $q \in \left(\mathrm{S}^2\right)^n$. Furthermore, the tangent bundle of $\left(\mathrm{S}^2\right)^n$, denoted as $\mathrm{T}\left(\mathrm{S}^2\right)^n$, is defined by:

$$\mathrm{T}\left(\mathrm{S}^2\right)^n = \left\{ (q, \eta) \in \mathbb{R}^{3n} : q \in \left(\mathrm{S}^2\right)^n, \eta \in \mathrm{T}_q \left(\mathrm{S}^2\right)^n \right\}. \tag{5.7}$$

In this context, $\mathrm{T}\left(\mathrm{S}^2\right)^n$ represents the collection of pairs where each pair consists of a point q belonging to $\left(\mathrm{S}^2\right)^n$ and a corresponding tangent vector η from the tangent space $\mathrm{T}_q \left(\mathrm{S}^2\right)^n$. Transitioning from the foundational mathematical concepts of the rotational group $\mathrm{SO}(3)$ and the 2-sphere (S^2), the focus now shifts to exploring Stochastic Hamiltonian dynamics on the 2-sphere (S^2).

5.3 A brief background on SHDE

The concepts introduced in section 4.2.1 of Chapter 4 serve as the foundation for the ideas presented in this subsection. Although the variables are represented by different symbols, the formulations are same here and and the same is rewritten for the sake of completeness. In a typical Hamiltonian system evolving on the manifold S^2, the dynamics are governed by a Hamiltonian function H, which represents the total energy of the system. The evolution of the system follows deterministic trajectories determined by Hamilton's equations, which are derived from the Hamiltonian function [7, 9]. In contrast, a stochastic Hamiltonian differential equation (SHDE) introduces randomness by incorporating a stochasticity in

the form of a Stratonovich integral into the system. This stochastic term represents the effect of external forces or uncertainties, which leads to probabilistic trajectories, where the state of the system evolves stochastically over time. Towards this, consider Lagrangian L of a non-conservative system as a function of the position $q \in \mathrm{S}^2$ and the angular velocity $\omega \in \mathrm{T}_q\mathrm{S}^2$ of the system evolving on S^2, whose action integral can be written in the following form,

$$\mathbb{A} = \int_{t_0}^{t_f} \tilde{L}(q,\omega)\mathrm{dt} - \int_{t_0}^{t_f} \mathrm{F}(q,\omega) \circ \mathrm{dW}(t) \tag{5.8}$$

where, F is a function representing intensity of the stochastic excitation and $\circ$ denotes the Stratanovich integral [20]. The Lagrangian can be converted to Hamiltonian utilising the Legendre transformation, and the modified action integral is written as,

$$\mathbb{A} = \int_{t_0}^{t_f} \left(\pi \cdot \omega - \mathrm{H}(q,\pi)\right) dt - \int_{t_0}^{t_f} \mathrm{h}_1 \circ dW(t) \tag{5.9}$$

where, π is the conjugate of angular velocity. Taking variation of $\mathbb{A}$, the following equation is obtained.

$$\begin{aligned}\delta\mathbb{A} = &\int_{t_0}^{t_f} \left(\pi \cdot \delta\omega - \frac{\partial \mathrm{H}(q,\pi)}{\partial q} \cdot \delta q + \left(\omega - \frac{\partial \mathrm{H}(q,\pi)}{\partial \pi}\right) \cdot \delta\pi\right) dt \\ &- \int_{t_0}^{t_f} \left(\frac{\partial \mathrm{h}_1(q,\pi)}{\partial \pi}\delta\pi + \frac{\partial \mathrm{h}_1(q,\pi)}{\partial q}\delta q\right) \circ dW(t)\end{aligned} \tag{5.10}$$

After proper substitution and rearrangement the stochastic Hamiltonian equation on the configuration manifold S^2 can be written as,

$$\begin{aligned}\dot{q} =& q \times \omega \\ =& q \times \frac{\partial \mathrm{H}(q,\pi)}{\partial \pi} + q \times \frac{\partial \mathrm{h}_1(q,\pi)}{\partial \pi} \circ \dot{W}(t) \\ \dot{\pi} =& \left(\omega \times \pi - q \times \frac{\partial \mathrm{H}(q,\pi)}{\partial q}\right) - q \times \frac{\partial \mathrm{h}_1(q,\pi)}{\partial q} \circ \dot{W}(t) \\ =& \left(-q \times \frac{\partial \mathrm{H}(q,\pi)}{\partial q} + \frac{\partial \mathrm{H}(q,\pi)}{\partial \pi} \times \pi\right) - \left(q \times \frac{\partial \mathrm{h}_1(q,\pi)}{\partial q} + \frac{\partial \mathrm{h}_1(q,\pi)}{\partial \pi} \times \pi\right) \circ \dot{W}(t)\end{aligned} \tag{5.11}$$

The Stratonovich integral in Eq. (5.11) is then converted to Itô integral with the help of Wong-Zakai corrrection term, and, the final expression of SHDE is written as,

$$\begin{aligned}\mathrm{d}q &= \left(-q \times \frac{\partial \mathrm{H}}{\partial \pi} - \frac{1}{2}\frac{\partial \mathrm{h}_k}{\partial \pi} \times \left(q \times \frac{\partial \mathrm{h}_k}{\partial \pi}\right)\right) dt - q \times \frac{\partial \mathrm{h}_k}{\partial \pi} \mathrm{d}W_k(t) \\ \mathrm{d}\pi &= \left(-q \times \frac{\partial \mathrm{H}}{\partial q} + \frac{\partial \mathrm{H}}{\partial \pi} \times \pi + \frac{1}{2}\left(q \times \frac{\partial \mathrm{h}_k}{\partial \pi}\right) \times \frac{\partial \mathrm{h}_k}{\partial q}\right) dt - \left(q \times \frac{\partial \mathrm{h}_k}{\partial q} - \frac{\partial \mathrm{h}_k}{\partial \pi} \times \pi\right) \mathrm{d}W_k(t)\end{aligned} \tag{5.12}$$

The stochastic Hamiltonian differential equation (SHDE) not only allows for the study of dynamical systems under stochastic excitation but also serves as a foundation for verifying the symplecticity of numerical integration methods. In this context, the following section presents a novel symplectic numerical integration technique specifically designed for systems evolving on the manifold S^2.

5.4 Proposed methodology

This section presents a geometric approach for the development of an Itô-Taylor based symplectic numerical integration scheme of order 1.0 strong for the solution of the stochastically excited dynamical system. For assessing the symplectic nature of the proposed scheme, a weak symplectic criteria which work towards the partial fulfilment of the symplectic condition.

5.4.1 Symplectic Itô-Taylor scheme on $\left(\mathbf{S}^2\right)^n$

The concepts introduced in section 4.2.2 of Chapter 4 serve as the foundation for the ideas presented in this subsection. Although the variables are represented by different symbols, the formulations are same here and and the same is rewritten for the sake of completeness. Consider an SDE for a vector valued variable $q(t)$ which evolves on the configuration manifold $(S^2)^n$ as,

$$dq(t) = \mathbf{a}(q(t), t)q(t)\mathrm{dt} + \sum_r \sigma_r(q(t), t)q(t)\mathrm{dW}_t \tag{5.13}$$

where, $\mathbf{a}$ and σ_r are matrix valued drift and diffusion coefficients, respectively. Given that the algebraic operation on the manifold would be implausible without an extensive utilization of differential geometry, which is incongruent with the current objective of this work, the employment of the concept of tangent space and Lie algebra becomes necessary in order to render the SDE in Eq. (5.13) solvable. It is to be noted that the manifold and its equivallent lie group $\mathrm{SO}(3)$ under consideration in this context are denoted as S^2 and $\mathrm{SO}(3)$, respectively. Towards this, utilizing Magnus expansion [22, 46], a solution of the following form is adopted.

$$q(t) = \mathbf{Exp}\left(\Psi(t)\right) q_0 \tag{5.14}$$

where $\mathbf{Exp}$ is the Matrix Exponential operator which is obtained from the Rodriguez Formula and Ψ denotes an additional matrix-valued variable defined on the Lie algebra $\mathfrak{so}(3)$ of the configuration manifold with the following SDE,

$$\mathrm{d}\Psi = \mathbf{p}\mathrm{dt} + \mathbf{s}\mathrm{dW}_t \tag{5.15}$$

where, $\mathbf{p}$ and $\mathbf{s}$ represents matrix valued drift and diffusion, respectively. Considering that q is a functional and in order to generalize it, assume it to have the form of $f\left(q(t), \Psi(t), t\right)$. With this assumption, and utilizing Taylor's Series Expansion upto 2^{nd}-order, differential of f is given as,

$$\mathrm{d}f = (\partial_q f \partial_{\Psi_{ij}} q)\mathrm{d}\Psi_{ij} + \frac{1}{2}\left(\partial_{\Psi_{kl}}(\partial_{\Psi_{ij}} q \partial_q f)\right)\mathrm{d}\Psi_{kl}\mathrm{d}\Psi_{ij} \tag{5.16}$$

As the Lie algebra $\mathfrak{so}(3)$ is an abstract tangent space on the identity of Lie group [47], it assumes the properties Euclidean geometry which makes it valid to use the Quadratic Variation Property of Wiener Process [29] on $\mathrm{T}_p S^2$ Eq. (5.15). Using the quadratic variation [15, 29] on $\Psi \in \mathfrak{so}(n)$ and substituting Eq. (5.15) in Eq. (5.16) we get,

$$df = \left(p\ \partial_q f\ \partial_{\Psi_{ij}} q + \frac{1}{2}\left(\partial_{\Psi_{kl}}(\partial_{\Psi_{ij}} q\ \partial_q f\right) s_{kl} s_{ij}\right)\mathrm{dt} + s_{ij}\ \partial_q f\ \partial_{\Psi_{ij}} q\ \mathrm{dW}_t \tag{5.17}$$

Here the Kolmogorov Operators can be defined as,

$$\Im^0 = p\ \partial_{\Psi_{ij}} q\ \partial_q(.) + \tfrac{1}{2} s^2 \partial_{\Psi_{kl}}\left(\partial_{\Psi_{ij}} q\ \partial_q(.)\right), \quad \Im^1 = s\partial_{\Psi_{ij}} q\ \partial_q(.) \tag{5.18}$$

It is important to highlight that the expression of the Kolmogorov operator in Eq. (5.18) is a general representation and can be simplified for specific cases. In this regard, Lemma 5.4.1 provides a reduced form for a particular scenario.

Lemma 5.4.1. *Let T_pS^2 represent the tangent space of the two-dimensional sphere S^2 at point p. T_pS^2 is analogous to the Lie algebra $\mathfrak{so}(3)$ and adopts the Euclidean formalism, denoted by $(.)^V$, which signifies mapping to Euclidean space. For the tangent space of manifold S^2, the Kolmogorov Operators for $\mathfrak{so}(3)$ can be expressed as:*

$$\begin{aligned} \Im^0 &= p^V \partial_{\Psi^V_{ij}} q \partial_q(.) + \tfrac{1}{2}(s^V)^2 \partial_{\Psi^V_{kl}}\left(\partial_{\Psi^V_{ij}} q \partial_q(.)\right) \\ \Im^1 &= s^V \partial_{\Psi^V_{ij}} q \partial_q(.) \end{aligned} \tag{5.19}$$

In the case of Euclidean space, where the manifold S^2 and the tangent space T_pS^2 coincide [15], the Kolmogorov Operators take the following form:

$$\begin{aligned} \Im^0 &= p^V \partial_q(.) + \tfrac{1}{2}(s^V)^2 \partial_{\Psi^V_{kl}}\left(\partial_q(.)\right) \\ \Im^1 &= s^V \partial_q(.) \end{aligned} \tag{5.20}$$

Proof: The expression of Kolmogorov operators for $\mathfrak{so}(3)$ in Eq. (5.19) has been simplified to match the Euclidean case. In Eq. (5.19), the variable $\psi \in \mathfrak{so}(3)$ is a function of $q \in \mathrm{S}^2$, connected through Eq. (5.29). p and s are drift and diffusion matrices in the SDE for ψ (Eq. (5.15)). $(\cdot)^V$ represents the mapping $\mathrm{T}_p S^2 \rightarrow \mathfrak{so}(3)$. In the Euclidean scenario, where curvature diminishes, $\psi \in \mathfrak{so}(3)$ aligns with

$q \in \mathrm{S}^2$. This leads to $\partial_{\Psi^V_{ij}} q$ vanishing, resulting in Eq. (5.20). This mirrors a similar expression in literature [15] for the Euclidean case.

Writing Eq.(5.17) in the integral form for the variable $\Psi \in \mathfrak{so}(n)$ and further expanding the integral by repeated substitution and only retaining the $\int\int \mathrm{dWdW}$ term, to get the Itô-Taylor Strong 1.0 Scheme on the Lie algebra $\mathfrak{so}(3)$.

$$\Psi(t) = \Psi(t_0) + p(t_0)\int_{t_0}^{t} \mathrm{ds} + s(t_0)\int_{t_0}^{t} \mathrm{dW}(s) + \Im^1 s(t_0)\int_{t_0}^{t}\int_{t_0}^{s_1} \mathrm{dW}_r(s_1)\mathrm{dW}_r(s_2) \tag{5.21}$$

where, $\int_{t_0}^{t} \mathrm{ds}$, $\int_{t_0}^{t} \mathrm{dW}(s)$ and, $\int_{t_0}^{s_1} \mathrm{dW}_r(s_1)\mathrm{dW}_r(s_2)$ are the multiple stochastic integrals (MSIs), which are evaluated and the following discretization for Itô-Taylor 1.0 Strong Scheme can be obtained on the Lie algebra $\mathfrak{so}(3)$ through the one-to-one correspondence between $\mathbb{R}^3$ and $\mathfrak{so}(3)$ through the following lemma.

Lemma 5.4.2. *Let g be the Lie algebra of the special orthogonal group $\mathfrak{so}(3)$, and let v be the vector space $\mathbb{R}^3$ equipped with the cross product as the Lie bracket operation. Then, there exists a Lie algebra isomorphism between g and v. This isomorphism allows for the utilization of multiple stochastic integrals in the Euclidean space $\mathbb{R}^3$ on the Lie algebra $\mathfrak{so}(3)$.*

Proof: The lemma states that there exists a Lie algebra isomorphism between the special orthogonal Lie algebra $\mathfrak{so}(3)$ and the Euclidean space $\mathbb{R}^3$. This means that the Lie algebra $\mathfrak{so}(3)$ and the vector space $\mathbb{R}^3$ are in one-to-one correspondence, and their respective operations can be related.

- Lie Bracket Operation: The Lie bracket operation $[\cdot]$ [46] on the Lie algebra $\mathfrak{so}(3)$ corresponds to the cross product operation in $\mathbb{R}^3$. For two elements X, Y $\in \mathfrak{so}(3)$, their Lie bracket $[X, Y]$ gives the corresponding cross product in $\mathbb{R}^3$: $[X, Y] \leftrightarrow X \times Y$.
- Exponential Map: The exponential map in the Lie algebra $\mathfrak{so}(3)$ [22] corresponds to the exponential map in $\mathbb{R}^3$. Given an element X $\in \mathfrak{so}(3)$, its exponential map exp(X) yields the corresponding rotation matrix in $\mathfrak{so}(3)$. In $\mathbb{R}^3$, the exponential map exp(x) gives the corresponding point on the unit sphere:$exp(X) \leftrightarrow$ Rotation matrix in $\mathfrak{so}(3)$ [2]. $exp(x) \leftrightarrow$ Point on the unit sphere in $\mathbb{R}^3$
- Lie Group Representation: The action of the Lie group $\mathfrak{so}(3)$ on a vector space V is equivalent to the action of the corresponding Lie algebra $\mathfrak{so}(3)$ on the same vector space. If g $\in \mathfrak{so}(3)$ is a rotation matrix and v $\in V$ is a vector, then the action of g on v is given by: $g \circ v \leftrightarrow R \circ v$. Here, $(\circ)$ denotes the action of the rotation matrix in $\mathfrak{so}(3)$, and X $\in \mathfrak{so}(3)$ is the corresponding element in the Lie algebra.

The existence of the isomorphism between the Lie algebra $\mathfrak{so}(3)$ and the Euclidean space $\mathbb{R}^3$ facilitates the application of multiple stochastic integrals in the Lie algebra setting. Therefore, Eq. (5.21) can be written as,

$$\Psi_{n+1} = \Psi_n + p\Delta\mathrm{t} + s\Delta\mathrm{W} + \frac{1}{2}\Im^1 s\left((\Delta\mathrm{W})^2 - \Delta\mathrm{t}\right) \tag{5.22}$$

Where , $\Delta\mathrm{W} \sim N(0, \Delta\mathrm{t})$. Here, the drift and diffusion coefficient matrices p and s were assumed and needs to be evaluated as the function of known drift and diffusion coefficients a and σ_r. From Baker's Inverse Identity [22] the assumed drift and diffusion function on the SDE which evolves in the Lie algebra $\mathfrak{so}(3)$ of the configuration Manifold are provided in Eq. (F.7), whose detailed derivation can be referred from Appendix F. Finally, the position q_{n+1} is updated using Eq. (5.29).

5.4.2 Multistepping Algorithm

In the preceding subsection, the non-symplectic numerical integration scheme was elucidated, as detailed in Section 4.2.2 of Chapter 4. The current subsection introduces a new multistepping approach, capable of imbuing symplecticity into the established geometric Taylor 1.0 strong scheme. To enhance the implicit nature of the update equation applied to the Lie algebra $\mathfrak{so}(3)$ using the multistepping concept [82, 83, 84, 85], the multistepping approach involves breaking down complex computations into smaller iterative steps, catering to a gradual update of the variables on Lie algebra $\mathfrak{so}(3)$. To implement the multistepping method, we employ the time integration in Eq. (5.22) and apply it to the variables ω and Psi on $\mathfrak{so}(3)$. This involves partitioning the time step t into M instances and iteratively updating on $\mathfrak{so}(3)$ with a superscript notation $(\cdot)^i$. At each instance, an intermediate value of ω on $\mathfrak{so}(3)$ are obtained as,

$$\omega_n^{i+1} = \omega_n^i + \lambda(q_n, \omega_n^i)\frac{\Delta\mathrm{t}}{M} + \epsilon(q_n, \omega_n^i)\Delta\mathrm{W} + \frac{1}{2}\Im^1\epsilon(q_n, \omega_n^i)\left((\Delta\mathrm{W})^2 - \frac{\Delta\mathrm{t}}{2M}\right) \tag{5.23}$$

Thereafter the update of ψ with respect to the variables $(q_n\omega_n^{i+1})$ is given as,

$$\Psi_{n+1}^i = \Psi_n^i + p(q_n, \omega_n^{i+1})\frac{\Delta\mathrm{t}}{M} + s(q_n, \omega_n^{i+1})\Delta\mathrm{W} + \frac{1}{2}\Im^1 s(q_n, \omega_n^{i+1})\left((\Delta\mathrm{W})^2 - \frac{\Delta\mathrm{t}}{M}\right) \tag{5.24}$$

Where, $i \in (0, 1, 2.....M)$ and the ω is defined by the SDE as:

$$\mathrm{d}\omega = \lambda(q_n, \omega_n)\Delta\mathrm{t} + \epsilon(q_n, \omega_n)\Delta\mathrm{W}_t \tag{5.25}$$

The final update value in the Lie algebra $\mathfrak{so}(3)$ is given by Ψ_n^M which is equals to Ψ_{n+1}. Here, the initial condition for the variables on $\mathfrak{so}(3)$ is given as,

$$\omega_n^0 = \omega_n, \quad \Psi_n^0 = 0 \tag{5.26}$$

The iterative step in Eq. (5.23) on $\mathfrak{so}(3)$ is made implicit rather than relying on an explicit update equation. By formulating the implicit update equation of ω in terms of position q and the same of ψ in tems of angular velocity ω, a more implicit and nuanced representation of the update process can be achieved.

$$\Psi_{n+1} = \Psi_n + p(q_n, \omega_{n+1})\Delta\mathrm{t} + s(q_n, \omega_{n+1})\Delta\mathrm{W} + \frac{1}{2}\Im^1 s(q_n, \omega_{n+1})\left((\Delta\mathrm{W})^2 - \Delta\mathrm{t}\right) \tag{5.27}$$

$$\omega_{n+1} = \omega_n + \lambda(q_{n+1}, \omega_n)\Delta\mathrm{t} + \epsilon(q_{n+1}, \omega_n)\Delta\mathrm{W} + \frac{1}{2}\Im^1 \epsilon(q_{n+1}, \omega_n)\left((\Delta\mathrm{W})^2 - \Delta\mathrm{t}\right) \tag{5.28}$$

This approach allows for a more refined and accurate update. By dividing the time step into smaller intervals, the implicit nature of the update equation becomes more pronounced as each intermediate value of ω contributes to the overall update of the Lie algebra $\mathfrak{so}(3)$. In the proposed scheme, the division of the time step (M) is deliberately set to 1, despite the potential for higher accuracy with increased division. This makes the variables $\omega_n^0 = \omega_n$ and $\omega_n^1 = \omega_{n+\frac{1}{2}}$. The reason behind this decision is to balance accuracy with computational resources. This approach ensures that the update equation remains implicit while managing the computational costs associated with the calculation of intermediate values of the angular velocity ω. After the update of variables ω and ψ on $\mathfrak{so}(3)$ in Eq. (5.27), position is updated by using the matrix exponential mapping as,

$$q_{n+1} = \mathbf{Exp}(\Psi_{n+1})q_n \tag{5.29}$$

It is worth noting that the position state within the Lie algebra $\mathfrak{so}(3)$ exhibits an implicit relationship with respect to the angular velocity $(q_n, \omega_{n+\frac{1}{2}})$, while the angular velocity in the tangent space demonstrates an implicit connection with respect to position (q_{n+1}, ω_n'). This multi-implicit nature of the scheme becomes evident when examining the results presented in the subsequent sections. A flowC5 of proposed approach through the schematic diagram is provided in the Fig. 5.1(a).

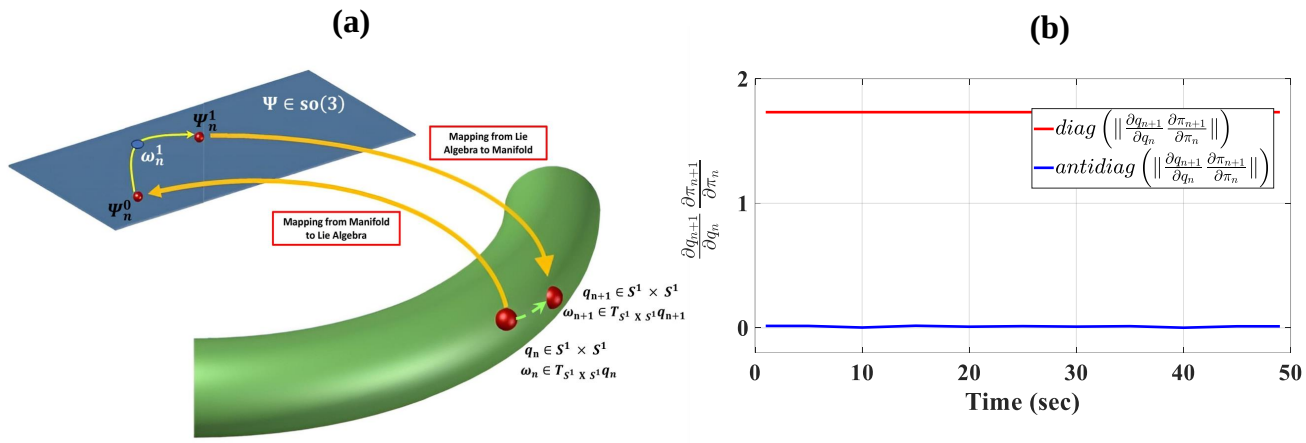

FIGURE 5.1: (a) Schematic diagram of flowC5 of the proposed framework, (b) preservation of weak symplectic condition for spherical pendulum system

5.4.3 Symplecticity of the proposed scheme

An integration scheme is considered to possess a symplectic nature when it exhibits the ability to preserve the essential geometric structure inherent in Hamiltonian systems [6, 86, 87, 88]. Specifically, this refers to the preservation of the symplectic structure or symplectic form, which plays a pivotal role in Hamiltonian dynamics by embodying energy conservation and the maintenance of phase space volume. The symplectic structure arises from the symplectic form, a mathematical construct that characterizes the fundamental properties of Hamiltonian systems. It provides a concise representation of the interplay between position and momentum variables, encapsulating the dynamic behavior and conservation principles of these systems.

Symplectic Conditions for a Numerical Scheme

1. *Shadowing property*: The shadowing characteristic represents a fundamental requirement for a numerical scheme to possess symplecticity. It asserts that, for a given step size, the numerial solution of the discrete system closely *shadows* or approximates the actual solution of the continuous system. It ensures that the long-term behavior, energy conservation, and geometric structure of the continuous system are accurately preserved by the numerical scheme. In the present study, evolution of Hamiltonian is considered to be the criteria for shadowing, and, the true solution is considered through the geometric Euler-Maruyama at very finer time step.

2. *Preservation of symplectic structure*: Symplectic numerical schemes are designed to preserve the symplectic structure of Hamiltonian systems. The symplectic structure of a Hamiltonian system

is characterized by a mathematical construct known as the symplectic form. This form possesses an antisymmetry property which encapsulates the conservation laws and geometric properties of the system by captures the fundamental relationship between position and momentum variables. Let $\mathbf{A}$ be a matrix connected to the canonical states of a Hamiltonian system, and let $\mathbf{J}$ be the symplectic matrix defined as follows,

$$\mathbf{J} = \begin{bmatrix} 0 & \mathbf{I} \\ -\mathbf{I} & 0 \end{bmatrix} \tag{5.30}$$

Then the antisymmetry property can be stated as,

$$\mathbf{A}^T \mathbf{J} \mathbf{A} = \mathbf{J} \tag{5.31}$$

This preservation entails maintaining the antisymmetry of the symplectic form and ensuring the integrity of the symplectic matrix, which is closely linked to the canonical variables [6, 88]. In addition to the antisymmetry of the symplectic form, symplectic numerical schemes also focus on maintaining the symplectic matrix, which guarantees the correct transformation between position and momentum coordinates, preserving the essential symplectic structure [89]. The motivation for introducing the weak symplectic condition stems from the challenge of analytically satisfying the antisymmetry property [89] described in Eq. (5.31) for nonlinear systems evolving on manifolds. The preservation of this property becomes a cumbersome task in such scenarios. Consequently, the formulation of the weak symplectic condition arises as a means to address this difficulty and provide a motivating solution.

Theorem 5.4.3. *Weak symplectic condition: For a numerical scheme to be symplectic, it must satisfy the following condition:*

$$\frac{\partial q_{n+1}}{\partial q_n} \frac{\partial \pi_{n+1}}{\partial \pi_n} = \mathbf{I} \tag{5.32}$$

where q_n *and* π_n *represent the discrete states of the Hamiltonian system at time step* n*, and* q_{n+1} *and* π_{n+1} *represent the corresponding states at time step* $(n+1)$*.*

Proof: To establish the preservation of symplectic structure, consider the matrix $\mathbf{A}$ given by:

$$\mathbf{A} = \begin{bmatrix} \frac{\partial q_{n+1}}{\partial q_n} & \frac{\partial \pi_{n+1}}{\partial q_n} \\ \frac{\partial q_{n+1}}{\partial \pi_n} & \frac{\partial \pi_{n+1}}{\partial \pi_n} \end{bmatrix} \tag{5.33}$$

Here, when Eq. (5.33) is substituted in Eq. (5.31), Eq. (5.32) is obtained, satisfying which ensures the preservation of symplectic structure. It is emphasized that the analytical satisfaction of Eq. (5.32) for geometric stochastic differential equations (SDEs) solved with a geometric implicit scheme is impractical. Consequently, this requirement is accomplished through numerical means, leading to the designation of this condition as the *weak symplectic condition*.

Proof of Symplecticity for the proposed Numerical Scheme

This section provides a sketch for numerically proving weak symplectic condition for the proposed scheme. The state in this are given by (q, π) on the $(\mathrm{S}^2)^n$. manifold where q is the position and π is the conjugate momentum vector. For a Hamiltonian system, the Stochastic Hamiltonian Differential Equation (SHDE) will have the following form,

$$\begin{aligned} \mathrm{d}q &= -q \times \nabla H_\pi \mathrm{dt} - q \times \nabla h_\pi \mathrm{dW}_k(t) \\ \mathrm{d}\pi &= \left(-q \times \nabla H_q + \nabla H_\pi \times \pi + \tfrac{1}{2}\left(q \times \nabla h_\pi\right) \times \nabla h_q\right) \mathrm{dt} - \left(q \times \nabla h_q - \nabla h_\pi \times \pi\right) \mathrm{dW}_k(t) \end{aligned} \tag{5.34}$$

where, $\mathrm{dW} = N(0, \sqrt{\mathrm{dt}})$ is white noise process, H is the Hamiltonian of the system, h is a function governing the stochasticity of the excitation and ∇A_B denotes $\frac{\mathrm{d}A}{\mathrm{d}B}$. For the solution of the given SHDE, proposed symplectic Itô-Taylor 1.0 strong scheme is used to provide the pathwise solution. The scheme starts with the partial update of the angular momentum $\pi \in \mathrm{T}_q\mathrm{S}^2$ at $n + \frac{1}{2}$ step in the Lie algebra $\mathfrak{so}(3)$, $\mathfrak{so}(3)$ as,

$$\begin{aligned} \pi_{n+\frac{1}{2}} &= \pi_n + \left(-q_n \times \nabla H_q + \nabla H_\pi \times \pi_n + \tfrac{1}{2}\left(q_n \times \nabla h_\pi\right) \times \nabla h_q\right) \tfrac{\Delta \mathrm{t}}{2} - \left(q_n \times \nabla h_q - \nabla h_\pi \times \pi_n\right) \Delta \mathrm{W} \\ &\quad -\tfrac{1}{2}\Im^1 \left(q_n \times \nabla h_q - \nabla h_\pi \times \pi_n\right) \left((\Delta \mathrm{W})^2 - \tfrac{\Delta \mathrm{t}}{2}\right) \qquad \forall \ (\pi_n, q_n) \end{aligned} \tag{5.35}$$

Following that, the full update of the position $q \in \mathrm{S}^2$ which is implicit with respect to $\pi \in \mathrm{T}_q\mathrm{S}^2$ on $\mathfrak{so}(3)$ is provided by,

$$\Psi_{n+1} = \Psi_n + S\left(\nabla H_\pi\right) \Delta \mathrm{t} + S\left(\nabla h_\pi\right) \Delta \mathrm{W}(t) + \tfrac{1}{2}\Im^1 S\left(\nabla h_\pi\right) \left((\Delta \mathrm{W})^2 - \tfrac{\Delta \mathrm{t}}{2}\right) \qquad \forall \ \left(\pi_{n+\frac{1}{2}}, q_n\right) \tag{5.36}$$

Which then is utilised for updating position $q \in \mathrm{S}^2$ as: $q_{n+1} = \mathbf{Exp}(\Psi_{n+1})q_n$. Finally, the update of angular momentum π which is implicit with respect to $q \in \mathrm{S}^2$ on $\mathrm{T}_q\mathrm{S}^2$ is provided by,

$$\begin{aligned}\pi_{n+1} \;=\; & \pi_n + \left(-q_{n+1} \times \nabla H_q + \nabla H_\pi \times \pi_n + \tfrac{1}{2}\left(q_{n+1} \times \nabla h_\pi\right) \times \nabla h_q\right)\Delta \mathrm{t} - \left(q_{n+1} \times \nabla h_q - \nabla h_\pi \times \pi_n\right)\Delta \mathrm{W} \\ & -\tfrac{1}{2}\Im^1\left(q_{n+1} \times \nabla h_q - \nabla h_\pi \times \pi_n\right)\left((\Delta \mathrm{W})^2 - \Delta \mathrm{t}\right) \qquad \forall\ (\pi_n, q_{n+1})\end{aligned} \tag{5.37}$$

Differentiating q_{n+1} with respect to q_n using Eq.(5.36), one can get the following expression,

$$\frac{\mathrm{d}q_{n+1}}{\mathrm{d}q_n} = \mathbf{Exp}\left(\Psi_{n+1}\right)\left(\mathbf{I} + \frac{\mathrm{d}\Psi_{n+1}}{\mathrm{d}q_n}\right) \qquad \forall\ \left(\pi_{n+\frac{1}{2}}, q_n\right) \tag{5.38}$$

Similarly, differentiating Eq.(5.37) with respect to π_n and assuming a variable separable Hamiltonian Function and an additive noise function one can get,

$$\begin{aligned}\frac{\mathrm{d}\pi_{n+1}}{\mathrm{d}\pi_n} =& \mathbf{I} - \Big(S\left(q_{n+1}\right)\nabla H_{q\pi} + S\left(\pi_n\right)\nabla H_{\pi\pi} - S\left(\nabla H_\pi\right) - \frac{1}{2}\left(S\left(q_{n+1} \times \nabla h_\pi\right)\nabla h_{q\pi}\right. \\ & \left. - S\left(q_{n+1} \times \nabla h_q\right)\nabla h_{\pi\pi}\right)\mathrm{dt} - \left(S\left(q_{n+1}\right)\nabla h_{q\pi} - S\left(\nabla h_\pi\right) + S\left(\pi_n\right)\nabla h_{\pi\pi}\right)\mathrm{dW} \\ & - \frac{1}{2}\frac{\mathrm{d}}{\mathrm{d}\pi_n}\Im^1\left(q_{n+1} \times \nabla h_q - \nabla h_\pi \times \pi_n\right)\left((\mathrm{dW})^2 - \mathrm{dt}\right) \qquad \forall\ (\pi_n, q_{n+1})\end{aligned} \tag{5.39}$$

where, $\nabla H_{xy} = \frac{\mathrm{dH}}{\mathrm{d}x\mathrm{d}y}$. Here, for a user defined system, Eq. (5.38) and Eq. (5.39) are numerically evaluated and weak symplectic condition from Eq. (5.32) is ensured along with the shadowing condition to prove the symplectic nature of the proposed algorithm towards the Hamiltonian system. For the better understanding of the reader, a stochastically excited spherical pendulum having unit mass and unit length with position $q \in \mathrm{S}^2$ and angular momentum $\pi \in T_q^\star\mathrm{S}^2$ is taken as an example towards the demonstration of the symplectic nature of the proposed algorithm. The Hamiltonian of the system is given by

$$\mathcal{H}(q,\pi) = \frac{1}{2}\left\|\omega\right\|^2 + g\left(q \cdot e_3\right) \tag{5.40}$$

where, g is the acceleration due to gravity and $e_3 = [0\ 0\ 1]$ is the direction of gravity acting on the system. The excitation is considered to the the white noise process and the function governing the stochasticity is taken as $h = \sigma_1 q + \sigma_2 \pi$. with these parameters, $\nabla H_x\ \forall\ x = (q,\pi)$, $\nabla H_{xy}\ \forall\ x, y = (q,\pi)$, $\nabla h_x\ \forall\ x = (q,\pi)$ and $\nabla h_{xy}\ \forall\ x, y = (q,\pi)$ are calculated and the final expression of $\frac{\mathrm{d}q_{n+1}}{\mathrm{d}q_n}$ and $\frac{\mathrm{d}\pi_{n+1}}{\mathrm{d}\pi_n}$ are obtained as,

$$\frac{\mathrm{d}\pi_{n+1}}{\mathrm{d}\pi_n}\frac{\mathrm{d}q_{n+1}}{\mathrm{d}q_n} = \left(\mathbf{I} + S\left(\sigma_2\right)\Delta W\right)\mathbf{Exp}\left(S\left(\pi_{n+\frac{1}{2}}\right)\mathrm{dt} + S\left(\sigma_2\right)\Delta W\right) \tag{5.41}$$

Eq. (5.41) is then numerically evaluated at every time step to validate the symplecticity of the proposed framework as per Theorem 5.4.3. The norm of the diagonal terms and the norm of anti-diagonal terms of $\frac{\mathrm{d}\pi_{n+1}}{\mathrm{d}\pi_n}\frac{\mathrm{d}q_{n+1}}{\mathrm{d}q_n}$ are portrayed in Fig. 5.1(b), which shows that Eq. (5.41) closely resembles the identity matrix throughout the simulation. In the further study, the aforementioned shadowing and weak symplectic conditions are validated by considering two distinct physical systems.

Algorithm 4 Geometric symplectic Taylor–1.0 strong algorithm for stochastic Hamiltonian system

Input: Drift and diffusion matrices for SDE on manifold ▷ $\mathbf{a}$ and σ
Initialization for the simulation:
for $n = 1 : N_{iteration}$ **do** ▷ Iteration for sample length
Estimate the drift $\mathbf{p}$ and diffusion $\mathbf{s}$ coefficients for SDE in lie algebra. ▷ Refer Eq. (F.7)
Estimate the kolC5mogorov operators for drift $\mathbf{p}$ and diffusion $\mathbf{s}$ matrices for q. ▷ Refer Eq. (5.18)
Update states $\psi_{ij}(n+1)$ on lie algebra implicitly with respect to ω_{n+1}. ▷ Refer Eq. (5.27)
Update states $q(n+1)$ on manifold using the exponential mapping from lie algebra. ▷ Refer Eq. (5.29)
Update states $\omega_{ij}(n+1)$ on lie algebra implicitly with respect to q_{n+1}. ▷ Refer Eq. (5.28)
Output: Geometry preserving response of the stochastic Hamiltonian system
Input: Evolution of the states q and ω at each time instance
Get the Lagrangian of the system $\mathcal{L}$
Obtain π through Legendre transformation. ▷ Refer Eq. (5.50)
Obtain $\frac{\mathrm{d}\pi_{n+1}}{\mathrm{d}\pi_n}\frac{\mathrm{d}q_{n+1}}{\mathrm{d}q_n}$ numerically. ▷ Refer Eq. (5.41)
Output: Weak symplectic condition: $\frac{\mathrm{d}\pi_{n+1}}{\mathrm{d}\pi_n}\frac{\mathrm{d}q_{n+1}}{\mathrm{d}q_n}$

5.5 Numerical Illustrations

To demonstrate the applicability of the proposed algorithm for dynamical systems evolving on the quadratic hyper-surface, numerical case studies of two physical systems are carried out. In this context, (i) two spherical pendulum connected with an elastic spring, and, (ii) Spherical pendulum connected to Three elastic strings are undertaken.

5.5.1 Two spherical pendulums connected with an elastic spring

This section provides application of the proposed algorithm for a physical system with two pendulum connected to a shared immovable support via a pivot that has no friction. Each pendulum can move in the three dimensional space and although the effect of gravity is ignored, there exists an elastic force between these pendulums. Each pendulum is considered to be a slender, rigid link with a concentrated mass of m situated L units away from the pivot [9]. An illustration of this system is provided in Fig. 5.2(a). Here, the position of pendulums y_i and their angular velocities ω_i represent the states of the pendulum mass on S^2 and $\mathrm{T}_y\mathrm{S}^2$, respectively. The configuration manifold of this system is

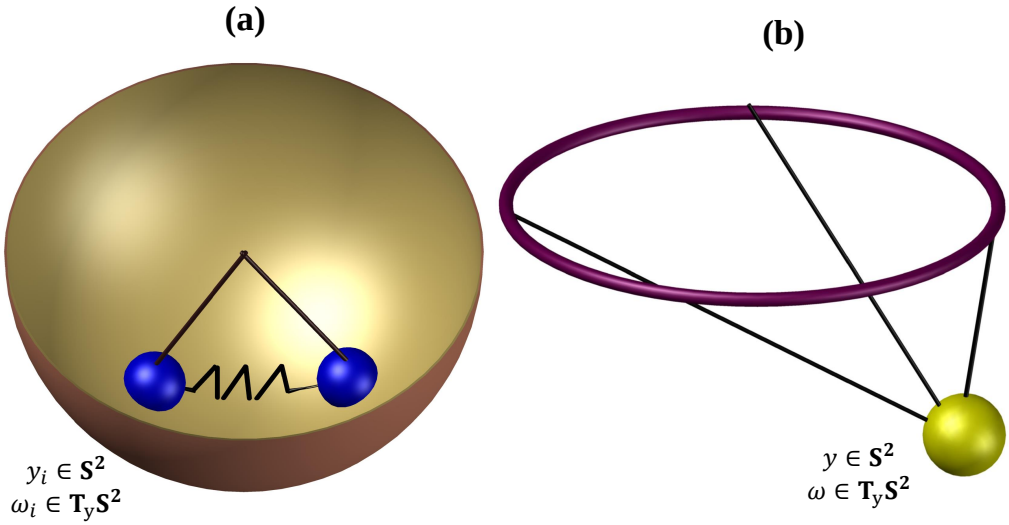

FIGURE 5.2: Schematic diagram of (a) Two Spherical Pendulum connected with Elastic Spring (b) Tensigrity configuration)

considered as $\left(\mathrm{S}^2\right)$. For the formulation of the equation of motion, consider the Lagrangian of the system $L : \mathrm{T}(\mathrm{S}^2)^n \to \mathbb{R}^1$ for position y_i and velocity $\dot{y}_i$ as,

$$\mathcal{L}(y, \dot{y}) = \frac{1}{2} m l^2 \left\|\dot{y}_1\right\|^2 + \frac{1}{2} m l^2 \left\|\dot{y}_2\right\|^2 - \xi \left(1 - y_1^T y_2\right) \tag{5.42}$$

where, $\xi \left(1 - y_1^T y_2\right)$ is the potential energy of the system with ξ as a positive elastic stiffness constant. It is to be noted that the elastic force vanishes when the two pendulums are col-linear in superimposed fashion where they occupy identical configuration space, as the elastic potential energy has zero gradient. The Lagrangian in Eq. (5.42) can be modified to be represented for states y_i and ω_i as,

$$\tilde{L}(y, \omega) = \frac{1}{2} m l^2 \left\|\omega_1\right\|^2 + \frac{1}{2} m l^2 \left\|\omega_2\right\|^2 - \xi \left(1 - y_1^T y_2\right) \tag{5.43}$$

The kinematics of the given configuration can be represented in the following form,

$$\dot{y}_i = S\left(\omega_i\right) y_i, \quad \forall i = 1, 2, 3 \tag{5.44}$$

where, $S(\cdot)$ represents the wedge operator for the mapping $\mathrm{T}_y\mathrm{S}^2 \subset \mathbb{R}^3 \to \mathfrak{so}(3)$. The integral of the modified Lagrangian along the system trajectory over the fixed initial and final points and and integral of the forcing function F over the Wiener process W can be written in the form of an action integral as,

$$\mathbb{A} = \int_{t_0}^{t_f} \tilde{L}(y\omega)\mathrm{dt} - \int_{t_0}^{t_f} \mathrm{F}(y, \omega) \circ \mathrm{dW}(t) \tag{5.45}$$

where, $\circ$ represents the Stratonovich Operator. The infinitesimal variation of the action integral provides the variation taken over all the differential curves $\gamma_i : [t_o, t_f] \rightarrow \mathbb{R}^3, \forall i = 1, ..., n$ on S^2 that satisfies the boundary condition of the system. The variation of the action integral over the variation of states is given by,

$$\delta\mathbb{A} = \int_{t_0}^{t_f} \left[\frac{\partial\tilde{L}}{\partial\omega_i}\delta\omega_i + \frac{\partial\tilde{L}}{\partial y_i}\delta y_i\right] \mathrm{dt} - \int_{t_0}^{t_f} \left[\frac{\partial \mathrm{F}}{\partial\omega_i}\delta\omega_i + \frac{\partial \mathrm{F}}{\partial y_i}\delta y_i\right] \circ \mathrm{dW}(t) \tag{5.46}$$

The infinitesimal variations of the y_i and ω_i along the differential curve $\gamma_i : [t_o, t_f] \rightarrow \mathbb{R}^3$ are given by [9]:

$$\begin{aligned} \delta\dot{y}_i &= S(\dot{\gamma}_i)y_i + S(\gamma_i)\dot{y}_i \\ \delta\omega_i &= S(\gamma_i)\omega_i + (I_{3x3} - y_i y_i^T)\dot{\gamma}_i \end{aligned} \tag{5.47}$$

After a series of substitution and rearrangement, the following form of the stochastic Euler-Lagrange equation is given by,

$$\left(I_{3\times3} - y_i y_i^T\right)\left[\frac{d}{\mathrm{dt}}\frac{\partial\tilde{L}}{\partial\omega_i} - 2\omega_i \times \frac{\partial\tilde{L}}{\partial\omega_i}\right] - y_i \times \frac{\partial\tilde{L}}{\partial y_i} = \left[\left(I_{3\times3} - y_i y_i^T\right)\omega_i \times \frac{\partial \mathrm{F}}{\partial\omega_i} + y_i \times \frac{\partial \mathrm{F}}{\partial y_i}\right] \circ \frac{\mathrm{dW}(t)}{\mathrm{dt}} \tag{5.48}$$

Now, considering the modified Lagrangian from Eq. (5.42), and stochastic Euler Lagrange equation from Eq. (5.48), the equation of motion for the undertaken two spherical pendulum connected with an elastic spring system is written as,

$$\begin{aligned} \dot{\omega}_1 &= \frac{\xi}{\mathrm{ml}^2} y_2 \times y_1 + \sigma_1 \circ \mathrm{dW}(t) \\ \dot{\omega}_2 &= \frac{\xi}{\mathrm{ml}^2} y_2 \times y_1 + \sigma_2 \circ \mathrm{dW}(t) \end{aligned} \tag{5.49}$$

For the present study, mass of both the pendulum is taken as 1kg, length of the string connecting both the pendulum mass to a common support is considered as 1m and both the intensities of the stochastic excitation σ_1 and σ_2 are considered as 0.1. The system is initially perturbed by the vector $y_0 = [0 \;\; 1 \;\; 0]$ and provided an initial angular velocity of $\omega_0 = [0 \;\; 0 \;\; 0]$. The simulation of the system is conducted using the Euler-Lagrange equation, as denoted by Eq. (5.49). In order to establish the symplecticity of the proposed numerical integration technique, the system's Hamiltonian is employed as a basis. For this, the conjugate of the angular velocity π can be estimated through the Legendre transformation which is given as

$$\pi_i = \left(\mathbf{I} - y_i y_i^T\right)\frac{\partial\mathcal{L}}{\partial\omega_i} \tag{5.50}$$

The Hamiltonian for the undertaken system for variables y and π is written as,

$$H\left(y,\pi\right)=\frac{1}{2ml^2}\|\pi_1\|^2+\frac{1}{2ml^2}\|\pi_2\|^2+\xi\left(1-y_1^Ty_2\right) \tag{5.51}$$

The Hamiltonian plays a crucial role in both verifying the symplecticity and assessing the effectiveness of the proposed framework, as detailed in Section 5.6. By leveraging the Hamiltonian, the preservation of important geometric properties of the system's phase space and symplectic symmetry are demonstrated. This analysis provides a mean to establish the symplecticity of the numerical integration technique, which is a desirable property for maintaining the accuracy and long-term stability of the simulations. The results presented in Section 5.6 showcase the practical implications and benefits of the proposed framework, providing evidence of its efficacy in capturing the dynamic behavior of the system while ensuring the preservation of key structural properties.

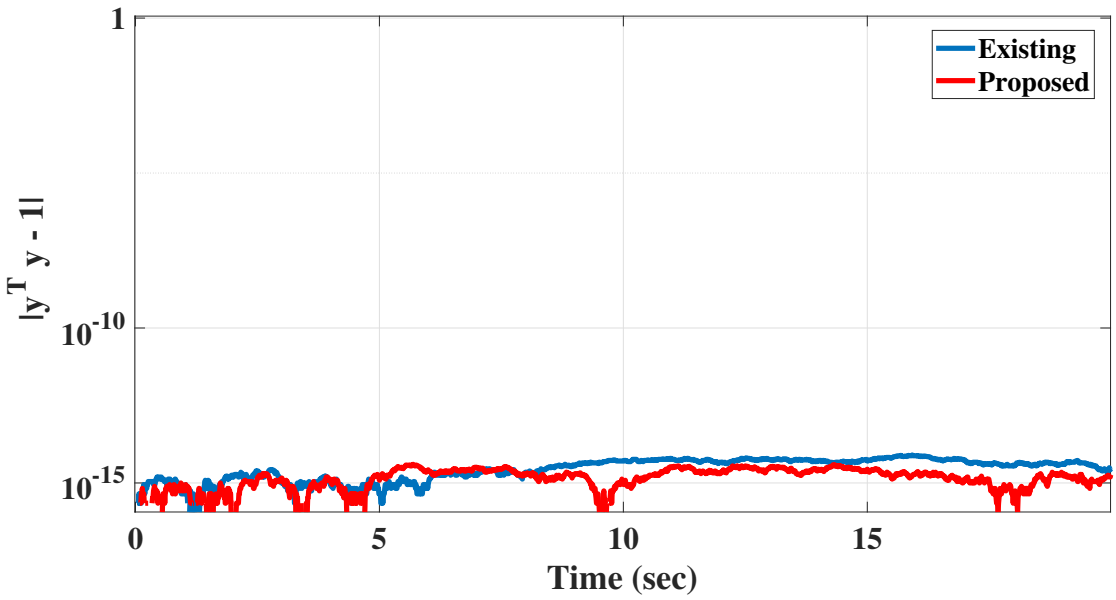

FIGURE 5.3: Measure of geometry preservation for Tensegrity Structure (dt = 0.01 sec and σ = 0.1)

5.5.2 Tensegrity Structure

This section provides application of the proposed algorithm towards tensegrity systems, particularly system consisting of a 3-dimensional pendulum connected to three elastic stings. These systems, often characterized by their lightweight and flexible nature, exhibit intriguing mechanical properties and have been widely explored in various fields of engineering [9, 90]. In the current study, a global formulation of the undertaken system under stochastic excitation is provided. The position of the pivot point of the

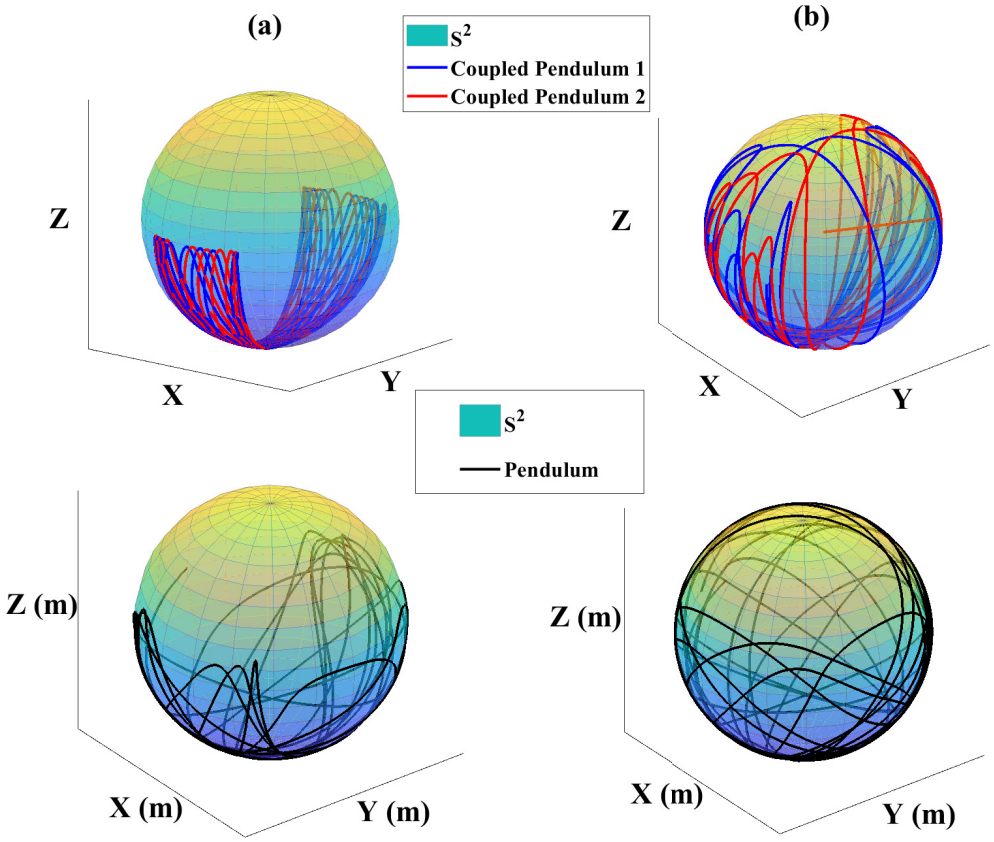

FIGURE 5.4: Comparison of trajectory for (a) Two Spherical Pendulum connected with Elastic Spring (dt = 0.01 sec and σ = 0.1) (b) Tensegrity Structure (dt = 0.01 sec and σ = 0.1)

center of mass of the pendulum is $y \in \mathrm{S}^2$. Mass of the pendulum, length of the string linking pendulum, stiffness of elastic strings and constant acceleration of gravity are denoted by m, l, k and g, respectively. One end of these elastic strings are attached to the center of mass of the pendulum and other end is attached to the fixed inertial support. An illustration of this system is provided in Fig. 5.2(b). For the current study, these three supports are provided at the location on the sphere with respect to the inertial frame as,

$$\phi_1 = \begin{bmatrix} -\frac{l}{2} \\ -\frac{l}{2\sqrt{3}} \\ 0 \end{bmatrix}, \quad \phi_2 = \begin{bmatrix} \frac{l}{2} \\ -\frac{l}{2\sqrt{3}} \\ 0 \end{bmatrix}, \quad \phi_3 = \begin{bmatrix} 0 \\ \frac{l}{\sqrt{3}} \\ 0 \end{bmatrix} \tag{5.52}$$

For the equation of motion, first a Lagrangian for this system is defined as,

$$\mathcal{L}(y, \omega) = \frac{1}{2}\left(m\|\omega\|^2 - mgl\,(y \times e_3) - \sum_{i=1}^{3} k\left(\|\xi_i\| - l\right)^2 \right) \tag{5.53}$$

where, $\xi_i = \phi_i - ly \ \in \mathbb{R}^3 \ \forall \ i = 1, 2, 3$ are the string vectors. The rotational kinematic for the pendulum link is written as $\dot{y} = \omega \times y$. The Lagrangian in Eq. (5.53) can be substituted in Eq. (5.48) to form

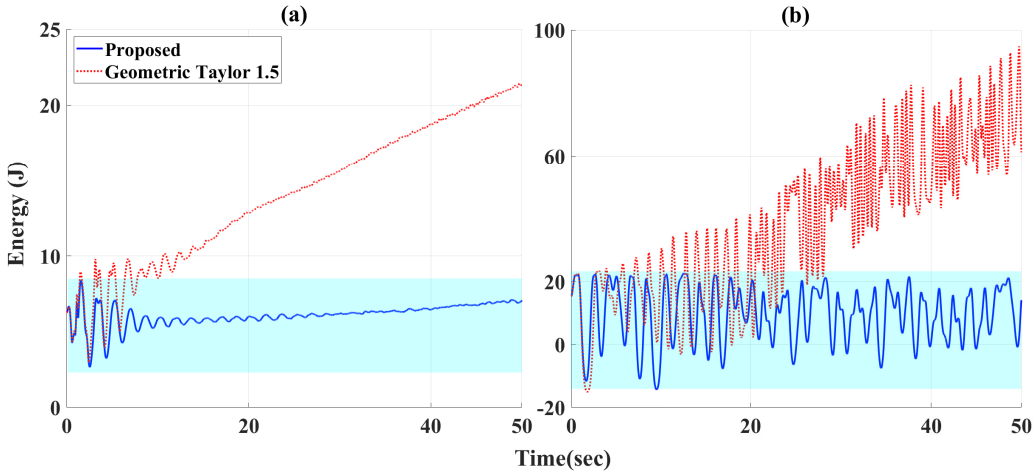

FIGURE 5.5: Comparison of Hamiltonian for (a) Two Spherical Pendulum connected with Elastic Spring (dt = 0.01 sec and σ = 0.1) (b) Tensegrity Structure (dt = 0.01 sec and σ = 0.1)

stochastic differential equations governing the motion of the system of the form,

$$\dot{\omega} = -q \times \left(\frac{mgl}{2} e_3 - l \sum_{i=1}^{3} k \left(\|\xi_i\| - l \right) sgn\left(\xi_i\right) \right) + \sigma \circ \left(\dot{W}\right) \tag{5.54}$$

where, $sgn\left(\cdot\right)$ is the signum function. In the current study, mass of the pendulum is taken as m $= 1$kg, unstreached length on the strings, $l = 1$m and elastic stiffness of the strings is taken as k $= 10$kN/m. For proving the symplecticity of the proposed algorithm, the Hamiltonian for the undertaken system for variables y and π is written as,

$$H\left(y, \pi\right) = \frac{1}{2ml^2} \|\pi_1\|^2 + \frac{1}{2mgl} \left(y \times e_3\right) + \sum_{i=1}^{3} \frac{k}{2} \left(\|\xi_i\| - l \right)^2 \tag{5.55}$$

where, π is the conjugate of the angular velocity and can be obtained through Eq. (5.50).

5.5.3 Pendulum cart system

The section analyses the motion characteristics of a spherical pendulum subjected to a constant gravitational force. This pendulum is affixed to the central point of a moving cart, which glides across a frictionless horizontal surface. The spherical pendulum is constructed using a slender, weightless rigid rod. At one end of this rod, there exists a concentrated mass, while the other end is connected to the cart through a spherical pivot or joint. The cart itself is portrayed as a system composed of a spring, a mass, and a damping mechanism. The system's arrangement can be referred from the literature. The cart's mass and the pendulum's mass are denoted as M and m respectively. Additionally, the pendulum's

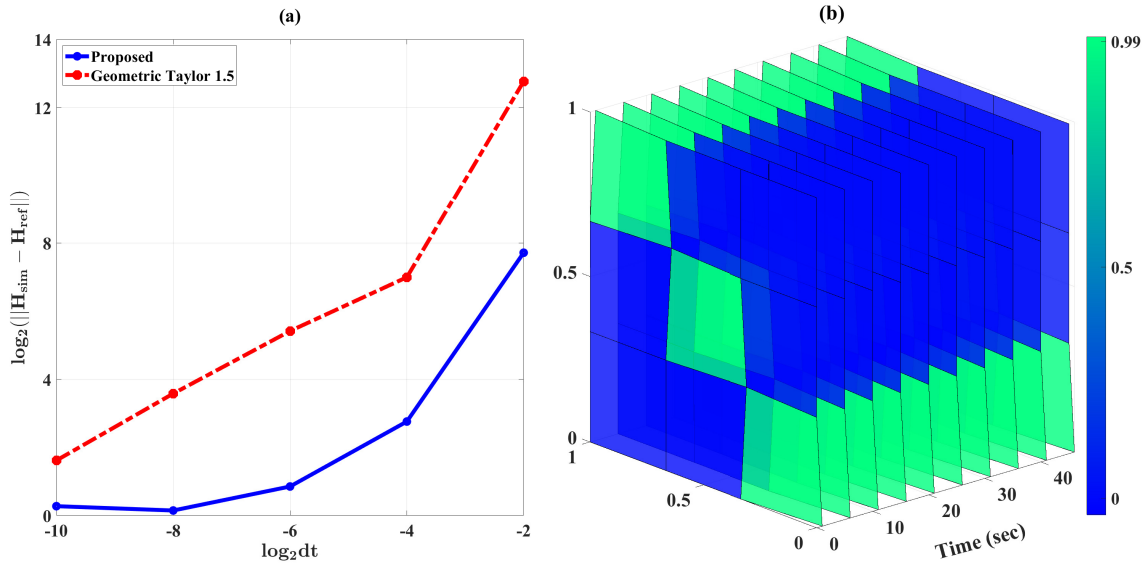

FIGURE 5.6: (a) Global error of the Hamiltonian for at dt = 2^{-10}, 2^{-8}, 2^{-6}, 2^{-4}, and 2^{-2}, using both the proposed scheme and the existing Taylor 1.5 scheme with geometric EM scheme at dt = 2^{-12} (benchmark), (b) weak symplectic condition for Tensegrity Structure (dt = 0.01 sec and σ = 0.1)

length is labeled as l. The cart's stiffness is designated as k, and the damping coefficient for the dashpot mechanism is denoted as c. As a result, the configuration of this interconnected system can be defined using coordinates (q, x). The Lagrangian function of the system can be expressed using the variables $q \in \mathrm{S}^2$ (position of pendulum), $x \in \mathbb{R}^2$ (position of cart), $\dot{x} \in \mathrm{T}_x\mathbb{R}^2$ (velocity of cart) and $\omega \in \mathrm{T}_q\mathrm{S}^2$ (angular velocity of pendulum) and the wedge operator as,

$$\mathrm{L}(q, x, \omega, \dot{x}) = \frac{1}{2}(M_c + m)\langle \dot{x}, \dot{x}\rangle - ml\dot{x}^T \mathbf{C}^T q^{\Lambda}\omega + \frac{1}{2}ml^2\langle \omega, \omega\rangle - mgle_3^T q - \frac{1}{2}k\langle x, x\rangle \tag{5.56}$$

where The matrix $\mathbf{C}$ is given as,

$$\mathbf{C} = \begin{bmatrix} 1 & 0 \\ 0 & 1 \\ 0 & 0 \end{bmatrix}$$

Afterwards, the Lagrangian in Equation (5.56) is applied in Equation (5.48), along with the inclusion of an external damping force on the cart, represented as $c\dot{x}$. This gives rise to an SDE, which is expressed as,

$$\begin{bmatrix} mL^2 I_{3\times 3} & -mLS^T(q)C \\ -mLC^T S(q) & (M+m)I_{2\times 2} \end{bmatrix} \begin{bmatrix} \dot{\omega} \\ \ddot{x} \end{bmatrix} + \begin{bmatrix} mgLq \times e_3 \\ mLC^T S(\omega)^2 q + kx + c\dot{x} \end{bmatrix} = \begin{bmatrix} \sigma_1 \circ \mathrm{dW}(t) \\ \sigma_2 \circ \mathrm{dW}(t) \end{bmatrix} \tag{5.57}$$

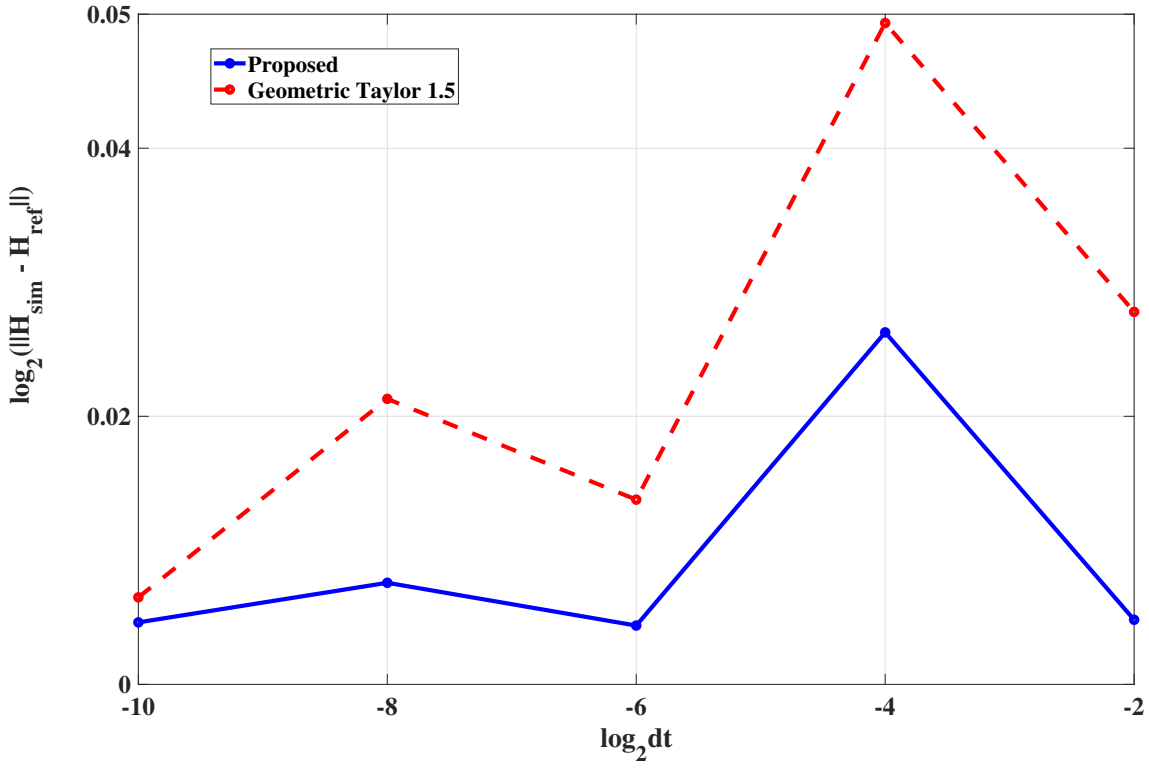

FIGURE 5.7: Global error of the Hamiltonian for at dt = 2^{-10}, 2^{-8}, 2^{-6}, 2^{-4}, and 2^{-2}, using both the proposed scheme and the existing Taylor 1.5 scheme with geometric EM scheme at dt = 2^{-12} (benchmark) for Pendulum cart system

In this case study, the cart's mass is taken as $M = 15$ kg, while the pendulum mass is set at $m = 0.09M$ kg. The length of the connecting string between the pendulum mass and the cart is $l = 1$ m. The cart's stiffness is considered as $k = 50$ N/m, and its damping coefficient is $c = 5$ Ns/m. Additionally, both intensities of the stochastic excitation, σ_1 and σ_2, are assumed to be 0.1. To initiate the system's behavior, the following initial conditions are considered: $q_0 = [0;;0;;-1]$, $x_0 = [0;;0]$, $\dot{x}_0 = [0;;0]$, and $\omega_0 = [0.2;;0.3;;0.5]$. To simulate the system's dynamics, the Euler-Lagrange equation defined by Equation (5.56) is employed. To ensure the preservation of symplecticity in the numerical integration technique, the system's Hamiltonian is utilized as the foundation. To achieve this, the angular velocity's conjugate variable π is computed through the Legendre transformation, yielding the system's Hamiltonian as follows:

$$\mathrm{H} = \langle p, \dot{x}\,(p)\rangle + \langle \pi, \omega\,(\pi)\rangle - \hat{\mathrm{L}}(x, \dot{x}\,(p)\,, p, \omega\,(\pi)) \tag{5.58}$$

here, π can be obtained through Eq. (5.50).

5.6 Results and discussion

This section presents the results and discussion of the findings, providing insights into the effectiveness and implications of the proposed method. Fig. 5.3 demonstrate the geometrical constraint preservation for the tensegrity structure for the recently developed geometric Itô-Taylor 1.5 strong scheme and the proposed algorithm. In this analysis, it is evident that the non-symplectic geometrical framework produces solutions that align with the configuration manifold. The preservation of geometrical constraints guarantees adherence to specific constraints, thereby maintaining the desired manifold geometry. However, it is crucial to note that while constraint preservation is upheld, it does not assure the accuracy of solution trajectories. To ensure the complete correctness of the numerical integration scheme, the preservation of the symplectic structure becomes necessary. Figs. 5.4(a) and 5.4(b) depict the trajectories of the simulated systems using both the proposed scheme and the existing geometric Taylor 1.5 strong scheme. It is evident from the figures that the trajectories stabilize when the proposed scheme is employed. Conversely, the trajectories generated by the existing scheme exhibit erratic behavior, with a tendency to diverge unpredictably for simulation times greater than 60 seconds. An additional insight can be gained by examining the temporal evolution of the Hamiltonian, as depicted in Fig. 5.5. It is evident that the Hamiltonian remains within bounds throughout the simulation, thereby substantiating the energy conservation of the proposed numerical technique.

The numerical validation of the symplectic conditions from Section 5.4.3 is carried out for the tensegrity configuration, as illustrated in Fig. 5.6. Fig. 5.6(a) displays the global error of the Hamiltonian at various time steps, specifically dt = 2^{-10}, 2^{-8}, 2^{-6}, 2^{-4}, and 2^{-2} seconds, using both the proposed scheme and the existing Taylor 1.5 scheme. The benchmark solution, obtained using the geometric EM scheme at dt = 2^{-12}, is used for comparison. The observed global error serves as validation for the shadowing condition, as the Hamiltonian computed using the proposed formulation shadows (closely aligns with) the benchmark solution, exhibiting significantly less error compared to the non-symplectic existing scheme. The same can be observed for the pendulum cart system in Fig. 5.7. The reduction in the global error achieved using the proposed formulation amounts to approximately 98$\%$ for the tensigrity structure and 60$\%$ for pendulum cart system, further highlighting the distinct advantages of the symplectic approach over the non-symplectic existing scheme.

In Figure 5.6(b), the evolution of the variable $\frac{\partial q_{n+1}}{\partial q_n}\frac{\partial \pi_{n+1}}{\partial \pi_n}$ is presented at different time points throughout

the simulation. This analysis aims to assess the preservation of the symplectic structure using the proposed scheme, as outlined in Theorem 5.4.3. The symplectic structure of the system is characterized by the presence of an asymmetric matrix, which gives rise to the aforementioned condition. Notably, Figure 5.6(b) clearly demonstrates that the matrices obtained at each time point closely approximate the identity matrix, thereby indicating the successful preservation of the symplectic structure throughout the simulation. Similar observations were made for the system involving two pendulums connected by an elastic spring. However, for the sake of brevity, the detailed results for this configuration are omitted in this discussion. Fig. 5.8 illustrates an important observation characterized by the emergence of new

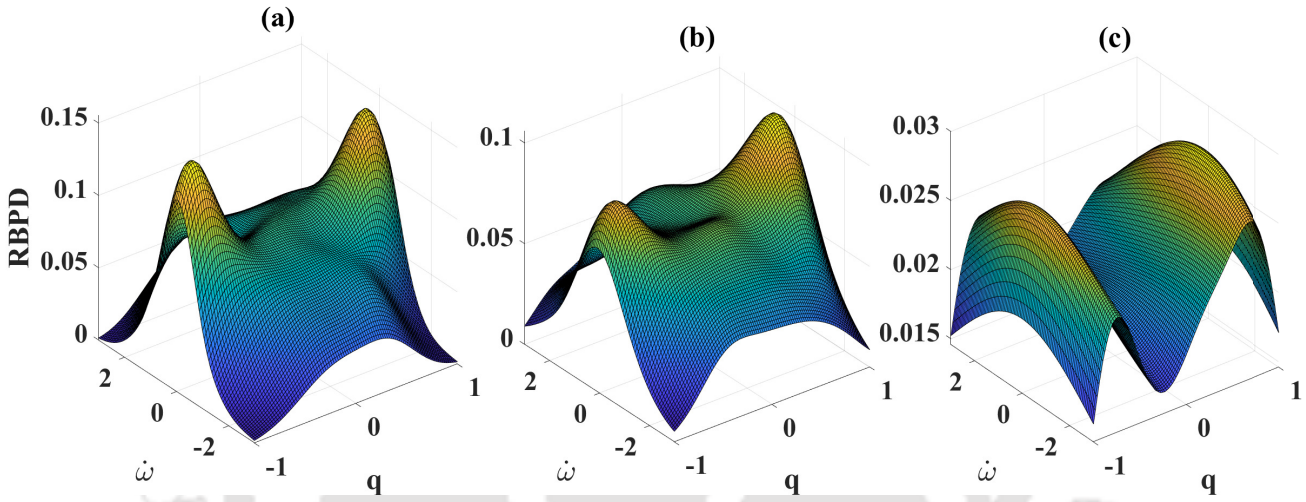

FIGURE 5.8: Response Basin Probability Density for (a) $\sigma = 0.01$, (b) $\sigma = 0.1$ and (c) $\sigma = 0.5$ for Tensegrity Structure

attractors at higher noise intensities, providing strong evidence of chaotic behavior in the system. In contrast, lower noise levels exhibit stable basins with smaller peak values of RBPD. The presence of these new attractors signifies a significant transition towards chaotic dynamics induced by the escalating intensity of noise. This insight emphasizes the sensitivity of the system to noise and highlights the intricate interaction between noise and attractor formation.

5.6.1 A note on the long-term simulation and stability of the proposed algorithm

Long-term simulation refers to the extended duration of numerical integration performed numerical integration scheme. It involves simulating the dynamics of the system over a substantial period to observe its behavior, stability, and properties over time. The term "long-term" signifies that the simulation covers a duration that is considered significant enough to capture relevant dynamics and provide insights into the system's long-term evolution. The specific duration of the long-term simulation may

vary depending on the characteristics of the system and the research objectives but generally implies a significant time span that goes beyond short-term or fast dynamics. In the present study, a long term simulation is conducted up to a duration of 1200 sec to explore the behaviour and stability of the proposed algorithm for the undertaken physical system. Throughout the simulation, the Hamiltonian remains bounded indicating the stability of the proposed framework. However, to facilitate a concise comparison with the existing geometric scheme, the simulation duration is limited and focused on capturing key aspects of interest.

The trajectory comparison has revealed that the proposed scheme yields stabilized trajectories, while the existing scheme exhibits erratic behavior and unpredictable divergence (see Fig. 5.4). This observation is also supported by Fig. 5.5, where the slope of the mean drift of the coupled pendulum system and tensegrity structures is approximately 0.3 and 1.6, respectively, when using the existing geometric Taylor framework over a duration of 50 seconds. However, when the proposed framework is employed, it is observed that the drift is almost negligible and the Hamiltonian remains bounded. This provides evidence of the stability of the proposed geometric symplectic framework in comparison to the existing geometric Taylor 1.5 scheme.

5.7 Research Findings

The outcomes of this chapter can be summarized as follows:

- Geometric Symplectic Itô-Taylor 1.0 Integration Scheme: This paper presents the development of a novel numerical integration scheme, termed the geometric symplectic Itô-Taylor 1.0 scheme, tailored for dynamical systems evolving on manifolds.
- Novel Weak Symplectic Condition: A unique weak symplectic condition is introduced, offering a practical means to verify the symplectic nature of the algorithm. This condition emphasizes the importance of numerical validation, making it more accessible compared to relying solely on analytical criteria.
- Numerical Experiment Validation: The proposed approach is comprehensively validated through numerical experiments conducted on two physical systems, providing valuable insights into its performance.

- Comparison with Existing Scheme: A comparison between the proposed scheme and the existing geometric Itô-Taylor 1.5 strong scheme underscores the necessity of employing a symplectic numerical integration scheme. The proposed formulation results in a remarkable reduction of approximately 98% in the Hamiltonian global error, highlighting the clear advantages of the symplectic approach.

- Trajectory Stability: Trajectory comparisons reveal that the proposed scheme produces stabilized trajectories, while the existing Geometric Taylor 1.5 Strong Scheme exhibits erratic behavior and unpredictable divergence.

- Hamiltonian Conservation: In the case of Coupled Pendulums and the tensegrity structure, the Hamiltonian remains bounded for a substantial portion of the simulation time (30% and 56%, respectively), confirming the energy conservation properties of the proposed numerical technique.

- Symplectic Conditions Validation: Validation of symplectic conditions for the tensegrity configuration demonstrates the effectiveness of the proposed formulation, resulting in a significant reduction in the global error compared to the non-symplectic existing scheme.

- Preservation of Symplectic Structure: Examination of the variable $\frac{\partial q_{n+1}}{\partial q_n}\frac{\partial \pi_{n+1}}{\partial \pi_n}$ confirms the preservation of the symplectic structure, reinforcing the superior performance and effectiveness of the proposed symplectic numerical integration scheme in accurately capturing the dynamics of physical systems.

- Sensitivity to Noise: An analysis using RBPD reveals that increasing noise intensities lead to the emergence of new attractors, indicating chaotic behavior in the system and highlighting its sensitivity to noise in shaping its behavior.

The transition from the current chapter to the next marks a shift in focus from the exploration of Stochastic Hamiltonian Differential Equations (SHDE) with specific attention to Hamiltonian systems and the utilization of a geometric Ito-Taylor 1.0 numerical integration scheme. In contrast, the upcoming chapter broadens the scope, addressing the modeling of systems on a general class of manifolds and employing a geometric Ito-Taylor 1.5 scheme. SHDEs have been pivotal in modeling complex natural phenomena, offering insights into the interaction of stochasticity and Hamiltonian mechanics

and enriching the understanding of intricate dynamics across diverse fields. Nonetheless, the challenges presented by these models, including non-linearity, stochasticity, geometric complexities, and their non-symplectic nature, necessitate advanced numerical techniques. The next chapter delves into the broader context of real-world phenomena unfolding within mathematical manifolds characterized by randomness and non-Euclidean geometries. Here, the core emphasis is on preserving the intrinsic geometric properties of the manifold and accurately addressing uncertainty, with the introduction of symplectic geometric Ito-Taylor 1.5 numerical integration scheme. This not only enhances the practical applicability of SHDEs but also ensures a more accurate representation of manifold-based systems within this extended framework.

Chapter 6

Symplectic Geometric Integration on a General Class of Manifolds

6.1 Introduction

In various scientific fields, real-world phenomena are often characterized by randomness and evolve within the mathematical framework of manifolds, which are complex mathematical spaces with non-Euclidean geometries. Stochastic Hamiltonian differential equations are frequently used to describe the evolution of stochastic phenomena on manifolds, combining deterministic dynamics with random fluctuations. Traditional numerical integration techniques for solving differential equations on manifolds struggle to adequately address uncertainty and preserve the manifold's intrinsic geometric properties, leading to inaccurate results [15, 29]. Symplectic integration schemes play a pivotal role in maintaining the integrity of phase space across diverse scientific and engineering domains. While numerous symplectic integration schemes exist to uphold the geometric properties of Hamiltonians in stochastic systems [75, 76, 77, 78, 79, 80, 81], there remains a notable gap in the literature concerning symplectic integration schemes tailored specifically for stochastic Hamiltonian systems evolving within geometric spaces or manifolds. The primary contribution of this chapter lies in the formulation based on the metric tensor and Christoffel symbol, while incorporating both stochastic and symplectic elements. The scope of this work encompasses a wide range of dynamical systems, including but not limited to stochastic Duffing oscillators, Kuramoto models, molecular dynamics, and the dynamics of magnetic dipoles on manifold geometry.

6.2 Motivations

- Real-world phenomena often exhibit randomness and evolve on manifolds, requiring the use of stochastic Hamiltonian differential equations for accurate modeling.

- Traditional numerical integration techniques on manifolds struggle to handle uncertainty and maintain geometric properties, leading to inaccuracies in results.
- The study aims to bridge the gap between deterministic and stochastic dynamics on manifolds by introducing a specialized numerical integration scheme that combines geometric accuracy and stochasticity.
- While previous research has explored deterministic dynamics on manifolds using Lie group-based approaches, existing integration schemes are not suitable for stochastic systems.
- The proposed framework expands the applicability of accurate representations across various scientific domains by accommodating both inherent randomness and complex manifold geometries.
- The study's objective is to provide a unified framework for stochastic Hamiltonian formulation on general manifolds, addressing challenges and unifying diverse systems within the stochastic Hamiltonian formulation paradigm.

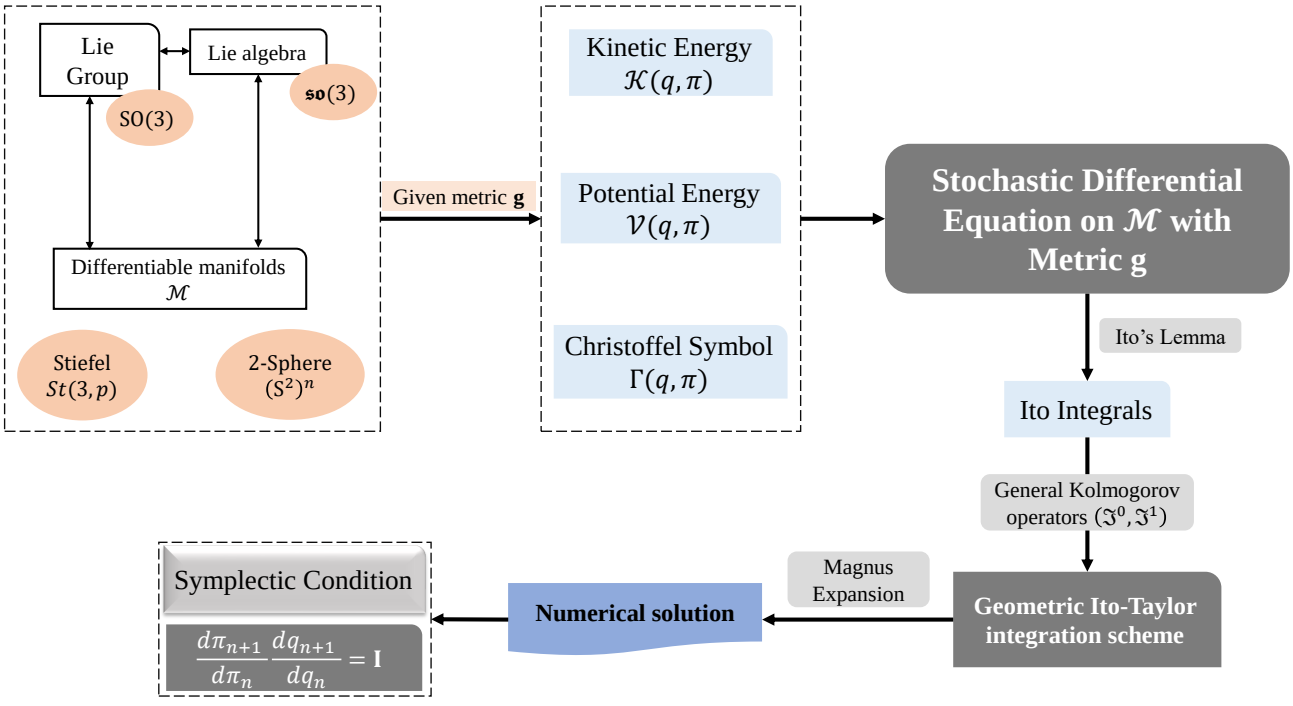

FIGURE 6.1: A schematic representation of the proposed methodology

A schematic of the proposed framework is provided in Fig. 6.1, where the formulation starts with considering a physical system evolving on a general manifold $\mathcal{M}$ with metric **g**. This is utilised for

forming the key components that are essential for the mathematical representation of the physical system, like energies and Christoffel symbol. These components are utilised to form geometric stochastic differential equations (GSDEs) on manifold $\mathcal{M}$. Thereafter, to solve the GSDEs, the framework formulates a symplectic Ito-Taylor-1.5 strong scheme for the stochastically excited systems evolving on the manifolds through establishing an association between manifold and lie algebra. This framework then provides a numerical solution for the undertaken system. Finally, the symplecticity of the proposed framework can be assessed with a symplectic condition provided in the subsequent section. The proposed framework in this study constitutes a major improvement in the field of geometric integration of stochastically excited dynamical systems. Specifically, it offers the following key contributions:

1. **Preservation of Geometry :** While traditional numerical integration methods often overlook the geometric essence of the manifold during simulations, the proposed Ito-Taylor scheme places a emphasis on satisfying the manifold's intrinsic geometric constraints at every discrete time step. This preservation is not only vital for accurate representations but also essential for retaining the system's true behavior in the manifold space.

2. **Incorporation of Uncertainty :** The Ito-Taylor integration scheme accounts for the inherent uncertainty in terms of stochastic forcing in the system. The method constructs a more inclusive representation of the real-world dynamics, wherein uncertainty plays a pivotal role in interpreting observed behaviors.

3. **Symplectic Nature :** A key contribution of the proposed scheme is its adherence to symplectic conditions. Symplectic algorithms, designed primarily for Hamiltonian systems, possess the unique property of conserving a particular mathematical str ucture known as the symplectic form. This property ensures that the algorithm preserves important characteristics of the system's dynamics, such as the volume conservation in phase space over extended periods of time. This preservation is crucial for accurate long-term simulations and mitigates issues like energy drift that often plague non-symplectic methods.

6.3 Essential notions from differentiable manifolds

This examines a manifold denoted as $\mathcal{M}$, which is embedded within the n-dimensional Euclidean space $\mathbb{R}^n$. This means that each point $q \in \mathcal{M}$ is described by a vector in $\mathbb{R}^n$, without resorting to specific

coordinate systems or inherent geometric properties. When dealing with an embedded manifold or submersion, it is assumed that the functional gradients under consideration exhibit linear independence when assessed on the manifold [9]. A differentiable n-dimensional manifold comprises a collection $\mathcal{A}$ of special pairs (U_q, ξ_q), known as charts. Here, U_q are open subsets of $\mathbb{R}^n$ and ξ_q are injective mappings that take points from U_q to points on the manifold $\mathcal{M}$. In other words, $\xi_q : U_q \subset \mathbb{R}^n \to \mathcal{M}$ provides a way to associate points in $\mathbb{R}^n$ with points on $\mathcal{M}$. At a specific point $q \in \mathcal{M}$, the parameterization of $\mathcal{M}$ is given by considering the image of U_q under ξ_q, which can be expressed as $q \in \xi_q(U_q)$.

A *differentiable curve* on $\mathcal{M}$ with $\gamma(0) = q \in \mathcal{M}$ is denoted by $\gamma : \boldsymbol{I} \to \mathcal{M}$, and its tangent vector on the manifold $\mathcal{M}$ at point q is given by $\frac{d\gamma(s)}{ds}|_{s=0}$. The set of all tangent vectors at $q \in \mathcal{M}$ is represented by $\omega \in \mathrm{T}_q\mathcal{M}$. The tangent bundle of the manifold $\mathcal{M}$ is the set of pairs $(q, \omega) \in \mathcal{M} \times \mathrm{T}_q\mathcal{M}$ represented by $\mathrm{T}\mathcal{M}$. The elements in the tangent space $\omega \in \mathrm{T}_q\mathcal{M} \subset \mathbb{R}^n$ are represented by the cotangents $\pi \in \mathrm{T}_q^\star\mathcal{M}$, which represent sets of all linear functional defined on the tangent space as $\mathrm{T}_q\mathcal{M} \to \mathbb{R}^1$ and are known as duals of $\mathrm{T}_q\mathcal{M}$. The cotangent bundle is the set of pairs $(q, \pi) \in \mathcal{M} \times \mathrm{T}_q^\star\mathcal{M}$, which has its own manifold structure, denoted by $\mathrm{T}^\star\mathcal{M}$. The Riemannian differential manifold is equipped with a local metric that has a bilinear positive definite form $\mathrm{g}_q = (\,\cdot\,)_q : \mathrm{T}_q\mathcal{M} \times \mathrm{T}_q\mathcal{M} \to \mathbb{R}^1$. It is also defined by a local norm $|\omega|_q = (\omega \cdot \omega)_q^{1/2}$ for all $\omega \in \mathrm{T}_q\mathcal{M}$. For any arbitrary smooth function $\phi(q) : \mathcal{M} \to \mathbb{R}^1$, the Riemannian gradient at $q \in \mathcal{M}$ is given by $grad_q\phi(q)$, which satisfies $(\mathrm{grad}\phi(q) \cdot \omega)_q = \mathrm{d}\phi_q(\omega)$ for all $\omega \in \mathrm{T}_q\mathcal{M}$.

The covariant derivative of a vector field $\omega \in \mathrm{T}\mathcal{M}$ along the differential curve $\gamma(s) : \boldsymbol{I} \to \mathcal{M}$ on the manifold $\mathcal{M}$, equipped with an affine connection ∇, is given by $\nabla_{\frac{\partial\gamma(s)}{\partial s}}\omega$. If a vector field $\omega \in \mathrm{T}\mathcal{M}$ is parallel along the curve $\gamma(s)$, i.e., $\nabla_{\frac{\partial\gamma(s)}{\partial s}}\omega = 0$, then transporting the vector $\omega|_{s=0} = \omega_0$ along the curve $\gamma(s)$ is called parallel transport. The exponential of the manifold $exp : \mathrm{T}\mathcal{M} \to \mathcal{M}$ and the logarithm of the manifold $log : \mathcal{M} \to \mathrm{T}\mathcal{M}$ are defined locally for any arbitrary points $q, w \in \mathcal{M}$ such that $\dot{q} = log_q(w) \in \mathrm{T}q\mathcal{M}$ and $exp_q(\dot{q}) = w$. The geodesic curve, a special curve on the manifold $\mathcal{M}$ that minimizes the arc length between two points $q_1, 1_2 \in \mathcal{M}$, can be defined as a counter to straight lines connecting two points in Euclidean space. The geodesic distance between these points $q_1, 1_2 \in \mathcal{M}$ is denoted as $\mathfrak{m}(q_1, q_2) = |log_{q_1}(q_2)|$.

6.4 A new Lagrangian formulation of Stochastically excited systems on general manifolds

To begin with, this section outlines a novel generalized mathematical formulation that pertains to a certain class of nonlinear stochastic Hamiltonian systems on a general class of manifolds . The basis of this formulation is the variational principle. Included in this formulation are stochastic Hamiltonian dynamics, the geometric formulation of an Ito-Taylor-1.5 strong numerical integration scheme, and, the evaluation of the symplectic nature of the integrator for SDEs that are defined on a general manifold with metric **g** [91, 92]. The groundwork for geometric stochastic Hamiltonian dynamics is drawn from Section 4.2.1 of Chapter 4. However, the formulation of geometric stochastic Hamiltonian dynamics for the generalized manifold endowed with metric **g** represents a novel contribution. When it comes to physical systems that involve non-conservative forces due to stochastic excitation $\dot{W}(t)$, where $W(t)$ is a Wiener process [15], the Lagrangian $\mathrm{L}\,(q,\omega)$ is considered. The action integral $\mathcal{S}$ can be expressed in the following way:

$$\mathbb{S} = \int_{t_0}^{t_f} \mathrm{L}(q,\omega)dt - \int_{t_0}^{t_f} \mathrm{h}_1 \circ dB(t) \tag{6.1}$$

where, B is a representation of wiener process and h_1 represents the stochastic excitation intensity, and the symbol $\circ$ signifies the Stratonovich integral [20]. Consider a smooth curve on the manifold, which is parameterized by a parameter t, such that $q(t) = (q_1(t), q_2(t), \ldots, q_n(t)) : [t_0, t_f] \to \mathcal{M}$, where n is the dimension of the manifold. The infinitesimal variation of the action integral can be written as,

$$\delta\mathbb{S} = \int_{t_0}^{t_f} \left(\frac{\partial \mathrm{L}(q,\omega)}{\partial \omega} \cdot \delta\omega + \frac{\partial \mathrm{L}(q,\omega)}{\partial q} \cdot \delta q \right) dt - \int_{t_0}^{t_f} \left(\frac{\partial h_1}{\partial \omega} \cdot \delta\omega + \frac{\partial h_1}{\partial q} \cdot \delta q \right) \circ dB(t) \tag{6.2}$$

A variation of the curve $q(t)$ can be defined as a smooth family of curves $q(\epsilon, t)$, where ϵ is a parameter that describes the variation. The curve $q(0, t)$ is the original curve $q(t)$. If each curve $q(\epsilon, t)$ is a geodesic, then the variation is said to be a geodesic variation [9].

To compute the variation of the curve q, the variation vector field $V(\epsilon, t)$ $\left(= \frac{\partial q}{\partial \epsilon(\epsilon,t)}\Big|_{\epsilon=0}\right)$ should be considered. This vector field describes how the curve is varying in the direction of t. One can express the variation of the curve q in terms of the geodesic variation equation, which relates the variation vector field V to the Riemann curvature tensor of the manifold [9]. However, extensive formulation of the curvature tensor of the manifold can be challenging in general. Therefore, it is helpful to adopt the concept of mapping between the manifold $\mathcal{M}$ and its tangent bundle T$\mathcal{M}$. This work has adopted the

concept of exponential mapping, which is important for the later part of the derivation. The variation of $q(t)$ can be defined as:

$$q_i(\epsilon, t) = e^{\epsilon \hat{\gamma}_{ij}} q_j(t) \tag{6.3}$$

here $(\hat{\cdot})$ is the wedge operator which is the mapping from a vector in $\mathbb{R}^3$ to a skew-symmetric matrix in $\mathbb{R}^{3\times3}$ and $\gamma_i : [t_0, t_f] \rightarrow T_q\mathcal{M} \subset \mathbb{R}^3$ is a differential curve on the tangent space satisfying conditions $\gamma_i(t_0) = \gamma_i(t_f) = 0$. As the differential curve γ_i lies on $T_q\mathcal{M}$, without any loss of generality, q_i and γ_i are assumed to be orthogonal to each other. The infinitesimal variation can be computed as

$$\delta q = \frac{\partial}{\partial \epsilon} q_i(\epsilon, t)\Big|_{\epsilon=0} = \hat{\gamma}_{ij}(t) q_j(t) \tag{6.4}$$

Since $\frac{d}{dt}\partial q = \partial \dot{q}$, according to the commutative property of variation and differentiation, $\partial \dot{q}$ can be expressed as

$$\delta \dot{q} = \hat{\dot{\gamma}}_{ij}(t) q_j(t) + \hat{\gamma}_{ij}(t) \dot{q}_j(t) \tag{6.5}$$

This can further be used to obtain the infinitesimal variation of angular velocity ω by using the kinematic relation $\omega = \hat{q}(t)\dot{q}(t)$ as

$$\delta \omega_i = \hat{\delta q}_{ij}(t) \dot{q}_j(t) + \hat{q}_{ij}(t) \partial \dot{q}_j(t) \tag{6.6}$$

Substituting Eqs. (6.4) and (6.5) in Eq. (6.6), it becomes

$$\delta\omega = (\gamma(t) \times q(t)) \times \dot{q}(t) + q(t) \times (\dot{\gamma}(t) \times q(t) + \gamma(t) \times \dot{q}(t)) \tag{6.7}$$

after using the properties of cross product and utilizing orthogonality of $q(t)$ with $\dot{q}(t)$ and $\gamma(t)$, a reduced form of Eq. (6.7) is written as,

$$\delta\omega_i = (q(t) \otimes q(t))\, \hat{\gamma}_{ij}(t) \omega_j(t) + (\mathbf{I} - q(t) \otimes q(t))\, \gamma_i(t) \tag{6.8}$$

where, $(q_i(t) \otimes q_i(t))$ represents the projection along the vector $q_i(t)$, and, $\hat{\gamma}_i(t)\omega_i(t)$ are collinear with $q_i(t)$. On the other hand, $(\mathbf{I} - q_i(t) \otimes q_i(t))$ represents the orthogonal projection of $\gamma(t)$. Therefore, the infinitesimal variation of angular velocity can be represented as,

$$\delta\omega_i = \hat{\gamma}_{ij}(t) \omega_j(t) + (\mathbf{I} - q(t) \otimes q(t))\, \dot{\gamma}_i(t) \tag{6.9}$$

Substituting Eqs. (6.4) and (6.9) in Eq. (6.2), the infinitesimal change in the action integral can be expressed as follows: written as,

$$\begin{aligned}\delta\mathbb{S} = &\int_{t_0}^{t_f}\left(\frac{\partial\mathcal{L}(q,\omega)}{\partial\omega_i}\cdot\left(\hat{\gamma}_{ij}\omega_j+\left(\mathbf{I}-q\otimes q\right)\dot{\gamma}_i\right)+\frac{\partial\mathcal{L}(q,\omega)}{\partial q_i}\cdot\hat{\gamma}_{ij}q_j\right)dt\\ &-\int_{t_0}^{t_f}\left(\frac{\partial h_1}{\partial\omega_i}\cdot\left(\hat{\gamma}_{ij}\omega_j+\left(\mathbf{I}-q\otimes q\right)\dot{\gamma}_i\right)+\frac{\partial h_1}{\partial q_i}\cdot\hat{\gamma}_{ij}q_j\right)\circ dB\end{aligned} \tag{6.10}$$

In the case of nonlinear oscillators evolving on a generic manifold equipped with the metric $\mathbf{g}(\cdot)$, the kinetic energy functional for the particle can be expressed as:

$$\mathcal{K}=\frac{1}{2}\mathrm{m}\left(\dot{q}\cdot\dot{q}\right)=\frac{1}{2}\mathrm{m}g_{ij}\dot{q}_i\dot{q}_j \tag{6.11}$$

where, m is mass of the particle and the potential energy is given as $\mathcal{V}_q(q)$. The Lagrangian function is given as

$$\mathcal{L}(q,\dot{q})=\frac{1}{2}\mathrm{m}g_{ij}\dot{q}_i\dot{q}_j-\mathcal{V}_q(q) \tag{6.12}$$

which can be modified for the angular velocity ω as,

$$\mathcal{L}(q,\omega)=\frac{1}{2}\mathrm{m}g_{ij}\omega_i\omega_j-\mathcal{V}_q(q) \tag{6.13}$$

Substituting Eq. (6.13) in Eq. (6.10), $\delta\mathbb{S}$ can be written as,

$$\begin{aligned}\delta\mathbb{S} = &\int_{t_0}^{t_f}\left(\mathrm{m}g_{ij}\omega_j\cdot\left(\hat{\gamma}_{ir}\omega_r+\left(\mathbf{I}-q\otimes q\right)\dot{\gamma}_i\right)+\left(\frac{1}{2}\mathrm{m}\frac{\partial g_{mn}}{\partial q_i}\omega_m\omega_n-\frac{\partial\mathcal{V}_q}{\partial q_i}\right)\cdot\hat{\gamma}_{ij}q_j\right)dt\\ &-\int_{t_0}^{t_f}\left(\frac{\partial h_1}{\partial\omega_i}\cdot\left(\hat{\gamma}_{ij}\omega_j+\left(\mathbf{I}-q\otimes q\right)\dot{\gamma}_i\right)+\frac{\partial h_1}{\partial q_i}\cdot\hat{\gamma}_{ij}q_j\right)\circ dB\end{aligned} \tag{6.14}$$

which then can be rearranged in the following form,

$$\begin{aligned}\delta\mathbb{S} = &\int_{t_0}^{t_f}\left(\left(\mathbf{I}-q\otimes q\right)\left(\mathrm{m}g_{ij}\omega_j dt-\frac{\partial h_1}{\partial\omega_i}\circ dB\right)\right)\cdot\dot{\gamma}\\ &-\int_{t_0}^{t_f}\left(\left(\mathrm{m}\hat{\omega}_{ir}g_{ij}\omega_j+\frac{1}{2}\mathrm{m}\hat{q}_{ir}\frac{\partial g_{mn}}{\partial q_i}\omega_m\omega_n-\hat{q}_{ir}\frac{\partial\mathcal{V}_q}{\partial q_i}\right)dt-\left(\hat{\omega}_{ir}\frac{\partial h_1}{\partial\omega_i}+\hat{q}_{ir}\frac{\partial h_1}{\partial q_i}\right)\circ dB\right)\cdot\gamma_r\end{aligned} \tag{6.15}$$

Integrating the term with $\dot{\gamma}$, one can get the following form,

$$\delta\mathbb{S} = \left((\mathbf{I} - q \otimes q)\left(\mathrm{m}g_{ij}\omega_j dt - \frac{\partial h_1}{\partial \omega_i} \circ dB\right)\right) \cdot \gamma \Big|_{t_f}^{t_f} - \int_{t_0}^{t_f} \frac{d}{dt}\left((\mathbf{I} - q \otimes q)\left(\mathrm{m}g_{ij}\omega_j dt - \frac{\partial h_1}{\partial \omega_i} \circ dB\right)\right) \cdot \gamma$$
$$- \int_{t_0}^{t_f} \left(\left(\mathrm{m}\hat{\omega}_{ir} g_{ij}\omega_j + \frac{1}{2}\mathrm{m}\hat{q}_{ir}\frac{\partial g_{mn}}{\partial q_i}\omega_m\omega_n - \hat{q}_{ir}\frac{\partial \mathcal{V}_q}{\partial q_i}\right) dt - \left(\hat{\omega}_{ir}\frac{\partial h_1}{\partial \omega_i} + \hat{q}_{ir}\frac{\partial h_1}{\partial q_i}\right) \circ dB\right) \cdot \gamma_r \tag{6.16}$$

here, the differentiable function γ satisfies $\gamma \cdot q$ and vanishes at t_0 and t_f. According to the Hamilton's principle, the incremental variations $\delta\mathbb{S}$ becomes zero, therefore,

$$\frac{d}{dt}\left((\mathbf{I} - q \otimes q)\left(\mathrm{m}g_{ij}\omega_j - \frac{\partial h_1}{\partial \omega_i} \circ \dot{B}\right)\right)$$
$$+ \left(\mathrm{m}\hat{\omega}_{ir} g_{ij}\omega_j + \frac{1}{2}\mathrm{m}\hat{q}_{ir}\frac{\partial g_{mn}}{\partial q_i}\omega_m\omega_n - \hat{q}_{ir}\frac{\partial \mathcal{V}_q}{\partial q_i}\right) - \left(\hat{\omega}_{ir}\frac{\partial h_1}{\partial \omega_i} + \hat{q}_{ir}\frac{\partial h_1}{\partial q_i}\right) \circ \dot{B} = 0 \tag{6.17}$$

by writing $(\mathbf{I} - q \otimes q)$ with indicial notation, one can modify Eq. (6.17) as,

$$\frac{d}{dt}\left(\hat{q}_{rs}\hat{q}_{si}\left(\mathrm{m}g_{ij}\omega_j - \frac{\partial h_1}{\partial \omega_i} \circ \dot{B}\right)\right)$$
$$+ \left(\mathrm{m}\hat{\omega}_{ir} g_{ij}\omega_j + \frac{1}{2}\mathrm{m}\hat{q}_{ir}\frac{\partial g_{mn}}{\partial q_i}\omega_m\omega_n - \hat{q}_{ir}\frac{\partial \mathcal{V}_q}{\partial q_i}\right) - \left(\hat{\omega}_{ir}\frac{\partial h_1}{\partial \omega_i} + \hat{q}_{ir}\frac{\partial h_1}{\partial q_i}\right) \circ \dot{B} = 0 \tag{6.18}$$

Taking the derivative of the first term in Eq. (6.18), it can be written as,

$$2\mathrm{m}\hat{\dot{q}}_{ri} g_{ij}\omega_j + \mathrm{m}\hat{q}_{ri}\frac{dg_{in}}{dq_m}\omega_m\omega_n + \mathrm{m}\hat{q}_{rs}\hat{q}_{si} g_{ij}\dot{\omega}_j - 2\hat{\dot{q}}_{ri}\frac{\partial h_1}{\partial \omega_i} \circ \dot{B} - \hat{q}_{rs}\hat{q}_{si}\frac{d}{dt}\left(\frac{\partial h_1}{\partial \omega_i}\right) \circ \dot{B}$$
$$+ \left(m\hat{\omega}_{ir} g_{ij}\omega_j + \frac{1}{2}m\hat{q}_{ir}\frac{\partial g_{mn}}{\partial q_i}\omega_m\omega_n - \hat{q}_{ir}\frac{\partial \mathcal{V}_q}{\partial q_i}\right) - \left(\hat{\omega}_{ir}\frac{\partial h_1}{\partial \omega_i} + \hat{q}_{ir}\frac{\partial h_1}{\partial q_i}\right) \circ \dot{B} = 0 \tag{6.19}$$

Dividing Eq. (6.19) with mg_{ij} and rearranging the terms, we get

$$\hat{q}_{rs}\hat{q}_{si}\dot{\omega}_i = -2\hat{\dot{q}}_{ri}\omega_i - \hat{\omega}_{ir}\omega_i + \hat{q}_{ir} g^{ij}\left(\frac{dg_{in}}{dq_m} - \frac{1}{2}\frac{\partial g_{mn}}{\partial q_i}\right)\omega_m\omega_n - \frac{1}{m}g^{ij}\hat{q}_{ri}\frac{\partial \mathcal{V}_q}{\partial q_j}$$
$$+ \frac{1}{m}g^{ij}\left(2\hat{\dot{q}}_{ri}\frac{\partial h_1}{\partial \omega_j} + \hat{q}_{rs}\hat{q}_{si}\frac{d}{dt}\left(\frac{\partial h_1}{\partial \omega_j}\right) + \hat{\omega}_{ir}\frac{\partial h_1}{\partial \omega_j} + \hat{q}_{ir}\frac{\partial h_1}{\partial q_j}\right) \circ \dot{B} \tag{6.20}$$

After substituting the constraints $\omega \cdot q = 0$, utilizing the expression of Christoffel symbol Γ_{ij}^k [93, 94, 95, 96], Eq. 6.20 can be re-written as,

$$\hat{q}_{rs}\hat{q}_{si}\dot{\omega}_i = m\hat{q}_{jr}\Gamma_{mn}^j\omega_m\omega_n - \frac{1}{m}g^{ij}\hat{q}_{ri}\frac{\partial \mathcal{V}_q}{\partial q_j}$$
$$+ \frac{1}{m}g^{ij}\left(2\hat{\dot{q}}_{ri}\frac{\partial h_1}{\partial \omega_j} + \hat{q}_{rs}\hat{q}_{si}\frac{d}{dt}\left(\frac{\partial h_1}{\partial \omega_j}\right) + \hat{\omega}_{ir}\frac{\partial h_1}{\partial \omega_j} + \hat{q}_{ir}\frac{\partial h_1}{\partial q_j}\right) \circ \dot{B} \tag{6.21}$$

Therefore, the final form of Lagrangian Equation of motion for a particle evolving on a general manifold endowed with a metric **g** under stochastic excitation can be written as,

$$\begin{aligned} \dot{q} &= \omega \times q \\ (\mathbf{I} - q \otimes q)\, m\dot{\omega} &= -mq \times \Gamma(\omega, \omega) - q \times \nabla_q \mathcal{V} + \mathcal{F} \circ \dot{B} \end{aligned} \tag{6.22}$$

where, the gradient of potential and the stochastic forcing intensity are defined as,

$$\begin{aligned} &\nabla_q \mathcal{V} = \mathbf{g}^{-1} \frac{\partial \mathcal{V}_q}{\partial q}, \\ &\mathcal{F} = 2(\omega \times q) \times \mathbf{g}^{-1} \frac{\partial h_1}{\partial \omega} + (\mathbf{I} - q \otimes q)\, \mathbf{g}^{-1} \frac{d}{dt}\left(\frac{\partial h_1}{\partial \omega}\right) + \omega \times \mathbf{g}^{-1} \frac{\partial h_1}{\partial \omega} + q \times \mathbf{g}^{-1} \frac{\partial h_1}{\partial q_j} \end{aligned}$$

Now, the variable π, which represents the conjugate variable of angular velocity, can be elegantly expressed in terms of angular velocity through the utilization of the Legendre transformation as,

$$\begin{aligned} \pi_k &= \left(\mathbf{I} - \mathbf{g}_{ij} \dot{q}_i \dot{q}_j\right) \frac{\partial \mathcal{L}(q,\dot{q})}{\partial \omega_k} \\ &= \mathrm{m} \mathbf{g}_{ki} \omega_i \end{aligned} \tag{6.23}$$

This transformative approach allows for a seamless transition between these two interconnected quantities within the domain of mechanics. Therefore, ω can be written as,

$$\omega_i = \frac{1}{\mathrm{m}} \mathbf{g}^{ki} \pi_k \tag{6.24}$$

The Legendre transformation serves as a pivotal tool in the field of classical mechanics, facilitating the conversion of a function's variables from one set of conjugate variables to another. In this particular scenario, it is employed to establish a functional relationship between the angular velocity ω and its conjugate counterpart π. So, the Hamiltonian for the undertaken mass point can be written as,

$$\begin{aligned} \mathcal{H}(q, \omega(\pi)) &= \pi_i \omega(\pi)_i - \frac{1}{2} \mathrm{m} \mathbf{g}_{ij} \omega(\pi)_i \omega(\pi)_j + \mathcal{V}_q(q) \\ &= \pi_i \frac{1}{\mathrm{m}} \mathbf{g}^{ki} \pi_k - \frac{1}{2} \mathrm{m} \mathbf{g}_{ij} \frac{1}{\mathrm{m}} \mathbf{g}^{ki} \pi_k \frac{1}{\mathrm{m}} \mathbf{g}^{lj} \pi_l + \mathcal{V}_q(q) \\ &= \frac{1}{2\mathrm{m}} \mathbf{g}^{ij} \pi_i \pi_j + \mathcal{V}_q(q) \\ &= \frac{1}{2\mathrm{m}} \pi^T \mathbf{g} \pi + \mathcal{V}_q(q) \end{aligned} \tag{6.25}$$

Utilising Eq. (6.24), Eq. (6.22) can be easily written as a function of q and π as,

$$\begin{aligned} \dot{q} &= \frac{1}{\mathrm{m}}\mathbf{g}^{-1}\pi \times q \\ (\mathbf{I} - q \otimes q)\,\dot{\pi} &= -\frac{\mathrm{g}}{\mathrm{m}} q \times \Gamma\left(\mathbf{g}^{-1}\pi, \mathbf{g}^{-1}\pi\right) - q \times \frac{\partial \mathcal{V}_q}{\partial q} + \mathbf{g}\mathcal{F} \circ \dot{B} \end{aligned} \tag{6.26}$$

6.5 Stochastic Dynamics on Unique Manifolds

This section provides a comprehensive analysis of several notable cases. It delves into the dynamics unfolding on the Stiefel manifold, investigating both the Euclidean and canonical metrics. Moreover, it explores the dynamics taking place on the quadratic hypersurface. This analysis offers valuable insights into the intricate dynamics within these diverse contexts.

6.5.1 Stochastic dynamics on the Stiefel manifold $\mathrm{St}(V, n, k)$

This section provides the application of the proposed framework on the (compact) Stiefel manifold [97, 93, 98, 99, 100], a mathematical construct where, let V denote a finite-dimensional real vector space with a dimension of n, and let k represent a positive integer such that $1 \leq k \leq n$. The Stiefel manifold $\mathrm{St}(V, n, k)$ is defined as the set of all orthonormal k frames in V, where a k frame is a collection of k linearly independent vectors $\mathbf{v}_1, \mathbf{v}_2, \ldots, \mathbf{v}_k \in V$ such that $\langle \mathbf{v}_i, \mathbf{v}_j \rangle = \delta_{ij}$ for all i and j, and δ_{ij} is the Kronecker delta. For defining the tangent Space at a Point, given a point $\mathbf{Q} = \{\boldsymbol{q}_1, \boldsymbol{q}_2, \ldots, \boldsymbol{q}_k\}$ on the Stiefel Manifold $\mathrm{St}(V, n, k)$, the tangent space $T_{\mathbf{Q}}\,\mathrm{St}(V, n, k)$ at $\mathbf{Q}$ is the set of all matrices $\mathbf{q} \in \mathbb{R}^{n \times k}$ such that each column of $\boldsymbol{\omega}$ is orthogonal to the corresponding column in $\mathbf{Q}$ and preserves the orthonormality constraint, i.e., for each column ω_i of $\boldsymbol{\omega}$ and $\boldsymbol{q}_j$ of $\mathbf{Q}$, $\langle \mathbf{q}_i, \boldsymbol{\omega}_j \rangle = 0$ and $\mathbf{q}^\top \mathbf{q} = \mathbf{I}_k$, where $\mathbf{I}_k$ is the $k \times k$ identity matrix. The normal space $N_{\mathbf{Q}}\,\mathrm{St}(V, n, k)$ at a point $\mathbf{Q}$ on the Stiefel Manifold $\mathrm{St}(V, n, k)$ is the orthogonal complement of the tangent space $T_{\mathbf{Q}}\,\mathrm{St}(V, n, k)$ in the ambient space $\mathbb{R}^{n \times k}$, denoted as $N_{\mathbf{Q}}\,\mathrm{St}(V, n, k) = \left\{\mathbf{Y} \in \mathbb{R}^{n \times k} \mid \langle \mathbf{Y}, \mathbf{q} \rangle = 0 \text{ for all } \mathbf{q} \in T_{\mathbf{Q}}\,\mathrm{St}(V, n, k)\right\}$. In other words, it consists of all matrices that are orthogonal to the tangent space at $\mathbf{Q}$ and satisfy the orthogonality condition $\langle \mathbf{Y}, \mathbf{q} \rangle = 0$.

Moving beyond theoretical discussions, the practical significance of the Stiefel manifold is evident in various real-world applications. Particularly, it serves as the cornerstone for signal representation through principal and minor component analysis [101]. It plays a pivotal role in blind source separation, intricately connected with signal pre-whitening and independent component analysis [102]. The

manifold's utility extends to nonnegative matrix factorization [103] and the domain of best basis search and selection [104]. However, the influence of the Stiefel manifold surpasses these boundaries. Its impact reaches into electronic structure computations, aiding in comprehending thermodynamics of bulk materials, surface dynamics, and crystal defects [105]. Moreover, it finds application in psychometrics, providing support for factor analysis [106].

Stochastic dynamics on St(n, p) with Euclidean Metric

The Euclidean metric between two tangent vectors $\mathbf{q}_1$ and $\mathbf{q}_2$ in the tangent space at a point $\mathbf{Q}$ can be defined as the Frobenius inner product:

$$\langle \mathbf{q}_1, \mathbf{q}_2 \rangle = \mathrm{tr}\left(\mathbf{q}_1^\top \mathbf{q}_2\right) \tag{6.27}$$

where $\mathrm{tr}(\cdot)$ is the trace of a matrix. Considering the Stiefel manifold denoted as $\mathrm{St}(n, p)$, the objective is to determine the Christoffel symbol $\Gamma_{\mathbf{q}}(\dot{\mathbf{q}}, \dot{\mathbf{q}})$, where $\dot{\mathbf{q}}$ signifies the tangent vector to a curve within this manifold. This form can be obtained through a variational principle, tailored to a specific metric. The variational principle is encapsulated as:

$$\int_0^1 \delta\, \mathrm{tr}\left(\dot{\mathbf{q}}^T \dot{\mathbf{q}}\right) dt = 0 \tag{6.28}$$

where δ denotes a variation and $\dot{\mathbf{q}}^T\dot{\mathbf{q}}$ corresponds to the metric tensor employed in the context of $\mathrm{St}(n, p)$. The goal is to find variations that render this integral equal to zero. Through a series of algebraic manipulations, the transformation of the integral to its final form can be written as [93]:

$$\int_0^1 \delta\, \mathrm{tr}\left(\dot{\mathbf{q}}^T \dot{\mathbf{q}}\right) dt = -2 \int_0^1 \mathrm{tr}\left(\ddot{\mathbf{q}}^T \delta\mathbf{q}\right) dt \tag{6.29}$$

where integration by parts has been utilized. The concept of variations comes into play, where $\delta\mathbf{q}$ symbolizes movement from a point along the curve $\mathbf{q}(t)$ to a point on a closely neighboring curve within $\mathrm{St}(n, p)$, both at time t. This variation corresponds to the tangent space $T_{\mathbf{q}}\,\mathrm{St}(n, p)$, capturing all feasible directions of change at point $\mathbf{q}$. The intrinsic form of the geodesic equation is established. For any arbitrary $\delta\mathbf{q}$ within the tangent space $T_{\mathbf{q}}\,\mathrm{St}(n, p)$, the condition $\mathrm{tr}(\ddot{\mathbf{q}}^T\delta\mathbf{q}) = 0$ holds, implying that the acceleration vector $\ddot{\mathbf{q}}$ is orthogonal to all variations in this tangent space. By verifying that $\ddot{\mathbf{q}}$ lies in the normal space $N_{\mathbf{q}}\,\mathrm{St}(n, p)$, the equation $\ddot{\mathbf{q}} = \mathbf{q}s$ is deduced, where s is a skew-symmetric matrix. Subsequently, by taking the second derivative of the constraint $\mathbf{q}^T\mathbf{q} = e$, where e is the identity

matrix, the geodesic equation $\ddot{\mathbf{q}} + \mathbf{q}\dot{\mathbf{q}}^T\dot{\mathbf{q}} = 0$ is formed. Substituting the derived expression for $\ddot{\mathbf{q}}$ into the derived geodesic equation, it is determined that $s = -\dot{\mathbf{q}}^T\dot{\mathbf{q}}$. Consequently, the final equation representing the geodesic paths on the Stiefel manifold is represented as

$$\ddot{\mathbf{q}} + \mathbf{q}\dot{\mathbf{q}}^T\dot{\mathbf{q}} = 0 \tag{6.30}$$

and, simultaneously the Christoffel symbol is represented as

$$\Gamma_{\mathbf{q}}(\dot{\mathbf{q}}, \dot{\mathbf{q}}) = \mathbf{q}(\dot{\mathbf{q}}^T\dot{\mathbf{q}}) \tag{6.31}$$

This expression describes the inner product of the vector $\dot{\mathbf{q}}$ with itself, considering the metric defined by $\mathbf{q}$ within the tangent space $T_{\mathbf{q}}\,\mathrm{St}(n,p)$. The derivation of the Christoffel form $\Gamma_{\mathbf{x}}(\cdot,\cdot)$ was accomplished using intrinsic coordinates exclusively, avoiding any reliance on extrinsic coordinate components. In order to finalize the extended Hamiltonian system, it is essential to compute the Riemannian gradient $\nabla_{\mathbf{q}}V$. The functional Riemannian gradient $V : \mathrm{St}(n,p) \to \mathbb{R}$ at a point $\mathbf{q} \in \mathrm{St}(n,p)$ is defined as the distinct matrix within $T_{\mathbf{q}}\,\mathrm{St}(n,p)$ that fulfills the following condition:

$$\mathrm{tr}\left(u^T\partial_{\mathbf{q}}V\right) = \langle u, \nabla_{\mathbf{q}}V\rangle_{\mathbf{q}} \quad \forall u \in T_{\mathbf{q}}\,\mathrm{St}(n,p). \tag{6.32}$$

This condition can be represented as $\mathrm{tr}\left(u^T\left(\partial_{\mathbf{q}}V - \nabla_{\mathbf{q}}V\right)\right) = 0$, leading to $\nabla_{\mathbf{q}}V = \partial_{\mathbf{q}}V + \mathbf{q}s$, where s is a symmetric matrix. Multiplying this equation by the matrix $\mathbf{q}^T$ results in $s + \mathbf{q}^T\partial_{\mathbf{q}}V = \mathbf{q}^T\nabla_{\mathbf{q}}V$. Transposing both sides of the equation and summing term by term leads to:

$$s = -\frac{1}{2}\left(\partial_{\mathbf{q}}^T V\mathbf{q} + \mathbf{q}^T\partial_{\mathbf{q}}V\right) + \frac{1}{2}\left(\nabla_{\mathbf{q}}^T V\mathbf{q} + \mathbf{q}^T\nabla_{\mathbf{q}}V\right). \tag{6.33}$$

Given that $\nabla_{\mathbf{q}}V \in T_{\mathbf{q}}\,\mathrm{St}(n,p)$, as per the property of the tangent space on the Stiefel manifold, the relation $\nabla_{\mathbf{q}}^T V\mathbf{q} + \mathbf{q}^T\nabla_{\mathbf{q}}V = 0$ holds. In conclusion, the desired Riemannian gradient is expressed as:

$$\nabla_{\mathbf{q}}V = \partial_{\mathbf{q}}V - \frac{1}{2}\mathbf{q}\left(\partial_{\mathbf{q}}^T V\mathbf{q} + \mathbf{q}^T\partial_{\mathbf{q}}V\right). \tag{6.34}$$

Stochastic dynamics on St(n,p) with Canonical Metric

This section introduces the dynamics within the Stiefel manifold, accompanied by a distinctive metric. This metric, represented as $\mathbf{g}$ in Equation (6.35), is not uniformly distributed across the manifold. It's defined as follows:

$$g = \left(e_n - \frac{1}{2}\mathbf{q}\mathbf{q}^T\right) \tag{6.35}$$

Continuing from the preceding section, by utilizing the variational principle, calculating the variation, and employing integration by parts, the subsequent equation emerges:

$$\frac{d}{dt}\left(\left(e_n - \frac{1}{2}\mathbf{q}\mathbf{q}^T\right)\dot{\mathbf{q}}\right) + \frac{1}{2}\dot{\mathbf{q}}\dot{\mathbf{q}}^T\mathbf{q} = \mathbf{q}\mathbf{s} \quad \mathbf{s} = -\dot{\mathbf{q}}^T\dot{\mathbf{q}} - \left(\mathbf{q}^T\dot{\mathbf{q}}\right)^2. \tag{6.36}$$

Expanding the aforementioned expressions leads to the derivation of the Christoffel function as follows:

$$\Gamma_{\mathbf{q}}(\dot{\mathbf{q}},\dot{\mathbf{q}}) = -\dot{\mathbf{q}}\dot{\mathbf{q}}^T\mathbf{q} - \mathbf{q}\dot{\mathbf{q}}^T\left(e_n - \mathbf{q}\mathbf{q}^T\right)\dot{\mathbf{q}}, \quad \dot{\mathbf{q}} \in T_{\mathbf{q}}\,\mathrm{St}(n,p). \tag{6.37}$$

Considering the potential function $V : \mathrm{St}(n,p) \to \mathbb{R}$, its Riemannian gradient at a point $\mathbf{q} \in \mathrm{St}(n,p)$ using the metric from Equation (6.35), is denoted as the unique matrix $\nabla_{\mathbf{q}}V$ within $T_{\mathbf{q}}\,\mathrm{St}(n,p)$, satisfying the condition:

$$\mathrm{tr}\left(\mathbf{u}^T\left(\partial_{\mathbf{q}}V - \left(e_n - \frac{1}{2}\mathbf{q}\mathbf{q}^T\right)\nabla_{\mathbf{q}}V\right)\right) = 0 \forall \mathbf{u} \in T_{\mathbf{q}}\,\mathrm{St}(n,p). \tag{6.38}$$

This condition is expressed as:

$$\partial_{\mathbf{q}}V - \left(e_n - \frac{1}{2}\mathbf{q}\mathbf{q}^T\right)\nabla_{\mathbf{q}}V = \mathbf{q}\mathbf{s} \quad \mathbf{s} = \frac{1}{2}\left(\mathbf{q}^T\partial_{\mathbf{q}}V + \partial_{\mathbf{q}}^T V\mathbf{q}\right). \tag{6.39}$$

Through the resolution of the Riemannian gradient, the final expression is given by:

$$\nabla_{\mathbf{q}}V = \partial_{\mathbf{q}}V - \mathbf{q}\partial_{\mathbf{q}}^T V\mathbf{q}. \tag{6.40}$$

Utilising the Christofel symbol in Eq. (6.37) and the potential Riemannian gradient in Eq. (6.40), GSDE for any system evolving on the manifold St(n,p) with cannonical metric can be easily expressed utilising Eq. (6.22).

Stochastic dynamics on a Unit 2-sphere

The unit 2-sphere (S^2) is defined as a manifold embedded in three-dimensional Euclidean space $(\mathbb{R}^3)$ that consists of all points at a unit Euclidean distance of in $\mathbb{R}^3$. Mathematically, S^2 can be described as the set of points $\mathbf{q}$ satisfying:

$$S^2 = \left\{\mathbf{q} \in \mathbb{R}^3 \mid \|\mathbf{q}\| = 1\right\} \tag{6.41}$$

where $\|\mathbf{v}\|$ represents the Euclidean norm (length) of a vector $\mathbf{v}$. Tangent Space of Unit S^2 at a Point: The tangent space $T_{\mathrm{p}}S^2$ at a point p on the unit 2-sphere (S^2) is the two-dimensional vector subspace of $\mathbb{R}^3$ that is tangent to the sphere's surface at that point. It can be defined as the orthogonal complement of the vector $\boldsymbol{\eta}$:

$$T_{\boldsymbol{\eta}}S^2 = \left\{\mathbf{v} \in \mathbb{R}^3 \mid \langle \mathbf{v}, \boldsymbol{\eta}\rangle = 0\right\} \tag{6.42}$$

Normal Space of Unit S^2 at a Point: The normal space $N_{\boldsymbol{\eta}}S^2$ at a point $\boldsymbol{\eta}$ on the unit 2-sphere (S^2) is the vector space orthogonal to the tangent space $T_{\mathrm{p}}S^2$ at that point. It can be defined as:

$$N_{\boldsymbol{\eta}}S^2 = \left\{\mathbf{w} \in \mathbb{R}^3 \mid \langle \mathbf{w}, \mathbf{v}\rangle = 0 \text{ for all } \mathbf{v} \in T_{\boldsymbol{\eta}}S^2\right\} \tag{6.43}$$

In this context, the normal space captures directions that are orthogonal to the tangent plane at the given point, considering the unit 2-sphere.

The norm corresponding to the inner product described in Equation (72) aligns with the standard vector norm. Customization of the Christoffel symmetric form leads to the following expression:

$$\Gamma_q(\omega, \omega) = -\omega^T \omega q, \quad \omega \in T_q S^{n-1}, \tag{6.44}$$

After finding the equation of motion for the system, it calls for the solution of the geometric SDE to obtain the trajectory of the given non-linear oscillator. Therefore, besides developing the Lagrangian formulation of canonical oscillators with known potential, this work also proposes a symplectoc Ito-Taylor based numerical integration scheme for the solution of aforementioned geometry SDE in the following section.

6.6 Symplectic numerical integration scheme on the manifold $\left(\mathbf{S}^2\right)^n$

The concepts introduced in section 5.4 of Chapter 5 serve as the foundation for the ideas presented in this section. Although the variables are represented by different symbols, the formulations are similar

here and and the same is rewritten for the sake of completeness. This section presents the development of implicit Ito-Taylor-1.5 strong scheme which is symplectic in nature. As this study deals with the systems evolving on a general class of manifolds, consider a Stochastic Differential Equation (SDE) describing the evolution of a vector-valued variable q(t) on a general manifold as

$$dq(t) = \boldsymbol{\mu}(q(t), t)q(t)\mathrm{dt} + \boldsymbol{\theta}_r(q(t), t)q(t)\mathrm{dB}_t \tag{6.45}$$

Here, the drift coefficient $\boldsymbol{\mu}$ and diffusion coefficients $\boldsymbol{\mu}$ are matrix-valued, imparting direction and stochasticity to the evolution. The evolution of the variable $q(t) \in \mathcal{M}$ on the manifold is intricate due to its non-Euclidean nature, which requires the rigorous use of differential geometry, which is beyond the scope of the current work. To simplify this complexity and facilitate robust solvability, the concept of Lie group theory are introduced. These mathematical tools offer a structured approach to solve the SDE in Eq. (6.45). Specifically, the configuration manifolds whose structure can be associated with the Lie group SO(3). This association with the Lie group provides a powerful framework for understanding the underlying symmetries and transformations within the problem. To provide a solution, the work employs the Magnus expansion [22], a valuable technique in numerical analysis which satisfies the following expression: $q(t) = \mathbf{Exp}\left(\mathcal{P}(t)\right) q_0$. Here, $\mathbf{Exp}$ represents the Matrix Exponential [22] and while $\mathcal{P}$ signifies an assumed matrix-valued variable that is defined on the Lie algebra $\mathfrak{so}(3)$. This variable is associated with the following Stochastic Differential Equation (SDE):

$$\mathrm{d}\mathcal{P} = \boldsymbol{\eta}\mathrm{dt} + \boldsymbol{\phi}\mathrm{dB}_t \tag{6.46}$$

where, $\boldsymbol{\eta}$ is the drift and $\boldsymbol{\phi}$ is the diffusion term of the assumed SDE. This transformation to the Lie group's tangent space at identity enables the manipulation of the equation in a more solvable manner. The generality of the variable q is addressed by considering it as a functional $\mho(q(t), \mathcal{P}(t), t)$. This extension broadens the application of the equation. By applying Taylor's Series Expansion up to the second order, the differential of $\mho$ can be expressed. With the variable $q \in \mathcal{M}$, $\mathcal{P} \in \mathfrak{so}(3)$, the Taylor expansion of the functional $\mho$ upto second order can be written as,

$$\mathrm{d}\mho = (\partial_q \mho \partial_{\mathcal{P}_{ij}} q)\mathrm{d}\mathcal{P}_{ij} + \frac{1}{2}\left(\partial_{\mathcal{P}_{kl}}(\partial_{\mathcal{P}_{ij}} q \partial_q \mho)\right)\mathrm{d}\mathcal{P}_{kl}\mathrm{d}\mathcal{P}_{ij} \tag{6.47}$$

It is important to note that the inherits properties akin to those of Euclidean geometry ($\mathbb{R}^2$). This allows one to apply established stochastic process properties on $\mathbb{R}^2$ to this abstract space $\mathfrak{so}(3)$. One such

property is the Quadratic Variation of the Wiener Process, which has been extensively studied and documented in works [29].

By incorporating this property into the equation that describes the evolution of $\mathcal{P}$ (Eq. (6.46))in the Lie algebra (6.46), a deeper understanding is established of its stochastic behavior. The Quadratic Variation Property essentially captures the variability and fluctuations inherent in the evolution process. By extending this understanding to $\mathcal{P} \in \mathfrak{so}(n)$, one can refine the original equation (6.47) as,

$$d\mho = \left(\boldsymbol{\mu}\, \partial_q \mho\, \partial_{\mathcal{P}_{ij}} q + \frac{1}{2} \left(\partial_{\mathcal{P}_{kl}} (\partial_{\mathcal{P}_{ij}} q\, \partial_q \mho)\, \boldsymbol{\phi}_{kl} \phi_{ij} \right) \right) \mathrm{dt} + \phi_{ij}\, \partial_q \mho\, \partial_{\mathcal{P}_{ij}} q\, \mathrm{dB}_t \tag{6.48}$$

where, the Kolmogorov Operators are defined as,

$$\Im^0 = \boldsymbol{\mu}\, \partial_{\mathcal{P}_{ij}} q\, \partial_q(.) + \tfrac{1}{2} \boldsymbol{\phi}^2 \partial_{\mathcal{P}_{kl}} \left(\partial_{\mathcal{P}_{ij}} q\, \partial_q(.) \right), \quad \Im^1 = \boldsymbol{\phi} \partial_{\mathcal{P}_{ij}} q\, \partial_q(.) \tag{6.49}$$

The expression for $p\partial_{\mathcal{P}_{ij}} q$ are derived using the Exponential Gradient Theorem [22], yielding the following result:

$$\begin{aligned} p\partial_{\mathcal{P}_{ij}} q &= p\partial_{\mathcal{P}_{ij}} \exp^{\mathcal{P}} q_0 \\ &= \mathrm{dexp}_{\mathcal{P}}(p_{ij}) q \end{aligned} \tag{6.50}$$

Similarly, $s\partial_{\mathcal{P}_{ij}} q$ is found as $\mathrm{dexp}_{\mathcal{P}}(\phi_{ij}) q$ And, $\partial_{\mathcal{P}_{kl}} (\partial_{\mathcal{P}_{ij}} q \partial_q \mho) \boldsymbol{\phi}_{kl} \phi_{ij}$ is given by:

$$\begin{aligned} \partial_{\mathcal{P}_{kl}} (\partial_{\mathcal{P}_{ij}} q \partial_q \mho) \boldsymbol{\phi}_{kl} \phi_{ij} &= \partial_{\mathcal{P}_{kl}} (\partial_q \mho) \boldsymbol{\phi}_{r,ij} \partial_{\mathcal{P}_{ij}} q \boldsymbol{\phi}_{r,kl} + (\partial_q \mho) \partial_{\mathcal{P}_{kl}} (\partial_{\mathcal{P}_{ij}} q) \boldsymbol{\phi}_{r,ij} \boldsymbol{\phi}_{r,kl} \\ &= (\partial_q (\partial_q \mho) \partial_{\mathcal{P}_{kl}} q + \partial_q (\partial_{\mathcal{P}_{kl}} q) \partial_q \mho) \boldsymbol{\phi}_{r,ij} \partial_{\mathcal{P}_{ij}} q \boldsymbol{\phi}_{r,kl} + (\partial_q \mho) \boldsymbol{\phi}_{r,ij} \boldsymbol{\phi}_{r,kl} \partial_{\mathcal{P}_{kl}} (\partial_{\mathcal{P}_{kl}} q) \\ &= (\partial_q \partial_q \mho) \mathrm{dexp}_{\mathcal{P}}(\boldsymbol{\phi}_r) q \mathrm{dexp}_{\mathcal{P}}(\boldsymbol{\phi}_r) q + (\partial_q \mho) (\mathrm{dexp}_{\mathcal{P}}(\boldsymbol{\phi}_r)^2 q + \mathrm{M}_r q) \end{aligned} \tag{6.51}$$

Where,

$$\mathrm{M_r} = \sum_{p=0}^{\infty} \sum_{q=0}^{\infty} \frac{1}{(p+q+2)} \frac{(-1)^p}{p!(q+1)!} \mathrm{ad}_{\mathcal{P}}^{\mathrm{p}} (\mathrm{ad}_{\boldsymbol{\phi}_\mathrm{r}} (\mathrm{ad}_{\mathcal{P}}^{\mathrm{q}} (\boldsymbol{\phi}_r))) \tag{6.52}$$

The Kolmogorov Operators are modified to take the following form:

$$\begin{aligned} \Im^0 \mho &= \partial_q \mho \left(\mathrm{dexp}_{\mathcal{P}}(\boldsymbol{\eta}) q + \tfrac{1}{2} \mathrm{dexp}_{\mathcal{P}}(\boldsymbol{\phi}_r)^2 q + \tfrac{1}{2} \mathrm{M_r} q \right) + \left(\tfrac{1}{2} \partial_q \partial_q f \mathrm{dexp}_{\mathcal{P}}(\boldsymbol{\phi}_\mathrm{r}) \mathrm{q} \right) \mathrm{dexp}_{\mathcal{P}}(\boldsymbol{\phi}_\mathrm{r}) \mathrm{q} \\ \Im^1 \mho &= \partial_q \mho \mathrm{dexp}_{\mathcal{P}}(\boldsymbol{\phi}_\mathrm{r}) q \end{aligned} \tag{6.53}$$

By substituting $\mho = q$, Eq. (6.47) can be expressed as follows:

$$dq = \left(\phi_{ij} \partial_{\mathcal{P}_{ij}} + \frac{1}{2} \phi_{ij} \phi_{kl} (\partial_{\mathcal{P}_{ij}} \partial_{\mathcal{P}_{kl}}) \right) q \mathrm{dt} + \phi_{ij} (\partial_{\mathcal{P}_{ij}}) q \mathrm{dB} \tag{6.54}$$

Equating Eq.(6.45) with Eq.(F.5) and using the values obtained from Eqs.(F.3), gives:

$$\begin{aligned}\boldsymbol{\mu} &= \left(\mathrm{dexp}_{\boldsymbol{\eta}}(\boldsymbol{\eta}) + \frac{1}{2}\mathrm{dexp}_{\mathcal{P}}(\boldsymbol{\phi}_r)^2 + \frac{1}{2}\mathrm{M_r}\right)\\ \boldsymbol{\theta}_r &= \mathrm{dexp}_{\mathcal{P}}(\boldsymbol{\phi}_\mathrm{r})\end{aligned} \tag{6.55}$$

Furthermore, the state space matrices for the Stochastic Differential Equation (SDE) evolving on $\mathfrak{so}(3)$ are obtained using Baker's Inverse Identity [22]. These matrices are given by:

$$\begin{aligned}\boldsymbol{\eta} &= \mathrm{dexp}_{\mathcal{P}}^{-1}(\boldsymbol{\mu}) - \frac{1}{2}\mathrm{dexp}_{\mathcal{P}}^{-1}(\boldsymbol{\theta}_r^2) - \frac{1}{2}\mathrm{dexp}_{\mathcal{P}}^{-1}(M_r)\\ \boldsymbol{\phi}_\mathbf{r} &= \mathrm{dexp}_{\mathcal{P}}^{-1}(\boldsymbol{\theta}_r)\end{aligned} \tag{6.56}$$

It is noteworthy that representation of the Kolmogorov operators in Eq. (6.49) is general in nature, which can be tailored to more specific instances. Towards this, consider the tangent space ($\mathcal{T}_q S^2$), which exhibits similarities with the Euclidean framework and draws parallels with the Lie algebra $\mathfrak{so}(3)$. The Kolmogorov Operators on $\mathcal{T}_q S^2$ are expressed as follows:

$$\begin{aligned}\Im^0 &= p^V \partial_{\mathcal{P}^V_{ij}} q \partial_q(.) + \tfrac{1}{2}(s^V)^2 \partial_{\mathcal{P}^V_{kl}}\left(\partial_{\mathcal{P}^V_{ij}} q \partial_q(.)\right)\\ \Im^1 &= s^V \partial_{\mathcal{P}^V_{ij}} q \partial_q(.)\end{aligned} \tag{6.57}$$

When the Euclidean space aligns with the manifold $\mathcal{S}^2$ [15], the Kolmogorov Operators can be expressed in these simplified forms:

$$\begin{aligned}\Im^0 &= p^V \partial_q(.) + \tfrac{1}{2}(s^V)^2 \partial_{\mathcal{P}^V_{kl}}\left(\partial_q(.)\right)\\ \Im^1 &= s^V \partial_q(.)\end{aligned} \tag{6.58}$$

When expressed in integral form for the variable $\mathcal{P} \in \mathfrak{so}(n)$, and subsequently expanded using repeated substitution, the Ito-Taylor Strong 1.5 Scheme on the Lie algebra $\mathfrak{so}(3)$ is formulated as follows.

$$\begin{aligned}\mathcal{P}_{ij}(t) = \;& \mathcal{P}_{ij}(t_0) + \eta_{ij}(t_0)\int_{t_0}^{t} \mathrm{d}r_1 + \phi_{r,ij}(t_0)\int_{t_0}^{t} \mathrm{d}W_r(r_1) + \Im^r \phi_{r,ij}(t_0)\int_{t_0}^{t}\int_{t_0}^{r_1} \mathrm{d}B(r_2)\,\mathrm{d}B(r_1)\\ &+\Im^0 \eta_{ij}(t_0)\int_{t_0}^{t}\int_{t_0}^{r_1} \mathrm{d}r_2 \mathrm{d}r_1 + \Im^r \eta_{ij}(t_0)\int_{t_0}^{t}\int_{t_0}^{r_1} \mathrm{d}B(r_2)\,\mathrm{d}r_1 + \Im^0 \phi_{r,ij}(t_0)\int_{t_0}^{t}\int_{t_0}^{r_1} \mathrm{d}r_2 \mathrm{d}W_r(r_1)\\ &+\Im^r \Im^r \phi_{r,ij}(t_0)\int_{t_0}^{t}\int_{t_0}^{r_1}\int_{t_0}^{r_2} \mathrm{d}B(r_3)\,\mathrm{d}B(r_2)\,\mathrm{d}B(r_1) + \tilde{\mathcal{R}}(\mathcal{O}^3)\end{aligned} \tag{6.59}$$

Eq. (6.59), without considering the remainder, represents the geometric Taylor-1.5 scheme on the Lie algebra. This mapping is applicable only within the neighbourhood of $\mathcal{P}_{ij}$, which is locally similar to a Euclidean space. As a result, when discretized, the MSIs in Equation (6.59) will adopt the same form as outlined in the literature [15]. This similarity arises due to the isomorphism between $\mathbb{R}^3$ and $\mathfrak{so}(3)$,

which is demonstrated through the following lemma.

Lemma 6.6.1. *An isomorphism within the domain of Lie group theory links* $\mathfrak{so}(3)$ *and* $\mathbb{R}^3$*, employing the cross product in the form of Lie bracket. This correspondence enables the application of MSIs in* $\mathbb{R}^3$ *concerning the Lie algebra* $\mathfrak{so}(3)$*.*

Proof: Let $\mathfrak{so}(3)$ be a Lie algebra and $\mathbb{R}^3$ be a three-dimensional Euclidean space. Assumeing there exists a transformation $T : \mathfrak{so}(3) \to \mathbb{R}^3$ that preserves the Lie bracket structure. Consider the following stochastic differential equations (SDEs):

$$\begin{aligned} dq &= A\ dt + B\ dB_t, \quad q \in \mathfrak{so}(3) \\ dp &= C\ dt + D\ dB_t, \quad p \in \mathbb{R}^3 \end{aligned} \tag{6.60}$$

The linear transformation T is introduced to preserve the Lie bracket structure:

$$T([X,Y]) \in \mathfrak{so}(3) = [T(X), T(Y)] \in \mathbb{R}^3 \tag{6.61}$$

Thereafter, applying transformation T to both sides of the SDEs: For $\mathfrak{so}(3)$:

$$\begin{aligned} T\left(dq\right) &= T\left(A\ dt\right) + T\left(B\ dB_t\right), \quad q \in \mathfrak{so}(3) \\ T\left(dp\right) &= T\left(C\ dt\right) + T\left(D\ dB_t\right), \quad p \in \mathbb{R}^3 \end{aligned} \tag{6.62}$$

The focus now shifts to proving the equivalence of the stochastic integrals involving B_t. The first SDE in Eq. (6.62) for $\mathfrak{so}(3)$ is considered and the stochastic integral of a process X_t with respect to B_t is defined as the limit of Riemann sums:

$$\int_0^t X_s, dB_s = \lim_{n\to\infty} \sum_{i=0}^{n-1} X_{t_i}(B_{t_{i+1}} - B_{t_i}) \tag{6.63}$$

Where t_i is a partition of the interval $[0, t]$. The goal is to demonstrate that the mapping T preserves this stochastic integral structure.Assuming $X_t = B_t$, the mapping T is applied to both sides of the stochastic integral equation:

$$T\left(\int_0^t B_s dB_s\right) = T\left(\lim_{n\to\infty} \sum_{i=0}^{n-1} B_{t_i}(B_{t_{i+1}} - B_{t_i})\right) \tag{6.64}$$

Utilizing properties of the linear transformation T and the definition of Riemann sums, the following expression is obtained:

$$T\left(\int_0^t B_s dB_s\right) = \lim_{n\to\infty} \sum_{i=0}^{n-1} T(B_{t_i})(T(B_{t_{i+1}}) - T(B_{t_i})) \tag{6.65}$$

Given the isomorphism property $T([X,Y]) \in \mathfrak{so}(3) = [T(X), T(Y)] \in \mathbb{R}^3$, it is inferred that $T([B_{t_i}, B_{t_{i+1}}]\mathfrak{so}(3)$ $[T(Bt_i), T(B_{t_{i+1}})]\mathbb{R}^3$. Considering that the Lie bracket in $\mathfrak{so}(3)$ corresponds to the cross product, it follows that $Bt_i \times B_{t_{i+1}}$ in $\mathfrak{so}(3)$.

$$T\left(\int_0^t B_s dB_s\right) = \lim_{n\to\infty} \sum_{i=0}^{n-1} T(B_{t_i}) \times T(B_{t_{i+1}}) \tag{6.66}$$

Through a meticulous mapping of the stochastic integrals using the isomorphism between the Lie algebras, and by establishing the equivalence of their forms, it is demonstrated that the multiple stochastic integrals are identical for both cases. Therefore, Eq. (6.59) can be written as,

$$\begin{aligned}\mathcal{P}_{ij}(n+1) = \; & \mathcal{P}_{ij}(n) + \eta_{ij}\Delta t + \phi_{r,ij}\Delta B + \Im^0\eta_{ij}\tfrac{(\Delta t)^2}{2} + \Im^0\phi_{r,ij} \;\; (\Delta B\Delta t - \Delta Z_r) \\ & + \Im^1\phi_{r,ij}\tfrac{(\Delta B)^2 - \Delta t}{2} + \Im^1\eta_{ij}\Delta Z_r + \Im^1\Im^1\phi_{r,ij}\left(\tfrac{(\Delta B)^3}{6} - \tfrac{\Delta B\Delta t}{2}\right)\end{aligned} \tag{6.67}$$

In this context, ΔW follows a normal distribution with mean 0 and variance Δt. It's important to note that the assumed state space matrices, denoted as p and s respectively, will need to be determined as functions of the known state space matrices a and $\boldsymbol{\theta}_r$.

Implicit Framework: An implicit framework is employed for the proposed method on the Lie algebra $\mathfrak{so}(3)$, utilizing a sequential iteration process to update the state variable. This approach involves decomposing complex computations into smaller iterative steps, ensuring a systematic and refined technique for managing the updates within the mathematical context of $\mathfrak{so}(3)$. The method focuses on the variables $\mathcal{P}$ and ω on $\mathfrak{so}(3)$. Here, $\mathcal{P}$ corresponds to the position variable $q \in \mathcal{M}$ on the Lie algebra, governed by the SDE in Eq. (6.46), while $\omega \in \mathrm{T}_q\mathcal{M}$ represents the angular velocity of the particle with its corresponding SDE.

$$d\omega = \boldsymbol{\mathcal{U}}\mathrm{dt} + \boldsymbol{\mathcal{W}}\mathrm{dB} \tag{6.68}$$

Towards the implicit framework, the partitioning of the time step dt is done into M time instances, giving rise to an iterative update process indicated by $(\cdot)^i$. During each iteration, an interim value of $\omega \in \mathfrak{so}(3)$ is calculated. This approach is formally shown as the following equations,

$$\begin{aligned}\omega_{n+1}^{i+1} = \; & \omega_n^i + \mathcal{U}(q_n,\omega_n^i)\tfrac{\Delta \mathrm{t}}{2M} + \mathcal{W}(q_n,\omega_n^i)\Delta\mathrm{W} + \Im^0\mathcal{U}(q_n,\omega_n^i)\tfrac{(\Delta t)^2}{2M^2} + \Im^0\mathcal{V}(q_n,\omega_n^i) \;\; \left(\Delta B\tfrac{\Delta t}{M} - \Delta Z\right) \\ & + \tfrac{1}{2}\Im^1\mathcal{V}(q_n,\omega_n^i)\left((\Delta\mathrm{W})^2 - \tfrac{\Delta \mathrm{t}}{M}\right) + \Im^1\mathcal{U}(q_n,\omega_n^i)\Delta Z + \Im^1\Im^1\mathcal{V}(q_n,\omega_n^i)\left(\tfrac{(\Delta B)^3}{6} - \tfrac{\Delta B\Delta t}{2M}\right) \\ \mathcal{P}_{n+1}^i = \; & \mathcal{P}_n^i + \eta(q_n,\omega_n^{i+1})\tfrac{\Delta \mathrm{t}}{M} + \phi(q_n,\omega_n^{i+1})\Delta\mathrm{B} + \Im^0\eta(q_n,\omega_n^{i+1})\tfrac{(\Delta t)^2}{2M^2} + \Im^0\phi(q_n,\omega_n^{i+1}) \;\; \left(\Delta B\tfrac{\Delta t}{M} - \Delta Z\right) \\ & + \tfrac{1}{2}\Im^1\phi(q_n,\omega_n^{i+1})\left((\Delta\mathrm{W})^2 - \tfrac{\Delta \mathrm{t}}{M}\right) + \Im^1\eta(q_n,\omega_n^{i+1})\Delta Z + \Im^1\Im^1\phi(q_n,\omega_n^{i+1})\left(\tfrac{(\Delta B)^3}{6} - \tfrac{\Delta B\Delta t}{2M}\right)\end{aligned} \tag{6.69}$$

The iterative process, indicated by $i \in (0, 1, 2, \ldots, M)$, makes the update equation implicit rather than relying on an explicit formulation. As the update of $\mathcal{P}$ at $(n+1)^{th}$ step is obtained, the position q is updated utilising the theory of Magnus expansion: $q_{n+1} = \mathbf{Exp}\left(\mathcal{P}_{n+1}\right) q_n$. It is to be noted that this framework is not exclusive for the variable set (q, ω), it can also be applied to the set (q, π) considering the SDE given in Eq. (6.26). Within this framework, the initial conditions for the variables within $\mathfrak{so}(3)$ are established as $\omega_n^0 = \omega_n$ and $\mathcal{P}_n^0 = 0$. Notably, the multi-implicit characteristic of this framework becomes evident in the outcomes of the numerical experiments.

6.6.1 Symplecticity of the proposed geometric symplectic Ito-Taylor-1.5 strong scheme

Assessing the Geometric Ito-Taylor Numerical Scheme's capacity to uphold Hamiltonian integrity over extended periods necessitates an evaluation of its long term stability characteristics. This can be achieved by the evaluation of Symplecticity of the proposed framework, ensuring the scheme maintains the Hamiltonian system's inherent symplectic structure. Towards this, the focus shifts on assessing the symplectic structure, defined as:

$$\boldsymbol{A}^T \boldsymbol{J} \boldsymbol{A} = \boldsymbol{J} \tag{6.70}$$

The Eq. (6.70) is commonly referred to as a symplectic congruence. This equation has significance within the framework of symplectic transformations and mechanics, particularly when dealing with canonical transformations that preserve the symplectic structure of a phase space [6, 88]. The matrix $\boldsymbol{A}$ represents a linear transformation which in the present scenario is the matrix relating to the states of the Hamiltonian System as,

$$\mathrm{A} = \begin{bmatrix} \frac{\partial p_{n+1}}{\partial p_n} & \frac{\partial p_{n+1}}{\partial q_n} \\ \frac{\partial q_{n+1}}{\partial p_n} & \frac{\partial q_{n+1}}{\partial q_n} \end{bmatrix} \tag{6.71}$$

and $\boldsymbol{J}$ is the symplectic matrix and the equation signifies that the transformation A preserves the symplectic structure [89], ensuring that the symplectic matrix property remains unchanged. Symplectic congruences play a pivotal role in maintaining the symplectic properties of Hamiltonian systems and their associated canonical transformations. Assuming the states be independent of each other, Eq. (6.71) can be reduced as,

$$\mathrm{A} = \begin{bmatrix} \frac{\partial p_{n+1}}{\partial p_n} & 0 \\ 0 & \frac{\partial q_{n+1}}{\partial q_n} \end{bmatrix} \tag{6.72}$$

It signifies that the various components of the state variables (such as positions and momenta) are considered to be independent of each other. This assumption simplifies the mathematical formulation and analysis, allowing for a more tractable treatment of the system's behavior. And the matrix $\boldsymbol{J}$ is given by,

$$\mathrm{J} = \begin{bmatrix} 0 & I \\ -I & 0 \end{bmatrix} \tag{6.73}$$

After explaining how to establish symplecticity, the focus shifts towards deriving the same for the GSDE, which involves using the Hamiltonian formalism in a space defined by (q_i, π_i), where q_i is position and π_i is conjugate momentum. The GSDE being considered includes noise added specifically to the conjugate momentum domain. Now, consider the SDE of q given by Eq. (6.45) and consider the SDE of π as,

$$d\pi = \boldsymbol{\mathcal{C}}\mathrm{dt} + \boldsymbol{\mathcal{D}}\mathrm{dB} \tag{6.74}$$

Therefore the update equations of q and π are simultaneously given as,

$$\begin{aligned} q_{n+1} &= \mathrm{Exp}\left(\mathcal{P}_n + \eta\Delta t + \phi\Delta B + \Im^0\eta\tfrac{(\Delta t)^2}{2} + \Im^0\phi\ \ (\Delta B\Delta t - \Delta Z_r)\right. \\ &\quad \left. + \Im^1\phi\tfrac{(\Delta B)^2 - \Delta t}{2} + \Im^1\eta\Delta Z_r + \Im^1\Im^1\phi\left(\tfrac{(\Delta B)^3}{6} - \tfrac{\Delta B\Delta t}{2}\right)\right) q_n \\ \pi_{n+1} &= \pi_n + \boldsymbol{\mathcal{C}}\Delta t + \boldsymbol{\mathcal{D}}\Delta B_t + \Im^0\boldsymbol{\mathcal{C}}\tfrac{(\Delta t)^2}{2} + \Im^0\boldsymbol{\mathcal{D}}\left(\Delta B\Delta t - \Delta Z_r\right) + \Im^1\boldsymbol{\mathcal{D}}\tfrac{(\Delta B)^2 - \Delta t}{2} \\ &\quad + \Im^1\boldsymbol{\mathcal{C}}\Delta Z_r + \Im^1\Im^1\boldsymbol{\mathcal{D}}\left(\tfrac{(\Delta B)^3}{6} - \tfrac{\Delta B\Delta t}{2}\right) \end{aligned} \tag{6.75}$$

After several transformations, when the updated state at the $(n+1)$ step is differentiated using Eq. (6.75), a clear pathway to mathematically represent $\frac{\partial q_{n+1}}{\partial q_n}$ and $\frac{\partial \pi_{n+1}}{\partial \pi_n}$ in relation to the variables q_n and π_n emerges. This analytical formulation becomes particularly important for addressing specific problems within the given context. Now, to prove the symplecticity of the proposed geometric symplectic Taylor-1.5 scheme for a given problem, applying the property of symplectic congruence from Eq. (6.70), the following expression can be obtained.

$$\begin{bmatrix} \frac{\partial q_{n+1}}{\partial q_n} & 0 \\ 0 & \frac{\partial \pi_{n+1}}{\partial \pi_n} \end{bmatrix}^T \begin{bmatrix} 0 & I \\ -I & 0 \end{bmatrix} \begin{bmatrix} \frac{\partial q_{n+1}}{\partial q_n} & 0 \\ 0 & \frac{\partial \pi_{n+1}}{\partial \pi_n} \end{bmatrix} = \begin{bmatrix} 0 & I \\ -I & 0 \end{bmatrix} \tag{6.76}$$

Therefore, the problem of proving symplecticity boils down to proving the following equation.

$$\frac{\partial q_{n+1}}{\partial q_n}\frac{\partial \pi_{n+1}}{\partial \pi_n} = I \tag{6.77}$$

While achieving this analytically remains viable for simpler systems, it becomes difficult for the geometric SHDEs with more added dimensions. As a result, substantiating the validity of Eq. (6.77) through analytic means becomes increasingly cumbersome. By employing these simulations, the symplectic behavior of Hamiltonian system with higher dimensions can be captured effectively by using Eq. (6.77).

Algorithm 5 Geometric symplectic Taylor–1.5 strong algorithm for stochastic Hamiltonian system

Input: A manifold with metric **g**
Lagrangian of the system ▷ Refer Eq. (6.13)
Determine Christoffel symbol depending on the metric **g** ▷ $\Gamma(\omega, \omega)$
Geometric stochastic differential equation (GSDE) with variables $q \in \mathcal{M}$ and $\omega \in \mathrm{T}_q\mathcal{M}$ ▷ Refer Eq. (6.22)
Initialization for the time integration
for $n = 1 : Sample$ **do** ▷ Iteration for sample length
Identify the drift $\boldsymbol{\mu}$ and diffusion $\boldsymbol{\theta}$ coefficients for GSDE on manifold. ▷ Refer Eq. (6.45)
Accordingly form an SDE on $\mathfrak{so}(3)$ ▷ Refer Eq. (6.46)
Form another SDE for ω on $\mathfrak{so}(3)$ ▷ Refer Eq. (6.74)
Estimate the Kolmogorov operators $\Im^0$ and $\Im^1$ for drift and diffusion matrices of SDE on $\mathfrak{so}(3)$. ▷ Refer Eq. (6.53)
Utilise multistepping approach to update $\mathcal{P}$ on $\mathfrak{so}(3)$ ▷ Refer Eq. (6.69)
Estimate the states $q(n+1) \in \mathcal{M}$ utilising Magnus expansion. ▷ $q_{n+1} = \mathbf{Exp}\left(\mathcal{P}_{n+1}\right) q_n$
Update states $\omega_{ij}(n+1)$ on $\mathfrak{so}(3)$ implicitly with respect to q_{n+1}. ▷ Refer Eq. (6.69)
Output: Updated states: q and ω
Input: Evolution of the states q and ω at each time instance
Obtain π through Legendre transformation. ▷ Refer Eq. (6.23)
Obtain $\frac{\mathrm{d}\pi_{n+1}}{\mathrm{d}\pi_n}\frac{\mathrm{d}q_{n+1}}{\mathrm{d}q_n}$ numerically. ▷ Refer Eq. (6.77)
IF $\frac{\mathrm{d}\pi_{n+1}}{\mathrm{d}\pi_n}\frac{\mathrm{d}q_{n+1}}{\mathrm{d}q_n} = \mathbf{I}$
Output: Symplectic condition satisfied

6.7 Numerical Experiments

6.7.1 Stochastic Duffing oscillator on S^2

The stochastic Duffing oscillator on the S^2 configuration manifold is considered in this section. The manifold's curvature introduces the geodesic distance measurement in its curved space, allowing the extension of known oscillator potential functions to Riemannian manifolds [53]. This concept enables a smooth adaptation of standard oscillators, which have familiar potential functions in flat Euclidean space, to the more complex landscape of Riemannian manifolds. Here, the metric tensor (g) is considered Euclidean [93], therefore, the kinetic and potential energies for the undertaken oscillator on S^2 are given as,

$$K = \frac{1}{2}\mathrm{m}\left(\omega \cdot \omega\right), \quad V = \frac{1}{2}\mathrm{k}\mathfrak{m}^2\left(q, r\right) + \frac{1}{4}\alpha\mathfrak{m}^4\left(q, r\right) \tag{6.78}$$

Now the GSDE for undertaken system, using the Christoffel symbol defined as per the Eq. (6.44) is written as

$$\begin{aligned} \dot{q} &= \omega \times q \\ (\mathbf{I} - q \otimes q)\, \mathrm{m}\dot{\omega} &= -\mathrm{m} q \times \omega^T \omega q - q \times [\mathrm{k} + \alpha \mathfrak{m}\,(q, r)] \log_p (r) + \mathcal{F} \circ \dot{B} \end{aligned} \tag{6.79}$$

where, $\mathfrak{m} = acos(q \cdot r)$ is the Riemannian distance and stochastic forcing intensity defined as,

$$\mathcal{F} = 2\,(\omega \times q) \times \frac{\partial h_1}{\partial \omega} + (\mathbf{I} - q \otimes q)\, \frac{d}{dt}\left(\frac{\partial h_1}{\partial \omega}\right) + \omega \times \frac{\partial h_1}{\partial \omega} + q \times \frac{\partial h_1}{\partial q_j}$$

where, $(q, \omega) \in \mathrm{S}^2 \times \mathrm{T}_p\mathrm{S}^2$ are state variables, and $\dot{p} = \omega \times p$ is the kinematic equation. Here,

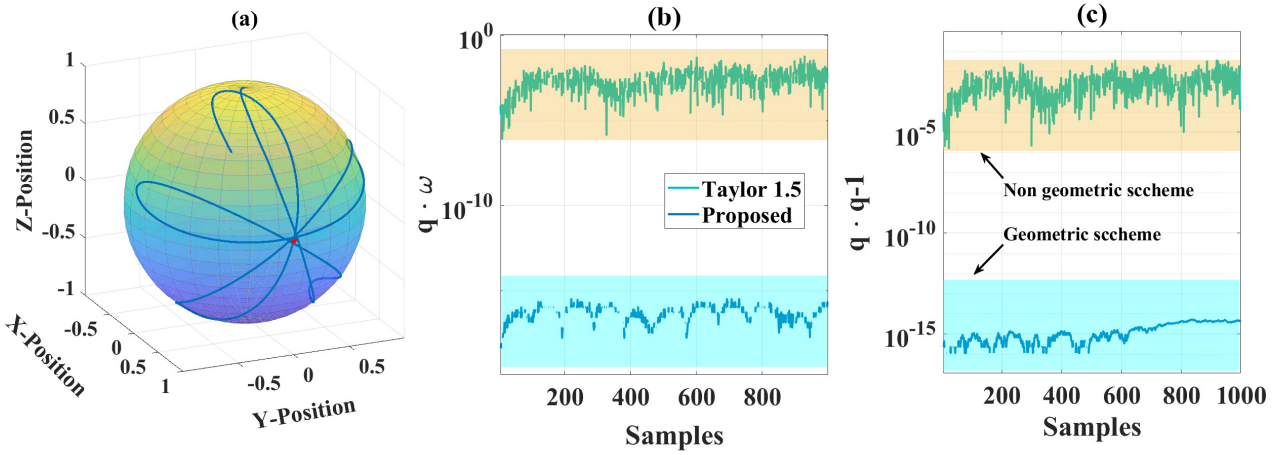

FIGURE 6.2: Stochastic duffing oscillator on S^2: (a) Response trajectory. Comparison of geometric constraints (b) on tangent space $\mathrm{T}_q\mathrm{S}^2$ (c) on sphere S^2 of the system solved using the proposed framework and existing non-geometric integrator.

$\mathrm{k} = 1$ is the linear coefficient, $\alpha = 0.5$ is non-linear coefficient and reference point is represented by $r = [1, 0, 0] \in \mathrm{S}^2$. The GSDE presented in Eq. (6.79) is numerically solved utilizing the proposed symplectic framework introduced in this study. The computed states, represented by the variables q and ω, capture the system's evolution without divergence. The trajectory of the system's response can be observed in Figure 6.2(a), where the evolution of the states q and ω is depicted. To further analyze the solution's characteristics, Figs. 6.2(b) and 6.2(c) provide insights into the geometric constraints imposed on the tangent bundle of the 2-sphere ($\mathrm{T}_q\mathrm{S}^2$) and the 2-sphere (S^2). From the Figs. 6.2(b) and 6.2(c), it can be observed that the error in the geometric constraints are of the order 10^{-3} for the solution through non geometric constraints, however the error reduces to 10^{-15} for the system solution through proposed framework. The comparison between the geometric and non-geometric schemes highlights the efficacy of the proposed geometric approach in reliably capturing the geometric

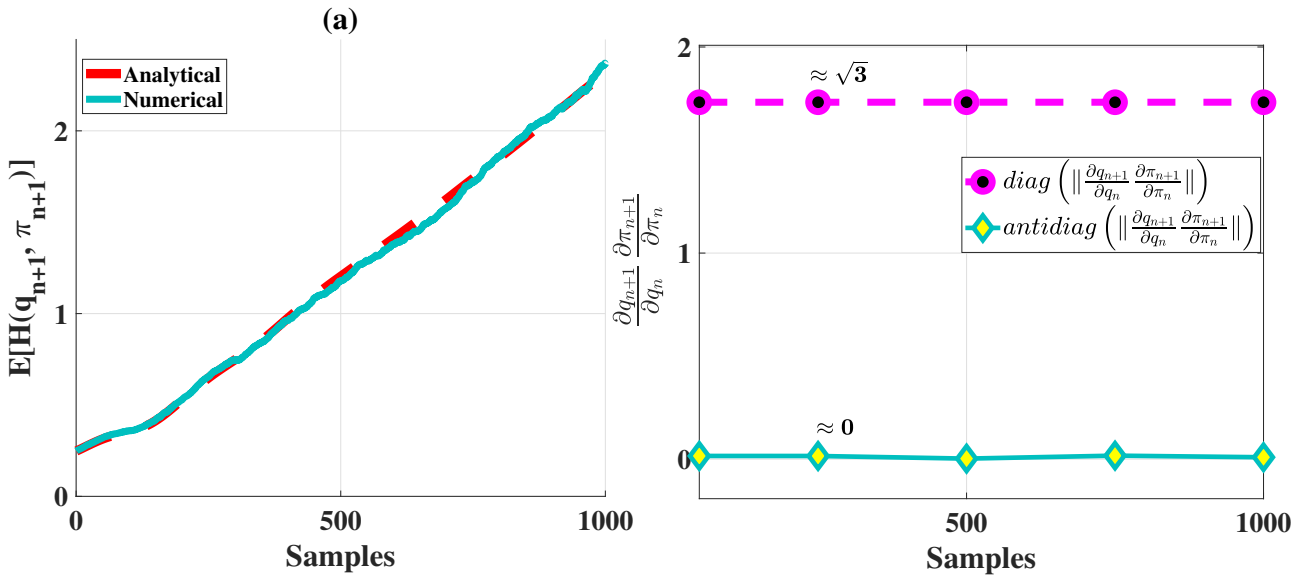

FIGURE 6.3: Stochastic duffing oscillator on S^2: (a) Comparison of analytical and numerical Hamiltonian function, (b) norms of the diagonal and anti-diagonal of $\frac{\mathrm{d}\pi_{n+1}}{\mathrm{d}\pi_n}\frac{\mathrm{d}q_{n+1}}{\mathrm{d}q_n}$ demonstrate the symplectic properties of the proposed framework

q

properties of the system trajectory. This study's findings underscore the importance of preserving the underlying geometric structure when numerically tackling dynamical systems governed by stochastic processes, as presented through the illustrative example of the GSDE in Equation (6.79). Upon investigating the system's geometric nature as established by the proposed framework, the focus now shifts towards a comprehensive analysis of its symplectic nature. An approach for accessing the symplectic characteristics of the proposed time integration approach involves monitoring the anticipated behavior of the numerical Hamiltonian with respect to its analytical counterpart. In the context of the present investigation, the Hamiltonian function is expressed in the following form:

$$\mathcal{H} = \frac{1}{2\mathrm{m}}\left(\pi \cdot \pi\right) + \frac{1}{2}\mathrm{k}\mathfrak{m}^2\left(q, r\right) + \frac{1}{4}\alpha\mathfrak{m}^4\left(q, r\right) \tag{6.80}$$

Here, π represents the conjugate of the angular velocity ω, a quantity derivable through the application of the Legendre transformation as outlined in Equation (6.24). Analytically, the expectation of update equation of the Hamiltonian yields,

$$\mathrm{E}\left[\mathcal{H}_{n+1}\right] = \mathrm{E}\left[\frac{1}{2\mathrm{m}}\left(\pi_{n+1} \cdot \pi_{n+1}\right) + \frac{1}{2}\mathrm{k}\mathfrak{m}^2\left(q_{n+1}, r\right) + \frac{1}{4}\alpha\mathfrak{m}^4\left(q_{n+1}, r\right)\right] \tag{6.81}$$

Subsequently, this expression is expanded to find a mathematical representation for $\mathrm{E}\left[\mathcal{H}(n+1)\right]$. This representation depends on the previous step's value $\mathrm{E}\left[\mathcal{H}(n)\right]$, as well as the states q_n and π_n. The next

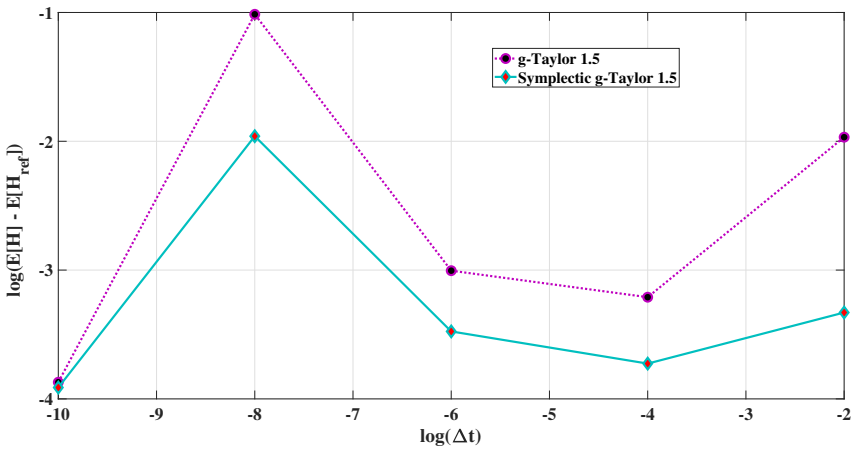

FIGURE 6.4: Stochastic duffing Oscillator on S^2: Comparison of Hamiltonian of the system solved using the proposed framework and existing non-symplectic integrator

step involves using Eq. (6.81) to numerically generate a set of Hamiltonian values, denoted as $\mathrm{E}\left[\mathcal{H}_{n+1}\right]$. By doing this, a comparison is made between these numerically obtained Hamiltonian values and the analytical ones. This comparison helps to determine the symplectic characteristics of the proposed computational framework. The graphical representation of these results, as shown in Fig. 6.3(a), clearly reveals a strong agreement between the numerical and analytical Hamiltonian values.

It's important to note that deriving the analytical form may become challenging when dealing with intricate systems featuring a larger number of states. As a result, this study employs an alternative methodology presented in Section 6.6.1, where the property of symplectic congruence is utilized. The analytical formulations for $\frac{\mathrm{d}\pi_{n+1}}{\mathrm{d}\pi_n}$ and $\frac{\mathrm{d}q_{n+1}}{\mathrm{d}q_n}$, pertinent to the considered system, are derived. These expressions capture the interrelationship between consecutive momenta and positions. Subsequently, these derived expressions are utilized to perform a numerical assessment of $\frac{\mathrm{d}\pi_{n+1}}{\mathrm{d}\pi_n}\frac{\mathrm{d}q_{n+1}}{\mathrm{d}q_n}$ at discrete time intervals. Fig. 6.3(b) shows the norm of the diagonal and anti-diagonal of $\frac{\mathrm{d}\pi_{n+1}}{\mathrm{d}\pi_n}\frac{\mathrm{d}q_{n+1}}{\mathrm{d}q_n}$ representing that Eq. (6.77) approximates the identity matrix, depicting symplectic nature of the proposed algorithm.

An alternative strategy for substantiating the improved performance of the symplectic framework in terms of system trajectory and energy preservation involves a comparative analysis of the maximum anticipated Hamiltonian. This is achieved by comparing the highest expected Hamiltonian values attained via the proposed scheme with those obtained using the geometric Euler-Maruyama method. This is done at finer time steps (dt $= 2^{-12}$ seconds) to ensure that it is the reference method. In Fig. 6.4, a graphical representation illustrating the variations in the global error of the Hamiltonian for varying

time steps change is presented. Specifically, the time step values considered are dt $= 2^{-10}$, 2^{-8}, 2^{-6}, 2^{-4}, and 2^{-2} seconds. The evaluation is conducted utilizing both the proposed scheme and the well-established non-symplectic geometric Taylor-1.5 scheme. The observed Hamiltonian error acts as a robust validation of the shadowing condition, which posits that the expection of Hamiltonian function computed through the proposed geometric symplectic scheme approximately aligns with the reference analytical solution. Evidently, the proposed scheme exhibits significantly lower error levels even at the coarser time steps in comparison to the non-symplectic geometric Taylor-1.5 scheme. The extent of error reduction achieved through the proposed formulation is $\approx 72\%$, further highlighting the benefits of the symplectic approach in contrast to non-symplectic methods. This analysis emphasizes the effectiveness of the proposed symplectic framework in precisely capturing the system's dynamics while preserving its energy across different time steps. The demonstrated reduction in global error corroborates with the robustness and reliability of the symplectic approach in simulating the system's behavior with significant precision and fidelity.

6.7.2 Stochastic duffing oscillator on St$(3, 1)$

Continuing from the preceding subsection, the current section undertakes an assessment of the effectiveness of the proposed framework for the Stochastic Duffing Oscillator on the Stiefel manifold denoted as St$(3, 1)$. In this context, the system's states are defined as $q \in St(3, 1)$, while their derivatives are $\dot{q} \in \mathrm{T}_q St$. Employing the Euclidean metric, the expression for the Kinetic energy can be formulated as follows:

$$K = \frac{1}{2}\mathrm{m}\dot{q}^T\dot{q} \tag{6.82}$$

By employing the identical potential energy as defined in Equation (6.78), and utilizing the Christoffel symbol outlined in Equation (6.31), the stochastic differential equation (SDE) can be represented as follows:

$$\begin{aligned} &(\mathbf{I} - q \otimes q)\,\mathrm{m}\dot{q} = -\mathrm{m}q\left(\dot{q}^T\dot{q}\right) - [\mathrm{k} + \alpha\mathfrak{m}\,(q, r)]\log_p(r) + \mathcal{F} \circ \dot{B} \\ &\dot{q}^T q + q^T\dot{q} = O \end{aligned} \tag{6.83}$$

where, $\mathcal{F}$ is the forcing function defined as a constant vector $[0.20.30.1]$. Fig. 6.5(a) illustrates a complex geometric relationship $\dot{q}^T q + q^T\dot{q}$ that emerges when applying the propsed geometric method to solve the stochastic differential equation (SDE) described in Eq. (6.83). This relationship highlights how the system's geometry interacts with its dynamic evolution. To confirm the algorithm's symplectic

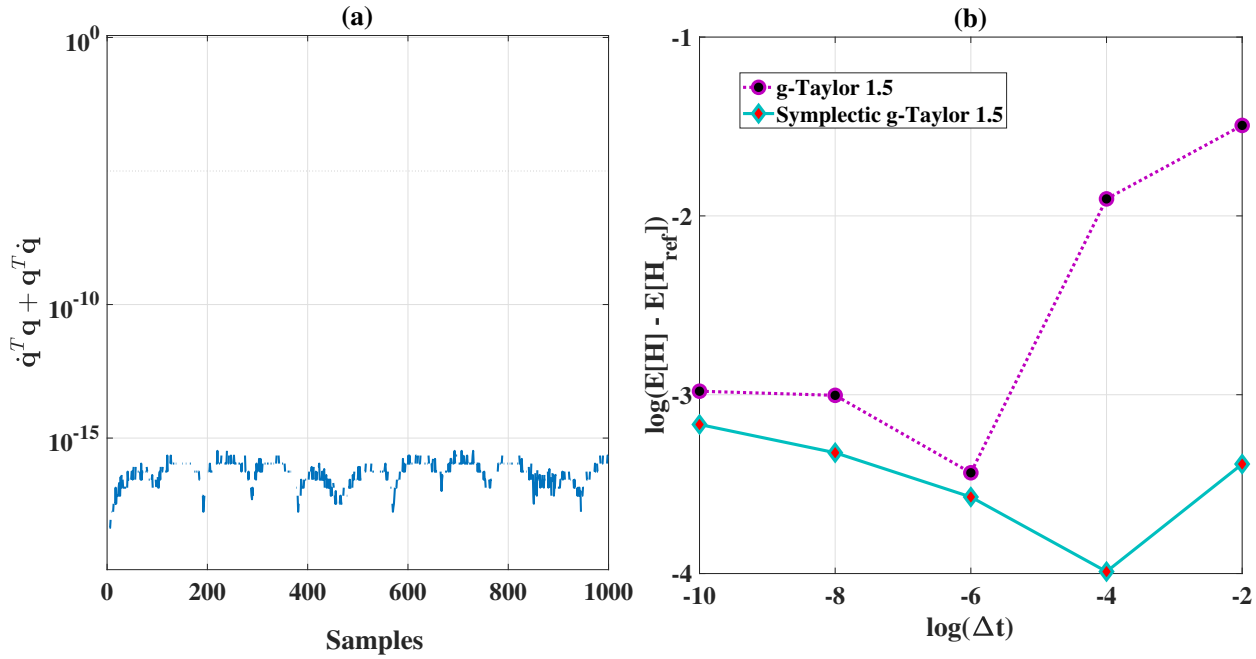

FIGURE 6.5: Stochastic duffing Oscillator on St$(3,1)$: Stochastic duffing Oscillator on S^2: Geometric constraints (a) on tangent space T_qSt$(3,1)$. (b) Comparison of Hamiltonian of the system solved using the proposed symplectic geometric Taylor 1.5 scheme and existing non-symplectic integrator

nature,Fig. 6.5(b) shows the global Hamiltonian error for different time steps: dt $= 2^{-8}$, 2^{-6}, 2^{-4}, and 2^{-2} seconds. The proposed symplectic approach is compared with the established geometric Taylor-1.5 scheme. For reference, the reference Hamiltonian ($E[H_{ref}]$) is computed using the geometric Euler-Maruyama (EM) scheme with a time step of dt $= 2^{-12}$ seconds. The observed global error validates the shadowing condition, confirming that the expectation of Hamiltonian function obtained through the proposed geometric approach aligns with the benchmark solution from the g-EM scheme. Notably, proposed approach demonstrates significantly lower error rates compared to the non-symplectic g-Taylor-1.5 scheme. An error reduction of around 60% is achieved, highlighting the substantial benefits of the symplectic framework over the non-symplectic one.

6.7.3 Molecular dynamics on S^2

The primary focus of this section revolves around the analysis of molecular dynamics on $\mathbb{S}^2$, the two-dimensional unit sphere [5]. Molecules are conceptualized methodically as discrete particles in constant motion on the surface of $\mathbb{S}^2$. The underlying dynamics of these molecules are governed primarily by two distinct forces: a force of long-range attraction and another force of short-range repulsion. The first one is noticeable over large distances, while the second one becomes more noticeable as molecules

get closer to each other. For each molecule indexed by i, two fundamental attributes are of central importance: the mass denoted as m and the molecular position vector $q_i \in \mathbb{S}^2$. It is to be noted that the interactions between different molecules are neglected. A pivotal mathematical framework utilized within this study is the Lennard-Jones potential [5], an effective model that aptly characterizes the intricate behaviors exhibited by molecules. This potential function serves as a mathematical approximation, offering insight into the manner in which molecules interact and manifest cohesive or repulsive tendencies within the confines of $\mathbb{S}^2$. The Lennard-Jones potential on 2-sphere is represented as

$$V\left(q_1, \ldots, q_n\right) = \frac{1}{2} \sum_{\substack{i,j=1 \\ j \neq i}}^{n} 4\varepsilon \left[\left(\frac{\sigma}{\|q_i - q_j\|} \right)^{12} - \left(\frac{\sigma}{\|q_i - q_j\|} \right)^{6} \right] \tag{6.84}$$

The first part of the equation represents the molecular repulsion phenomenon that occurs when molecules are very close to each other. On the other hand, the second part of the equation explains the attractive interactions that take place over larger distances. These interactions are due to van der Waals forces. ε represents the strength of the mutual potential between interacting molecules in proportion. On the other hand, the constant σ represents the typical size or magnitude of the intermolecular force. In addition, the kinetic energy is formulated with consideration for the Euclidean metric, represented as,

$$K = \frac{1}{2} \mathrm{m} \omega_i \omega_i \tag{6.85}$$

Utilising the Christoffel symbol in Eq. (6.44), the SDE for the i^{th} molecule can be written as,

$$\begin{aligned} \dot{q}_i &= \omega_i \times q_i \\ \left(\mathbf{I} - q_i \otimes q_i\right) \mathrm{m} \dot{\omega}_i &= -\mathrm{m} q_i \times \omega_i^T \omega_i q_i - q_i \times \sum_{\substack{j=1 \\ j \neq i}}^{n} 4\varepsilon \frac{q_i - q_j}{\|q_i - q_j\|} \left[\frac{12\sigma^{12}}{\|q_i - q_j\|^{13}} - \frac{6\sigma^6}{\|q_i - q_j\|^7} \right] + \mathcal{F} \circ \dot{B} \end{aligned} \tag{6.86}$$

where, stochastic forcing intensity is defined as,

$$\mathcal{F} = 2\left(\omega_i \times q_i\right) \times \frac{\partial h_1}{\partial \omega_i} + \left(\mathbf{I} - q_i \otimes q_i\right) \frac{d}{dt} \left(\frac{\partial h_1}{\partial \omega_i} \right) + \omega_i \times \frac{\partial h_1}{\partial \omega_i} + q_i \times \frac{\partial h_1}{\partial q_i}$$

for $i \in \{1, \ldots, n\}$. Here,

Fig. 6.6(a) visually presents the arrangement of 10 molecules, uniformly distributed across a spherical surface. In Fig. 6.6(b), the response trajectory of these molecules is graphically depicted, illustrating

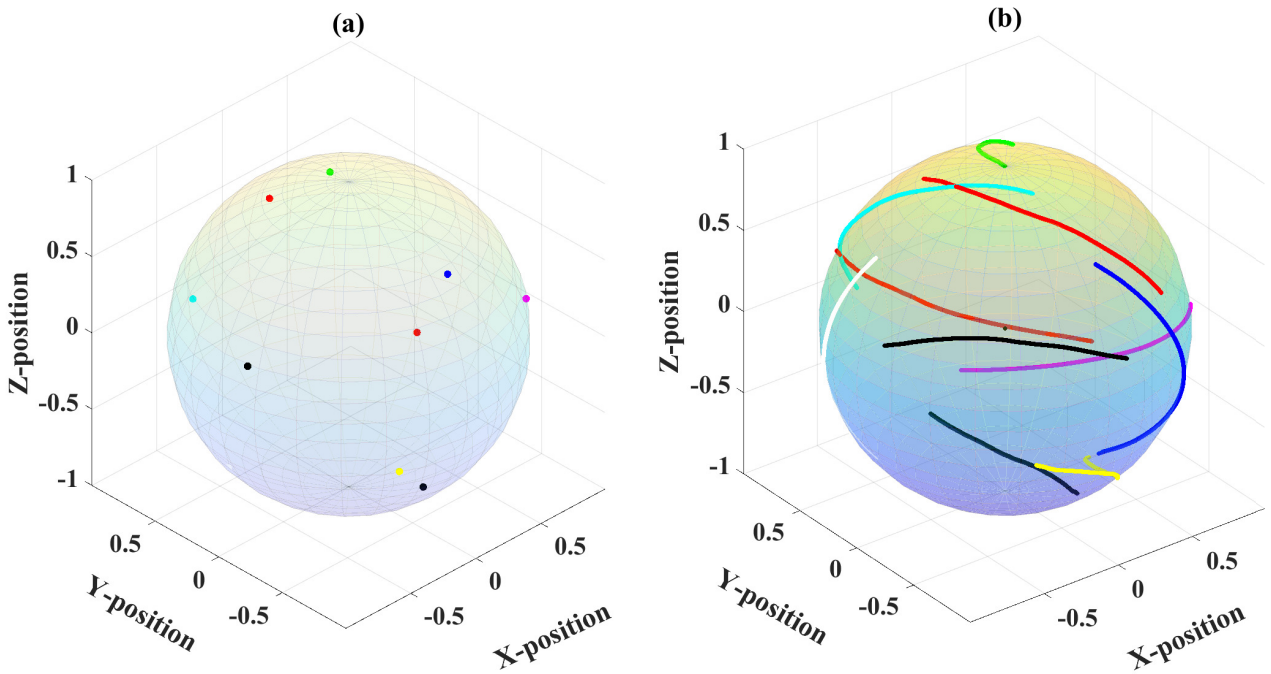

FIGURE 6.6: Molecular dynamics on S^2: (a) Visual representation of molecules, and, (b) their trajectory.

their dynamic evolution over time. The trajectory provides insights into the motion and interactions of the molecules as they navigate on the spherical surface. For a deeper investigation into the solution's inherent characteristics, Figs. 6.7(a) and 6.7(b) serve as insightful tools. These figures portrays the geometric constraints on both the tangent bundle of the 2-sphere (T_qS^2) and the 2-sphere (S^2). To validate the algorithm's symplectic nature, Fig. 6.7(c) displays the global Hamiltonian error across different time steps: dt $= 2^{-8}$, 2^{-6}, 2^{-4}, and 2^{-2} seconds. Both the proposed symplectic scheme and the established Taylor-1.5 scheme are utilized for this evaluation. A reference benchmark is established using the geometric Euler-Maruyama (EM) scheme with a time step of dt $= 2^{-12}$ seconds for comparison. The global Hamiltonian error as a robust indicator of the shadowing condition, validating the alignment of the expected Hamiltonian function computed through the proposed geometric scheme formulation with the reference solution. Notably, the proposed scheme demonstrates substantially lower error rates when contrasted with the non-symplectic Taylor-1.5 scheme. The achieved error reduction through the proposed formulation totals approximately 93%, firmly underscoring the marked advantages that the symplectic approach holds over its non-symplectic counterpart.

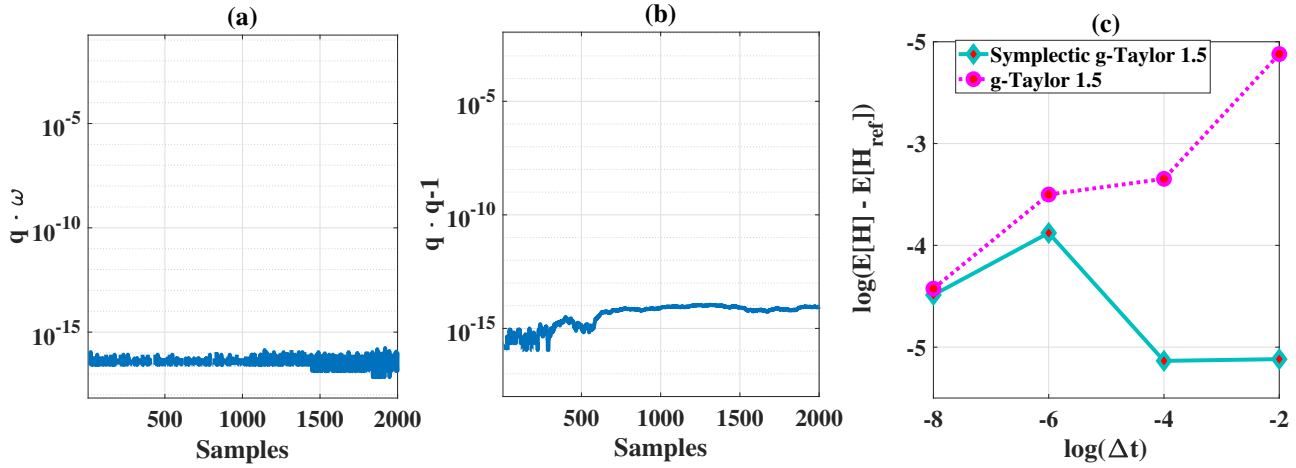

FIGURE 6.7: Molecular dynamics on S^2: Geometric constraints (a) on tangent space T_qS^2 (b) on sphere S^2. (c) Comparison of Hamiltonian of the system solved using the proposed framework and existing non-symplectic integrator.

6.7.4 Magnetic dipoles on S^2

This section considers a system comprising 'n' magnetic dipoles, each arranged in a three dimensional Euclidean space ($\mathbb{R}^3$). The nature of each magnetic dipole is captured using a model resembling a spherical compass. This model resembles a slender rod-like magnet, held in place by a frictionless pivot mechanism [5]. This special pivot mechanism gives the dipole two degrees of freedom, allowing dynamic interactions to arise from their magnetic fields' influence on each other [107]. The mass of the i^{th} magnet is denoted by the variable m_i, and its length is described by l_i. The fundamental aspect of a magnetic dipole lies in its magnetic moment. This phenomenon is represented as the product of two components: magnetic dipole moment denoted by v_i and the magnetic north pole direction relative to the pivotal point, indicated as $q_i \in S^2$. These components come together to create a collective configuration space called $(\mathbb{S}^2)^n$, which encompasses the spatial arrangements of all the magnetic dipoles.

The system's inherent rotational movement is measured using the inertia matrix M. This matrix takes on a diagonal form, where the element at the intersection of 'i' and 'j' is $\frac{1}{12}m_i l_i^2$ when 'i' is equal to 'j'. This value represents the rotational inertia of the i^{th} magnetic dipole. In contrast, all the elements outside the diagonal are set to zero, indicating that there's no direct rotational connection between different magnetic dipoles. The vectors that describe the relationships between pivot points are denoted as $r_{ij} \in \mathbb{R}^3$. The total potential energy arising from interactions among the various magnetic dipoles is

then mathematically formulated as follows:

$$V(q_1,\ldots,q_n)=\frac{1}{2}\sum_{\substack{i,j=1\\ j\neq i}}^{n}\frac{\mu v_i v_j}{4\pi\left\|r_{ij}\right\|^3}\left[(q_i\cdot q_j)-\frac{3}{\left\|r_{ij}\right\|^2}(q_i\cdot r_{ij})(q_j\cdot r_{ij})\right] \tag{6.87}$$

Utilizing the Euclidean metric, both the kinetic energy and the Christoffel symbol can be expressed in a manner analogous to Equations (6.90) and (6.44), respectively. With these formulations in place, the stochastic differential equations (SDEs) governing the behavior of each magnetic component can now be deduced as,

$$\begin{aligned}\dot{q}_i&=\omega_i\times q_i\\ \frac{1}{12}\mathrm{m}_i l_i^2\dot{\omega}_i&=-q_i\times\sum_{\substack{j=1\\ j\neq i}}^{n}\frac{\mu v_i v_j}{4\pi\left\|r_{ij}\right\|^3}\left[q_j-\frac{3}{\left\|r_{ij}\right\|^2}r_{ij}(q_j\cdot r_{ij})\right]+\mathcal{F}\circ\dot{B}\end{aligned} \tag{6.88}$$

where, stochastic forcing intensity is defined as,

$$\mathcal{F}=2(\omega_i\times q_i)\times\frac{\partial h_1}{\partial\omega_i}+(\mathbf{I}-q_i\otimes q_i)\frac{d}{dt}\left(\frac{\partial h_1}{\partial\omega_i}\right)+\omega_i\times\frac{\partial h_1}{\partial\omega_i}+q_i\times\frac{\partial h_1}{\partial q_i}$$

for $i\in\{1,\ldots,n\}$.

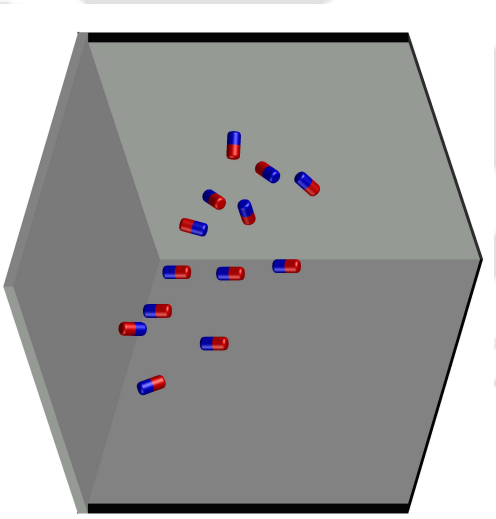

FIGURE 6.8: A representation of spatial arrays of spherical Magnetic dipole

Fig. 6.8 visually presents the arrangement of 13 magnetic dipoles, placed inside a cube like structure. These dipoles are fixed in place and acts like an individual spherical compass. All of these dipoles have same mass, length and magnetic moments i.e. $\mathrm{m}_i=50g$, $\mathrm{l}_i=20mm$, $\mathrm{v}_i=10^5 Amm^2$. Figs. 6.9(a) and 6.9(b) serve as insightful tools. These figures shed light on the intricate geometric constraints exerted upon both the tangent bundle of the 2-sphere ($\mathrm{T}_q\mathrm{S}^2$) and the 2-sphere (S^2). To validate the algorithm's

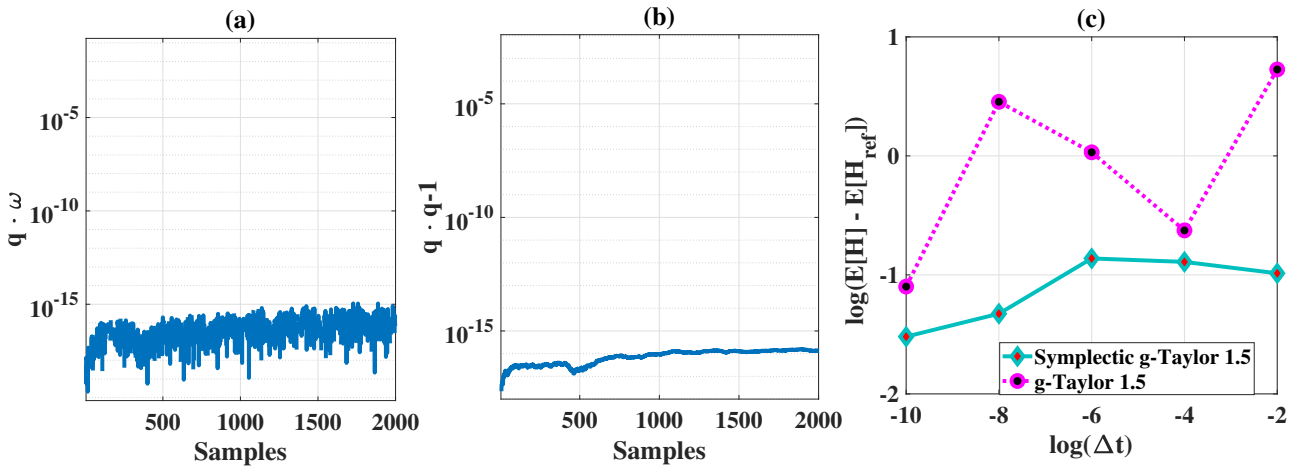

FIGURE 6.9: spherical Magnetic dipoles: Geometric constraints (a) on tangent space T_qS^2 (b) on sphere S^2. (c) Comparison of Hamiltonian of the system solved using the proposed framework and existing non-symplectic integrator.

symplectic nature, Fig. 6.9(c) displays the global expected Hamiltonian error across different time steps. Both the proposed symplectic scheme and the established Taylor-1.5 scheme are utilized for this evaluation. A reference benchmark of the Hamiltonian (H_{ref}) is obtained for comparison using the geometric Euler-Maruyama (EM) scheme with a time step of dt $= 2^{-12}$ seconds. The observed global Hamiltonian error serves as a robust indicator of the shadowing condition, validating the alignment of the solution through the proposed formulation with the reference solution. Notably, the proposed scheme demonstrates substantially lower error rates when contrasted with the non-symplectic Taylor-1.5 scheme. The achieved error reduction through the proposed formulation totals approximately 84%, firmly underscoring the marked advantages that the symplectic approach holds over its non-symplectic counterpart.

6.7.5 High dimensional Kuramoto model on St$(3, 2)$

This section primarily focuses on a general Kuramoto model discussed in references [108]. In this model, particles interact with their nearby counterparts on the Stiefel manifold [108]. The Stiefel manifold, denoted as $(\mathrm{St}(p, n), |\cdot|)$, is embedded in the Euclidean space $\mathbb{R}^{n\times p}$. This embedding utilizes the Frobenius (or Euclidean) norm for measuring distances. The state ensemble of particles is represented as $\mathcal{Q} = (q_1, \cdots, q_N)$. Moving forward, the concept of the potential function $\mathcal{V}$ becomes significant. This function encompasses all the differences within its formulation and involves a connectivity matrix

$\mathcal{A} = (a_{ik})$ known for its symmetry properties.

$$\mathcal{V}(\mathcal{Q}) = \frac{\kappa}{N^2} \sum_{i,k=1}^{N} a_{ik} \left\| \boldsymbol{q}_i - \boldsymbol{q}_k \right\|_{\mathrm{F}}^2, \quad a_{ik} = a_{ki} > 0 \tag{6.89}$$

Taking into account the Euclidean metric, the Kinetic energy will be given by,

$$K = \frac{1}{2} \mathrm{m} \dot{q}_i \dot{q}_i \tag{6.90}$$

Thereafter, the Christoffel symbol and the Riemannian gradient of the potential will be given by Eqs. (6.31) and (6.34). Considering the potential in Eq. (6.89), $\nabla_q \mathcal{V}$ will be obtained as,

$$\begin{aligned} \nabla_q \mathcal{V} = \; & \tfrac{\kappa}{N} \Big(\textstyle\sum_{k=1}^{N} a_{ik} \left[q_k - \tfrac{1}{2} \left(q_i q_i^\top q_k + q_i q_k^\top q_i \right) \right] - \tfrac{1}{2} q \Big(\textstyle\sum_{k=1}^{N} a_{ik} \left[q_k - \tfrac{1}{2} \left(q_i q_i^\top q_k + q_i q_k^\top q_i \right) \right]^T q \\ & + q^T \textstyle\sum_{k=1}^{N} a_{ik} \left[q_k - \tfrac{1}{2} \left(q_i q_i^\top q_k + q_i q_k^\top q_i \right) \right] \Big) \Big) \end{aligned} \tag{6.91}$$

Given these established formulations, the ensuing step involves the derivation of the stochastic differential equations (SDEs), including generalized natural frequencies $\Omega_i \in \mathfrak{so}(p)$, that dictate the dynamics of each component. This yields:

$$\begin{aligned} \mathrm{m} \ddot{q}_i = -\mathrm{m} q_i \dot{q}_i^\top \dot{q}_i + q_i \Omega_i + \nabla_q \mathcal{V} + \mathcal{F} \circ \dot{B}, \quad t > 0, \\ \dot{q}_i^T q_i + q_i^T \dot{q}_i = O, \quad i = 1, \cdots, N, \end{aligned} \tag{6.92}$$

where, stochastic forcing intensity is defined as,

$$\mathcal{F} = 2 \left(\omega_i \times q_i \right) \times \frac{\partial h_1}{\partial \omega_i} + \left(\mathbf{I} - q_i \otimes q_i \right) \frac{d}{dt} \left(\frac{\partial h_1}{\partial \omega_i} \right) + \omega_i \times \frac{\partial h_1}{\partial \omega_i} + q_i \times \frac{\partial h_1}{\partial q_i}$$

for $i \in \{1, \ldots, n\}$.

Fig. 6.10(a) provides insight into the intricate geometric constraint $\dot{q}i^{t,0} q i^0 + q_i^{t,0} \dot{q}_i^0$, which naturally emerges as a consequence of implementing the proposed geometric scheme to solve the stochastic differential equation (SDE) described in Eq. (6.92). To verify the algorithm's symplectic nature, Fig. 6.10(b) presents the global Hamiltonian error across varying time steps. A reference benchmark is established using the g-EM scheme with a time step of dt $= 2^{-12}$ seconds for meaningful comparison. This evaluation involves the proposed symplectic scheme and the established geometric Taylor-1.5 scheme. Affirming the close alignment of the Hamiltonian obtained through the proposed scheme with respect to the reference solution, the expected Hamiltonian error serves as a robust validation of the shadowing condition. Notably, the proposed scheme showcases notably lower error rates compared to

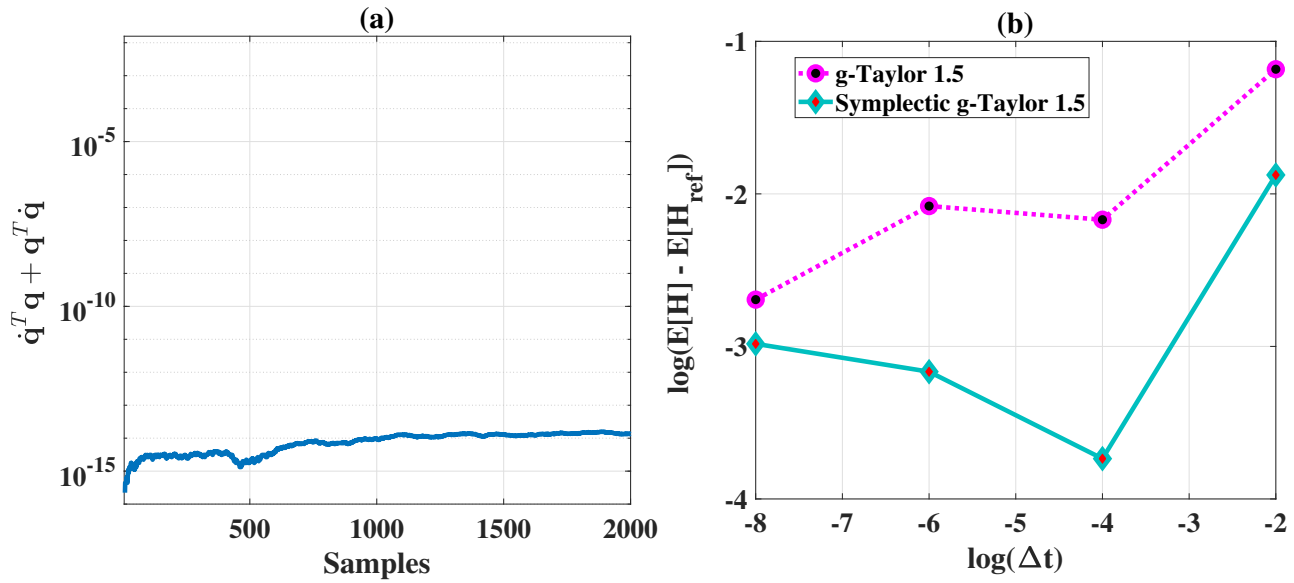

FIGURE 6.10: Kuramoto model on $\mathrm{St}(3,2)$: Geometric constraints (a) on tangent space $\mathrm{T}_q\mathrm{St}(3,2)$. (b) Comparison of Hamiltonian of the system solved using the proposed framework and existing non-symplectic integrator

the non-symplectic Taylor-1.5 scheme. The achieved error reduction through the proposed approach totals approximately 60%, effectively underscoring the significant advantages that the symplectic framework offers in comparison to its non-symplectic counterpart.

6.8 Research Findings

The outcomes of this chapter can be summarized as follows:

- Symplectic Type Geometric Ito-Taylor-1.5 Strong Framework: This paper makes a significant contribution by introducing a specialized symplectic-type geometric Ito-Taylor-1.5 strong framework designed explicitly for the numerical integration of dynamical systems evolving on a broad class of manifolds.

- Intrinsic Stochastic Differential Equations (SDEs): The research establishes a comprehensive conceptual framework for creating intrinsic stochastic differential equations (SDEs) tailored for systems evolving on smooth differentiable manifolds. These SDEs are derived for the Stiefel manifold and the unit hypersphere with a metric g.

- Validation Through Numerical Experiments: The method's effectiveness is rigorously validated through extensive numerical experiments spanning diverse domains, including stochastic duffing

oscillator dynamics, molecular dynamics, magnetic dipole systems, and a Kuramoto model.

- Symplectic Properties Evaluation: The symplectic properties of the proposed numerical integration method are thoroughly evaluated using multiple approaches, highlighting the significance of adopting a symplectic numerical integration approach.
- Reduction in Global Hamiltonian Error: A notable achievement is the substantial reduction in the global Hamiltonian error achieved by the proposed geometric symplectic scheme—72%, 93%, 84%, and 60% reductions for stochastic duffing oscillator dynamics, molecular dynamics, magnetic dipole systems, and a Kuramoto model, respectively.
- Symplectic Nature Preservation: The preservation of the symplectic nature is convincingly demonstrated by analyzing the variable $\frac{\partial q_{n+1}}{\partial q_n}\frac{\partial \pi_{n+1}}{\partial \pi_n}$, which closely approximates the identity matrix.
- Enhanced Accuracy for Complex Dynamics: These findings provide tangible evidence for the effectiveness of the proposed algorithm in accurately representing complex dynamics on manifolds. The algorithm's ability to preserve the symplectic structure enhances its credibility and applicability in various scientific and engineering contexts.
- Fundamental Conservation Principles: The algorithm's capability to uphold fundamental conservation principles intrinsic to Hamiltonian systems further underscores its credibility and broad utility in scientific and engineering applications.

The transition from the current chapter to the next signifies a shift from the domain of stochastic Hamiltonian differential equations and their symplectic numerical integration to a fresh exploration focused on nonlinear data analysis within a differentiable manifold. In various scientific fields, real-world phenomena, often characterized by randomness, unfold within the mathematical framework of manifolds, intricate mathematical spaces with non-Euclidean geometries. The next chapter introduces Recursive Principal Geodesic Analysis (RPGA), a method applicable to nonlinear data on differentiable manifolds, offering a novel perspective on real-time monitoring through eigen space exploration. This progressive shift is a central focus of the current research. The current chapter, serving as a bridge, provides a foundation for accurate trajectory estimation, which will be instrumental in tackling the inverse problem – the health monitoring of manifold-based systems in the chapters that follow.

Chapter 7

Real-time structural health monitoring on S^2

The chapter aims to introduce Recursive Principal Geodesic Analysis (RPGA), which is applicable to nonlinear data on any differentiable manifold, thus presenting a new perspective in the domain of real-time monitoring through eigen space exploration, a focus of my current research. To perform such an analysis effectively, Principal Component Analysis (PCA) [34, 109, 110, 111, 112, 113] and its recursive counterpart, RPCA [34, 109, 111, 114], can be valuable tools. However, it's important to note that these techniques are inherently linear, relying on results from linear algebra, and therefore require data to exist in a Euclidean space. In the quest to transcend these limitations, this chapter delves into the concepts and methods that underpin the transition from linear to nonlinear data analysis, extending our understanding and capabilities in monitoring complex systems across various domains. The very first step towards this exploration necessitates defining means on the manifold setting.

7.1 Means on Manifolds

To generalize means to manifolds, it is wise to borrow the knowledge from the Euclidean case. The point $\bar{x}$, derived from a collection of points $x_1, \ldots, x_N \in \mathbb{R}^d$, is defined as the average calculated as $\bar{x} = \frac{1}{N}\sum_{i=1}^{N} x_i$. This point possesses the special property of minimizing the sum of squared Euclidean distances to the given data [115, 116],

$$\bar{x} = \underset{x \in \mathbb{R}^d}{\operatorname{argmin}} \sum_{i=1}^{N} \|x - x_i\|^2 . \tag{7.1}$$

This well-established concept extends its reach by introducing a comprehensive range of mean estimators, tailored to the specific distance metric under consideration. Given that the manifold in question might not conform to a linear space, the calculation of additive means may pose a challenge. One potential remedy for this challenge lies in employing the aforementioned characterization as an organic

extension of the mean for nonlinear scenarios. Nevertheless, it's essential to acknowledge that this definition heavily relies on the chosen distance metric, which must be thoughtfully selected to achieve the most intuitively natural means extension for manifolds. This consideration prompts us to explore a more suitable distance metric that inherently defines the mean, offering us an intrinsic definition of this fundamental statistical concept.

7.1.1 Extrinsic notion

In the context of an embedding represented by $\Phi : M^p \to \mathbb{R}^d$, the extrinsic mean is defined as follows for any given set of points $x_1, \ldots, x_N \in M^p$ [116, 117]:

$$\mu_\Phi = \underset{x \in M^p}{\operatorname{argmin}} \sum_{i=1}^{N} \|\Phi(x) - \Phi(x_i)\|^2 \tag{7.2}$$

By utilizing the Euclidean norm, denoted as $|\cdot|$, on $\mathbb{R}^p$, the extrinsic mean can be equivalently computed as the conventional arithmetic mean of the transformed points $\Phi(x_i)$, followed by the projection of this mean onto the manifold M^p. To establish this equivalence, it is necessary to introduce a projection mapping $\pi : \mathbb{R}^d \to M^p$, which can be defined as follows:

$$\pi(x) = \underset{y \in M^p}{\operatorname{argmin}} \|\Phi(y) - x\|^2, \quad \forall x \in \mathbb{R}^p, \tag{7.3}$$

which leads to the following expression:

$$\mu_\Phi = \pi\left(\frac{1}{N}\sum_{i=1}^{N} \Phi(x_i)\right) \tag{7.4}$$

This operation is essentially the projection of the arithmetic mean of the data onto the manifold. In Fig. 7.1, you can observe an example demonstrating the computation of the extrinsic mean. This computation employs the gradient descent algorithm to minimize the sum-of-square distance function as defined in Equation (7.2). In this illustrative example, the extrinsic mean are, denoted as μ_Φ, for the white dots situated on the manifold M^2 embedded in $\mathbb{R}^3$. The embedding function is defined as $\Phi : M^2 \to \mathbb{R}^3$, where each point u maps to $\Phi(u) = \left(x, y, 9 - \left(\sqrt{x^2 + y^2}\right)\right)$. The process begins with an initial estimate of the extrinsic mean, denoted as μ_0. Subsequently, one can iteratively minimize the sum-of-square distance function, as expressed in Equation (7.2). This minimization involves taking successive steps, represented by the orange trajectory in the graph, in the positive gradient direction of

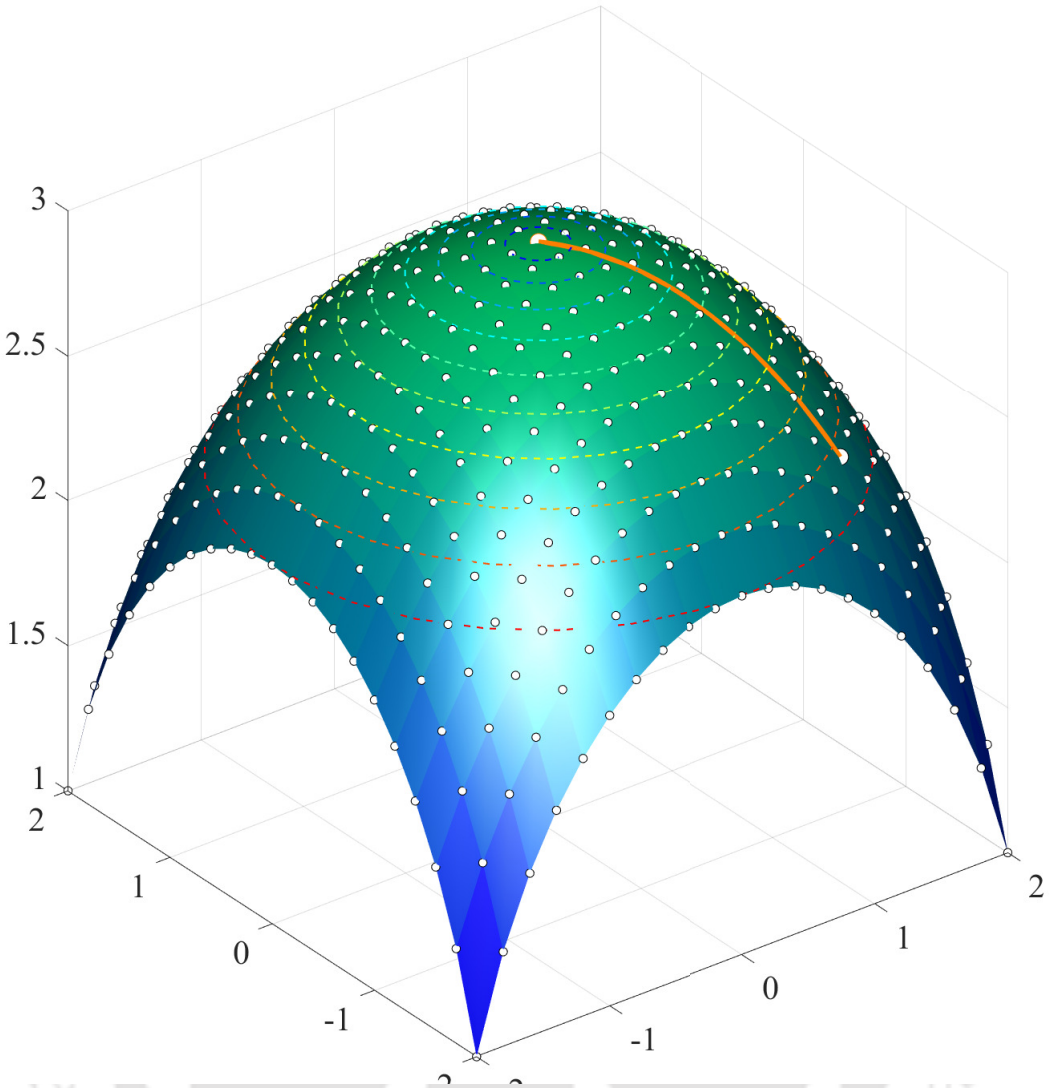

FIGURE 7.1: Computing the extrinsic mean with the gradient descent algorithm.

the function at the current estimate of the mean. Additionally, dotted lines on the graph are included to illustrate the equipotential levels of the objective function. These lines transition from red to blue as the intensity decreases, providing a visual representation of the optimization process.

Nonetheless, this definition of the mean possesses certain limitations, primarily because it necessitates the manifold to be embedded within a larger Euclidean space. This requirement proves to be problematic since the existence of the manifold is independent of whether it is embedded in a Euclidean space or not. Additionally, it may not always be feasible to express a manifold explicitly for every given problem. Consequently, an extrinsic definition of the mean, contingent upon an additional embedding of the manifold, may not represent the most natural means of defining the concept of a mean. This concern prompts us to explore an alternative approach, focusing on the development of a more suitable distance metric to define the mean. Such an intrinsic definition of the mean would offer a more intuitive

and flexible means of conceptualizing this fundamental statistical concept.

7.1.2 Intrinsic notion

In order to derive a coherent definition of means on Riemannian manifolds, it is essential to leverage the inherent distance metric made available through the presence of a metric tensor on the manifold. This natural distance is known as the geodesic distance, and it exclusively relies on the intrinsic geometry of the manifold. Assuming a pathwise connected Riemannian manifold denoted as M^p and the natural geodesic distance function [43, 115, 116, 117], denoted as $d(\cdot,\cdot)$, defined on it, the intrinsic mean for a set of points $x_1,\ldots,x_N \in M^p$ is defined as follows:

$$\mu = \underset{x\in M^p}{\operatorname{argmin}} \sum_{i=1}^{N} d\left(x, x_i\right)^2 \tag{7.5}$$

The computation of the intrinsic mean is, therefore, analogous to the minimization of the sum-of-square distance function:

$$f(x) = \frac{1}{2N} \sum_{i=1}^{N} d\left(x, x_i\right)^2 \tag{7.6}$$

This optimization problem assumes that $x_1,\ldots,x_n \in M^p$ are situated within a sufficiently small neighborhood, ensuring the existence and uniqueness of the solution to the problem.

To address this optimization challenge, this study employs the widely recognized gradient descent algorithm, also referred to as the steepest descent algorithm. This algorithm is designed to locate local minima of a given function by taking iterative steps in the direction opposite to the gradient of the function at the current point. In our particular case, it's possible to express the gradient of the function $f(x)$ using the logarithmic map.

Theorem 7.1.1. ***Gradient descent**: Consider $x \in M^p$ and a set of points $x_1,\ldots,x_N \in M^p$ situated within a sufficiently small neighborhood U of x, where the exponential map is a diffeomorphism. In this context, the gradient of the sum-of-square distance function defined in Equation (7.6) is given by:*

$$\nabla f(x) = -\frac{1}{N} \sum_{i=1}^{N} \log_x\left(x_i\right) \tag{7.7}$$

with $\log_x(\cdot)$ the logarithmic map at x.

Proof: The comprehensive proof of this result, as outlined in [118], can be referenced for a deeper understanding. This proof encompasses additional background concepts from manifold theory that extend beyond the scope of this thesis.

When the points $x_1, \ldots, x_N$ are located within a neighborhood denoted as U where the exponential map functions as a diffeomorphism, it becomes feasible to redefine the geodesic distance using the logarithmic map, as indicated in Equation (7.8). Consequently, for any pair of points x and y within this neighborhood, for all $x, y \in U$, the expression is as follows:

$$d(x, y) = \|\log_x(y)\| \tag{7.8}$$

This results in a revised expression for f for all $x \in M^p$:

$$f(x) = \frac{1}{2N} \sum_{i=1}^{N} \|\log_x (x_i)\|^2 . \tag{7.9}$$

If a point $p \in M^p$ is selected that is in close proximity to x, one can approximate the expression above as follows:

$$f(x) \simeq \frac{1}{2N} \sum_{i=1}^{N} \left\|\log_p(x) - \log_p (x_i)\right\|^2 = \frac{1}{2N} \sum_{i=1}^{N} \|\tilde{x} - \tilde{x}_i\|^2 = \tilde{f}(\tilde{x}), \tag{7.10}$$

Here, $\tilde{x} = \log p(x)$ and $\tilde{x}i = \log p\,(xi)$ are introduced. Given that $T_p\,(M^p)$ is linearly isomorphic to $\mathbb{R}^p$, it follows that the arithmetic mean $\tilde{\mu} \in T_p\,(M^p)$ is the point that minimizes the right-hand side of the equation:

$$\tilde{\mu} = \frac{1}{N} \sum_{i=1}^{N} \log_p (x_i) = \frac{1}{N} \sum_{i=1}^{N} \tilde{x}_i = \underset{\tilde{x} \in \mathbb{R}^p}{\operatorname{argmin}} \frac{1}{2N} \sum_{i=1}^{N} \|\tilde{x} - \tilde{x}_i\|^2 . \tag{7.11}$$

In this context, $\tilde{\mu}$ serves as a directional vector from point p to the function f's minimum. To compute $\nabla f(x)$, the process is reversed by parallel transporting $\tilde{\mu}$ along the minimal geodesic that connects points p and x.

$$\nabla f(x) = -\nabla_v \left(\frac{1}{N} \sum_{i=1}^{N} \log_p (x_i) \right) \tag{7.12}$$

Here, ∇_v signifies the parallel transport of $\tilde{\mu}$ along the minimal geodesic that connects x and p. Lastly, since p is in sufficiently close proximity to x, one can make the following approximation:

$$\nabla f(x) = -\nabla_v \left(\frac{1}{N} \sum_{i=1}^{N} \log_p (x_i) \right) \simeq -\frac{1}{N} \sum_{i=1}^{N} \log_x (x_i) \tag{7.13}$$

With a current estimate denoted as μ_j for the extrinsic mean, the equation for updating this mean by taking a single step in the negative direction is outlined as follows (also refer to Fig. 7.2):

$$\mu_{j+1} = \mathrm{Exp}_{\mu_j}\left(\frac{\tau}{N}\sum_{i=1}^{N}\log_{\mu_j}(x_i)\right) \tag{7.14}$$

The parameter τ represents the step size in the equation. Given that the gradient descent algorithm

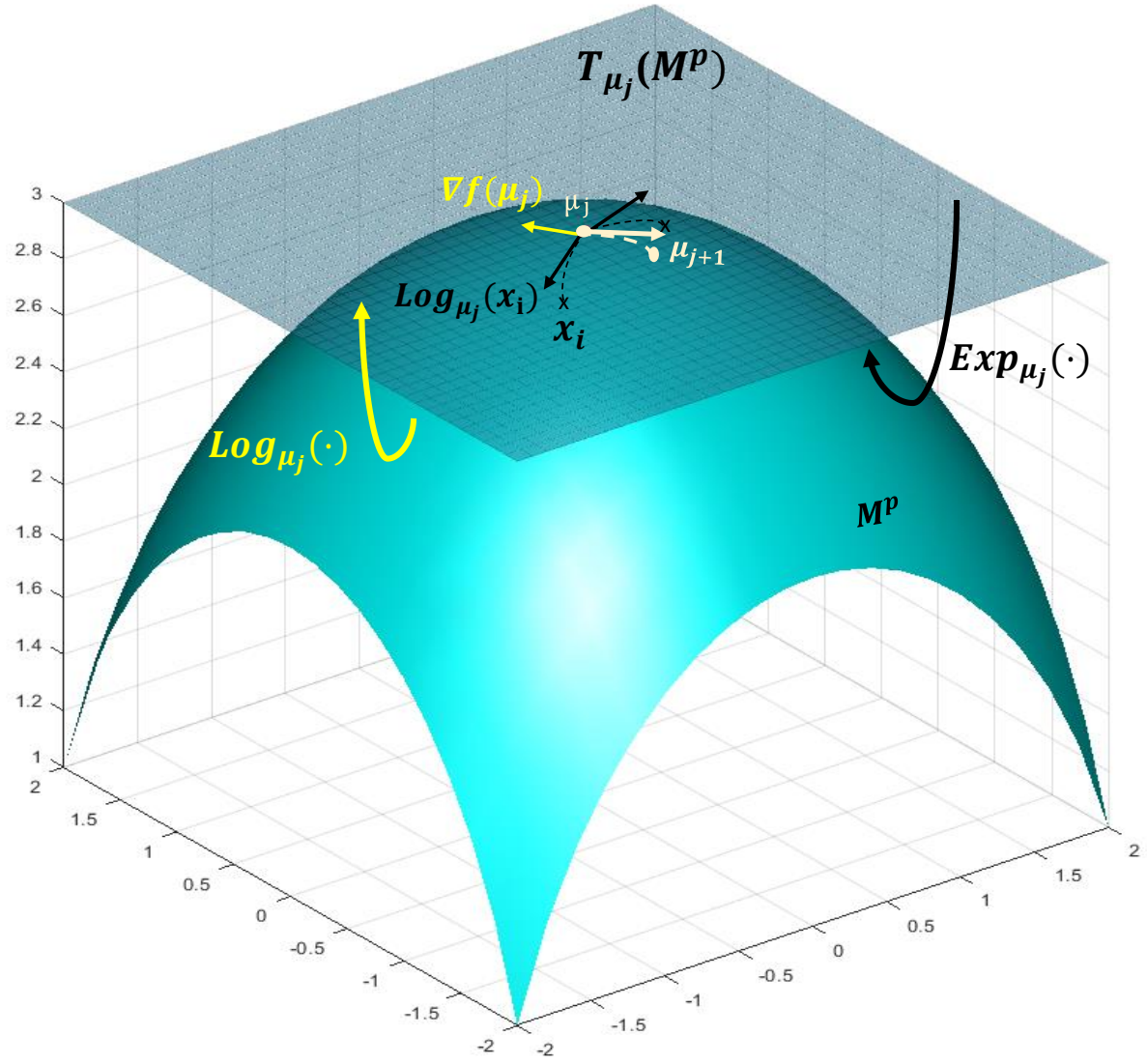

FIGURE 7.2: Computing the intrinsic mean with the gradient descent algorithm.

tends to converge locally, it is crucial to make thoughtful choices for both the initial estimate μ_0 of the intrinsic mean and the step size parameter τ. For well-localized data, a reasonable choice for the initial estimate μ_0 is one of the data points, such as x_1. However, determining an appropriate value for τ is more nuanced and depends on the specific manifold. Fig.7.2 illustrates a single step of the gradient descent algorithm employed in computing the intrinsic mean. With a current estimate denoted as μ_j, the

algorithm calculates the gradient at this point and proceeds along the geodesic in the opposite direction for a duration of τ units of time.

7.2 Principal Geodesics Analysis

Let's introduce Principal Geodesic Analysis (PGA) [43, 115, 116, 117] , which is akin to Principal Components Analysis (PCA) [34, 109, 110, 111, 112, 113] but tailored for manifolds. Our goal here is to work with a set of points denoted as $x_1, \cdots, x_N \in M^p$ and uncover two distinct sequences of geodesic submanifolds: First, the aim is to identify a series of nested geodesic submanifolds, denoted as $H_1 \subsetneq H_2 \subsetneq \cdots \subsetneq H_p = M^p$. These nested geodesic submanifolds, known as principal geodesic submanifolds, are instrumental in efficiently exploring the data's variability [43]. We achieve this by examining how the data projects onto each of these submanifolds. Next, a sequence of one-dimensional geodesic submanifolds are considered, labeled as $V_1, \cdots, V_p \subset M^p$. These geodesic submanifolds, referred to as the principal geodesic components, serve as a means to reinterpret the data as a sequence of "independent" components, much like how PCA functions with principal components [43, 115, 119]. In essence, PGA provides a tailored approach for analyzing data on manifolds, offering insights into its intrinsic structure and variability.

Consider a set of well-localized points $x_1, \cdots, x_N \in M^p$, which allows us to calculate the intrinsic mean of the data, denoted as μ. Now, let's take a neighborhood denoted as $U \subset T_\mu(M^p)$ that contains the origin (0). This neighborhood has the property that the projection is well-defined (ensuring existence and uniqueness) for all geodesic submanifolds within $\operatorname{Exp}\mu(U)$. Furthermore, $\operatorname{Exp}\mu : U \to \operatorname{Exp}_\mu(U)$ acts as a local diffeomorphism.

In this context, the first principal geodesic submanifold, denoted as H_1, should maximize the variance of the data when projected onto it. Utilizing the diffeomorphism provided by the exponential map and ensuring well-defined projection, one can express H_1 as $H_1 = \operatorname{Exp}\mu(\operatorname{span}\{v1\} \cap U)$. Consequently, the choice of $v_1 \in T_\mu(M^p)$ should satisfy the following condition:

$$v_1 = \underset{\|v\|=1}{\operatorname{argmax}} \frac{1}{N} \sum_{i=1}^{N} \left\| \log_\mu(\pi_H(x_i)) \right\|^2, \tag{7.15}$$

First, the first principal geodesic submanifold is defined, denoted as H_1, as $H_1 = \operatorname{Exp}\mu(\operatorname{span}\{v1\} \cap U)$. To ensure a unique solution, one also set $|v_1| \mid= 1$ [43]. The first principal geodesic component

is equivalent to H_1, given by $V_1 = H_1 = \mathrm{Exp}\,\mu\,(\mathrm{span}\,\{v1\} \cap U)$. We'll delve into interpreting these principal geodesic components later. Moving on, with the first principal geodesic submanifold $H_1 = \mathrm{Exp}\,\mu\,(\mathrm{span}\,\{v1\} \cap U)$ in place, one can define the second principal geodesic submanifold, denoted as H_2. It is constructed as $H_2 = \mathrm{Exp}\,\mu\,(\mathrm{span}\,\{v1, v_2\} \cap U)$. Here, the tangent vector $v_2 \in T_\mu\,(M^p)$ is selected to maximize the variance of the data when projected onto the two-dimensional geodesic submanifold $H = \mathrm{Exp}\,\mu\,(\mathrm{span}\,\{v1, v_2\} \cap U)$.

$$v_2 = \underset{\|v\|=1}{\mathrm{argmax}} \frac{1}{N} \sum_{i=1}^{N} \left\| \log_\mu\left(\pi_H\left(x_i\right)\right) \right\|^2. \tag{7.16}$$

The second principal geodesic component, denoted as V_2, is characterized by: $V_2 = \mathrm{Exp}\,\mu\,(\mathrm{span}\,\{v2\} \cap U)$.

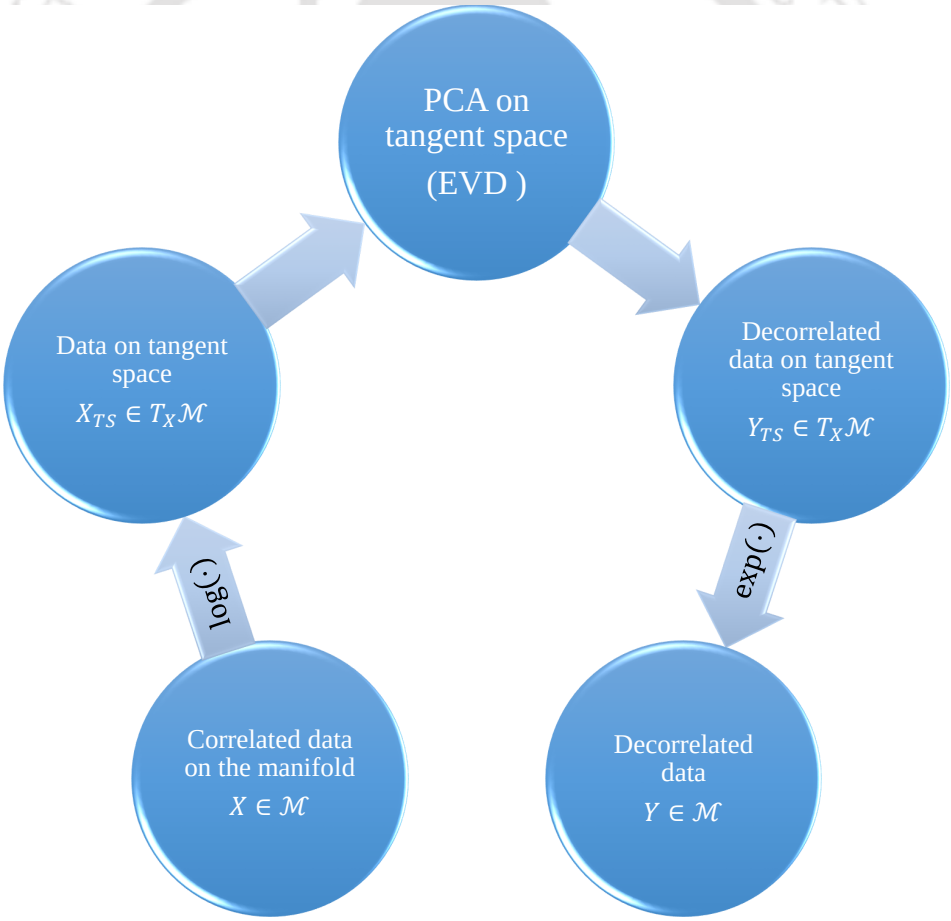

FIGURE 7.3: A flow of principal geodesic analysis algorithm

7.3 Computing PGA

Efficiently computing PGA hinges on a key observation: once the tangent vector $v_k \in T_\mu(M^p)$ are obtained, one can fully determine the geodesics H_k and V_k. Therefore, our primary focus is on the computation of v_k. Consider the scenario where $v_1, \ldots, v_{k-1} \in T_\mu(M^p)$ are already computed, and our aim is to calculate v_k. Here's how one can proceed:

$$v_k = \underset{\substack{\|v\|=1 \\ v \in \text{span}\{v_1, \cdots, v_{k-1}\}^\perp}}{\text{argmax}} \frac{1}{N} \sum_{i=1}^{N} \left\| \log_\mu \left(\pi_H \left(x_i \right) \right) \right\|^2, \tag{7.17}$$

where, $H = \exp_\mu \left(\text{span} \left\{ v_1, \cdots, v_{k-1}, v \right\} \cap U \right)$. Notably, since $\{v_1, \cdots, v_{k-1}, v\}$ forms an orthogonal basis, one can transform the equation as follows:

$$v_k \simeq \underset{v \in \text{span}\{v_1, \cdots, v_{k-1}\}^\perp}{\text{argmax}} \frac{1}{N} \sum_{i=1}^{N} \left\langle \log_\mu \left(x_i \right), v \right\rangle^2. \tag{7.18}$$

Given that $T_\mu(M^p)$ is a linear space, one can recognize that $\frac{1}{N} \sum_{i=1}^{N} \left\langle \log \mu \left(xi \right), v \right\rangle^2$ corresponds to the classic sample variance of the data $\log \mu \left(xi \right)$ projected onto the one-dimensional linear subspace spanned by v. Consequently, Eq. (7.18) can be reinterpreted as follows: Find $v_k \in \text{span} \left\{ v_1, \cdots, v_{k-1} \right\}^\perp$ such that $\text{Var} \left(\left\langle \log \mu \left(xi \right), v_k \right\rangle \right)$ is maximized. This reinterpretation essentially aligns with classic Principal Component Analysis (PCA) computed on the data $\log \mu \left(xi \right)$, assuming that $v_1, \cdots, v_{k-1}$ represent the first $k-1$ principal components. As a result, one can demonstrate by induction that a reasonable approximation for the v_k values would be the principal components obtained from PCA computed on the data $\log \mu \left(xi \right)$. Once these principal components are obtained, the data in the tangent space $T_\mu(M^p)$ can be decorrelated along the direction of the principal components v_k, denoted as $y_i = v_k \left(\pi_H \left(x_i \right) \right)$. The decorrelated data on the given manifold can then be retrieved by applying the exponential map $\exp \mu \left(yi \right)$ in the direction of the orthogonal basis v_k. A concise representation of the entire PGA algorithm is presented in Fig. 7.3 as a flowchart.

7.3.1 PGA and orthogonal projections

Geodesics, the fundamental paths on Riemannian manifolds, serve as crucial constructs in various fields, including differential geometry, physics, and machine learning. Notably, in the realm of shape analysis and manifold learning, geodesic paths play a pivotal role in capturing intrinsic structures and relationships within data. Principal Geodesic Analysis (PGA), a powerful framework for analyzing

shape spaces, leverages geodesic paths to uncover the underlying structure of data sets, enabling efficient representation, comparison, and interpolation of shapes. Building upon this foundation, we delve into the interaction between geodesics and orthogonal modes, exploring how geodesics can be conceptualized as orthogonal projections onto shape spaces, thus providing a comprehensive understanding of their geometric properties and applications. This investigation not only enriches our theoretical understanding of geodesics but also paves the way for practical implementations in various data-driven tasks, from shape modelling to dimensionality reduction.

Theorem 7.3.1. *Assume that $\mathcal{G}$ is a Lie group operating isometrically on $\mathcal{M}$, and $\mathcal{M}$ is a Riemannian manifold. Under these conditions, a geodesic on $\mathcal{M}$ that is horizontal at one point stays horizontal everywhere.*

While horizontal geodesics exhibit this property, vertical geodesics do not universally maintain their character along their length due to the non-constancy of Killing vector fields [120]. Notably, geodesics can be vertical in Kendall's shape spaces at isolated points exclusively [121]. This concept extends to non-manifold quotients as follows:

Definition 4.1 A curve on $\mathcal{Q}$ is considered a generalized geodesic if it originates from projecting a horizontal geodesic on $\mathcal{M}$ in the context of a quotient map from a Riemannian manifold $\mathcal{M}$ to its quotient space $\mathcal{Q}$ by a Lie group $\mathcal{G}$ acting isometrically on $\mathcal{M}$. The set of generalized geodesics on $\mathcal{Q}$, denoted $\Gamma(\mathcal{Q})$, comprises curves of the form $\delta = \pi \circ \gamma$, where γ is a horizontal geodesic on $\mathcal{M}$. Given $\delta \in \Gamma(\mathcal{Q})$ with $\delta(0) = q$, there exists a unique lift γ on $\mathcal{M}$ such that $\pi \circ \gamma = \delta$ and $\gamma(0) = p$. Another lift η of δ can be expressed as $\eta(\cdot) = g\gamma(\cdot)$ for some $g \in \mathcal{G}$. Generalized geodesics through a common point are orthogonal if their lifts through that point are orthogonal.

Theorem 7.3.2. *In the scenario where a finite-dimensional Riemannian manifold $\mathcal{M}$ is subject to an isometric action by a compact Lie group $\mathcal{G}$, the orthogonal projection q_δ is unique for any generalized geodesic δ on $\mathcal{Q}$, except for a set of measure zero.*

Defining the regular space $\mathcal{M} := \{p \in \mathcal{M} : I_p = id\}$ concerning the quotient $\mathcal{M}/\mathcal{G} = \mathcal{Q}$ and the singular space $\mathcal{M}^o := \{p \in \mathcal{M} : I_p \neq id\}$ is essential. Assuming an effective action, $\mathcal{M} \neq \emptyset$. We then project onto the regular quotient.

$$\pi|_{\mathcal{M}^*} : \mathcal{M}^* \to \mathcal{Q}^* := \mathcal{M}^*/\mathcal{G} \tag{7.19}$$

In the context of a Riemannian submersion, certain sectional curvatures of $\mathcal{Q}^*$ may tend to infinity as one approaches a singular point. Principal Component Analysis (PCA) involves deriving the principal components by identifying the eigenvectors of the covariance matrix of the data, which denote the directions of maximum variance. Each principal component v_i is orthogonal to the others, collectively forming a basis for the data space. Similarly, Principal Geodesic Analysis (PGA) operates within the tangent space of a manifold. At every point p on the manifold, the tangent space (T_pM) encompasses all potential tangent vectors at that location, offering a local linear approximation to the manifold. The orthogonal modes on the tangent space, denoted as ξ_i, capture the local deformation of the manifold. These modes are obtained by analyzing the principal geodesics, which are the paths of maximum deformation along the manifold. Mathematically, the modes ξ_i are orthogonal to each other and form a basis for the tangent space T_pM. For a manifold based dynamical system with the responses on manifold as $\mathbf{X} = [x_1, \cdots, x_N]$, the mean μ can be obtained using the Karchar's mean [118] and the covariance matrix $R = \frac{1}{N-1}\left[\log_\mu(\mathbf{X})\right]\left[\log_\mu(\mathbf{X})\right]^T$ can be expressed as a standard Eigenvalue problem as,

$$\mathbf{RV} = \mathbf{V\Lambda} \tag{7.20}$$

where, $\mathbf{V}$ and $\mathbf{\Lambda}$ are the eigenvectors and eigenvalues on the T_pM. These eigenvectors can be used to obtain the orthogonal responses on T_pM as $\mathbf{V}^T\left(\log_\mu(\mathbf{X})\right)$ and then it can be projected back to the manifold as $\mathrm{Exp}_\mu\left(\mathbf{V}^T\left(\log_\mu(\mathbf{X})\right)\right)$. In Principal Component Analysis (PCA), each principal component captures a unique source of variation present in the data. Similarly, in Principal Geodesic Analysis (PGA), each orthogonal mode signifies a distinct direction within the data space, representing specific patterns or structures inherent in the dataset. This framework finds applications in analyzing and understanding complex data represented on curved manifolds, such as shape analysis, image processing, and dimensionality reduction.

7.4 Recursive Principal geodesic analysis

With a grasp of the underlying concept of the intrinsic mean, it becomes possible to define a recursive version of Principal Geodesics Analysis (PGA) as an analog of Recursive Principal Components Analysis (RPCA) specifically designed for manifolds. The objective is to extract the principal geodesics, which play a crucial role in comprehending dynamical systems within the context of the present study. To begin this process, it is essential to comprehend the workings of Batch PGA, as it will furnish the

initial estimates for the recursive algorithm while ensuring its stability. Let us consider a set of points, denoted as $\mathbf{X} = [x_1, \cdots, x_N]$, belonging to the manifold M^p. The primary goal is to derive the principal geodesics, which are fundamental components for understanding the dynamics of the systems being investigated. In order to achieve this, a recursive version of PGA is introduced, mirroring the Recursive Principal Components Analysis approach but tailored for manifolds. The initial step involves grasping the functioning of Batch PGA, which serves two key purposes. Firstly, it provides the initial estimates required for the recursive algorithm to commence its iterative procedure. Secondly, it ensures the stability of the entire process. By employing Batch PGA, a preliminary understanding of the principal geodesics can be obtained, serving as a solid foundation for the subsequent recursive analysis.

A preliminary step in the Recursive Principal Geodesics Analysis (PGA) involves conducting Batch PGA using a batch of 100-500 samples from the dataset $\mathbf{X}$. The intrinsic mean of the batch data is calculated as follows:

$$\mu = \frac{1}{N} \sum_{i=1}^{N} \log_{x_1} (x_i) \tag{7.21}$$

In Equation 7.21, x_i represents the i^{th} sample in the dataset $\mathbf{X}$, and N denotes the total number of samples in the batch. The intrinsic mean, μ, provides an estimate of the central tendency of the batch data in terms of their logarithmic coordinates with respect to a chosen reference point, x_1. Subsequently, the batch data is projected onto the tangent space at the intrinsic mean, denoted as $T_\mu M^p$. This projection is necessary because the typical calculus operations are not directly defined on the manifold M^p. By transferring the batch data to the tangent space at the mean, it becomes feasible to perform computations and analyses in a manner analogous to $\mathbb{R}^p$, thus enabling the application of conventional mathematical techniques. The choice of the intrinsic mean as the reference point for the tangent space projection ensures that the resulting tangent space captures the local geometry of the data around the mean. This facilitates the processing and analysis of the data within the tangent space framework, enabling the application of statistical and geometric techniques that are well-defined in Euclidean spaces [34, 40, 114, 122]. By performing Batch PGA and projecting the data onto the tangent space at the intrinsic mean, the subsequent processing and analysis of the dataset $\mathbf{X}$ can be carried out effectively. This approach leverages the intrinsic mean as a reference point and utilizes the tangent space to perform computations and analyses analogous to those in Euclidean spaces. Therefore, the projected data can be written as

$\log_\mu(x_i)$. This data is then utilized for the formation of data covariance matrix as,

$$\mathbf{R}_k = \frac{k}{k-1}\mathbf{R}_{k-1} + \frac{1}{k-1}\left[\log_\mu(x_k)\right]\left[\log_\mu(x_k)\right]^T \tag{7.22}$$

The subsequent crucial step in Recursive Principal Geodesics Analysis (RPGA) involves the eigen decomposition of the covariance matrix. This process can be framed as an optimization problem known as the Standard Eigenvalue Problem (SEVP) [123]. Formally, the SEVP is defined as follows:

$$\max_{\mathbf{V}} \left(\mathbf{V}^T\mathbf{R}\mathbf{V}\right), \text{ subject to } \mathbf{V}^T\mathbf{V} = \mathbf{I}, \tag{7.23}$$

where $\mathbf{R} \in \mathbb{R}^{d\times d}$ is the covariance matrix. By solving this optimization problem, the resulting solution provides the SEVP with matrices $\mathbf{V} \in \mathbb{R}^{d\times d}$ and $\mathbf{\Lambda} \in \mathbb{R}^{d\times d}$, representing the eigenvectors and eigenvalues, respectively. This can be expressed as:

$$\mathbf{R}\mathbf{V} = \mathbf{V}\mathbf{\Lambda}. \tag{7.24}$$

The obtained solution from the SEVP represents the initial eigenspace, which serves as a basis for subsequent recursive updates in PGA. The recursive update process consists of three main components: updating the intrinsic mean, updating the covariance matrix, and updating the eigenspace using an eigen perturbation technique. In each iteration of the recursive update, the intrinsic mean is refined based on the updated estimates obtained from the previous iteration. This involves considering the logarithmic coordinates of the data points with respect to the updated mean. Similarly, the covariance matrix is updated by incorporating the information from the updated intrinsic mean and the logarithmic coordinates of the data points. This updated covariance matrix captures the local variations and correlations within the dataset. Furthermore, the eigenspace is updated by applying an eigen perturbation technique, which involves incorporating small variations to the eigenvectors and eigenvalues obtained from the previous iteration. This allows for the adaptation of the eigenspace to capture the evolving structure of the data. By iteratively performing these three components, the recursive PGA algorithm refines the estimates of the principal geodesics, leading to an improved understanding of the dynamical systems under analysis. The recursive update process ensures that the algorithm converges towards a more accurate representation of the underlying data structure, facilitating effective analysis and interpretation. Then, given a

current estimate μ_k for the extrinsic mean, the equation for updating the mean is:

$$\mu_{k+1} = \frac{1}{N}\mu_k + \mathrm{Exp}_{\mu_k}\left(\frac{N-1}{N}\sum_{i=1}^{N}\log_{\mu_k}(x_k)\right) \tag{7.25}$$

And thus the block covariance matrix can be recursively updated as,

$$\mathbf{R}_k = \frac{k-1}{k}\boldsymbol{\Sigma}_k^{-1}\boldsymbol{\Sigma}_{k-1}\mathbf{R}_{k-1}\boldsymbol{\Sigma}_{k-1}\boldsymbol{\Sigma}_k^{-1} + \frac{1}{k}\left(\log_{\mu_k}(x_k)\right)^T\left(\log_{\mu_k}(x_k)\right) \tag{7.26}$$

Using $\mathbf{R}_k = \mathbf{V}_k\boldsymbol{\Lambda}_k{\mathbf{V}_k}^T$ Eq. (7.26) can be re-written as,

$$\mathbf{V}_k\boldsymbol{\Lambda}_k{\mathbf{V}_k}^T = \hat{\mathbf{V}}_{k-1}\left[(1-\lambda)\boldsymbol{\Lambda}_{k-1} + \lambda\hat{\mathbf{V}}^T\left(\log_{\mu_k}(x_k)\right)\left(\log_{\mu_k}(x_k)\right)^T\hat{\mathbf{V}}_k\right]\hat{\mathbf{V}}_{k-1}^T \tag{7.27}$$

where, λ is the memory depth parameter [34] with a range of $0 \leq \lambda \leq 1$, which can be assumed according to the necessity. Here, λ can be taken as $\frac{1}{k}$. As the sample size increases, evaluating the covariance estimate through Eqs. (7.26) at each time step becomes computationally demanding. To address this issue, an eigen perturbation techniques is used for , which involve updating the eigenvectors and eigenvalues of the covariance matrix as follows:

$$\mathbf{V}_k = \mathbf{V}_{k-1}\left(I + \boldsymbol{\Delta}_V\right), \quad \boldsymbol{\Lambda}_k = \left(\boldsymbol{\Lambda}_{k-1} + \boldsymbol{\Delta}_\Lambda\right) \tag{7.28}$$

where, $\boldsymbol{\Delta}_V$ and $\boldsymbol{\Delta}_\Lambda$ are small perturbations applied on the eigenspaces. Substituting these perturbations on Eq. (7.24), the equation can be re-written as,

$$\begin{aligned}\mathbf{V}_k\boldsymbol{\Lambda}_k{\mathbf{V}_k}^T = \mathbf{V}_{k-1}\big[&\boldsymbol{\Lambda}_{k-1} + \boldsymbol{\Delta}_\Lambda + \boldsymbol{\Lambda}_{k-1}{\boldsymbol{\Delta}_V}^T \\ &+\boldsymbol{\Delta}_V\boldsymbol{\Lambda}_{k-1} + \boldsymbol{\Delta}_\Lambda{\boldsymbol{\Delta}_V}^T + \boldsymbol{\Delta}_V\boldsymbol{\Delta}_\Lambda\big]{\mathbf{V}_{k-1}}^T\end{aligned} \tag{7.29}$$

Now, comparing Eqs. (7.27) and (7.29), it can be observed that the first order perturbation excluding second order terms (i.e. $\boldsymbol{\Delta}_\Lambda{\boldsymbol{\Delta}_V}^T$ and $\boldsymbol{\Delta}_V\boldsymbol{\Delta}_\Lambda$), can be expressed as follows,

$$\begin{aligned}&\boldsymbol{\Delta}_\Lambda + \boldsymbol{\Lambda}_{k-1}{\boldsymbol{\Delta}_V}^T + \boldsymbol{\Delta}_V\boldsymbol{\Lambda}_{k-1} \\ &= \hat{\mathbf{V}}^T\left((1-\lambda)\boldsymbol{\Sigma}_k^{-1}\Delta\mu_k\Delta\mu_k^T\boldsymbol{\Sigma}_k^{-1} + \lambda\left(\log_{\mu_k}(x_k)\right)\left(\log_{\mu_k}(x_k)\right)^T\right)\hat{\mathbf{V}}_k\end{aligned} \tag{7.30}$$

Once the perturbation matrices have been evaluated using Eq. (7.30), the eigenspaces can be updated accordingly, as per Eq. (7.28). However, due to the recursive nature of the framework, the updated eigenspaces may suffer from permutation ambiguity [41]. To resolve this ambiguity, the eigenvectors can be rearranged based on the decreasing order of their corresponding eigenvalues [41]. Thereafter, as the changes are happening in the system evolving in the manifold, so the principal geodesics are also

defined in the manifold. For this, the framework projects back the principal components from $T_{\mu_k}M^p$ to M^p as,

$$\psi_k = \mathrm{Exp}_{\mu_k}\left(\hat{\mathbf{V}}_k^T\left(\log_{\mu_k}(x_k)\right)\right) \tag{7.31}$$

Monitoring changes in the eigenspace alone may be inadequate to capture the damage instance, necessitating the use of a condition indicator that can amplify the effect of changes in the eigenspace, making it more observable.

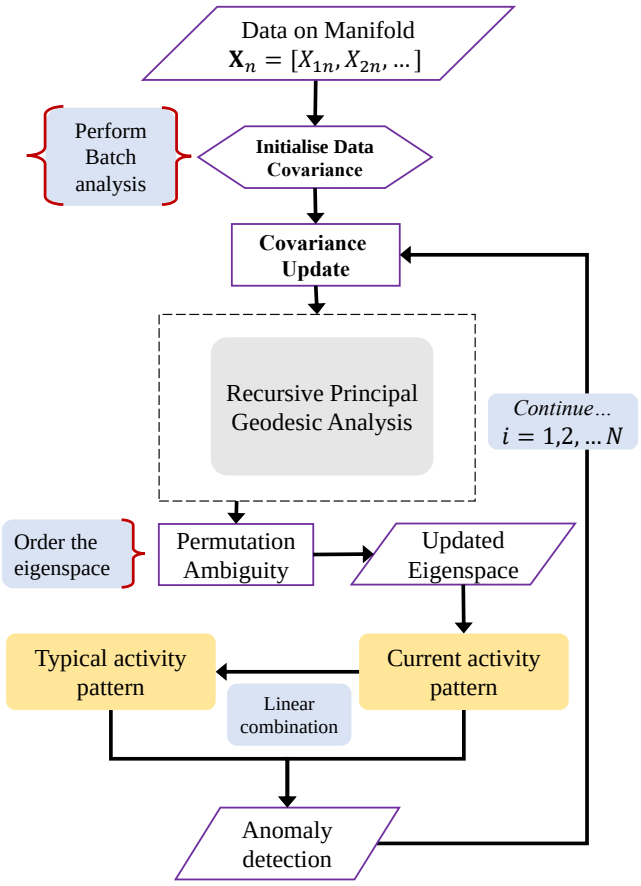

FIGURE 7.4: Flow chart illustrating the RPGA framework, showcasing the functionality of the condition indicator.

7.4.1 Condition indicator (CI)

To make the algorithms self-reliant, condition indicators (CI) are utilized to assess any alterations in the updated eigenspace, with the purpose of amplifying the changes in the eigenspace. In this study, a new condition indicator has been developed to identify change in the eigenspace thereby detecting temporal damage in the system evolving in the manifold. The CI computes the dissimilarity between the current transformed vector and a reference pattern, which is derived from a linear combination of

the current pattern [124]. This approach allows for the detection of changes in the system based on a comparison with the base pattern. The current framework considers response on the transformed space ψ_k as input for the processing. For capturing the changes in eigenspace, fist the maximum covariance of ψ_k is calculated as,

$$\Phi_k = \arg\max_{\mathbf{V}_k} \left(\psi_k \left(\psi_k \right)^T \right) \tag{7.32}$$

A sequence of Φ_k with embedding dimension d can be defined as the current pattern which forms a Hankel matrix as,

$$\Gamma_k = \begin{bmatrix} \Phi_k & \Phi_{k-1} & \Phi_{k-2} & \dots & \Phi_{k-d+1} \end{bmatrix}^T \tag{7.33}$$

Thereafter a reference pattern of the eigenstructure is established as a linear combination of current pattern.

$$\rho_k = \eta \sum_{i=1}^{d} c_i \Phi_{k-i+1} \tag{7.34}$$

where, η is a normalizing constant to ensure that ρ_k is a orthogonal vector. The normalizing constant can be evaluated as $\eta = 1/\sqrt{\nu}$, where, ν is the eigenvalues of the Hankel covariance matrix $\Gamma_k \Gamma_k^T$. The estimation of reference pattern ρ_k necessitates the optimization of linear combination coefficient c_i based on extremum principle as,

$$c_k = \arg\max_{\gamma} \left\| \sum_{i=1}^{d} \gamma_k(i) \Phi_{t-i+1} \right\|^2 \tag{7.35}$$

where, γ is the eigenvectors of the Hankel covariance matrix $\Gamma_k \Gamma_k^T$. The CI representing the contrariety between current and reference pattern is then estimated as

$$\mathbf{CI}(k) = {\rho_{k-1}}^T \Phi_k \tag{7.36}$$

This technique identifies dissimilarity in the reference pattern and the current one, thereby identifying any damage instances. A distortion in the values of the CI represents damage at that particular instant of time. A flow chart illustrating the RPGA framework, showcasing the functionality of the condition indicator is presented in Fig. 7.4

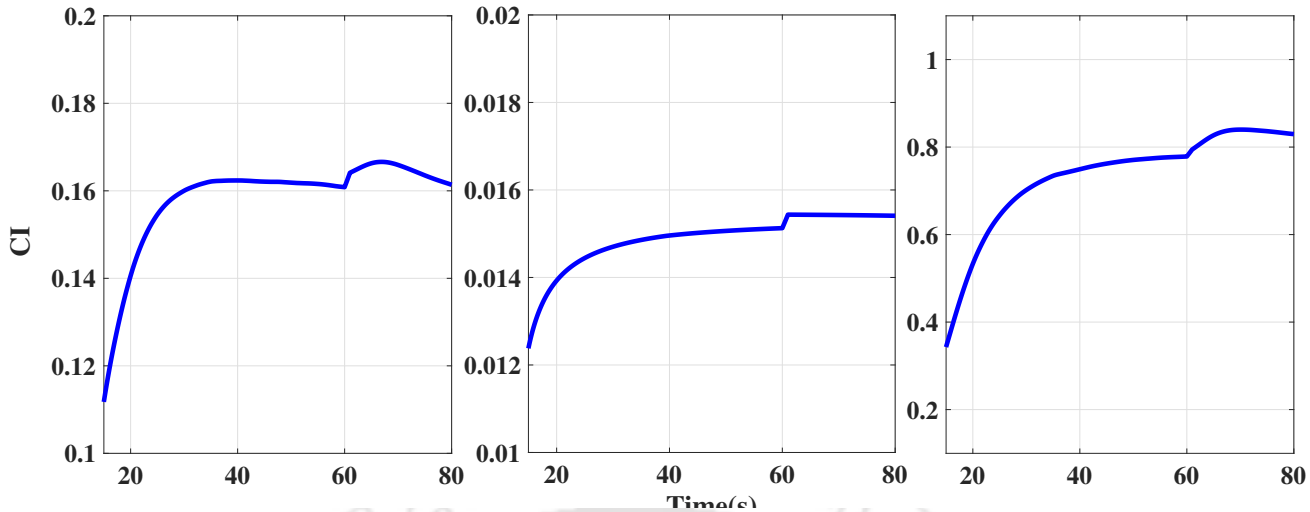

FIGURE 7.5: Stochastic linear system: Representation of the condition indicator using RPCA framework.

7.5 Numerical Experiments

This section presents the efficacy of the proposed RPGA framework for anomaly detection to three distinct systems: stochastic geometric oscillator on S^2, spherical pendulum, and an inverted spherical pendulum suspended from a cart. This comprehensive exploration demonstrates RPGA's versatility and adaptability, making it a valuable tool for diverse real-world systems with complex dynamics.

7.5.1 Geometric description of a stochastic linear oscillator on S^2

Oscillators have garnered significant attention due to their capacity to simulate intricate physical phenomena and contemporary structures within Euclidean space. Presently, researchers are exploring the application of these oscillators in modeling satellite and drone trajectories, as well as controlling artificial limbs and modeling robots, within manifold spaces [24, 67, 68]. This section aims to furnish a geometrically precise solution of a linear oscillator situated on a sphere, thereby validating the effectiveness of the proposed algorithm. Towards this, consider

$$m\ddot{x} + c\mathbf{Q}\dot{x} + k\mathbf{Q}x = \sigma\dot{W} \tag{7.37}$$

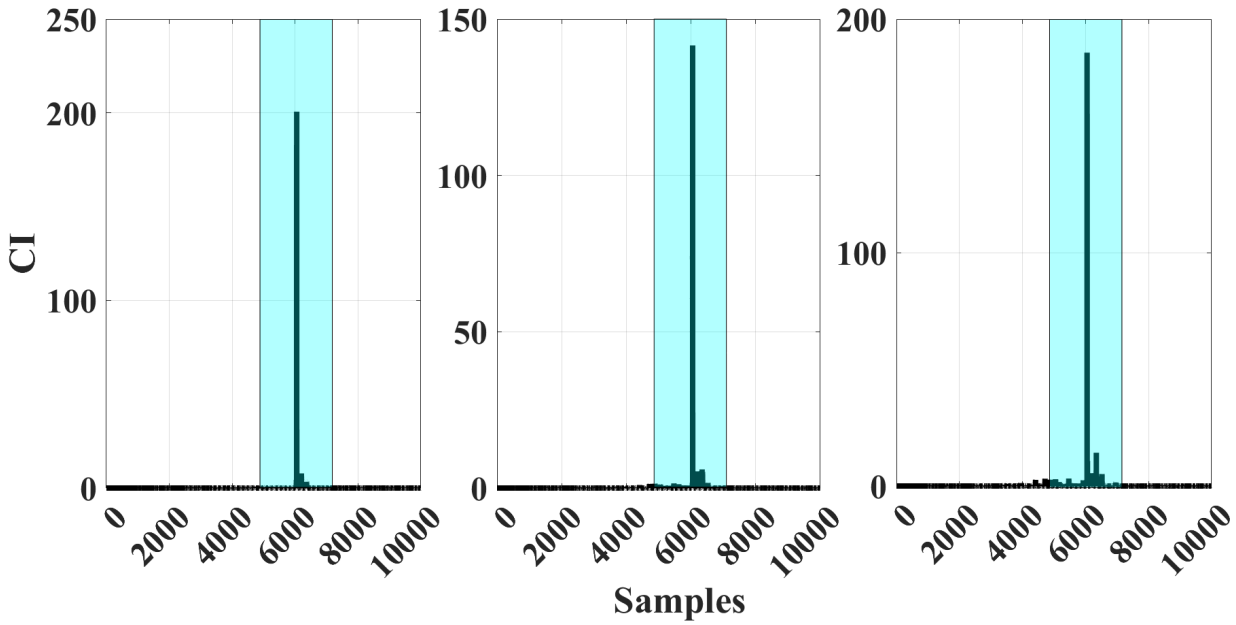

FIGURE 7.6: Geometric stochastic linear system: Representation of the condition indicator using manifold based RPGA framework.

where, m, c and k represents the generic system properties, and, $\mathbf{Q} = \begin{bmatrix} 2 & -1 & 0 \\ -1 & 2 & -1 \\ 0 & -1 & 1 \end{bmatrix}$. σ is a representation of the magnitude of the stochastic excitation $\dot{W}$. Eq. (7.37) characterizes a single-mass three-degree-of-freedom (3DOF) system, with its degrees of freedom designated along the x, y, and z directions, denoted as $(x_1, x_2, x_3) \in \mathbb{R}^3$. In the state-space representation, Eq. (7.37) can be represented as,

$$\begin{aligned} \dot{x} &= y \\ \dot{y} &= -\tfrac{c}{m}\mathbf{Q}y - \tfrac{k}{m}\mathbf{Q}x + \sigma\dot{W} \end{aligned} \tag{7.38}$$

.

Operating within the Euclidean space and devoid of geometric constraints, the RPCA algorithm [34], tailored for Euclidean spaces, effectively discerns instances of damage in the system. However, the complexity intensifies when the system is confined to evolve on a spherical surface, introducing constraints. In this scenario, the task of damage identification becomes more intricate. The foundational work outlined in literature [53] provides the base for extending the conventional potential function to operate on the curved space by substituting the generic distance on the Euclidean spae with the Riemannian distance. In the current study, $\mathfrak{d}(a, b) = |\log_a(b)|_a$ is the Riemannian distance function. In

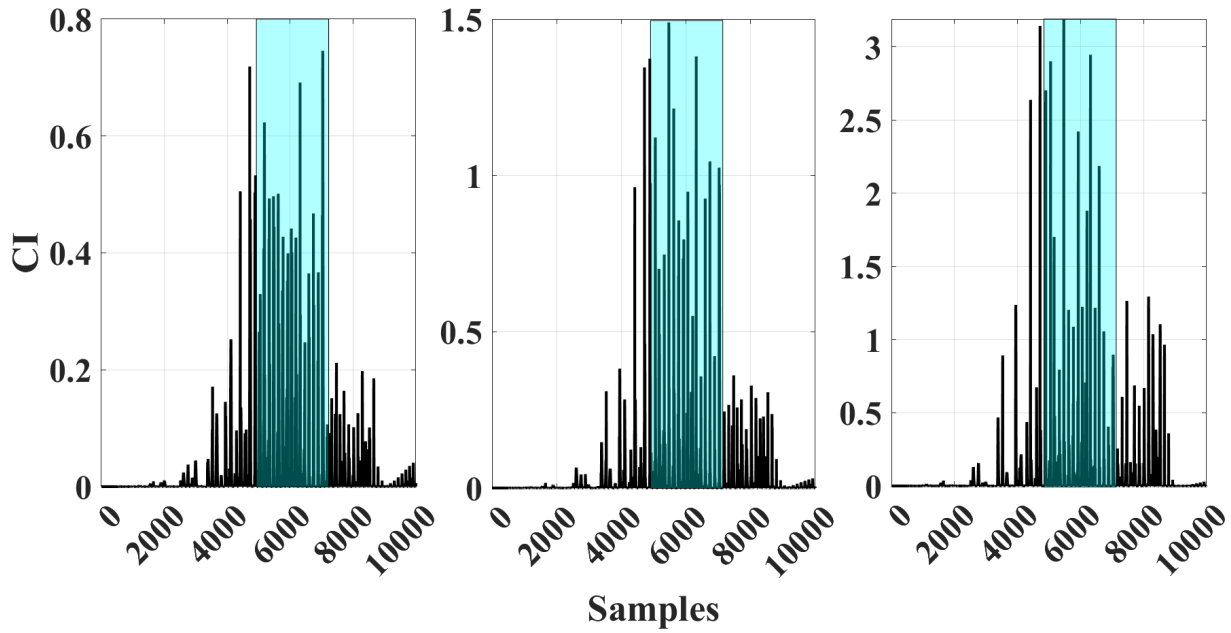

FIGURE 7.7: Stochastic spherical pendulum: Representation of the condition indicator using Euclidean based RPCA framework.

the context of the geometric oscillator under consideration, driven by a white Gaussian process $\dot{\mathrm{W}}$, the expressions for kinetic and potential energies are delineated as follows:

$$K = \frac{1}{2}\langle \omega, \omega \rangle, \quad V = \frac{1}{2}\gamma \mathfrak{d}^2 (p, r) \tag{7.39}$$

Through the formulation of the Lagrangian function and the application of the stochastic variational principle, one can derive the governing equation for the motion of undertaken system as:

$$\dot{\omega} = \gamma \left(p \times \log_p (r) \right) - \eta \langle \omega, \omega \rangle^{(\nu-1)} (\omega \times p) + F cos (\zeta t) + \beta \dot{\mathrm{W}} \tag{7.40}$$

In this context, $(p, \omega) \in \mathrm{S}^2 \times \mathrm{T}_p\mathrm{S}^2$ represent the state variables. The damping coefficient is denoted as $\eta = 0.5 \in \mathbb{R}$, the damping degree as $\nu = 1.3 \in \mathbb{R}$, the coefficient $\gamma = 1 \in \mathbb{R}$, and $r = [1, 0, 0] \in \mathrm{S}^2$ signifies the pivotal point. The kinematic equations are given by $\dot{p} = \omega \times p$. The harmonic excitation has an amplitude $F = 0.1$ and a forcing frequency $\zeta = 1$. Simulation on S^2 with the canonical metric utilizes results from [53] for the estimation of distance metric and matrix logarithm. Initial position and angular velocity are $[\sqrt{3}; \sqrt{3}; \sqrt{3}]^T$ and $[0.2; 0.3; -0.4]^T$, respectively. The system exhibits an anomaly that is artificially introduced by abruptly reducing the coefficient γ to 80% of the existing stiffness at 6000^{th} sample. The obtained results for the damage identification are illustrated in Fig. 7.6, wherein a distinct and prominent peak at the 6000^{th} sample clearly indicates the presence of the anomaly within

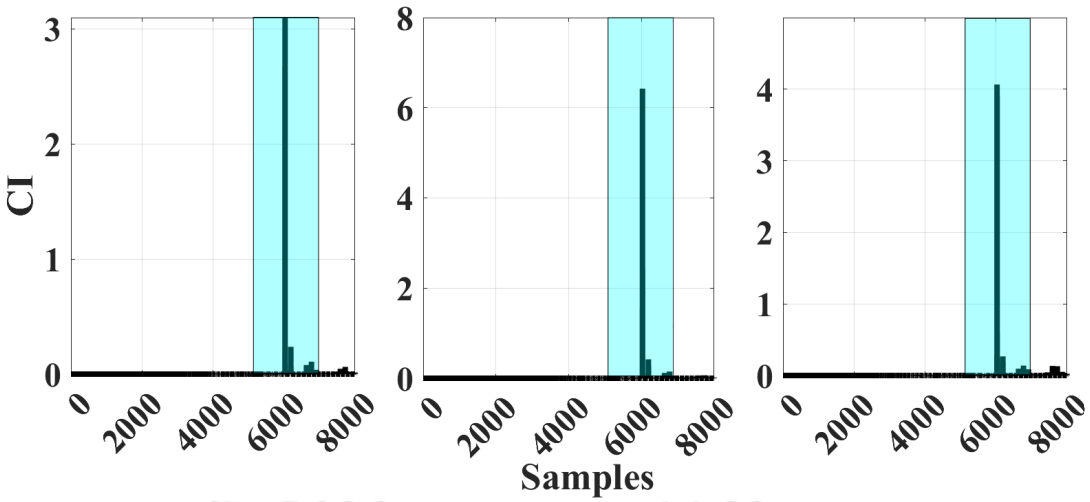

FIGURE 7.8: Stochastic spherical pendulum: Representation of the condition indicator using manifold based RPGA framework.

the system. Whereas, Fig. 7.7 shows the anomaly identification using Euclidean based algorithm RPCA, which provides an erroneous eigenspace thereby fails to provide the instance of anomaly in the undertaken system.

7.5.2 Stochastic spherical Pendulum

In this section, the effectiveness of the proposed algorithm for anomaly detection is demonstrated using the spherical pendulum, where $p \in \mathrm{S}^2$ and $\omega \in \mathrm{T}_x\mathrm{S}^2$ represent the position and angular velocity of the pendulum, respectively. To formulate the equation of motion, we consider the Lagrangian of the system $L : \mathrm{T}(\mathrm{S}^2)^n \to \mathbb{R}^1$ for the position y_i and velocity $\dot{y}_i$:

$$\mathcal{L}(y, \dot{y}) = \frac{1}{2} m l^2 \left\| \dot{y}_1 \right\|^2 + \frac{1}{2} m l^2 \left\| \dot{y}_2 \right\|^2 - \xi \left(1 - y_1^T y_2\right) \tag{7.41}$$

In this expression, $\xi \left(1 - y_1^T y_2\right)$ denotes the potential energy of the system, where ξ represents a positive elastic stiffness constant. It's worth noting that the elastic force disappears when the two pendulums are collinear, as the elastic potential energy has a zero gradient. The Lagrangian in Eq. (7.41) can be adapted to represent states y_i and ω_i as follows:

$$\tilde{L}(y, \omega) = \frac{1}{2} m l^2 \left\| \omega_1 \right\|^2 + \frac{1}{2} m l^2 \left\| \omega_2 \right\|^2 - \xi \left(1 - y_1^T y_2\right) \tag{7.42}$$

The kinematics of the provided configuration can be expressed as follows:

$$\dot{y}_i = S\left(\omega_i\right) y_i, \quad \forall i = 1, 2, 3 \tag{7.43}$$

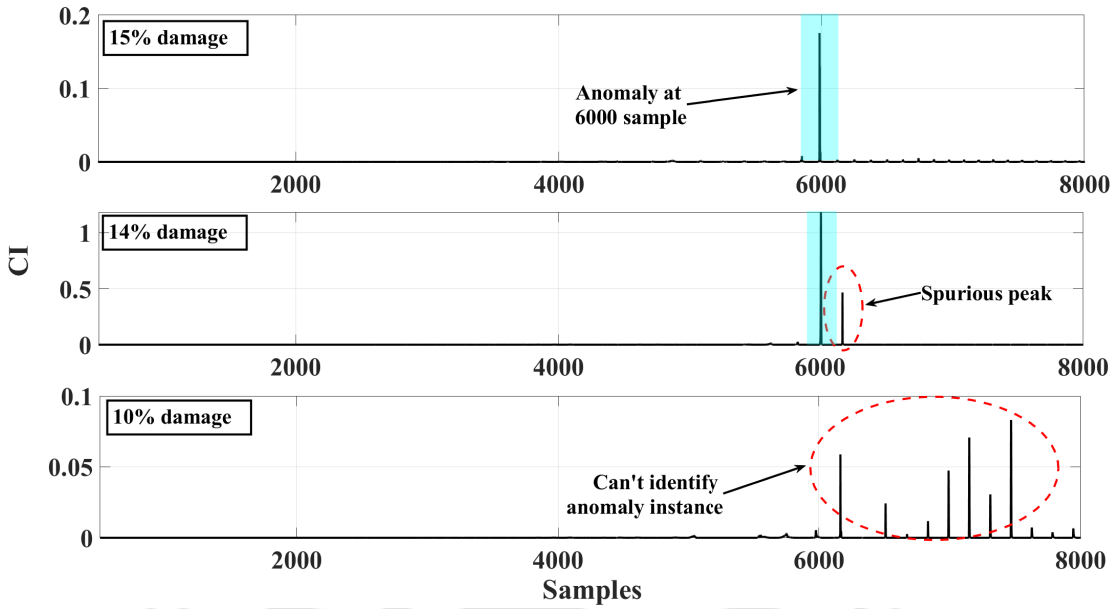

FIGURE 7.9: Stochastic spherical pendulum: Damage sensitivity test for 15%, 14% and 10% damage.

The integral over the modified Lagrangian system trajectory, combined with the forcing function F over the Wiener process W, can be formulated as an action integral. This action integral involves the wedge operator $S(\cdot)$, which maps $\mathrm{T}_y\mathrm{S}^2 \subset \mathbb{R}^3$ to $\mathfrak{so}(3)$.

$$\mathbb{A} = \int_{t_0}^{t_f} \tilde{L}(y\omega)\mathrm{dt} - \int_{t_0}^{t_f} \mathrm{F}(y,\omega) \circ \mathrm{dW}(t) \tag{7.44}$$

The Stratonovich Operator is symbolized by $\circ$. Within the infinitesimal variation of the action integral, we consider the variation over all differential curves $\gamma_i : [t_o, t_f] \to \mathbb{R}^3$ on S^2 satisfying the system's boundary condition. This variation encompasses all n curves, where i ranges from 1 to n. When it comes to the variation of states, the action integral expresses it in the following manner:

$$\delta\mathbb{A} = \int_{t_0}^{t_f} \left[\frac{\partial\tilde{L}}{\partial\omega_i}\delta\omega_i + \frac{\partial\tilde{L}}{\partial y_i}\delta y_i\right]\mathrm{dt} - \int_{t_0}^{t_f} \left[\frac{\partial\mathrm{F}}{\partial\omega_i}\delta\omega_i + \frac{\partial\mathrm{F}}{\partial y_i}\delta y_i\right] \circ \mathrm{dW}(t) \tag{7.45}$$

According to [9], the infinitesimal variations of y_i and ω_i along the differential curve $\gamma_i : [t_o, t_f] \to \mathbb{R}^3$ are expressed as follows:

$$\begin{aligned} \delta\dot{y}_i &= S(\dot{\gamma}_i)y_i + S(\gamma_i)\dot{y}_i \\ \delta\omega_i &= S(\gamma_i)\omega_i + (I_{3x3} - y_i y_i^T)\dot{\gamma}_i \end{aligned} \tag{7.46}$$

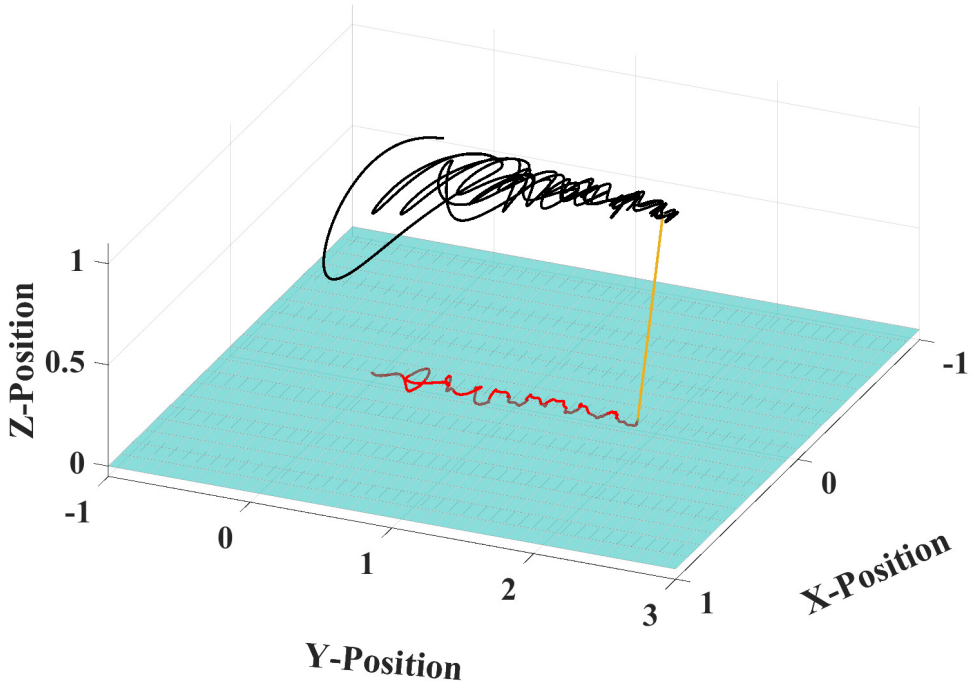

FIGURE 7.10: Stochastic pendulum cart system: Global trajectory of the cart in $\mathbb{R}^3$ (red line) and pendulum on S^2 (black line) with the initial conditions $x(0) = [0,0,0], \dot{x} = [0,0,0], q = [0,0,-1], \omega = [0.2, 0.3, 0.5]$.

Following a sequence of substitutions and rearrangements, we arrive at the following expression for the stochastic Euler-Lagrange equation:

$$\left(I_{3\times3} - y_i y_i^T\right)\left[\frac{d}{\mathrm{dt}}\frac{\partial \tilde{L}}{\partial \omega_i} - 2\omega_i \times \frac{\partial \tilde{L}}{\partial \omega_i}\right] - y_i \times \frac{\partial \tilde{L}}{\partial y_i} = \left[\left(I_{3\times3} - y_i y_i^T\right)\omega_i \times \frac{\partial \mathrm{F}}{\partial \omega_i} + y_i \times \frac{\partial \mathrm{F}}{\partial y_i}\right] \circ \frac{\mathrm{dW}(t)}{\mathrm{dt}} \tag{7.47}$$

Now, when considering the modified Lagrangian,

$$\hat{\mathrm{L}}(p,\omega) = +\frac{1}{2}ml^2\langle\omega,\omega\rangle - mgle_3^T p \tag{7.48}$$

After manipulating the modified Lagrangian and the stochastic Euler-Lagrange equation obtained from Eq. (7.47), we directly express the system's equation of motion in state space form on the Lie algebra $(\hat{\mathbf{p}}, \hat{\boldsymbol{\omega}}) \in T_{\mathcal{E}}S^2$.

$$\underbrace{\mathrm{d}\begin{bmatrix}\hat{\mathbf{p}}\\ \hat{\boldsymbol{\omega}}\end{bmatrix}}_{\tau} = \underbrace{\begin{bmatrix}\omega^{\Lambda}\\ -\left(A_{11}\left(mglp\times r\right) + A_{12}\left(ml\mathbf{Q}^T\left(\omega^{\Lambda}\right)^2 p\right)\right)^{\Lambda}\end{bmatrix}\mathrm{d}t}_{\gamma} + \underbrace{\begin{bmatrix}0\\ \left(A_{11}p\times\beta_1\right)\mathrm{d}B_1 + \left(A_{12}\beta_2\right)\mathrm{d}B_2\end{bmatrix}}_{\delta_r\ \mathrm{dB}_r} \tag{7.49}$$

where, $\begin{bmatrix}(A_{11})_{3\times3} & (A_{12})_{3\times2}\end{bmatrix} = \begin{bmatrix}\frac{1}{ml^2}I_3 & \frac{1}{mlp^{\Lambda}\mathbf{Q}}\end{bmatrix}$. The stochastic differential equation (SDE) presented in Eq. (7.49) governing the variables $\hat{\mathbf{p}}$ and $\hat{\boldsymbol{\omega}}$ adheres to the structure within the Lie algebra and

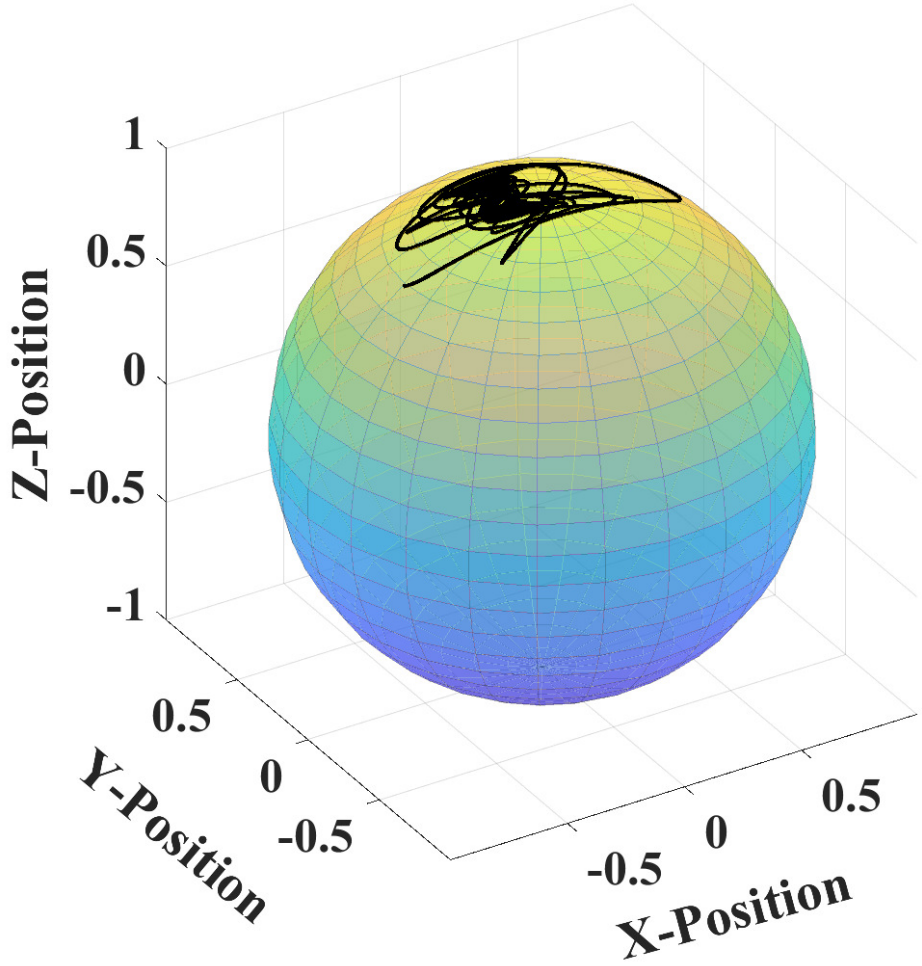

FIGURE 7.11: Stochastic pendulum cart system: Local trajectory of the pendulum on S^2 with the initial conditions $q = [0, 0, -1], \omega = [0.2, 0.3, 0.5]$.

is subjected to simulation using the proposed Taylor–1.5 framework. The Lie algebra $(\hat{\mathbf{p}}(n+1), \hat{\boldsymbol{\omega}}(n+1))$ is solved, and then the following update equations are used: $p\,(n+1) = \exp^{\hat{\mathbf{p}}(n+1)} p\,(n)$. Additionally, $\boldsymbol{\omega}(n+1) = \boldsymbol{\omega}(n) + \hat{\boldsymbol{\omega}}^{\mathrm{V}}(n+1)$. The position and angular velocity final solutions are effectively obtained from these equations. The starting point and angular velocity for the simulation are set to $[0; 0; -1]^T$ and $[0.2; 0.3; 0.5]^T$, respectively. The parameters taken for this study are: $m = 10$kg, $l = 1$m, $g = 9.81$m/s^2. The spherical Pendulum exhibits an anomaly that is artificially introduced by abruptly reducing the mass of the pendulum to 85% of its current value at the 6000^{th} sample. The obtained results are illustrated in Fig. 7.8, wherein a distinct and prominent peak at the 6000th sample clearly indicates the presence of the anomaly within the system. Concerning sensitivity analysis, Fig. 7.9 depicts the confidence intervals (CIs) for the system across different damage scenarios. The visualization highlights the framework's capability in detecting damage instances of up to 15%, albeit

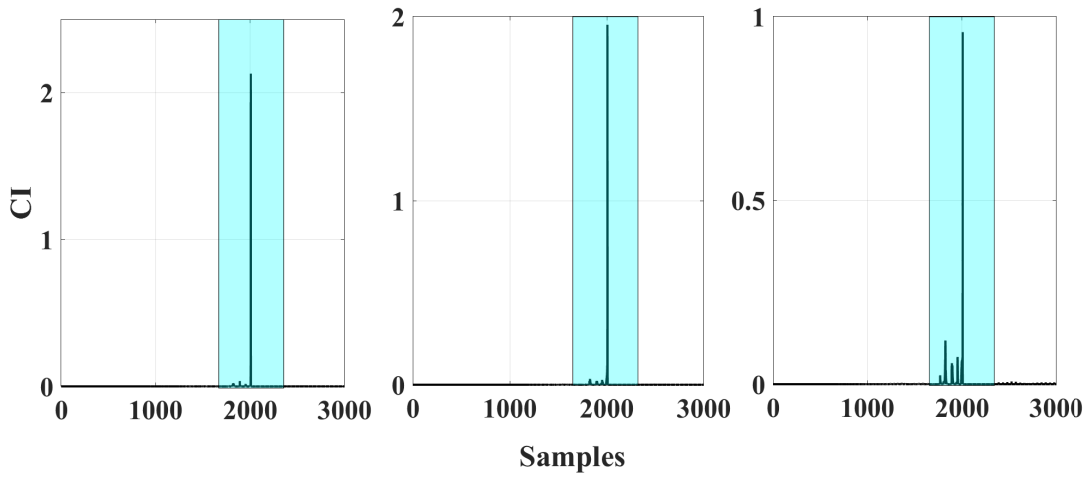

FIGURE 7.12: Stochastic pendulum cart system: Representation of the condition indicator using manifold based RPGA framework.

beyond this threshold, spurious peaks emerge alongside the damage indication. It is noteworthy that the proposed algorithm struggles to discern any damage at or below the 10% threshold for structural damage.

7.5.3 Inverted pendulum cart system moving on a rough surface

This section provides the efficacy of the proposed algorithm for the anomaly detection of the inverted spherical pendulum cart system traversing on a rough surface with $p \in \mathrm{S}^2$ and $\omega \in \mathrm{T}_x\mathrm{S}^2$ are the position and angular velocity of the pendulum, and, $x \in \mathbb{R}^3$ and $\dot{x} \in \mathbb{R}^3$ being displacement and velocity of the cart. The lagrangian of the system can be formulated as:

$$\hat{\mathrm{L}}(p, x_c, \omega, \dot{x_c}) = \frac{1}{2}(M_c + m)\langle \dot{x_c}, \dot{x_c}\rangle - ml\dot{x_c}^T p^{\Lambda}\omega + \frac{1}{2}ml^2\langle\omega, \omega\rangle - mgle_3^T p - \frac{1}{2}k\langle x_c, x_c\rangle \tag{7.50}$$

where $e_3 = [0, 0, 1]$ will be in the positive z direction. The equation of motion is directly formulated in the Lie algebra $(\hat{\mathbf{p}}, \hat{\boldsymbol{\omega}}) \in T_{\mathcal{E}}S^2$ in the state space form after the kinematic equation of the pendulum integrating the stochastic term is included:

$$\underbrace{\mathrm{d}\begin{bmatrix}\hat{\mathbf{p}}\\ \hat{\boldsymbol{\omega}}\\ x_c\\ \dot{x_c}\end{bmatrix}}_{\tau} = \underbrace{\begin{bmatrix}\omega^{\Lambda}\\ -\left(A_{11}\left(mglp \times r\right) + A_{12}\left(ml\left(\omega^{\Lambda}\right)^2 p + C\dot{x_c} + Kx_c\right)\right)^{\Lambda}\\ \dot{x_c}\\ -A_{21}\left(mglp \times r\right) - A_{22}\left(ml\left(\omega^{\Lambda}\right)^2 p + C\dot{x_c} + Kx_c\right)\end{bmatrix}}_{\gamma}\mathrm{d}t + \underbrace{\begin{bmatrix}0\\ \left(A_{11}p \times \beta_1\right)\mathrm{d}B_1 + \left(A_{12}\beta_2\right)\mathrm{d}B_2\\ 0\\ \left(A_{21}p \times \beta_1\right)\mathrm{d}B_1 + \left(A_{22}\beta_2\right)\mathrm{d}B_2 + \sigma\mathrm{d}B_3\end{bmatrix}}_{\delta_r\ \mathrm{d}B_r} \tag{7.51}$$

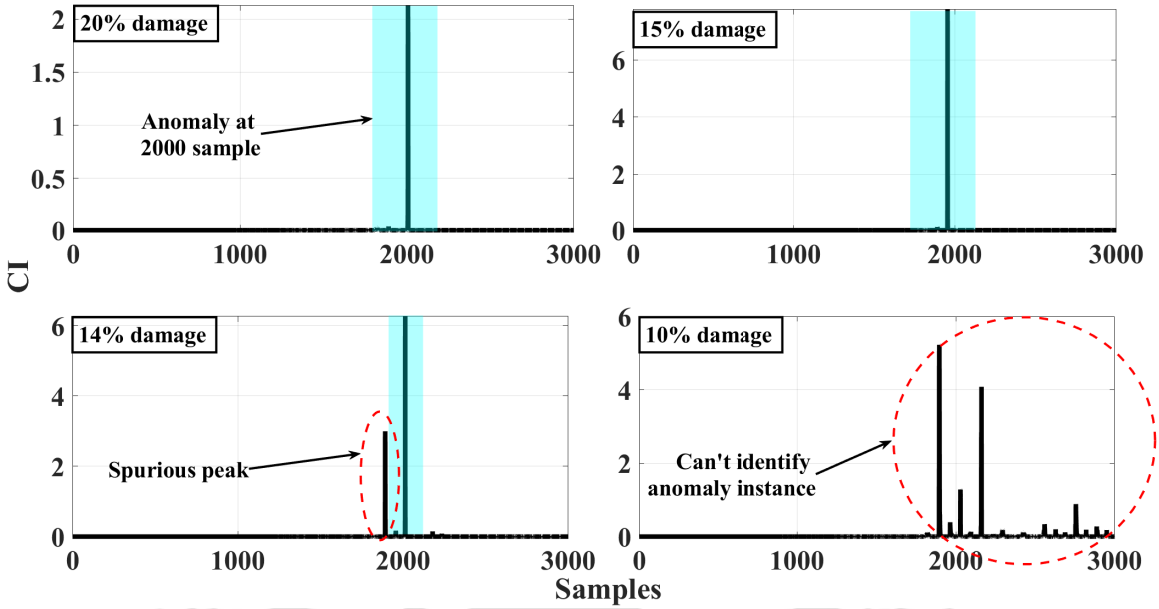

FIGURE 7.13: Stochastic pendulum cart system: Damage sensitivity test for 20%, 15%, 14% and 10% damage.

where, $\begin{bmatrix} (A_{11})_{3\times3} & (A_{12})_{3\times2} \\ (A_{21})_{2\times3} & (A_{22})_{2\times2} \end{bmatrix} = \begin{bmatrix} ml^2 I_3 & mlp^{\Lambda} \\ -mlp^{\Lambda} & (M+m) \end{bmatrix}^{-1}$. For this study's simulation, the parameters used are $M_c = 100$kg, $m = 0.9$kg, $l = 1$m, $k = 1000$N/m, and $g = 9.81$m/s^2. Here, $\hat{p}_0 = [0, 0, -1]^T$ and $\hat{\omega}_0 = [0.2, 0.3, 0.5]^T$. The stochastic differential equation (SDE) detailed in Eq. (7.51), governing $\hat{\mathbf{p}}$ and $\hat{\boldsymbol{\omega}}$, conforms to the Lie algebraic structure and undergoes simulation using the geometric Ito-Taylor–1.5 framework. Regarding the SDEs in Eq. (7.49), we obtain the Kolmogorov operators for variables x_c and $\dot{x}_c$, and then apply the proposed framework for updating the system states. The surface roughness is simulated using a stochastic process in z-direction with zero mean and σ as 0.1. The inverted Pendulum-cart system exhibits an anomaly that is artificially introduced by abru ptly reducing the stiffness of the cart to 80% of the original stiffness at the 2000^{th} sample. Fig. 7.10 shows the trajectory of the cart (red line) on $\mathbb{R}^3$ and the trajectory of the inverted spherical pendulum (black line) on S^2. For the better clarification Fig. 7.11 shows that the response of inverted pendulum lies on a unit 2-sphere. The obtained results for the damage identification are illustrated in Fig. 7.12, wherein a distinct and prominent peak at the 2000^{th} sample clearly indicates the presence of the anomaly within the system. In regard to sensitivity analysis, Fig. 7.13 illustrates the confidence intervals (CIs) for the system under various damage scenarios. The figure reveals that the proposed framework can effectively detect damage instances of up to 15%, but beyond that threshold, it exhibits

spurious peaks alongside the damage indication. Notably, the proposed algorithm fails to identify any damage at or below the 10% threshold for structural damage which is the same conclusion as in the case of spherical pendulum system. Another aspect of the analysis involves conducting a study to as-

M_c	Detectability	m	Detectability	l	Detectability	k	Detectability
10	yes	0.01	yes	0.1	yes	100	yes
50	yes	0.5	yes	0.5	yes	500	yes
200	yes	5	No	1.5	yes	2000	yes
400	No	10	No	2.0	No	3500	yes
600	No	20	No	2.5	No	5000	yes

TABLE 7.1: Damage detectability for varying parameters for inverted pendulum cart system

sess the sensitivity of parameters within the system under consideration. This examination delves into how variations or perturbations in specific parameters affect the overall behavior and performance of the system. By systematically varying the parameters M_c, m, l and k independently, while maintaining the remaining parameters constant, insights can be gleaned into the system's response and its susceptibility to changes in different factors. The damage detectability for varying parameter scenarios is given in Table 7.1. This parameter sensitivity study provides valuable information for understanding the system's robustness, identifying critical parameters that significantly influence its behavior, and refining the modeling and control strategies to enhance overall performance.

7.6 A note on the connection between RPCA on $\mathbb{R}^n$ and RPGA on S^2

The algorithm RPGA, constitutes a approach to damage detection rooted in the domain of First order eigen perturbation (FOEP) [34, 109]. It finds its unique niche when dealing with data residing on the spherical manifold S^2. In this intricate mathematical framework, the data points are not just raw numerical values but are situated on the spherical surface, adding complexity to the analysis. To unravel the underlying structure, RPGA projects this data onto the tangent bundle, TS^2, a space where tangent vectors capture the local geometry of the manifold. The covariance metrix can be expressed as:

$$\mathbf{R}_k = \frac{k}{k-1}\mathbf{R}_{k-1} + \frac{1}{k-1}\left[\log_{\mu_k}(x_k)\right]\left[\log_{\mu_k}(x_k)\right]^T \tag{7.52}$$

where, the mean μ_k is obtained through the intrinsic formulation of the mean as expressed in Eq. (7.14). The principal geodesics are then extracted from this transformed space in real time, effectively

characterizing the essential features of the data. Operations on the tangent space becomes possible owing to the Euclidean-tangent space diffeomorphism. This process results in the formation of an eigenspace that encapsulates the intrinsic properties of the spherical data.

Now, what makes this connection between RPGA and RPCA intriguing is the transformation of perspective. Imagine merging the manifold S^2 and its associated tangent space TS^2 into a unified Euclidean subspace which negates the projection of the data to TS^2. By doing so, we transition from the intricate spherical representation to a more conventional Euclidean space $\mathbb{R}^n$ and the block covariance matrix takes up the form

$$\mathbf{R}_k = \frac{k}{k-1}\mathbf{R}_{k-1} + \frac{1}{k-1}x_k x_k^T \tag{7.53}$$

In this new setting, the RPGA algorithm essentially converges to RPCA, a widely used technique for data analysis in Euclidean spaces. This transition highlights the interaction between different geometric spaces and how the choice of representation can significantly impact the choice and performance of data analysis algorithms, shedding light on the powerful connection between RPGA on S^2 and RPCA on $\mathbb{R}^n$.

7.7 Research Findings

The outcomes of this chapter can be summarized as follows:

- RPGA Formulation: This research introduces Recursive Principal Geodesic Analysis (RPGA) as a novel method for conducting health monitoring of systems operating within differentiable manifolds. RPGA offers a robust framework for extracting meaningful information from manifold-based data, enabling more accurate and precise health assessments.
- Considered Systems: The study systematically applies RPGA to three distinct systems: the stochastic geometric oscillator on S^2, the spherical pendulum, and a spherical pendulum suspended from a cart. This comprehensive exploration demonstrates RPGA's versatility and adaptability, making it a valuable tool for diverse real-world systems with complex dynamics.
- Comparative Analysis: To gauge RPGA's effectiveness, the research performs a comparative analysis by contrasting health monitoring results obtained through RPGA with those generated by RPCA, a monitoring scheme tailored for $\mathbb{R}^2$. This rigorous comparison underscores RPGA's

superiority in providing accurate health assessments for systems on differentiable manifolds, thereby emphasizing its practical significance in the field of complex systems analysis.

- Sensitivity Testing: The study includes a sensitivity test to determine the threshold at which the proposed RPGA algorithm starts producing erroneous results. Findings reveal that the proposed framework effectively detects damage instances of up to 15%, but beyond this threshold, it exhibits spurious peaks alongside damage indications. Notably, RPGA fails to identify any damage at or below the 10% threshold for structural damage.

In summary, this research journey has encompassed a wide spectrum of mathematical modeling, numerical integration, and health monitoring within manifold-based systems. It has included an exploration of foundational principles related to stochastic Hamiltonian dynamics, an enhancement of real-time modal identification towards both Euclidean and non-Euclidean domains, the development of symplectic geometric integration schemes for smooth differentiable manifolds, and their practical application to real-world problems. As we approach the concluding chapter, it is essential to reflect on the key insights acquired and the potential avenues for future studies that can further advance our comprehension and capabilities within the domain of dynamic systems.

Chapter 8

Conclusions and Future studies

8.1 Conclusion

In this study, I have arrived at several key conclusions that address critical aspects of the research. These findings encompass quick convergence in real-time modal identification, innovative techniques for solving stochastic systems on manifolds, and a novel framework for studying stochastic Hamiltonian systems. Additionally, a damage detection algorithm designed for systems evolving on configuration manifold S^2 is also introduced. Each of these conclusions contributes significantly to the understanding of structural dynamics and geometric numerical integration, which can be summarized as follows:

1. First part of the work introduces an error adaptive approach for real-time modal identification using first-order eigen perturbation techniques, demonstrating significantly improved convergence compared to alternative algorithms in this category. The approach focuses on estimating error feedback for first-order error terms rather than using higher-order perturbation formulations. Numerical examples and a benchmark problem showcase the algorithm's quick convergence, independence of sampling frequency, thus highlighting its adaptive error handling capabilities. Additionally, it also shows promise in real-time modal control applications, although comprehensive real-time under-determined modal identification remains a future research direction.

2. Second part of the work introduces a novel approach for solving stochastic systems on manifolds while preserving their geometric characteristics. By employing an Ito-Taylor expansion and leveraging the manifold-tangent space connection, new formulation for Kolmogorov operators using geometric preserving framework are developed leading to a new geometric Taylor 1.5 scheme which demonstrates its effectiveness compared to a non-geometric counterpart.

3. The study focuses on systems evolving on the S^2 manifold under stochastic excitation and validates the accuracy of the proposed scheme by comparing it with an existing g-EM scheme. The results show a reduction in global error for coarser time steps, highlighting the computational efficiency and accuracy of the proposed method.

4. The research contributes to the field of stochastic dynamics by presenting a new framework for studying stochastic Hamiltonian systems on manifolds. By establishing stochastic Hamiltonian differential equations (SHDEs) and utilizing geometric symplectic Ito-Taylor expansion-based numerical integration schemes, the proposed method accurately computes response trajectories while preserving the underlying geometry and Hamiltonian. The formulation of SHDEs and geometric symplectic numerical integration scheme are extended towards general class of manifold using metric tensor and intrinsic formulation. The accuracy of the proposed approach is demonstrated through benchmark case studies and concrete examples, showcasing significant reductions in global error and computational costs.

5. Finally, a damage detection algorithm viz. recursive principal geodesic analysis (RPGA), a counterpart of a well known technique RPCA (on the Euclidean space) is proposed for the systems evolving on configuration manifolds. The findings from the damage identification study for manifold based systems demonstrate the successful identification of an anomaly in geometric systems such as spherical pendulum, stochastic duffing on S^2 and the inverted spherical Pendulum-cart system through the implementation of a geometric algorithm.

8.2 Recommendations for future study

During the extensive research conducted for this dissertation, numerous aspects of the current work have come to light. In light of these discoveries, several promising directions for future research and expansion can be outlined:

1. **Extension of error adapted FOEP framework**: This extension could involve experimental validation of the real-time health monitoring algorithm, particularly with a focus on its applicability to real-time structural control.

2. **Hybrid Approaches**: The current geometric numerical simulation approach still suffers from the view of computational complexity when dealing with a large number of dimensions. Therefore, it

is necessary to investigate hybrid approaches that combine the strengths of the proposed methods with other numerical techniques or machine learning algorithms to address complex problems in structural dynamics, control, and monitoring.

3. **Interaction of non-linearity and stochasticity**: Exploring the interaction between non-linearity and stochasticity in geometric simulation techniques represents a noteworthy research direction less in the current study. Investigating this interaction holds the potential to yield valuable insights into complex system behaviors and enhance the predictive accuracy of the simulation approach.

4. **Application to Different Types of Stochastic Systems**: One possible extension of the present work could be to explore the versatility of th e proposed framework, extending its applicability beyond Hamiltonian systems, and evaluate its effectiveness when applied to practical engineering systems in real-world contexts like:

   (a) Stochastic Processes on the Earth's Surface: Study the movement of particles or agents on the Earth's surface, taking into account environmental variability and randomness. This could be applied to the modeling of pollutant dispersion, animal migration, or the spread of diseases, where both geographic constraints and stochastic factors play a significant role.

   (b) Stochastic Control of Autonomous Vehicles on Curved Terrains: Investigate the control of autonomous vehicles, such as drones or self-driving cars, moving on surfaces with complex geometries, like hilly terrains, roads, or underwater environments. Develop control algorithms that adapt to both the non-Euclidean geometry of the terrain and stochastic disturbances.

   (c) Stochastic Dynamics of Molecular Systems on Energy Landscapes: Analyze the stochastic motion of molecules, like proteins, on energy landscapes represented by high-dimensional manifolds. Explore how randomness affects processes like protein folding, conformational changes, and binding interactions, which are essential in biochemistry and drug discovery.

   (d) Biological Systems with Stochasticity: Extending the current work, one potential direction is to apply manifold-based analysis to health monitoring and statistical analysis of human organs, such as the brain and heart, which are inherently manifold-based structures. This

extension opens opportunities for enhancing diagnostic capabilities and advancing personalized healthcare.

5. **Application of Geometric Algorithms in PTMDs Control**: Implementation the proposed geometric algorithms, leveraging geometric control and optimization techniques on manifolds, to control Pendulum Tuned Mass Dampers (PTMDs) in structural systems. Assessing their effectiveness in reducing structural vibrations and enhancing system stability for the systems on manifold.

6. **Stochasticity in System Parameters**: Factoring in stochasticity within the inherent system characteristics represents a potential extension of the current work. This extension broadens the horizons for simulation, control, and monitoring of geometric systems, providing a more comprehensive and robust approach to system analysis.

Appendix A

Remainder terms for the Ito-Taylor expansion

Remainder terms for the Ito-Taylor expansion

For the Taylor series expansion of the function g (t) in Eq. (4.21), the remainder terms are given as,

$$\begin{aligned}\mathcal{R} \;=\; & I_{000}\left(\Im^0\Im^0\Im^0\mathbf{g}(s_3)\right)+I_{100}\left(\Im^r\Im^0\Im^0\mathbf{g}(s_3)\right)+I_{010}\left(\Im^0\Im^r\Im^0\mathbf{g}(s_3)\right)\\ & +I_{110}\left(\Im^{r_1}\Im^{r_2}\Im^0\mathbf{g}(s_3)\right)+I_{001}\left(\Im^0\Im^0\Im^r\mathbf{g}(s_3)\right)+I_{101}\left(\Im^{r_1}\Im^0\Im^{r_2}\mathbf{g}(s_3)\right)\\ & +I_{011}\left(\Im^0\Im^{r_1}\Im^{r_2}\mathbf{g}(s_3)\right)+I_{111}\left(\Im^{r_1}\Im^{r_2}\Im^{r_3}\mathbf{g}(s_3)\right)\end{aligned} \tag{A.1}$$

The remainder terms corresponding to the truncated Ito-Taylor expansion for the geometric Taylor 1.5 scheme is obtained as,

$$\begin{aligned}\tilde{\mathcal{R}} = & I_{000}\left(\Im^0\Im^0\alpha_{ij}\left(s_3\right)\right)+I_{001}\left(\Im^0\Im^0\beta_{r,ij}\left(s_3\right)\right)+I_{010}\left(\Im^0\Im^r\alpha_{ij}\left(s_3\right)\right)\\ & +I_{101}\left(\Im^{r_1}\Im^0\beta_{r_2,ij}\left(s_3\right)\right)+I_{100}\left(\Im^r\Im^0\alpha_{ij}\left(s_3\right)\right)+I_{011}\left(\Im^0\Im^{r_1}\beta_{r_2,ij}\left(s_3\right)\right)\\ & +I_{110}\left(\Im^{r_1}\Im^{r_2}\alpha_{ij}\left(s_3\right)\right)+I_{0111}\left(\Im^0\Im^{r_1}\Im^{r_2}\beta_{r_3,ij}\left(s_4\right)\right)+I_{1111}\left(\Im^{r_1}\Im^{r_2}\Im^{r_3}\beta_{r_4,ij}\left(s_4\right)\right)\end{aligned} \tag{A.2}$$

Appendix B

Quadratic variation

Consider a continuous function g defined on the interval $[0, t]$. The Quadratic Variation (QV_n) [29] of g can be expressed as the limit of a sum as follows:

$$QV_n\left(g, t\right) = \sum_{i=1}^{n} \left(g\left(s_i\right) - g\left(s_{i-1}\right)\right)^2 \tag{B.1}$$

The interval $[0, t]$ is divided into n partitions (P_n) such that $P_n\left([0, t]\right) : 0 = s_0 < s_1 < \ldots < s_n = t$. For the case of Wiener process i.e. $g = B\left(t\right)$ and $n \to \infty$, it holds that:

1. $QV_n = \sum_{i=1}^{n} \left(B_k\left(s_i\right) - B_k\left(s_{i-1}\right)\right)^2 \xrightarrow{2} \int_0^t \left(dB_k\left(s\right)\right)^2 = t$
2. $QV_n = \sum_{i=1}^{n} \left(B_k\left(s_i\right) - B_k\left(s_{i-1}\right)\right)\left(B_l\left(s_i\right) - B_l\left(s_{i-1}\right)\right) \xrightarrow{2} \int_0^t dB_k\left(s\right) dB_l\left(s\right) = 0$

where, $\xrightarrow{2}$ denotes the convergence in mean square.

Proof: (i) $\quad QV_n = \sum_{i=1}^{n} \left(B_k\left(s_i\right) - B_k\left(s_{i-1}\right)\right)^2 \xrightarrow{2} \int_0^t \left(dB_k\left(s\right)\right)^2 = t$

To prove the above statement, the following results are required to be established: $E\left[QV_n\right] = t$ and $Var\left[QV_n\right] = 0$ as $n \to \infty$.

$$\begin{aligned}
E\left[QV_n\right] &= E\left[\sum_{i=1}^{n} \left(B_j\left(s_i\right) - B_j\left(s_{i-1}\right)\right)^2\right] \\
&= \sum_{i=1}^{n} E\left(B_j\left(s_i\right) - B_j\left(s_{i-1}\right)\right)^2 \\
&= \sum_{i=1}^{n} \left(E\left[\left(B_j\left(s_i\right)\right)^2\right] + E\left[\left(B_j\left(s_{i-1}\right)\right)^2\right] - 2E\left[B_j\left(s_i\right) B_j\left(s_{i-1}\right)\right]\right) \\
&= \sum_{i=1}^{n} \left(s_i + s_{i-1} - 2s_{i-1}\right) \quad \text{(using the properties of Wiener process)} \\
&= \sum_{i=1}^{n} \left(s_i - s_{i-1}\right) = t
\end{aligned} \tag{B.2}$$

$$\begin{aligned} Var\left[QV_n\right] &= Var\left[\sum_{i=1}^{n}\left(B_j\left(s_i\right)-B_j\left(s_{i-1}\right)\right)^2\right] \\ &= \sum_{i=1}^{n} Var(B_j\left(s_i\right)-B_j\left(s_{i-1}\right))^2 \end{aligned} \tag{B.3}$$

Again,

$$\begin{aligned} Var(B_j\left(s_i\right)-B_j\left(s_{i-1}\right))^2 &= E\left[\left(B_j\left(s_i\right)-B_j\left(s_{i-1}\right)\right)^2\right]-\left(E\left[\left(B_j\left(s_i\right)-B_j\left(s_{i-1}\right)\right)^2\right]\right)^2 \\ &= 3(Var\left(B_j\left(s_i\right)-B_j\left(s_{i-1}\right)\right))^2-\left(s_i-s_{i-1}\right)^2 \\ &= 2\left(s_i-s_{i-1}\right)^2 \end{aligned} \tag{B.4}$$

$$\begin{aligned} Var\left[QV_n\right] &= 2\sum_{i=1}^{n}\left(s_i-s_{i-1}\right)^2 \\ &\leq 2\underbrace{\max}_{1\leq i\leq n}\left(s_i-s_{i-1}\right)\sum_{i=1}^{n}\left(s_i-s_{i-1}\right) \\ &\leq 2\underbrace{\max}_{1\leq i\leq n}\left(s_i-s_{i-1}\right)\left(s_n-s_0\right) \\ &\to 0,\ n\to\infty \end{aligned} \tag{B.5}$$

$$\therefore \sum_{i=1}^{n}\left(B_k\left(s_i\right)-B_k\left(s_{i-1}\right)\right)^2 \xrightarrow{2} \int_0^t \left(dB_k\left(s\right)\right)^2 = t$$

$$(ii)\, QV_n = \sum_{i=1}^{n}\left(B_k\left(s_i\right)-B_k\left(s_{i-1}\right)\right)\left(B_l\left(s_i\right)-B_l\left(s_{i-1}\right)\right) \xrightarrow{2} \int_0^t dB_k\left(s\right)dB_l\left(s\right) = 0$$

Similar to the previous proof, here it is required to establish that $E\left[QV_n\right]=0$ and $Var\left[QV_n\right]=0$ as $n\to\infty$.

$$\begin{aligned} E\left[QV_n\right] &= E\left[\sum_{i=1}^{n}\left(B_k\left(s_i\right)-B_k\left(s_{i-1}\right)\right)\left(B_l\left(s_i\right)-B_l\left(s_{i-1}\right)\right)\right] \\ &= \sum_{i=1}^{n}\left(E\left[\left(B_k\left(s_i\right)-B_k\left(s_{i-1}\right)\right)\right]E\left[\left(B_l\left(s_i\right)-B_l\left(s_{i-1}\right)\right)\right]\right) \\ &= 0 \end{aligned} \tag{B.6}$$

$$
\begin{aligned}
Var\left[QV_n\right] &= Var\sum_{i=1}^{n}\left(B_k\left(s_i\right)-B_k\left(s_{i-1}\right)\right)\left(B_l\left(s_i\right)-B_l\left(s_{i-1}\right)\right) \\
&= \sum_{i=1}^{n} E\left[\left(B_k\left(s_i\right)-B_k\left(s_{i-1}\right)\right)^2\right] E\left[\left(B_l\left(s_i\right)-B_l\left(s_{i-1}\right)\right)^2\right] \\
&= \sum_{i=1}^{n}\left(s_i-s_{i-1}\right)^2 \\
&\leq \underbrace{\max}_{1\leq i\leq n}\left(s_i-s_{i-1}\right)\sum_{i=1}^{n}\left(s_i-s_{i-1}\right) \\
&\leq \underbrace{\max}_{1\leq i\leq n}\left(s_i-s_{i-1}\right)\left(s_n-s_0\right) \\
&\to 0,\ n\to\infty
\end{aligned}
\tag{B.7}
$$

$$
\therefore \sum_{i=1}^{n}\left(B_k\left(s_i\right)-B_k\left(s_{i-1}\right)\right)\left(B_l\left(s_i\right)-B_l\left(s_{i-1}\right)\right) \xrightarrow{2} \int_0^t dB_k\left(s\right)dB_l\left(s\right)=0
$$

Appendix C

Simplification of MSIs

For the evaluation of the simplified forms of the MSIs in Eq. (2.5), first consider the case of two independent Wiener processes B^{j_1} and B^{j_2}. The integrals $I_{(j_1,j_2)}$ and $I_{(j_2,j_1)}$ occur in pairs in Eq. (2.3). Now using Ito's formula [29], the MSIs $I_{(j_1,j_2)} + I_{(j_2,j_1)}$ for $(j_1 \neq j_2)$ can be simplified as:

$$\begin{aligned} I_{(j_1,j_2)} + I_{(j_2,j_1)} &= \int_t^{t+h} \int_t^{s_1} dB^{j_1}(s_2) dB^{j_2}(s_1) + \int_t^{t+h} \int_t^{s_1} dB^{j_2}(s_2) dB^{j_1}(s_1) \\ &= \int_t^{t+h} dB^{j_1}(s) \int_t^{t+h} dB^{j_2}(s) \\ &= \Delta B^{j_1} \Delta B^{j_2} \end{aligned} \tag{C.1}$$

For the case when $j_1 = j_2$, the calculation is further simplified as:

$$\begin{aligned} I_{j_1,j_1} &= \int_t^{t+h} \int_t^{s_1} dB^{j_1}(s_2) dB^{j_1}(s_1) \\ &= \int_t^{t+h} B^{j_1}(s_1) dB^{j_1}(s_1) - \int_t^{t+h} B(t) dB^{j_1}(s_1) \end{aligned} \tag{C.2}$$

Consider the Ito's formula as:

$$B^{j_1}(t) dB^{j_1}(t) = \frac{1}{2} \left(\left(dB^{j_1} \right)^2 (t) - dt \right)$$

Now, Eq. (C.2) is evaluated as:

$$\begin{aligned} I_{j_1,j_1} &= \tfrac{1}{2} \int_t^{t+h} \left(dB^{j_1} \right)^2 (t) - \tfrac{1}{2} \int_t^{t+h} dt - B^{j_1}(t) \Delta B^{j_1}(t) \\ &= \tfrac{1}{2} (B^{j_1})^2 (t+h) - \tfrac{1}{2} (B^{j_1})^2 (t) - \tfrac{1}{2} h - B^{j_1}(t) B^{j_1}(t+h) + (B^{j_1})^2 (t) \\ &= \tfrac{1}{2} \left((\Delta B^{j_1})^2 - \Delta t \right) \end{aligned} \tag{C.3}$$

Appendix D

Variational Calculus

The calculus of variations encompasses the fundamental lemma, which exists in multiple distinct formulations. Initially, the classical version is summarized, which applies when the configuration manifold is $\mathbb{R}^n$. Subsequently, variations are summarized for cases where the curved space is either a Lie group embedded in $\mathbb{R}^{n\times n}$ or an embedded manifold in $\mathbb{R}^n$.

Fundamental Lemma on $\mathbb{R}^n$ for Variational Calculus

In $\mathbb{R}^n$, the fundamental lemma of the calculus of variations posits that when considering continuous functions x mapping from $[t_0, t_f]$ to $\mathbb{R}^n$ and functions F mapping from $[t_0, t_f]$ to $\mathbb{R}^n$, if

$$\int_{t_0}^{t_f} F(t) \cdot \delta x(t) dt = 0, \tag{D.1}$$

Applies to all continuous perturbations $\delta x : [t_0, t_f] \to \mathbb{R}^n$ with the conditions $\delta x\,(t_0) = \delta x\,(t_f) = 0$, this leads to the conclusion that

$$F(t) = 0, \quad t_0 \leq t \leq t_f \tag{D.2}$$

In simpler terms, if $F(t)$ is not equal to zero for any point within the interval $[t_0, t_f]$, then there exists a neighborhood around that point where $F(t)$ maintains a fixed sign. Within this neighborhood, one can construct a variation that violates the initial assumption, leading to a contradiction, and thus proving the statement's validity.

The Fundamental Lemma of Variational Calculus on an Embedded Manifold

Let's examine a differentiable manifold M that is embedded within $\mathbb{R}^n$. The fundamental principle of calculus of variations on this manifold can be expressed in the following manner: Assuming we have continuous functions $x : [t_0, t_f] \to M$ and $F : [t_0, t_f] \to (\mathbb{R}^n)^*$, if the integral equation is satisfied:

$$\int_{t_0}^{t_f} F(t) \cdot \xi(t) dt = 0 \tag{D.3}$$

is valid for every continuous variation $\xi : [t_0, t_f] \to \mathrm{T}x(t)M$ with the conditions $\xi(t_0) = \xi(t_f) = 0$, it consequently suggests that.

$$F(t) \cdot \xi = 0, \quad t_0 \leq t \leq t_f, \tag{D.4}$$

This implies that $F(t)$ is perpendicular to the tangent space $\mathrm{T}xM$ at every point $t_0 \leq t \leq t_f$.

Fundamental Lemma of Variational Calculus on a Lie Group

Furthermore, it is possible to broaden the scope of the fundamental lemma of the calculus of variations to encompass a Lie group G, where the tangent space is linked to the Lie algebra $\mathfrak{g}$. Let $\mathfrak{g}^*$ denote the vector space comprising linear functionals on $\mathfrak{g}$. This expansion results in the following proposition:

The fundamental lemma of the calculus of variations within the context of the Lie group G can be articulated as follows: Suppose we have a continuous function $g : [t_0, t_f] \to \mathrm{G}$ and a continuous function $F : [t_0, t_f] \to \mathfrak{g}^*$. If the integral equation is satisfied:

$$\int_{t_0}^{t_f} \langle F(t) \cdot \eta \rangle dt = 0 \tag{D.5}$$

is valid for all continuous variations $\eta : [t_0, t_f] \to \mathfrak{g}$ with the conditions $\eta(t_0) = \eta(t_f) = 0$, then it signifies.

$$\langle F(t) \cdot \eta \rangle = 0, \quad t_0 \leq t \leq t_f \tag{D.6}$$

This implies that $F(t)$ is perpendicular to $\mathfrak{g}$ for every $t_0 \leq t \leq t_f$. In this context, $\langle F \cdot \eta \rangle$ represents the pairing of a covector $F \in \mathfrak{g}^*$ and a vector $\eta \in \mathfrak{g}$.

Appendix E

Definitions on manifold

1. Tensors

   A tensor is an object that is invariant under a change of co-ordinates and has components that change in a special predictable way under the change of co-ordinates. A tensor is a collection of vectors and co-vectors combined together using the tensor product. Tensors follow two transformation rules: 1. Forward Transformation(F) 2. Backward Transformation(B), such that $FB = I$.

2. Co-vectors

   A function that takes a vector and produces a scalar is called a co-vector. Spaces of co-vectors are called dual space. Co-vectors are invariant but co-vector components are not invariant.

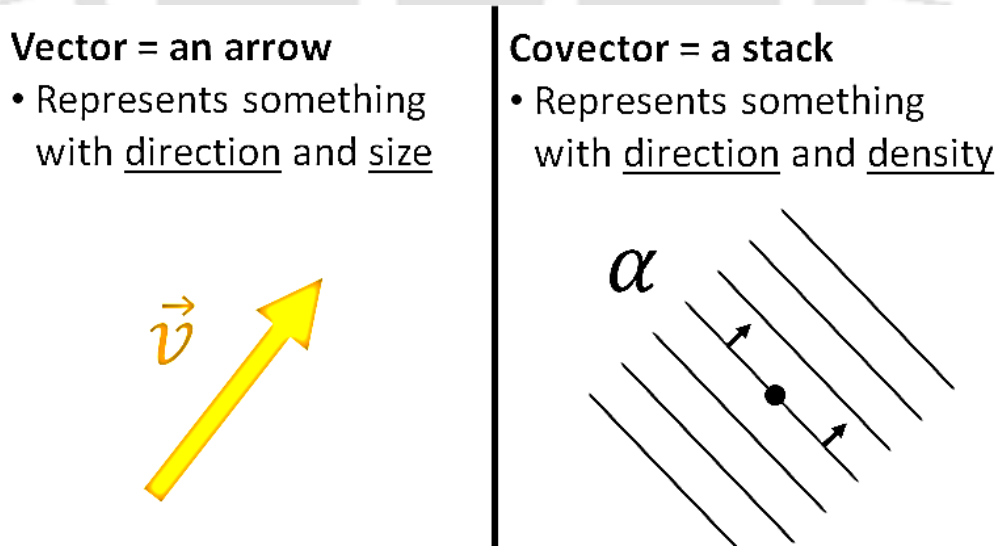

FIGURE E.1: Comparisons of Vectors and Covectors

3. Metric Tensor

A metric tensor g is an additional structure on a manifold $\mathcal{M}$ in the field of differential geometry that allows for the definition of distances and angles, much like the inner product $(\cdot)$ on a Euclidean space does. A metric tensor g on $\mathcal{M}$ is made up of metric tensors at each point $p \in \mathcal{M}$ that vary smoothly with p, and a metric tensor at a point $p \in \mathcal{M}$ is a bilinear form defined on the tangent space at p. Metric Tensor is one of the most important objects in Manifolds as it is the metric tensor which allow us to do mathematical operations, such as finding the area, shortest distance, etc in manifolds. Consider the example of the Pythagoras theorem, which finds us the hypotenuse distance in a triangle, but is only valid in the orthonormal basis, so for the operations on a manifold metric tensor g is required.

There are two methods available to define the metric tensor. These are

(a) *Intrinsic Approach*: The intrinsic approach in differential geometry is a foundational framework for characterizing geometric structures without reference to external coordinates or embeddings. It revolves around the notion of an intrinsic metric tensor, denoted as g, which defines the inner product between tangent vectors at each point on the manifold. Geodesics, described by the equation $\nabla_{\dot{\gamma}}\dot{\gamma}$, are the paths of shortest distance on the manifold, and they provide essential information about the geometry. In this approach, the focus is on the intrinsic properties of the manifold, where the covariant derivative $\nabla_{(\cdot)}(\cdot)$ encodes information about how vectors change as they move along the manifold. This approach enables the characterization of curvature and other geometric properties directly on the manifold, independent of any external reference. By employing the tool of differential geometry, one can investigate and analyze complex geometric structures with a high degree of generality and without reliance on specific coordinate systems, making it a powerful tool for various mathematical and physical inquiries.

(b) *Extrinsic Approach*: A manifold's extrinsic view is a portion of a larger space, typically a space with more dimensions. In that case, the manifold can be described by an equation that indicates which points it takes up in the larger space. For instance, the unit sphere is seen as a subset of Euclidean 3-space when viewed extrinsically. This is also referred to as the "birds eye view".

Mathematically, a metric tensor g is the inner product of the basis vectors of the manifold under consideration.

$$\mathrm{g} = \begin{bmatrix} g_{ii} & g_{ij} \\ g_{ji} & g_{jj} \end{bmatrix} \tag{E.1}$$

Where, the components of the metric tensor are the inner products of the basis vectors in the intrinsic space, $g_{ij} = e_i.e_j$. This is the intrinsic definition where the manifold under consideration is the sphere. In case of extrinsic view, the metric tensor is defined as follows:

$$G = \begin{bmatrix} e_x e_x & e_x e_y & e_x e_z \\ e_y e_x & e_y e_y & e_y e_z \\ e_z e_x & e_z e_y & e_z e_z \end{bmatrix} \tag{E.2}$$

Where the e basis vectors are from the Euclidean space. Once this is established, the operations on geometrical surfaces can be performed. The Metric Tensor is also called as the *First Fundamental Form*.

4. Geodesics

The straightest possible path can be draw on surfaces between two points is called a geodesic. A curve that minimises length locally is a geodesic. It is, in effect, the path that a particle that is not accelerating would take. The geodesics are lines that are straight in the plane. The geodesics on the sphere are large circles. The notions of distance and acceleration are impacted by the Riemannian metric, which also affects the geodesics in a space[125]. In addition to having many other intriguing qualities, geodesics maintain a direction on a surface. Any point on a geodesic arc has a normal vector that runs parallel to the surface there. The Equation of Geodesic is given by:

$$\frac{d^2u^k}{d\lambda^2} + \Gamma^k_{ij}\frac{du^i}{d\lambda} \cdot \frac{du^j}{d\lambda} = 0 \tag{E.3}$$

An example of geodesic curve between two points in a Sphere is provided in Fig. E.2.

5. Christoffel Symbols

The Christoffel symbols are a set of numbers that represent the metric link between mathematics and physics. A metric can be used to measure distances on surfaces or other manifolds thanks to the metric connection, a specialisation of the affine connection. The Christoffel symbols give

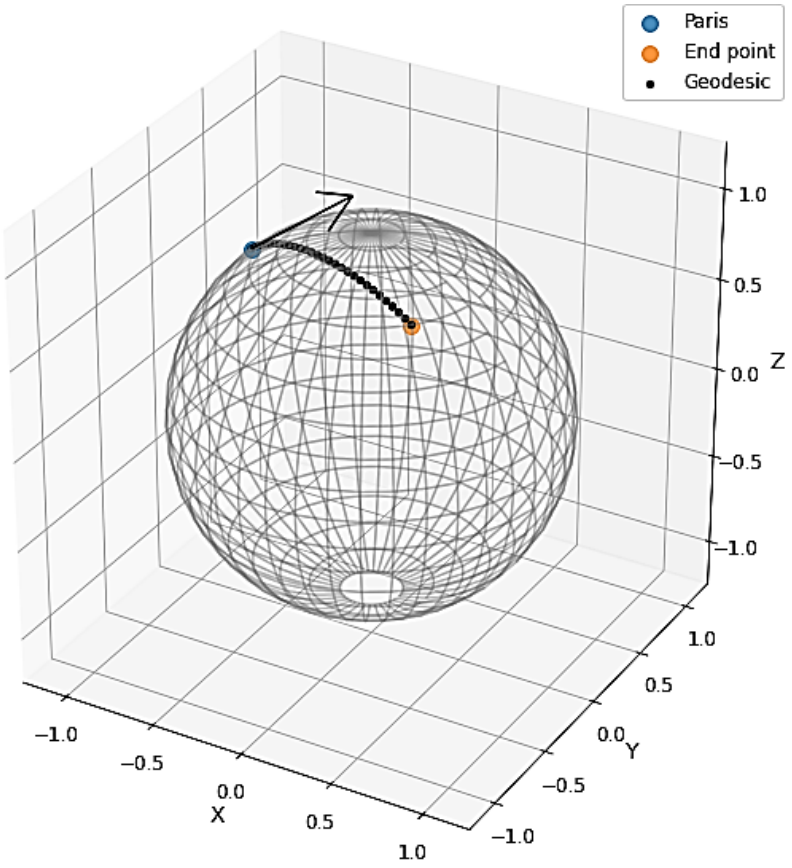

FIGURE E.2: Geodesic between two points in a Sphere

a concrete illustration of how coordinates on the manifold relate to (pseudo-)Riemannian geometry. Then, more ideas, such as parallel transportation, geodesics, etc., can be expressed using Christoffel symbols. When there is some symmetry between the coordinate system and the metric tensor, many of the Christoffel symbols are zero. Below is a small derivation on how geodesic equation is obtained and the role of Christoffel symbols in the geodesics of a surface. Note that the Einstein's Summation notation is followed. Methods to find the geodesic equation the following needs to be solved.

$$\frac{d^2\vec{R}}{d\lambda^2} = \frac{d^2\vec{R}}{d\lambda^2}^{tangential} + \frac{d^2\vec{R}}{d\lambda^2}^{normal} \tag{E.4}$$

Now, Tangential Component = 0, on expanding the above equation one can obtain,

$$\frac{d^2R^j}{d\lambda^2} = \left(\frac{d^2u^k}{d\lambda^2} + \Gamma^k_{ij}\frac{du^i}{d\lambda}\frac{du^j}{d\lambda}\right)\frac{\partial\vec{R}}{\partial u^k} + L_{ij}\frac{du^i}{d\lambda}\frac{du^j}{d\lambda}\hat{n} \tag{E.5}$$

here, the geodesic equation is represented as,

$$\frac{d^2u^k}{d\lambda^2} + \Gamma^k_{ij}\frac{du^i}{d\lambda}\frac{du^j}{d\lambda} = 0 \tag{E.6}$$

and the Christoffel symbol is expressed as,

$$\Gamma^k_{ij} = \frac{\partial^2\vec{R}}{\partial u^j \partial u^j}.\frac{\partial\vec{R}}{\partial u^l}g^{lk} \tag{E.7}$$

Here u^i and u^j are the basis vectors and R is the position vector. And g^{lk} is the component of inverse metric tensor.

6. Covariant Derivative and Parallel Transport

Covariant Derivative

The covariant derivative in mathematics is a method of expressing a derivative along tangent vectors of a manifold. In contrast to the method provided by a main connection on the frame bundle, the covariant derivative is a manner of introducing and dealing with a connection on a manifold through the use of a differential operator[94].

Derivation:

Consider a vector field A(x^i) Writing in terms of basis vectors

$$\mathrm{d}\mathbf{A} = \mathrm{d}(\mathrm{A}^i\mathrm{d}\mathrm{e}_i) \tag{E.8a}$$

$$= (\mathrm{dA}^i)\mathrm{e}_i + \mathrm{A}^i(\mathrm{de}_i) \tag{E.8b}$$

$$= \left(\frac{\partial A^i}{\partial x^j}\mathrm{d}x^j\right)e_i + A^i\left(\frac{\partial e_i}{\partial x^j}\mathrm{d}x^j\right) \tag{E.8c}$$

$$= \left(\frac{\partial A^i}{\partial x^j}\mathrm{d}x^j\right)e_i + A^i\Gamma^k_{ij}e_k\mathrm{d}x^j \tag{E.8d}$$

$$= \left(\frac{\partial A^i}{\partial x^j} + A^i\Gamma^k_{ij}\right)e_k\mathrm{d}x^j \tag{E.8e}$$

$$= \left(\nabla_j A^k\right)e_k\mathrm{d}x^j \tag{E.8f}$$

The transformation done in the second last line is termed as the covariant derivative of a vector field $\mathbf{A}$, where Γ^k_{ij} is the Christoffel symbol.

$$\nabla_j A^k \equiv \frac{\partial \mathrm{A}^k}{\partial \mathrm{x}^j} + \mathrm{A}^i\Gamma^k_{ij} \tag{E.9}$$

Parallel Transport

Parallel transport is a technique used in geometry to move geometrical information along a manifold's geodesic paths. If the manifold has an affine connection, one can move the manifold's vectors along curves while maintaining their parallelism with regard to the connection. Thus, the parallel transport for a connection provides a means of connecting the geometries of close-by points, or in certain ways moving the local geometry of a manifold along a curve. There may be other parallel transport concepts, but this definition only refers to one method of joining the geometries of points on a curve. In actuality, parallel transport is the infinitesimal analogue of the conventional notion of connection. The connection here is referred to the covariant derivative[94]. The notion of covariant derivative is closely tied to the notion of parallel transport along

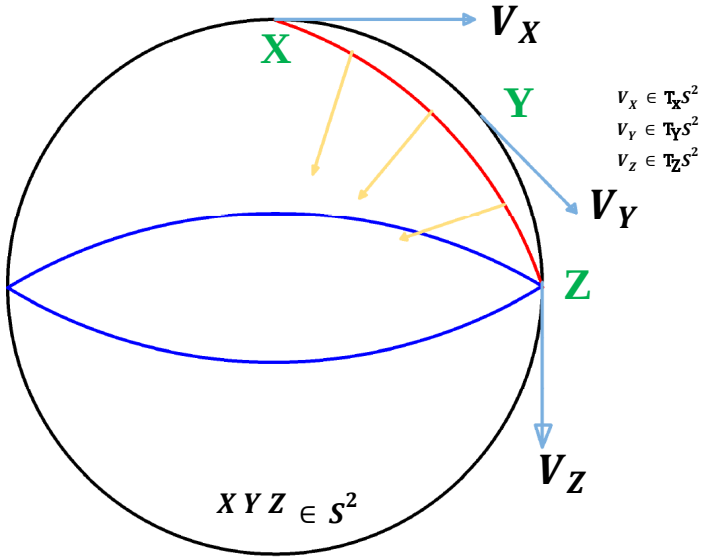

FIGURE E.3: Parallel transport of a vector in manifold, here a velocity vector is transported along three different point which has a unique tangent space

a curve. The parallel transport operator $\mathrm{P}_r^{x\to y} : \mathrm{T}_{\gamma(x)}M \to \mathrm{T}_{\gamma(y)}M$ associated with the curve $\gamma : \mathrm{I} \to \mathrm{M}$ with

$\theta \in I$, $\gamma(0) = x'$, and $u, w \in T_{x'}(u, w)$

$$G_{\gamma(t)}(P_\gamma^{0\to t}(v), P_\gamma^{0\to t}(w)) = G_{x'}(u, w) \tag{E.10}$$

The covariant derivative of a vector field $\mathrm{E} \in \mathrm{X(M)}$ in the direction ω is related to the parallel transport operator by

$$\nabla_\omega E = \frac{d}{dt} P_t^{\epsilon\to 0} E(\gamma(t))|_{t=0} \tag{E.11}$$

if vector field E satisfies the condition

$P_t^{\epsilon \to 0} E(\gamma(x)) = E(\gamma(y))$

the field $\vec{t}$ is said to be parallel along r. The parallelism term in terms of covariant derivative is

$\nabla_{\dot{\gamma}} E = 0$

A geodesic in manifold M with connection $\vec{\nabla}$ and associated parallel translation operator P^G, is a curve γ such that $\dot{\gamma}$ is parallel translated along r itself.

$$\mathrm{P}_{\gamma}^{G_{s \to t}}(\dot{\gamma(s)}) = \dot{\gamma(t)} \tag{E.12}$$

7. Exponential Mapping

In Riemannian geometry, an exponential map refers to a mapping from a subset of the tangent space T_pM of a Riemannian manifold M to the manifold itself. This exponential map is determined by the canonical affine connection established by the Riemannian metric. The geodesic equation, given by[94]

$$\ddot{x}^k + \sum_{i,j} \Gamma_{ij}^k(\gamma) \dot{x}^i \dot{x}^j = 0 \tag{E.13}$$

describes the behavior of geodesics on the manifold. For any vector V in T_xM, there exists an interval I around the origin O and a unique geodesic $\gamma(t, x) : I \to M$ such that $\gamma(0) = x$ and $\dot{\gamma} = v$. The exponential map, denoted as $\exp : T_xM \to M$, maps each vector v in the tangent space to a point on the manifold, denoted as $\exp_x v$, given by $\gamma(1; x, v)$.

A manifold M is said to be geodesically complete if the domain of the exponential map, denoted as Exp, covers the entire tangent space T_xM for every x in M.

8. Logarithmic Mapping

In Riemannian geometry, it is the inverse of the exponential mapping, such that it returns a vector which belongs to the tangent space of M which is the direction vector between two point in the manifold.

Appendix F

Kolmogorov operators on SO(3)

The expression of $p\partial_{\Psi_{ij}}q$ can be obtained from the Exponential Gradient Theorem, it is given by:

$$\begin{aligned} p\partial_{\Psi_{ij}}q &= p\partial_{\Psi_{ij}}\exp^{\Psi}q_0 \\ &= \mathrm{dexp}_{\Psi}(p_{ij})q \end{aligned} \tag{F.1}$$

Similarly, $s\partial_{\Psi_{ij}}q$ is found as $\mathrm{dexp}_{\Psi}(s_{ij})q$ And, $\partial_{\Psi_{kl}}(\partial_{\Psi_{ij}}q\partial_q f)s_{kl}s_{ij}$ is given by:

$$\begin{aligned} \partial_{\Psi_{kl}}(\partial_{\Psi_{ij}}q\partial_q f)s_{kl}s_{ij} &= \partial_{\Psi_{kl}}(\partial_q f)s_{r,ij}\partial_{\Psi_{ij}}qs_{r,kl} + (\partial_q f)\partial_{\Psi_{kl}}(\partial_{\Psi_{ij}}q)s_{r,ij}s_{r,kl} \\ &= (\partial_q(\partial_q f)\partial_{\Psi_{kl}}q + \partial_q(\partial_{\Psi_{kl}}q)\partial_q f)s_{r,ij}\partial_{\Psi_{ij}}qs_{r,kl} + (\partial_q f)s_{r,ij}s_{r,kl}\partial_{\Psi_{kl}}(\partial_{\Psi_{kl}}q) \\ &= (\partial_q\partial_q f)\mathrm{dexp}_{\Psi}(s_r)q\mathrm{dexp}_{\Psi}(s_r)q + (\partial_q f)(\mathrm{dexp}_{\Psi}(s_r)^2q + \mathrm{M}_r q) \end{aligned} \tag{F.2}$$

Where,

$$\mathrm{M_r} = \sum_{p=0}^{\infty}\sum_{q=0}^{\infty}\frac{1}{(p+q+2)}\frac{(-1)^p}{p!(q+1)!}\mathrm{ad}^{\mathrm{p}}_{\Psi}(\mathrm{ad}_{\mathrm{s_r}}(\mathrm{ad}^{\mathrm{q}}_{\Psi}(s_r))) \tag{F.3}$$

The Kolmogorov Operators can be modified as:

$$\begin{aligned} \Im^0 f &= \partial_q f\left(\mathrm{dexp}_{\Psi}(\mathrm{p})q + \tfrac{1}{2}\mathrm{dexp}_{\Psi}(s_r)^2q + \tfrac{1}{2}\mathrm{M_r}q\right) + \left(\tfrac{1}{2}\partial_q\partial_q f\mathrm{dexp}_{\Psi}(\mathrm{s_r})\mathrm{q}\right)\mathrm{dexp}_{\Psi}(\mathrm{s_r})\mathrm{q} \\ \Im^1 f &= \partial_q f\mathrm{dexp}_{\Psi}(\mathrm{s_r})q \end{aligned} \tag{F.4}$$

Substituting $f = q$, Eq.(6.47) can be written in the following form:

$$dq = \left(p_{ij}\partial_{\Psi_{ij}} + \frac{1}{2}s_{ij}s_{kl}(\partial_{\Psi_{ij}}\partial_{\Psi_{kl}})\right)q\mathrm{dt} + s_{ij}(\partial_{\Psi_{ij}})q\mathrm{dW} \tag{F.5}$$

Equating Eq.(6.45) with Eq.(F.5) and using the values obtained from Eqs.(F.3) we get:

$$\begin{aligned} a &= \left(\mathrm{dexp}_{\Psi}(\mathrm{p}) + \frac{1}{2}\mathrm{dexp}_{\Psi}(s_r)^2 + \frac{1}{2}\mathrm{M_r}\right) \\ \sigma_r &= \mathrm{dexp}_{\Psi}(\mathrm{s_r}) \end{aligned} \tag{F.6}$$

And, from Baker's Inverse Identity we get the assumed drift and diffusion matrices on the SDE which evolves in the Lie algebra $\mathfrak{so}(3)$ of the configuration Manifold. This is given by:

$$\begin{aligned}\mathbf{p} &= \mathrm{dexp}_{\Psi}^{-1}(a) - \frac{1}{2}\mathrm{dexp}_{\Psi}^{-1}(\sigma_r^2) - \frac{1}{2}\mathrm{dexp}_{\Psi}^{-1}(M_r)\\ \mathbf{s_r} &= \mathrm{dexp}_{\Psi}^{-1}(\sigma_r)\end{aligned} \tag{F.7}$$

Bibliography

[1] AJ Roffel, R Lourenco, S Narasimhan, and S Yarusevych. "Adaptive compensation for detuning in pendulum tuned mass dampers". In: *J. Struct. Eng.* 137.2 (2011), pp. 242–251.

[2] Alexey V Borisov, Ivan S Mamaev, and Ivan A Bizyaev. "The hierarchy of dynamics of a rigid body rolling without slipping and spinning on a plane and a sphere". In: *Regul. Chaotic Dyn.* 18.3 (2013), pp. 277–328.

[3] Budhaditya Hazra. "Hybrid Time and Time-Frequency Blind Source Separation Towards Ambient System Identi cation of Structures". PhD thesis. University of Waterloo, 2010.

[4] Yoon-Jae Whang. *Econometric analysis of stochastic dominance: Concepts, methods, tools, and applications*. Cambridge University Press, 2019.

[5] Taeyoung Lee, Melvin Leok, and N Harris McClamroch. "Lagrangian mechanics and variational integrators on two-spheres". In: *International Journal for Numerical Methods in Engineering* 79.9 (2009), pp. 1147–1174.

[6] GQ Li and ZH Zhu. "Long-term dynamic modeling of tethered spacecraft using nodal position finite element method and symplectic integration". In: *Celestial Mechanics and Dynamical Astronomy* 123 (2015), pp. 363–386.

[7] Darryl D Holm and Tomasz M Tyranowski. "Stochastic discrete Hamiltonian variational integrators". In: *BIT Numer. Math.* 58.4 (2018), pp. 1009–1048.

[8] Miroš Pirner. "Actual behaviour of a ball vibration absorber". In: *J. Wind Eng. Ind. Aerod.* 90.8 (2002), pp. 987–1005.

[9] Taeyoung Lee, Melvin Leok, and N Harris McClamroch. *Global formulations of Lagrangian and Hamiltonian dynamics on manifolds*. Springer, 2017.

[10] Francesco Bullo and Andrew D Lewis. *Geometric control of mechanical systems: modeling, analysis, and design for simple mechanical control systems*. Vol. 49. Springer, 2019.

[11] Budhadtiya Hazra, Ayan Sadhu, Aaron J Roffel, and Sriram Narasimhan. "Hybrid time-frequency blind source separation towards ambient system identification of structures". In: *Computer-Aided Civil and Infrastructure Engineering* 27.5 (2012), pp. 314–332.

[12] Liangkun Wang, Weixing Shi, Xiaowei Li, Quanwu Zhang, and Ying Zhou. "An adaptive-passive retuning device for a pendulum tuned mass damper considering mass uncertainty and optimum frequency". In: *Structural Control and Health Monitoring* 26.7 (2019), e2377.

[13] AJ Roffel, S Narasimhan, and T Haskett. "Performance of pendulum tuned mass dampers in reducing the responses of flexible structures". In: *Journal of Structural Engineering* 139.12 (2013), p. 04013019.

[14] Elena Celledoni and Brynjulf Owren. "Lie group methods for rigid body dynamics and time integration on manifolds". In: *Comput. Methods Appl. Mech. Eng.* 192.3-4 (2003), pp. 421–438.

[15] Tapas Tripura, Ankush Gogoi, and Budhaditya Hazra. "An Ito–Taylor weak 3.0 method for stochastic dynamics of nonlinear systems". In: *Appl. Math. Model.* 86 (2020), pp. 115–141.

[16] Breiffni Fitzgerald, Biswajit Basu, and Søren RK Nielsen. "Active tuned mass dampers for control of in-plane vibrations of wind turbine blades". In: *Structural Control and Health Monitoring* 20.12 (2013), pp. 1377–1396.

[17] Sigurd Skogestad and Ian Postlethwaite. *Multivariable feedback control: analysis and design*. Vol. 2. Wiley New York, 2007.

[18] Vikram Pakrashi, Alan O'Connor, and Biswajit Basu. "Effect of tuned mass damper on the interaction of a quarter car model with a damaged bridge". In: *Structure and Infrastructure Engineering* 6.4 (2010), pp. 409–421.

[19] Saptarshi Sarkar, Breiffni Fitzgerald, Biswajit Basu, and Arunasis Chakraborty. "Magneto-rheological Tuned Liquid Column Dampers to Improve Reliability of Wind Turbine Towers". In: *Advances in Rotor Dynamics, Control, and Structural Health Monitoring: Select Proceedings of ICOVP 2017*. Springer. 2020, pp. 467–496.

[20] Peter E Kloeden and Eckhard Platen. *Numerical Solution of Stochastic Differential Equations, First ed., Vol. 23*. Stochastic Modelling and Applied Probability. Springer-Verlag Berlin Heidelberg, 1992.

[21] Elena Celledoni, Håkon Marthinsen, and Brynjulf Owren. "An introduction to Lie group integrators–basics, new developments and applications". In: *J. Comput. Phys.* 257 (2014), pp. 1040–1061.

[22] Goran Marjanovic and Victor Solo. "Numerical methods for stochastic differential equations in matrix lie groups made simple". In: *IEEE Trans. Autom. Control* 63.12 (2018), pp. 4035–4050.

[23] M Ableidinger and E Buckwar. "Weak stochastic Runge–Kutta Munthe-Kaas methods for finite spin ensembles". In: *Appl. Numer. Math.* 118 (2017), pp. 50–63.

[24] Elena Celledoni, Ergys Çokaj, Andrea Leone, Davide Murari, and Brynjulf Owren. "Lie Group integrators for mechanical systems". In: *Int. J. Comput. Math.* 99.1 (2022), pp. 58–88.

[25] Vladimir Semenovich Pugachev and Igor Nikolaevich Sinitsyn. *Stochastic systems: theory and applications*. World Scientific Publishing Company, 2002.

[26] Rodrigo Astroza, Hamed Ebrahimian, and Joel P Conte. "Material parameter identification in distributed plasticity FE models of frame-type structures using nonlinear stochastic filtering". In: *Journal of Engineering Mechanics* 141.5 (2014), p. 04014149.

[27] Stefano Soatto, Ruggero Frezza, and Pietro Perona. "Motion estimation via dynamic vision". In: *IEEE Trans. Autom. Control* 41.3 (1996), pp. 393–413.

[28] Krystyna Twardowska. "Wong-Zakai approximations for stochastic differential equations". In: *Acta Appl. Mathe.* 43.3 (1996), pp. 317–359.

[29] Debasish Roy and G Visweswara Rao. *Stochastic dynamics, filtering and optimization*. Cambridge University Press, 2017.

[30] B Hazra, AJ Roffel, S Narasimhan, and MD Pandey. "Modified cross-correlation method for the blind identification of structures". In: *Journal of Engineering Mechanics* 136.7 (2010), pp. 889–897.

[31] Budhaditya Hazra and Sriram Narasimhan. "Gear fault diagnosis using synchro-squeezing transform based feature analysis". In: *Key Engineering Materials*. Vol. 569. Trans Tech Publ. 2013, pp. 449–456.

[32] B Bhowmik, T Tripura, B Hazra, and V Pakrashi. "Robust linear and nonlinear structural damage detection using recursive canonical correlation analysis". In: *Mechanical Systems and Signal Processing* 136 (2020), p. 106499.

[33] B Bhowmik, T Tripura, B Hazra, and V Pakrashi. "Real time structural modal identification using recursive canonical correlation analysis and application towards online structural damage detection". In: *Journal of Sound and Vibration* 468 (2020), p. 115101.

[34] Basuraj Bhowmik, Tapas Tripura, Budhaditya Hazra, and Vikram Pakrashi. "First-order eigenperturbation techniques for real-time damage detection of vibrating systems: Theory and applications". In: *Applied Mechanics Reviews* 71.6 (2019).

[35] B Hazra, A Sadhu, AJ Roffel, PE Paquet, and S Narasimhan. "Underdetermined blind identification of structures by using the modified cross-correlation method". In: *Journal of engineering mechanics* 138.4 (2012), pp. 327–337.

[36] Rune Brincker and Carlos Ventura. *Introduction to operational modal analysis*. John Wiley & Sons, 2015.

[37] Matthew S Allen, Michael W Sracic, Shashank Chauhan, and Morten Hartvig Hansen. "Output-only modal analysis of linear time-periodic systems with application to wind turbine simulation data". In: *Mechanical Systems and Signal Processing* 25.4 (2011), pp. 1174–1191.

[38] Rahul Rana and TT Soong. "Parametric study and simplified design of tuned mass dampers". In: *Engineering structures* 20.3 (1998), pp. 193–204.

[39] Anant Hegde, Jose C Principe, Deniz Erdogmus, Umut Ozertem, Yadunandana N Rao, and Hemanth Peddaneni. "Perturbation-based eigenvector updates for on-line principal components analysis and canonical correlation analysis". In: *Journal of VLSI signal processing systems for signal, image and video technology* 45.1-2 (2006), pp. 85–95.

[40] M Krishnan, B Bhowmik, B Hazra, and V Pakrashi. "Real time damage detection using recursive principal components and time varying auto-regressive modeling". In: *Mechanical Systems and Signal Processing* 101 (2018), pp. 549–574.

[41] Tapas Tripura, Basuraj Bhowmik, Vikram Pakrashi, and Budhaditya Hazra. "Real-time damage detection of degrading systems". In: *Structural Health Monitoring* 19.3 (2020), pp. 810–837.

[42] M Mirmomeni, C Lucas, BN Araabi, B Moshiri, and MR Bidar. "Recursive spectral analysis of natural time series based on eigenvector matrix perturbation for online applications". In: *IET signal processing* 5.6 (2011), pp. 515–526.

[43] P Thomas Fletcher, Conglin Lu, Stephen M Pizer, and Sarang Joshi. "Principal geodesic analysis for the study of nonlinear statistics of shape". In: *IEEE transactions on medical imaging* 23.8 (2004), pp. 995–1005.

[44] Valentin Duruisseaux, Thai Duong, Melvin Leok, and Nikolay Atanasov. "Lie Group Forced Variational Integrator Networks for Learning and Control of Robot Systems". In: *arXiv preprint arXiv:2211.16006* (2022).

[45] Leonardo Colombo, Manuela Gamonal Fernández, and David Martín de Diego. "Variational integrators for non-autonomous Lagrangian systems". In: *J. Comput. Appl. Math.* 424 (2023), p. 114966.

[46] Zhenyu Wang, Qiang Ma, Zhen Yao, and Xiaohua Ding. "The Magnus expansion for stochastic differential equations". In: *J. Nonlinear Sci.* 30.1 (2020), pp. 419–447.

[47] Gregory S Chirikjian. *Stochastic models, information theory, and Lie groups, volume 2: Analytic methods and modern applications*. Vol. 2. Springer Science & Business Media, 2011.

[48] Peter Kloeden and Eckhard Platen. "Numerical methods for stochastic differential equations". In: *Stochastic Hydrology and Hydraulics* 5.2 (1991), pp. 172–172.

[49] Peter E Kloeden and Eckhard Platen. "Stratonovich and Itô stochastic taylor expansions". In: *Mathematische Nachrichten* 151.1 (1991), pp. 33–50.

[50] Leo Dostal and Navaratnam Sri Namachchivaya. "First passage time of nonlinear diffusion processes with singular boundary behavior". In: *J. Sound Vib.* 476 (2020), p. 115284.

[51] Mircea Grigoriu. *Stochastic calculus: applications in science and engineering*. Springer Science & Business Media, New York, 2013.

[52] Vladimir G. Ivancevic and Tijana T. Ivancevic. *Lecture Notes in Lie Groups,* arXiv:1104.1106. 2011. arXiv: 1104.1106 [math.DG].

[53] Simone Fiori, Italo Cervigni, Mattia Ippoliti, and Claudio Menotta. "Synthetic nonlinear second-order oscillators on Riemannian manifolds and their numerical simulation". In: *Discrete & Continuous Dynamical Systems-B* 27.3 (2022), p. 1227.

[54] Jérémie Deray and Joan Solà. "Manif: A micro Lie theory library for state estimation in robotics applications". In: *Journal of Open Source Software* 5.46 (2020), p. 1371. DOI: 10.21105/joss.01371. URL: https://doi.org/10.21105/joss.01371.

[55] Fereidoun Amini and Vida Ghasemi. "Adaptive modal identification of structures with equivariant adaptive separation via independence approach". In: *Journal of Sound and Vibration* 413 (2018), pp. 66–78.
[56] AJ Roffel, R Lourenco, S Narasimhan, and S Yarusevych. "Adaptive compensation for detuning in pendulum tuned mass dampers". In: *Journal of Structural Engineering* 137.2 (2010), pp. 242–251.
[57] A Sadhu, B Hazra, and S Narasimhan. "Decentralized modal identification of structures using parallel factor decomposition and sparse blind source separation". In: *Mechanical Systems and Signal Processing* 41.1-2 (2013), pp. 396–419.
[58] Gene H Golub and Charles F Van Loan. *Matrix computations*. Vol. 3. JHU press, 2012.
[59] Tosio Kato. *Perturbation theory for linear operators*. Vol. 132. Springer Science & Business Media, 2013.
[60] Wenliang Zhou and David Chelidze. "Generalized eigenvalue decomposition in time domain modal parameter identification". In: *Journal of Vibration and Acoustics* 130.1 (2008).
[61] Gilbert W Stewart. "Error and perturbation bounds for subspaces associated with certain eigenvalue problems". In: *SIAM review* 15.4 (1973), pp. 727–764.
[62] Liangyue Cao. "Practical method for determining the minimum embedding dimension of a scalar time series". In: *Physica D: Nonlinear Phenomena* 110.1-2 (1997), pp. 43–50.
[63] Jeremy Schmitt. "Stochastic Variational Integrators". In: ().
[64] Boris A Kuperschmidt. *The variational principles of dynamics*. Vol. 13. World Scientific Publishing Company, 1992.
[65] Mario Di Paola and Giovanni Falsone. "Stochastic dynamics of nonlinear systems driven by non-normal delta-correlated processes". In: (1993).
[66] Wilhelm Magnus. "On the exponential solution of differential equations for a linear operator". In: *Commun. Pure Appl. Math.* 7.4 (1954), pp. 649–673.
[67] Robert J Burston. "Earth-like planetary magnetotails as non-linear oscillators". In: *Annales Geophysicae Discussions* (2020), pp. 1–32.
[68] Shinya Aoi and Kazuo Tsuchiya. "Locomotion control of a biped robot using nonlinear oscillators". In: *Autonomous robots* 19.3 (2005), pp. 219–232.
[69] Lautaro Cilenti and Balakumar Balachandran. "Transient probability in basins of noise influenced responses of mono and coupled Duffing oscillators". In: *Chaos: An Interdisciplinary Journal of Nonlinear Science* 31.6 (2021), p. 063117.
[70] Lautaro Cilenti, Maria Cameron, and Balakumar Balachandran. "Most probable escape paths in periodically driven nonlinear oscillators". In: *Chaos: An Interdisciplinary Journal of Nonlinear Science* 32.8 (2022), p. 083140.
[71] Jiandong Zhu. "High-dimensional Kuramoto model limited on smooth curved surfaces". In: *Phys. Lett. A* 378.18-19 (2014), pp. 1269–1280.
[72] Max Lipton, Renato Mirollo, and Steven H Strogatz. "The Kuramoto model on a sphere: Explaining its low-dimensional dynamics with group theory and hyperbolic geometry". In: *Chaos* 31.9 (2021), p. 093113.
[73] Lapo Casetti, Marco Pettini, and EGD Cohen. "Geometric approach to Hamiltonian dynamics and statistical mechanics". In: *Physics Reports* 337.3 (2000), pp. 237–341.
[74] Darryl D Holm. "Variational principles for stochastic fluid dynamics". In: *Proceedings of the Royal Society A: Mathematical, Physical and Engineering Sciences* 471.2176 (2015), p. 20140963.
[75] Jialin Hong and Liying Sun. *Symplectic integration of stochastic Hamiltonian systems*. Vol. 2314. Springer Nature, 2023.
[76] Cristina Anton. "Explicit pseudo-symplectic Runge-Kutta methods for stochastic Hamiltonian systems". In: *Applied Numerical Mathematics* 185 (2023), pp. 18–37.

[77] Raffaele D'Ambrosio and Stefano Di Giovacchino. "Long-term analysis of stochastic Hamiltonian systems under time discretizations". In: *SIAM Journal on Scientific Computing* 45.2 (2023), A257–A288.

[78] Cristina Anton. "Explicit pseudo-symplectic methods based on generating functions for stochastic Hamiltonian systems". In: *Journal of Computational and Applied Mathematics* 373 (2020), p. 112433.

[79] Qingyi Zhan, Jinqiao Duan, Xiaofan Li, and Yuhong Li. "Symplectic numerical integration for Hamiltonian stochastic differential equations with multiplicative Lévy noise in the sense of Marcus". In: *Mathematics and Computers in Simulation* 215 (2024), pp. 420–439.

[80] Grigori N Milstein, Yu M Repin, and Michael V Tretyakov. "Numerical methods for stochastic systems preserving symplectic structure". In: *SIAM Journal on Numerical Analysis* 40.4 (2002), pp. 1583–1604.

[81] Jian Deng, Cristina Anton, and Yau Shu Wong. "High-order symplectic schemes for stochastic Hamiltonian systems". In: *Communications in Computational Physics* 16.1 (2014), pp. 169–200.

[82] Simeon Ola Fatunla. *Numerical methods for initial value problems in ordinary differential equations*. Academic Press, 2014.

[83] Weidong Zhao, Yu Fu, and Tao Zhou. "New kinds of high-order multistep schemes for coupled forward backward stochastic differential equations". In: *SIAM Journal on Scientific Computing* 36.4 (2014), A1731–A1751.

[84] David Francis Griffiths and Desmond J Higham. *Numerical methods for ordinary differential equations: initial value problems*. Vol. 5. Springer, 2010.

[85] John Charles Butcher. *Numerical methods for ordinary differential equations*. John Wiley & Sons, 2016.

[86] Julien Tranchida, Steven J Plimpton, Pascal Thibaudeau, and Aidan P Thompson. "Massively parallel symplectic algorithm for coupled magnetic spin dynamics and molecular dynamics". In: *Journal of Computational Physics* 372 (2018), pp. 406–425.

[87] Grigori N Milstein, Yu M Repin, and Michael V Tretyakov. "Symplectic integration of Hamiltonian systems with additive noise". In: *SIAM J. Numer. Anal.* 39.6 (2002), pp. 2066–2088.

[88] Nikolaj Nordkvist and Poul G Hjorth. "Classical mechanics and symplectic integration". In: *Classical Mechanics and Symplectic Integration*. 2005.

[89] Ernst Hairer, Christian Lubich, and Gerhard Wanner. *Geometric Numerical integration: structure-preserving algorithms for ordinary differential equations*. Springer, 2006.

[90] Mauricio C Oliveira and Robert E Skelton. *Tensegrity systems*. Springer, 2009.

[91] Ovidiu Calin and Der-Chen Chang. *Geometric mechanics on Riemannian manifolds: applications to partial differential equations*. Springer, 2005.

[92] Constantin Udriste and Ionel Tevy. "Geometric dynamics on Riemannian manifolds". In: *Mathematics* 8.1 (2020), p. 79.

[93] Simone Fiori. "Extended Hamiltonian learning on Riemannian manifolds: Theoretical aspects". In: *IEEE transactions on neural networks* 22.5 (2011), pp. 687–700.

[94] Simone Fiori. "Nonlinear damped oscillators on Riemannian manifolds: Fundamentals". In: *Journal of Systems Science and Complexity* 29 (2016), pp. 22–40.

[95] Syed Altaf Ganihar, Shreyas Joshi, Shankar Shetty, and Uma Mudenagudi. "Metric tensor and christoffel symbols based 3d object categorization". In: *ACM SIGGRAPH 2014 Posters*. 2014, pp. 1–1.

[96] Sebastian Echeandia and Patrick M Wensing. "Numerical methods to compute the coriolis matrix and christoffel symbols for rigid-body systems". In: *Journal of Computational and Nonlinear Dynamics* 16.9 (2021), p. 091004.

[97] Rudrasis Chakraborty and Baba C Vemuri. "Statistics on the Stiefel manifold: theory and applications". In: (2019).

[98] Bin Gao, Nguyen Thanh Son, P-A Absil, and Tatjana Stykel. "Riemannian optimization on the symplectic Stiefel manifold". In: *SIAM Journal on Optimization* 31.2 (2021), pp. 1546–1575.

[99] Pavan Turaga, Ashok Veeraraghavan, Anuj Srivastava, and Rama Chellappa. "Statistical computations on Grassmann and Stiefel manifolds for image and video-based recognition". In: *IEEE Transactions on Pattern Analysis and Machine Intelligence* 33.11 (2011), pp. 2273–2286.

[100] Tetsuya Kaneko, Simone Fiori, and Toshihisa Tanaka. "Empirical arithmetic averaging over the compact Stiefel manifold". In: *IEEE Transactions on Signal Processing* 61.4 (2012), pp. 883–894.

[101] Lei Xu, Erkki Oja, and Ching Y Suen. "Modified Hebbian learning for curve and surface fitting". In: *Neural Networks* 5.3 (1992), pp. 441–457.

[102] Elena Celledoni and Simone Fiori. "Neural learning by geometric integration of reduced 'rigid-body'equations". In: *Journal of computational and applied mathematics* 172.2 (2004), pp. 247–269.

[103] Jiho Yoo and Seungjin Choi. "Orthogonal nonnegative matrix factorization: Multiplicative updates on Stiefel manifolds". In: *International conference on intelligent data engineering and automated learning*. Springer. 2008, pp. 140–147.

[104] Kenneth Kreutz-Delgado and Bhaskar D Rao. "Sparse basis selection, ICA, and majorization: Towards a unified perspective". In: *1999 IEEE International Conference on Acoustics, Speech, and Signal Processing. Proceedings. ICASSP99 (Cat. No. 99CH36258)*. Vol. 2. IEEE. 1999, pp. 1081–1084.

[105] Alan Edelman, Tomás A Arias, and Steven T Smith. "The geometry of algorithms with orthogonality constraints". In: *SIAM journal on Matrix Analysis and Applications* 20.2 (1998), pp. 303–353.

[106] Lars Eldén and Haesun Park. "A Procrustes problem on the Stiefel manifold". In: *Numerische Mathematik* 82.4 (1999), pp. 599–619.

[107] XZ Cheng, MBA Jalil, and Hwee Kuan Lee. "Time-quantified monte carlo algorithm for interacting spin array micromagnetic dynamics". In: *Physical Review B* 73.22 (2006), p. 224438.

[108] Seung-Yeal Ha, Myeongju Kang, and Dohyun Kim. "Emergent behaviors of high-dimensional Kuramoto models on Stiefel manifolds". In: *Automatica* 136 (2022), p. 110072.

[109] B Bhowmik, M Krishnan, B Hazra, and V Pakrashi. "Online Damage Detection using Recursive Principal Component Analysis". In: *Procedia engineering* 199 (2017), pp. 2108–2113.

[110] Mario A DE Oliveira and Daniel J Inman. "PCA-based method for damage detection exploring electromechanical impedance in a composite beam". In: *Structural Health Monitoring 2015* (2015).

[111] Weihua Li, H Henry Yue, Sergio Valle-Cervantes, and S Joe Qin. "Recursive PCA for adaptive process monitoring". In: *Journal of process control* 10.5 (2000), pp. 471–486.

[112] Manish Misra, H Henry Yue, S Joe Qin, and Cheng Ling. "Multivariate process monitoring and fault diagnosis by multi-scale PCA". In: *Computers & Chemical Engineering* 26.9 (2002), pp. 1281–1293.

[113] A-M Yan, Gaëtan Kerschen, P De Boe, and J-C Golinval. "Structural damage diagnosis under varying environmental conditions—part II: local PCA for non-linear cases". In: *Mechanical Systems and Signal Processing* 19.4 (2005), pp. 865–880.

[114] M Krishnan, B Bhowmik, AK Tiwari, and B Hazra. "Online damage detection using recursive principal component analysis and recursive condition indicators". In: *Smart Materials and Structures* 26.8 (2017), p. 085017.

[115] P.T. Fletcher, Conglin Lu, S.M. Pizer, and Sarang Joshi. "Principal geodesic analysis for the study of nonlinear statistics of shape". In: *IEEE Transactions on Medical Imaging* 23.8 (2004), pp. 995–1005. DOI: 10.1109/TMI.2004.831793.

[116] Xavier Pennec, Stefan Sommer, and Tom Fletcher. *Riemannian geometric statistics in medical image analysis*. Academic Press, 2019.

[117] Xavier Pennec. "Intrinsic statistics on Riemannian manifolds: Basic tools for geometric measurements". In: *Journal of Mathematical Imaging and Vision* 25 (2006), pp. 127–154.

[118] Hermann Karcher. "Riemannian center of mass and mollifier smoothing". In: *Communications on pure and applied mathematics* 30.5 (1977), pp. 509–541.

[119] P Thomas Fletcher and Sarang Joshi. "Riemannian geometry for the statistical analysis of diffusion tensor data". In: *Signal Processing* 87.2 (2007), pp. 250–262.

[120] Thomas Schürmann. "On momentum operators given by Killing vectors whose integral curves are geodesics". In: *Physics* 4.4 (2022), pp. 1440–1452.

[121] David George Kendall, Dennis Barden, Thomas K Carne, and Huiling Le. *Shape and shape theory*. John Wiley & Sons, 2009.

[122] BF Feeny and R Kappagantu. "On the physical interpretation of proper orthogonal modes in vibrations". In: *Journal of sound and vibration* 211.4 (1998), pp. 607–616.

[123] Ivo Babuška and John Osborn. "Eigenvalue problems". In: (1991).

[124] Tsuyoshi Idé and Hisashi Kashima. "Eigenspace-based anomaly detection in computer systems". In: *Proceedings of the tenth ACM SIGKDD international conference on Knowledge discovery and data mining*. 2004, pp. 440–449.

[125] Andrew N Pressley. *Elementary differential geometry*. Springer Science & Business Media, 2010.

List of Publications

Scholarly Contributions Stemming from my Ph.D. research

1. **Panda, S**; Hazra, B: Symplectic Geometric Integration for Stochastically excited Hamiltonian systems on General Manifolds, Mechanical Systems and Signal Processing (Manuscript Submitted)

2. **Panda, S**; Prasad, R; Hazra, B (2023): A new symplectic integrator for stochastic Hamiltonian systems on manifolds, Probabilistic Engineering Mechanics 2023, p.103526.

3. **Panda, S**., Gogoi, A., Hazra, B., & Pakrashi, V. (2023). Geometry preserving Ito-Taylor formulation for stochastic hamiltonian dynamics on manifolds. Applied Mathematical Modelling, 119, 626-647.

4. **Panda, S**. and Hazra, B., 2023. Stochastic dynamics on manifolds based on novel geometry preserving Ito–Taylor scheme. Journal of Sound and Vibration, 550, p.117599.

5. **Panda S**, Tripura T and Hazra B. First order error-adapted eigen perturbation for real-time modal identification of vibrating structures. Journal of Vibration and Acoustics 2021; 1–25.

Publications Beyond My Ph.D. Thesis

1. **Panda S**, Gogoi A, Hazra B and Pakrashi V. A novel mean square formulation of stochastic nonlinear dynamic systems based on Adomian decomposition. Probabilistic Engineering Mechanics 2023;

2. **Panda S** and Hazra B. Single-sensor analytics for real-time monitoring of dynamical systems through error-feedback mechanism VETOMAC 2022. (Conference Presented)

3. **Panda S**, Tripura T and Hazra B. Online damage detection of earthquake exited structure based on near real-time envelope extraction. Structural Health Monitoring 2022;

4. **Panda S**, Bhowmik B, Hazra B and Pakrashi V. Feedback-driven error-corrected single-sensor analytics for real-time condition monitoring. International Journal of Mechanical Sciences 2022;

5. Gogoi A, **Panda S** and Hazra B. A computational framework for mean square responses of bidirectional nonlinear systems under correlated stochastic excitation. Journal of sound and vibration 2022.

6. **Panda, S**; Shivakumar, D; Majumder, Y; Gupta, CN; Hazra, B (2023): Probabilistic dynamic brain response to live Indian classical vocal stimulus. TechRxiv. Preprint.

7. **Panda, S**., Das, S., Bhowmik, B., Hazra, B. (2023). Mastering Complex Modes: A New Method for Real-Time Modal Identification of Vibrating Systems. ArXiv. /abs/2303.17349.